Dispergierte Fluoreszenzspektroskopie von isolierten Aromaten und wasserstoffbrückengebundenen Clustern in der Gasphase

INAUGURAL-DISSERTATION

zur Erlangung des Doktorgrades
der Mathematisch-Naturwissenschaftlichen Fakultät
der Heinrich-Heine-Universität Düsseldorf
vorgelegt von

Christian Henrichs
aus Hamm

Düsseldorf, Februar 2021

Gedruckt mit der Genehmigung der
Mathematisch-Naturwissenschaftlichen Fakultät der
Heinrich-Heine-Universität Düsseldorf

Berichterstatter:

1. Professor Dr. Michael Schmitt
2. Professor Dr. Rainer Weinkauf

Tag der mündlichen Prüfung: 10.03.2021

Dispersed fluorescence spectroscopy of isolated aromatics and hydrogen-bonded clusters in the gas phase

by
Christian Henrichs

Dissertation in chemistry

created on
Institute for Physical Chemistry and Electrochemistry I
Chair for High Resolution UV Laser Spectroscopy

submitted to the
Mathematical and Natural Sciences Faculty of
Heinrich-Heine-University Düsseldorf

February 2021

Das Leben ist eine Komödie; geschrieben von einem humoristischen Sadisten

Café Society

Contents

1 Symbols and Abbreviations

Physical constants from Reference[1]

h	Planck constant $h = 6.62607015 \cdot 10^{-34}\ Js$
$\hbar$	reduced Planck constant $\hbar = h/2\pi = 1.054571817 \cdot 10^{-34}\ Js$
e_0	Elementary charge $e = 1.602176634 \cdot 10^{-19}\ C$
k_B	Boltzmann constant $k_B = 1.380649 \cdot 10^{-23}\ JK^{-1}$
R_0	molar gas constant $R_0 = 8.314462618\ JK^{-1}mol^{-1}$
m_{el}	Mass of the electron $m_{el} = 9.1093837015(28) \cdot 10^{-31}\ kg$
ϵ_0	Vacuum electric permittivity $\epsilon_0 = 8.8541878128 \cdot 10^{-12}\ Fm^{-1}$
a_0	Bohr radius $a_0 = 4\pi\epsilon_0\hbar^2/\epsilon_0^2 m_{el} = 5.29177210903 \cdot 10^{-11}\ m$
c	Speed of light in vacuum $c = 299792458\ ms^{-1}$
R_∞	Rydberg constant $R_\infty = m_{el}\epsilon_0^4/8h^3c\epsilon_0^2 = 1097731.568160\ m^{-1}$
E_h	Hartree energy $E_h = 2hcR_\infty = 4.3597447222071(85) \cdot 10^{-18}\ J$

Methods and equipment

LIF	Laser induced fluorescence
HRLIF	High resolution laser induced fluorescence
DF	Dispersed fluorescence
HF	Hartree-Fock theory
ICCD	Intensified Charge-Coupled Device
YAG	Yttrium Aluminium Garnet
BBO	Beta Barium Borate
KDP	Potassium Dihydrogen Phosphate
SHG	Second Harmonic Generation
THG	Third Harmonic Generation
DFT	Density Functional Theory
MP2	Møller-Plesset pertubation theory
CCSD	Coupled-Clusters Singles and Doubles
CC2	second-order approximate coupled cluster singles and doubles model
RI	Resolution of the Identity
SCS	Spin-Component Scaling
cc-pVTZ	Correlation Consistent Polarised Valence Triple Zeta Basis Set
FC	Franck-Condon

Mathematical components

ρ	Electron Density
P	Density matrix of a molecule
S	Atomic orbital overlap matrix
$\hat{H}$	Hamilton Operator
∇	Nabla Operator
∇^2	Laplacian Operator
$\hat{F}$	Fock Operator
$\hat{J}$	Coulomb Operator
$\hat{K}$	Exchange Operator
N	Normalization Constant
H_ν	Hermite Polynomial
S	Duschinsky Matrix
L	Transformation Matrix Containing the Eigenvectors of the Duschinsky Matrix
T	Hougen-Watson Axis Switching Matrix
C	Displacement Matrix
λ_ω	Matrix in Form $\lambda_\omega = diag(\sqrt{\omega_1}\sqrt{\omega_2}\cdots\sqrt{\omega_N})$
P	Transformation Matrix $P = JQJ^T$
R	Transformation Matrix $R = QJ^T$
Q	Transformation Matrix $Q = (1 + J^T J)^{-1}$
J	Transformation Matrix $J = \lambda_{\omega''} S \lambda_{\omega'}^{-1}$
δ	Vector $\delta = \dfrac{\lambda_{\omega'} d}{\sqrt{\hbar}}$

Variables and Parameters

ν	Frequency [Hz]
$\tilde{\nu}$	Frequency [cm^{-1}]
λ	Wavelength [nm]
E	Energy (of different components e.g. electronic state)
τ	Lifetime
k	Rate Constant
ζ	Orbital Exponent
Z	Nuclear Charge
R	Cartesian Coordinate/Distance of Nuclei (R) or Electrons (r)
ρ	Electron Density
q	Mass-weighted Cartesian Coordinate
Q	Normal Coordinate

FC	Franck-Condon Factor
I	Intensity
T	Temperatur [K]
K_n	Knudsen Number
d	Nozzlediameter
d_{mol}	Diameter of the Molecule
p	Pressure
I_{Ph}	Photoinduced current
ϕ_e	Quantum efficiency
η_λ	Quantum yield
U	Voltage
Z	Nuclear charge
n	Density
λ	Eigenvalue of a Matrix
Ψ	Total Wavefunction
ψ	Partial Wavefunction (with a Subscript)
ν	Vibrational State (with a Superscript)
el	Electronic (as a Subscript)
vib	Vibratory (as a Subscript)
rot	Rotationally (as a Subscript)
mol	Molecular Property (as a Subscript/Superscript)
k	Core Property (as a Subscript)
$''$	Ground State (as a Superscript)
$'$	Excited State or occupied Spin-Orbital (as a Superscript)

General Abbreviations

S	Singlet State
T	Triplet State
Fl	Fluorescence
Ph	Phosphorescence
VR	Vibrational Relaxation
IC	Internal Conversion
ISC	Intersystem Crossing
IVR	Internal Vibrational Redistribution
Ex	Excitation (as a Subscript)
Em	Emission (as a Subscript)
UV	Ultraviolet

2 Introduction

To determine the molecular structure, the nuclear and the electronic parameter of the molecule can be investigated by different techniques of spectroscopy. Different measurement methods like microwave, infrared or ultraviolet spectroscopy vary in their technical realization and are routinely used to investigate the properties of the ground state of molecules. The electronic excited state molecular properties are more challenging to investigate. On account of the importance of excited states for many chemical, biochemical, but also technical applications, the experimental and theoretical investigation of excited electronic states is a very important field of research. Since theoretical methods have been improved considerably in recent years, it is particularly interesting to compare experimental with theoretical data. To determine the excited state geometry and the differences between theoretical and experimental data and their accuracy is the aim of this work.
The investigation of excited states raises a series of problems. First of all the energetic distance between excited electronic states can be small, which causes a coupling between two or more states and their interaction. In this work, this problem occurs mainly with the substituted indoles, since the two electronic states are very close to each other and can therefore exchange their energetic order with different substitution positions. Furthermore, the N dimensionality of the molecules must be considered. A molecule with N atoms has a structure that can be represented by 3N-6 coordinates in the excited state. In the case of the simple indole, this means 42 coordinates that have to be determined. This is challenging with the help of both theoretical and experimental data. It should be noted that not enough experimental data for the electronically excited state can be determined from one experiment. Thus, the structure of the electronically excited state can be achieved with a combination of different data sets. Namely, from a combination of theoretical data with the rotational constants from the high-resolution laser-induced fluorescence spectroscopy and the vibronic transition intensities in dispersed fluorescence spectra. The geometry from the ab initio calculations is used as a starting point and can be distorted stepwise. This distortion can be confirmed with the help of the experimental data. As a result, an improvement of the theoretical values is possible with the help of the experimentally determined parameters. Electronic spectroscopy, like fluorescence spectroscopy, is a powerful tool to describe these parameters of molecules. In this work the fluorescence spectroscopy in supersonic jets is used to investigate, both the ground and excited state properties, due to their reachability by absorption and the resulting observeable fluorescence. The method which is used is the *dispersed fluorescence*. The used frequency doubled laser light in the UV spectral region ($\sim$ 33000-38000 cm^{-1}), tuneable with different dyes, excites the molecule to different vibrations of the first electronic excited state. Due to the supersonic co-expansion measurement conditions the *fluorescence* is the predominant pathway for the molecule to relax in the electronic ground state. The excitation energy can be subtracted from the fluorescence energy, making the spectral region around 3000 cm^{-1} reachable. Thus, the fingerprint region is accessible at 500 - 1500 cm^{-1}, which contains many vibrations, which carry structural

information. Another way to access this region is absorption spectroscopy. Due to the need of THz detectors and narrowband light sources this method is more expensive and only quantum cascade lasers or free electron lasers achieve good results.[2–5]
In this work, the ground state and the first excited electronic state structure of two molecular systems are investigated, which are otherwise used as common building blocks in organic and biochemistry.

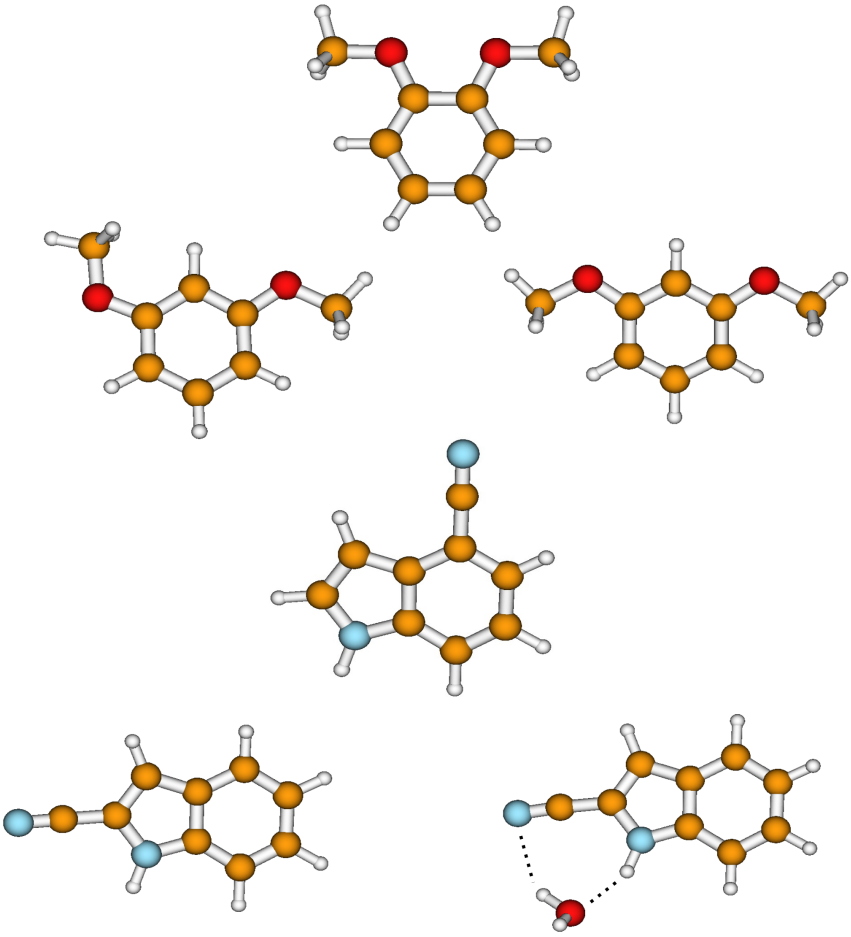

Figure 1: All investigated systems in this work. Starting in the top with 1,2-dimethoxybenzene, both rotamers of 1,3-dimethoxybenzene, 4-cyanoindole, 2-cyanoindole and the one water 2-cyanoindole cluster.

The first system is the disubstituted benzene. The two structural isomers of dimethoxybenzene, the 1,2-dimethoxybenzene (1,2-DMB) and the 1,3-dimethoxybenzene (1,3-DMB), are of great interest due to investigation of effects of different substituted position at the benzene molecule and their effect on the excited state geometry. The electron-donating effect of the methoxy groups differs between the two relative positions in the benzene ring and this allows an examination of their effect on the heavy atom frame upon electronic excitation. The accuracy of the excited state structure is improved by the use of rotational constants of the molecule without and with deuterisation

in different positions, which also stem from our working group. In case of the dimethoxybenzenes for both molecules the dimethoxy groups have been deuterated. The rotational constants of 1,2-DMB could be obtained for the deuterated as well as for the undeuterated species.[6] The results for the 1,3-DMB are still pending.

The second system are the cyanoindoles. Substituted indoles are very interesting systems in terms of excited states, since they are close to each other and can exchange their position through substitution and interstate coupling can occur. Hence, excited state calculations of substituted indoles are a real challenge for theory. The indole is substituted at the second position in case of the 2-cyanoindole (2-CI) and at the fourth position in case of the 4-cyanoindole (4-CI). The two lowest electronic excited states in indoles can be determined as $^1\mathrm{L}_a/^1\mathrm{L}_b$ due to the nomenclature of Platt.[7] In case of the 2-cyanoindole the cluster with one water molecule was investigated.

The rotational constants for the cyanoindoles were determined by Hebestreit *et al.*.[8,9] All investigated systems are represented in figure 1.

For the investigated molecules, the geometry change upon electronic excitation can be reached stepwise by analysing and evaluating the measured dispersed fluorescence spectra with a *Franck-Condon analysis*. If finally the intensities of the vibronic transitions, observed in the *laser induced fluorescence* spectra, agree within the experimental error to these calculated with the Franck-Condon factors from the new structure, the excited electronic state geometry is successfully improved. Hence, with the help of a start geometry and rotational constants, the absorption and the dispersed fluorescence intensity pattern allow to find an improvement of the theoretically predicted geometry change which happens upon electronic excitation. This method is described in chapter 4.9 and the program FC_{FIT}, written previously in our workgroup, is used to achieve the geometry change from the line intensities in the dispersed fluorescence spectra.

The starting geometries of both electronic states are calculated at the second order coupled cluster (CC2) level of theory with the $Turbomole$ progam package. The methods and the theoretical background for the quantum mechanical calculations is given in chapter 4. Due to an improvement of the fit with the addition of rotational constant changes of investigated molecules these are determined with high resolution laser induced fluorescence spectroscopy in our workgroup. Additionally possible isotopologes and their rotational constants can be measured and have been included.

Chapter three describes the theortical background of the measurement principle, taking into account the laser principle with special reference to the measurement techniques of laser-induced and dispersed fluorescence spectroscopy. The theoretical background of the nomenclature of Platt is also presented, as it is relevant for the determination of the lowest excited states of the indoles. For the discussion of the results, the theoretical foundations of the bond order and the molecular orbital theory are described. In the following chapter four, the basics of quantum mechanical calculations are outlined. The individual components of the calculation methods (basis sets and coupled cluster methods) as well as the principles used for the fit are explained. The experimental setup for the

laser induced and dispersed fluorescence spectroscopy is described in chapter five. This includes the laser system, the photo detectors and the molecular co-expansion technique and helps to understand the experimental setup. The results of this work are outlined in the section “Publications”, in which the already published work or the results which are intended to be published, is presented.

3 Theoretical Background

To provide the basic information upon the complex and wide field of electronic spectroscopy this chapter gives a short overview over the measurement and computational principles used in this work. This should allow a better understanding of the publications in chapter 6.

3.1 Measurement Principles

3.1.1 Laser

The fundamental character of laserspectroscopy for the research in this study leads to this chapter. Due to its monochromatic and great coherence length as well as a small divergence, Light Amplification by Stimulated Emission of Radiation (LASER) light can be used in many ways in the field of spectroscopy. To get lasing, population inversion in the lasermedium is recommended. This means a higher, excited state has more members than a lower, ground state. In the following the nomenclature for the electronic ground state is indicated *via* a double prime ($''$) while the electronic excited state is indicated *via* a single prime ($'$). The relation of the population can be described by the Maxwell-Boltzmann distribution 1.

$$N'/N'' = (g_2/g_1) * e^{-(E'-E'')/(k_B \cdot T)} \tag{1}$$

In this equation the relation of the population density N_i for the given state is calculated *via* the statistical weight g_i and the energy level E_i of the given states, the boltzmann constant k_b and the temperature T of the given system.

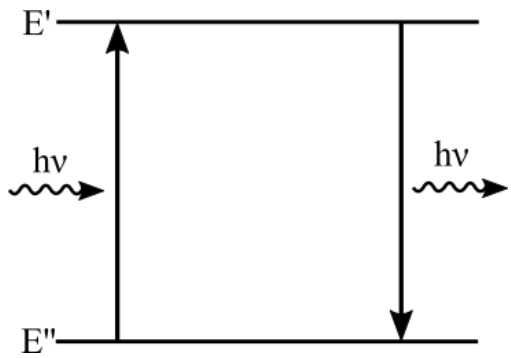

Figure 2: Schematic diagram of the interaction of light and a two energy system.[10]

In this system are various processes between the ground and the excited state. If a system absorbs a photon with the energy $h\nu$, it can correlate with the energy gap ΔE between the two states.

$$\Delta E = E' - E'' = h\nu \tag{2}$$

In this case the system is excited from the lower energy level E″ to the higher energy level E′. This process is called induced absorption.[10]

The energy of the absorbed photon is now stored in the electronic excited state of the system until the energy gets disposed and the system returns to the electronic ground state. There are several pathways to dispose the energy. These processes can be visualised in the *Jablonski diagram*, a scheme invented by Aleksander Jablonski.[11] The simplified figure 3 shows only two singlet and one triplet state to explain the mentioned pathways.

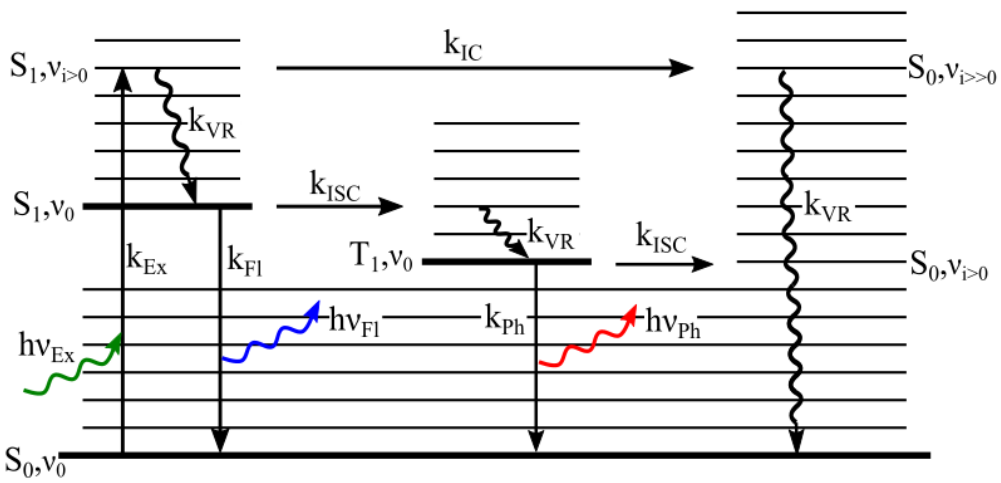

Figure 3: Jablonski diagram. All pathways after excitation are shown. S=singlet state, T=triplet state, ν=vibrational state, $h\nu$=photon energy, k=rate constant of given process, Fl=fluorescence, Ph=phosphorescence, VR=vibrational relaxation, IC=internal conversion, ISC=inter system crossing, black waving arrows indicate vibrational relaxation, waving colored arrows indicate photons with different energys decreasing from blue to red, straight arrows indicate transitions.

If the electrons in the electronic gorund state are paired, according to Hund's rules and the electron spin of the state is zero, this electronic ground state can be described as singlet state S_0. For the most organic molecules the electronic ground state is the singlet state S_0. If the energy of the photon $h\nu$ is higher than the energie gap ΔE between the electronic ground and the electronic excited state, the photon yields a vibrational state of the electronic excited state. To get back in the electronic ground state there are non-radiative pathways like *vibrational relaxation* VR, radiative pathways like *fluorescence* Fl and *phosphorescence* Ph and isoenergetic pathways like *intersystem crossing* ISC and *internal conversion* IC.

The *vibrational relaxation* can be described by collisions between molecules which disperse the energy of the excited state over the system. It leads to the vibrational ground state of the adressed electronic state. This process is one of the main processes in condensed phase. In this case the amount of collision partners is high enough to allow this process to be the fastest. If the velocity distribution of the molecules is equalised and reduced, like in a molecular beam with adiabatic cooling, the VR is prevented. In this case the common *Kasha's rule* occures and fluorescence from the vibrational excited states takes place.

Other non-radiative, horizontal and therefore isoenergetic channels are the *internal conversion* IC, the *intersystem crossing* ISC and the *intramolecular vibrational redistribution* IVR. These three pathways open new possibilitys to relax the system which where inaccessible from the starting electronic excited state.

The *internal conversion* leads from an isoenergetic high lying electronic singlet state to the electronic ground state through conical intersections. The process has a rate k_{IC} between $10^6 - 10^{12} s^{-1}$ depending on the involved states. Both vibrational states need the same multiplicity for this process. A vibrational coupling between states of different multiplicity leads to *intersystem crossing* ISC. The rate of this process is slower in comparison to internal conversion, because the transition is forbidden due to the reversion of the electron spin. This means ISC is a process between a singlet and a triplet state. Therefore ISC is found in systems with spin-orbit coupling. If the ISC took place, the energy can be lowered by vibrational relaxation and be either take a second step of ISC into a lower singlet state or by emitting a photon *via* phosphorescence.

The *phosphorescence* is one pathway of luminescence to emit a photon. Phosphorescence takes place between electronic excited triplet state and electronic ground state. The energy gap between T_1 and S_0 is rather small. This means the wavelength of the emitted photon shifts to red wavelengths. Due to the reversion of the electron spin in case of the *phosphorescence*, the rate is slow compared to the other lumincescence process the *fluorescence* (compare 1.

Fluorescence occurs for example between S_1 and S_0 or from T_2 to T_1. This means both states need the same multiplicity. Because of the *Stokes shift*[12] the red shift between absorption and emission occurs. The fluorscence can be forced by another photon or can occur spontaneous. Both processes are in competition. The process required for laser light is the *induced fluorescence*.

In a two-level-system the two fluorescence processes, the stimulated emission and the *amplified*

Table 1: Time constants for given processes in Figure 3.[13]

Process	designation	scale in s^-1
Absorption Ex	k_{Ex}	10^{15}
Internal conversion IC	k_{IC}	$10^6 - 10^{12}$
Intersystem crossing ISC (eg. $S_1 \rightarrow T_1$)	k_{ISC}	$10^6 - 10^{12}$
Intersystem crossing ISC (eg. $T_1 \rightarrow S_0$)	k_{ISC}	$\leq 10^9$
Vibrational relaxation VR	k_{VR}	$10^{12} - 10^{13}$
Fluorescence Fl	k_{Fl}	$10^7 - 10^9$
Phosphorescence Ph	k_{Ph}	$\leq 10^6$

spontaneous emission ASE, are in competition with each other. The ASE does not only increase the photons either it forces different states to emit photons. The forcing of photons occurs through undesirable resonators like cuvette walls. Through emitting out of different states and the undesirable forcing of photons the emerging light has no coherence and has a great spectral latitude and is therefore not useable in a laser device. For a two-level system there is no population inversion in thermal equilibrium. Therefore three or four-level-systems are used instead of a two-level-system. In a three-level-system the B-state is populated first. After this the system relaxes to state C. The

transition between state C and the ground state A emits a photon.

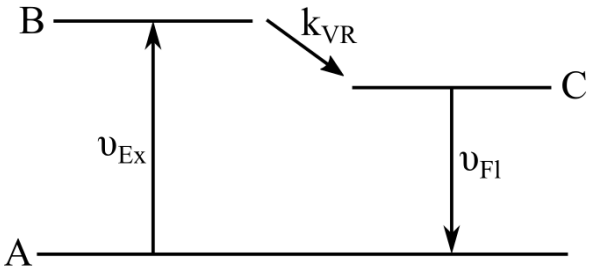

Figure 4: Schematic diagram of processes in a three niveau laser system, with the rate constant of vibrational relaxation k_{VR} and the excitation and fluorescence process ν_{Ex} and ν_{Fl}.

To force stimulated emission a population inversion between the states C and A is required. The population inversion is only possible when the transition between the states $B \rightarrow C$ is faster than the transition between $C \rightarrow A$. A more efficient system than the three-level-system is the four-level-system. Therefore between the emitting states a second faster non-emitting transition is established (compare 5).

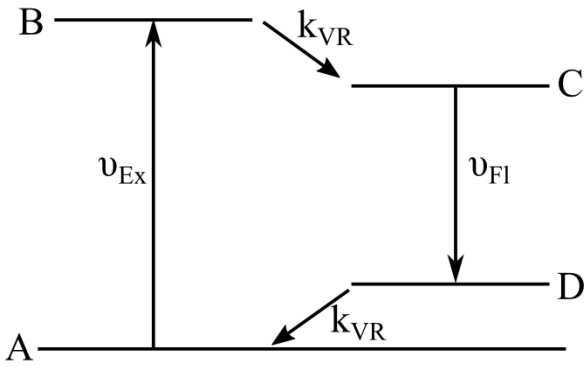

Figure 5: Schematic diagram of processes in a four niveau laser system, with the rate constant of vibrational relaxation k_{VR} and the excitation and fluorescence process ν_{Ex} and ν_{Fl}.

The emitting transition $C \rightarrow D$ is slower than the transitions $B \rightarrow C$ and $D \rightarrow A$ and a population inversion is reached. In dye laser systems the idealised systems in Figure 4 and Figure 5 are not established. In dye laser systems not only one state is adressed for exitation but more nearby states. This means a flash lamp can be used to adress these states due to the brought emission spectrum of this device. In this case adjustable resonators are established to achieve the required wavelength. In Nd:YAG laser systems only four emission wavelengths are used and therefore any resonator is needed.

3.1.2 Laser Induced Fluorescence

The *laser induced fluorescence* LIF can be achieved via scanning the wavelength of the laser system. If the laser is resonant with a vibronic transition of the investigated system, a fluorescence signal can be detected (compare Figure 6). In case of a fluorescence signal the energetic position of each vibrational mode of electronic excited states, especially for the first electronic excited state S_1, can be achieved. In Figure 6 an example scheme is shown. The blue line correlates to the energy $h\nu$ of the absorbed, the black lines with the emitted photons. The emitted photons are detected with a avalanche photodiode. In this case the fluorescence signal can be integrated, because the only needed parameter of these measurements is the excitation wavelength. The results of the LIF-measurements are required for the *dispersed fluorescence* to adress the vibrational states.

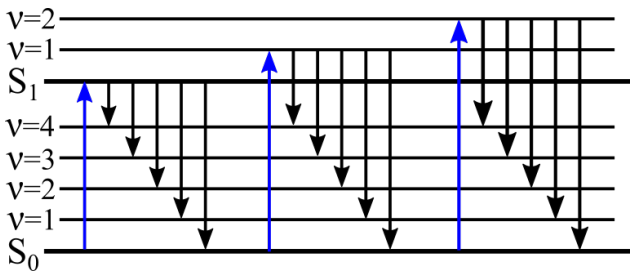

Figure 6: Jablonski diagram specailized to the laser induced fluorescence.

3.1.3 Dispersed Fluorescence

After the investigation of the vibrational levels of the excited state via LIF-spectroscopy, the investigation of the vibrational ground state levels can be achieved by *dispersed fluorescence* DF - spectroscopy. Therefore the wavelength of a resonant transition is adressed. Then the fluorescence light is dispersed on a holographic grating and detected *via* an ICCD-camera (compare chapter 5.4). The intensity standardized on the strongest transition and plotted against the fluorescence wavenumber relative to the scattered excitation light wavenumber.
The results of this measurements can correspond directly to far infrared frequencies of vibrational modes in the electronic ground state. The difference between these two measurement principles is the intensity gain from Franck-Condon integrals between the wavefunctions of ground and the excited state instead from vibrational excitation in case of IR-spectroscopy. Because of different selection rules different ground state vibrations can be visible in dispersed fluorescence spectra and IR-spectra. In these cases IR and DF-spectroscopy can provide complementary information.

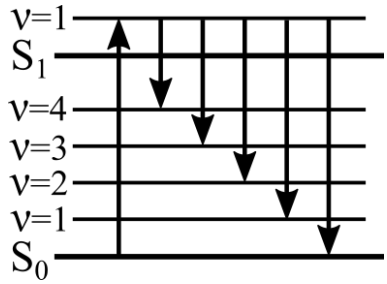

Figure 7: Jablonski diagram specialized to the dispersed fluorescence.

3.1.4 The Franck-Condon Principle

The importance of the Franck-Condon principle due to dispersed fluorescence spectroscopy is obvious. The Franck-Condon principle says: *Electronic transitions happen without any change in the nuclear geometry and starting from their equilibrium geometry.*[14–16] In general the masses of electrons are much smaller than of nuclei, so the movement of electrons is much faster than the motions of nuclei. This means the electronic excitation happens without direct movement of the nuclei but with movement of the electron density. After this movement the nuclei react on the modified forcefield and relax through vibrations.

Therefore the wavefunction of a molecule can be seperated into the *nuclear* wavefunction Ψ_{nuc} and the *electronic* wavefunction Ψ_{el} due to the Born-Oppenheimer approximation.[17]

$$\Psi = \psi_{el}(r) * \psi_{nuc}(R) \tag{3}$$

This means nuclei and electrons can be investigated seperately in case of vibrational transitions. Changing the coordinate system from cartesian coordinates R to normal coordinates Q the nuclear wavefunction Ψ_{nuc} transforms into the *vibrational* wavefunction Ψ_{vib} which is N_{vib}-dimensional of the number of normal modes ν of the molecule. The geometrical difference between ground and excited state is therefore now described by eq. 5 and not with the one-dimensional shift ΔR_0. The overlap integral over all nuclear coordinates determines the transition probability. It is anti proportional to the shift of the two potential curves R_{eq}.

$$\int [\Psi'_{vib}(Q')] \cdot \Psi''_{vib}(Q'')dQ' = \langle \nu'_1 \cdots \nu'_{N_{vib}} | \nu''_1 \cdots \nu''_{N_{vib}} \rangle \tag{4}$$

The part of the wavefunction determining the excited state is called *bra* $\langle \nu' |$ and the part determing the ground state *ket* $| \nu'' \rangle$. The normal coordinates are linked, as mentioned above, by the linear orthogonal transformation invented by Duschinsky with the N_{vib}-dimensional normal coordinates for electronic ground Q'' and excited state Q', the $N_{vib} x N_{vib}$ rotation matrix called *Duschinsky matrix* and the displacement vector $\vec{d}$ which is also N_{vib}-dimensional.

$$Q' = SQ'' + \vec{d} \tag{5}$$

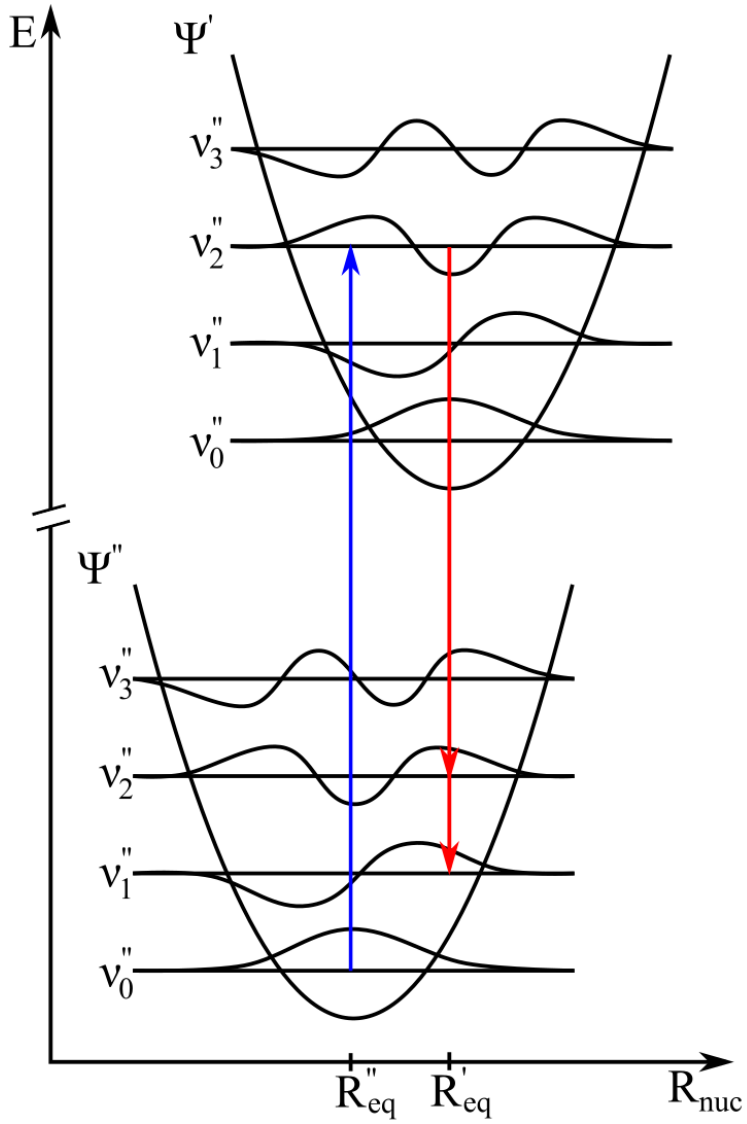

Figure 8: Energy level diagram of harmonic energy potential levels. The transitions between the energy states E'' and E'. The blue arrow illustrates the excitation from ν_0'' to ν_3'. The orange arrow illustrates the vibronic transitions from ν_3' to possible different vibrational states of the energy state E''.

Further information of the Transformation principle is given in section 4.8. The *vibronic transition dipole moment* M_{vib} is calculated with the *electronic transition dipole moment* $\hat{\mu}_{el}(Q)$ with the elementary electric charge e_0 and the g-th electron vector position $\vec{r}_g$.

$$\begin{aligned} M_{vib} &= \langle \Psi'_{vib} | \hat{\mu}_{el}(Q) | \Psi''_{vib} \rangle \\ \hat{\mu}_{el}(Q) &= \langle \Psi'_{el} | \mu_r | \Psi''_{el} \rangle \\ \mu_r &= \sum_r e_0 \vec{r}_g \end{aligned} \tag{6}$$

Therefore the integrated vibrational transition dipole moment can be calculated *via* the electronic and the vibronic transition with the associated wave functions and the dipoleoperator μ for the transition between electronic ground and excited state.

$$M_{e''e'} = \langle \psi''_{el} \psi''_{vib} | \mu | \psi'_{el} \psi'_{vib} \rangle = \langle \psi''_{vib} | \psi'_{vib} \rangle * \langle \psi''_{el} | \mu | \psi'_{el} \rangle + \langle \psi''_{el} | \psi'_{el} \rangle * \langle \psi'_{vib} | \mu | \psi''_{vib} \rangle \tag{7}$$

The second term of equation 7 becomes zero due to the orthogonality of the electronic wavefunctions of both involved states. The *orbital selection rule* for the underlying electronic transition is given by the integral $\langle \psi''_{el} | \psi'_{el} \rangle$. The integral of the overlap of the vibrational wavefunctions $\langle \psi''_{vib} | \psi'_{vib} \rangle$ can be described as *Franck-Condon Integral*. The square of this overlap integral is a value of the strength of a transition and is called *Franck-Condon factor*.[18]

3.2 Platt Nomenclature

With the prework of Platt on a nomenclature cata-condensed hydrocarbons[7] and the adaption of this nomenclature for indole derivates by Weber[19] the designation for the lowest excited states of substituted indoles in ${}^1L_a$ and ${}^1L_b$ is possible. Platt postulates that *the classification of π-orbitals in cata-condensed systems is like that of the orbitals of a free electron traveling in a one-dimensional loop of constant potential around the perimeter*.[7] The energy of the free electron can be calculated *via* following equation.

$$E_{box} = \frac{q^2 h^2}{2 m_{el} l^2} \tag{8}$$

With the constant values for the Planck constant h and the mass of the electron m_{el} the energy E_{box}, measured upward from the constant potential, is direct proportional to the ring quantum number *q* and anti-proportional to the length of the conjugatet π-system *l* in angstrom. The levels of the box are quadratically spaced and, except of the lowest with q=0, doubly degenerate while the elecetrons in the system can rotate clockwise or counterclockwise (compare figure 9 left).

Due to the nomenclature of Platt, in for example naphthalene, the highest occupied state will be the f-state while the first unoccupied state is the g-state (compare figure 9 right). If electronic excitation of an electron of an occupied state into an unoccupied state the total ring quantum num-

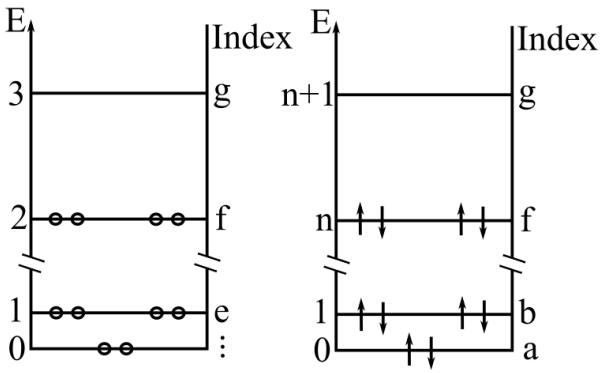

Figure 9: Left: Possible energetic states for the π-electrons in a cata-condensed aromatic, labeled with the ring quantum number q and the Platt index. Right: Energetic states of the π-electrons in the naphthalene molecule as an example for a possible occupation. Following ref.[7]

ber Q will rise or fall with the involved ring quantum number q. For the excited states total ring quantum number Q can be namend for $= 0, 1, 2, ... \rightarrow A, B, C...$ and for $Q = 2n, 2n+1, 2n+2, ...$ $\rightarrow K, L, M$. This means if the f-electron goes into the G-state the calculation $Q = (n+1) \pm n$ will lead to the B-state for $Q = 1$ and to the L-state for $Q = 2n + 1$. Both states are doubly degenerate and present as singlet and triplet state. The sublevels of the states can be described as *a* or *b* due to the molecular orbital orientation of the nodal planes. For a b-state the electron density is localised on the bonds while for the a-state the electron density is localised on the atoms. The state with the highest total ring quantum number Q will be the energetically lower state according to Hund's rule.[20] This means that the L-state will always be lower than the B-state due to our calculation above. As already mentioned Weber[19] adapted the nomenclature of Platt because of the same amount of π-electrons in indole compared to naphthaline. This can be done, because both systems are isoelectronic with 10 π-electrons.

3.3 Molecular Orbital theory

The term *molecular orbital* (MO) is used to describe a mathematical function that characterizes the location and wave-like behavior of an electron in a molecule. This model was invented by Robert Mulliken, to simplify the term *one-electron orbital wavefunction*.[21] To describe the electron wavefunctions of an atom the term refers to *atomic orbitals* (AO) while describing the electron location in a molecule the combined atomic orbtials are called *molecular orbitals* (MO). There are three types of molecular orbitals. The *bonding orbitals* describing the chemical bond within a molecule. The energy of the bonding orbtials are lower than the energy of the forming AOs. If the energy is higher than the energy of the forming AOs the *antibonding orbitals* are formed, which describe the opposite of a bonding orbital. If the energy of the MO is the same than the consisting AOs they are called *nonbonding orbital* which have no effect on the bonding within the molecule.

To describe the bonding of a molecule with quantum chemical calculations the *linear combination of atomic orbitals* (LCAO) approximation was invented by J.E. Lennard Jones.[22] Therefore the MOs can be calculated *via* the sums and differences of the atomic wavefunctions. This means the bonding molecular orbital Ψ and antibonding molecular orbital Ψ^* of a diatomic molecule can be described with the atomic wavefunctions φ_i and the adjustable coefficients c_i.

$$\Psi = c_a\varphi_a + c_b\varphi_b \Psi^* = c_a\varphi_a - c_b\varphi_b \tag{9}$$

The coefficents can have variable values positive or negative and represent the energies and symmetries of every atomic orbtial which is contained in the calculation.
In quantum mechanical calulations intermediates between atomic orbtials and molecular orbitals are used to calculate the electron density distribution between atoms in molceules. On that account the concept of *natural orbitals* was invented by Per-Olov Löwdin.[23] This concept is used to describe the bonding orbitals with a maximum electron density as *natural bonding orbital* NBO. Due to the Pauli limit of two electrons this means the occupancy should be 2.000 at the maximum. Thus the natural Lewis structure of a molecule can be described.[24] In this work the program NBO 7.0 was used to calculate and analyse the NBOs of investigated molecules.[25,26]

3.4 Bond Order

The bond between two atoms in a molecule can be described by the *bond order*. This concept was invented by Linus Pauling and describes the number of electron pairs between two atoms.[27,28] The bond order can be calculated with a variety of quantum mechanical methods. Coulson $etal$[29] invented one of the simplest ways to calculate bond orders for π-orbitals at the Hückel level. This means the bond order between the two atoms A and B can be calculated with sum of the coefficiants c_{ik} of the atomic orbitals φ_k of the Atoms k.

$$B_{AB}^{cou} = \sum_i c_{iA}c_{iB} \tag{10}$$

The ith doubly occupied molecular orbital θ_i and normalization is inculed in the coefficiants *via* equation 11.

$$\theta_i = \sum_i c_{ik}\varphi_k \tag{11}$$

The density matrix of a molecule P is the summation of all n_i occupied molecular orbitals.

$$P_{st} = \sum_i^{occ} n_i c_{rs} c_{rt} \tag{12}$$

The electron density ρ of a molecule can be described with the density matrix.

$$\rho = \sum_s \sum_t P_{st} \varphi_s \varphi_t \tag{13}$$

To describe the bond order beyond the simplest Hückel approach molecular orbtials also involve orbitals on the atomic centers. Consequently equation 10 has to be generalized.[29]

$$B_{AB} = \sum_s^{onA} \sum_t^{onB} P_{st} \tag{14}$$

The bond order calculations used for the investigated molecules are the Mayer and the Wiberg bond order models. The Wiberg bond order can be calculated with the P matrix as well, with the square of the off-diagonal elements of the matrix.

$$B_{AB}^{Wiberg} = \sum_s^{onA} \sum_t^{onB} P_{st}^2 \tag{15}$$

The Wiberg bond orders have positive values and can describe the classic bond valences very well. The atomic orbital overlap matrix S which is used to calculate the total number of electrons in a molecule N.

$$N = \sum_s P_{ss} + \sum_s \sum_{t \neq s} P_{st} S_{st} \tag{16}$$

The off-diagonal matrix elements of PS can be used to describe the strength of a chemical bond and the contribution of the orbitals and are also known as Mulliken overlap populations. These are used by Mayer to define the bond order as:

$$B_{AB}^{Mayer} = \sum_s^{onA} \sum_t^{onB} (PS)_{st} (PS)_{ts} \tag{17}$$

4 Quantum Chemical Calculations and Fit procedure

The following chapter introduces into the *ab initio* methods and calculations which are needed for the Franck-Condon fit of the measured spectra with an overview of the used basis set, methods, Franck-Condon-Factors and the program FC_{Fit}.
To optimise the electronic geometries of ground and excited state of the investigated substances the *coupled-cluster theory* CC2-method is used. To improve the results the *resolution of the identity* approximation (RI) and the *spin-component scaling* (SCS) were used. The *ab intio* calculations were performed on the HPC-Cluster of the Center for Information and Media Technology (ZIM) at Heinrich-Heine-Universität Düsseldorf with the program TURBOMOLE version 6.6.[30] The starting geometries for the *ab initio* calculations were develeoped with the program TmoleX19.[31]
For further calculations and simulations in the fit procedure the program FC_{Fit} was used, which was developed previously in our workgroup.[32] The program FC_{Fit} needs the optimized structures of the electronic ground and excited state as a basis and the numerically calculated vibrational frequencies and other input files like the hessian-matrix. The program calculates Franck-Conon factors with the values of the input files and simulates vibronic spectra of the electronic ground and excited state. For the fit the geometry of the electronic excited state is distorted from the *ab inito* calculated geometry. After this procedure the program simulates again vibronic spectra for given states.

4.1 Quantum Chemical Calculations

In computational chemistry the potential energy surface (PES) is the general concept for describing the relationship between energy and geometry of a molecule. With the Born-Oppenheimer approxiamtion this concept is a powerful tool in computational chemistry cause it allows to calculate electronic energies before nuclear repulsion energies and therefore simplifies the Schrödinger equation of molecules.
When geometry optimization is mentioned in this work, the optimization of the energy towards a general minimum on the PES is meant. This means the starting geometry is systematically distorted until the minimum on the PES is found. To approach this minimum the coupled cluster method on the basis of Hartee-Fock calculations is used.
Therefore the time-independent Schrödinger equation with the *Hamilton Operator* $\hat{H}$, the total wavefunction of the state i Ψ_i, the eigenvalue of the total wavefunction E_i and the nuclear (R) and electronic coordinates (r) has to be solved.

$$\hat{H}\Psi_i(r,R) = E_i\Psi_i(r,R) \tag{18}$$

The Hamilton Operator can be defined as:

$$\hat{H} = \sum_i \frac{\hbar^2}{2m_e}\nabla_i^2 - \sum_k \frac{\hbar^2}{2m_k}\nabla_k^2 - \sum_i \sum_k \frac{e^2 Z_k}{r_{ik}} + \sum_{i<j} \frac{e^2}{r_{ij}} + \sum_{k<l} \frac{e^2 Z_k Z_l}{r_{kl}} \tag{19}$$

with the mass of the electrons m_e, the mass of the nuclei m_k, the charge on the electron e, the atomic number Z, r_{ab} as the distance of nuclei k, l and electrons i, j and the Laplacian ∇^2, which is defined for cartesian coordinates as:

$$\nabla^2 = \frac{\delta^2}{\delta x_i^2} + \frac{\delta^2}{\delta y_i^2} + \frac{\delta^2}{\delta z_i^2} \tag{20}$$

If we choose atomic units as operating system, most of the constants in Eq.19 are equal to one.[33] Additionally all equation parts, considering the nuclei, become constant parameters due to the Born-Oppenheimer approximation.

The electronic configuration of a system is of certain interest. Therefore Slater used a matrix to describe the situation for each electron with a spinorbital χ_N with N as the total number of electrons in the system. The rows in the matrix present the available spinorbital and the columns the occupation of each spinorbital. If at least two identical columns occur, which means the electrons with the same spin occur in the same orbital, the determinant is zero. This refers to the Pauli principle due to the fact that the so called *fermi hole* is represented.[34]

$$\Psi_{SD} = |\chi_1\chi_2\chi_3 \cdots \chi_N\rangle = \frac{1}{\sqrt{N!}} \begin{pmatrix} \chi_1(1) & \chi_2(1) & \cdots & \chi_N(1) \\ \chi_1(2) & \chi_2(2) & \cdots & \chi_N(2) \\ \vdots & \vdots & \ddots & \vdots \\ \chi_1(N) & \chi_2(N) & \cdots & \chi_N(N) \end{pmatrix} \tag{21}$$

The simplest approach to solve the Schrödinger equation is the Hartree-Fock method. Therefore a Slater determinant of occupied spin orbitals is used to solve approximately the total wavefunction Ψ to minimize the value. The Hartree-Fock method is *self-consistent* due to the simple way of continuously solving one-electron Schrödinger equations for every electron in the molecule until the total wavefunction is solved. The equation is a non-linear eigenvalue problem of the wavefunction of the electrons (so the $_{el}$ label is omitted), with the Fock-operator $\hat{F}$ acting on a number of molecular orbital ψ_n.

$$\hat{F}|\psi_n\rangle = \langle E_n|\psi_n\rangle \tag{22}$$

with the molecular orbital $\psi_n = det(\chi_1\chi_2 \cdots \chi_N)$ and the Fock-operator with the number of electrons N_{el}.

$$\hat{F} = \hat{h}_k + \sum_j^{N_{el}} \langle\psi_n|\hat{h}_{el}|\psi_n\rangle - |\psi_n\rangle\langle\psi_n|\hat{h}_{el} \tag{23}$$

for the one electron part the Hamiltonian $\hat{h}_k$ and for the two-electron part the Hamiltonian $\hat{h}_{el}$ is used.

$$\hat{h}_k = -\frac{\Delta r}{2} - \sum_k^{N_k} \frac{e_k}{|r - R_k|}; \qquad \hat{h}_{el} = \frac{1}{r_1 - r_2} \tag{24}$$

With the charge of the nucleus e_k, the distance between the electron to the kth nucleus and the distance between two electrons $r_1 - r_2$. The sum in the equation of the Fock-operator runs over the orbitals of all electrons j and the sum in equation 24 runs over all nuclei k. If the electrons in the system are paired, the system can be called *closed shell system*. Therefore the *self-consistent-field* method (SCF) can be used to solve the equation 23. This means the Fock-operator can be simplified into the one electron Hamiltonian $\hat{h}_{el=1}$ and the sum over all electrons of the Coulomb-operator $\hat{J}_j$ and $\hat{K}_j$ which describe the repulsion between electrons.

$$\hat{F} = \hat{h}_{el=1} + \sum_{j=1}^{N_{el}} [2\hat{J}_j - \hat{K}_j] \tag{25}$$

The electron-electron repulsion calculated in this setup is called *mean-field* approximation due to describing the repulsion of an electron with all the other electrons *assuming that their spatial distribution is described by a set of orbitals.*[35] Therefore the total energy of a polyelectronic system is not exactly calculated.

4.2 Basis Sets

The basis set is a mathematically basis function from which the wavefunctions are based on. Each *molecular orbital* (MO) is constructed by a linear combination of basis functions. The basis function are mostly centered, but not necessary, on the atomic nuclei. The approach of this mathematical method is called *linear combination of atomic orbitals* LCAO. As basis set function in molecular calculations Slater and Gaussian functions are used. The Slater functions are used in semiemperical calculations, like the extended Hückel method,[36] the Gaussian functions are used in *ab initio* calculations in this work.
In terms of Cartesian coordinates the Gaussian type orbitals can be determined as:[37]

$$\chi_{k,m,n} = N x^k y^m z^n e^{-\zeta r^2} \tag{26}$$

With the normalization constant N and the orbital exponent ζ. The sum of the exponents k,m and n refers to the type of orbital.
The number of functions is an important factor in choosing the right basis set. With a *minimum basis set* a set of electrons for a neutral atom can be described throught the amount of functions. With the *Double Zeta* type basis the amount of all basis functions is doubled. This means in case of a hydrogen not only a single s-function is given (like in the minimum basis set) but the two s-

functions (1s and 1s'). This gets important with bond interactions between atoms. With the *Triple Zeta* basis set, three times as many functions as in the minimum basis set are used.
The basis set used in this work is the *cc polarized valence triple-split zeta*, in short cc-pVTZ, basis set.[38] This means the basis set contains lager shells of polarisation and only valence orbitals are described. Therefore importance of valence electrons in molecular bonding is taken into account.

4.3 Configuration interaction Calculation

As pointed out previously the ground state electron wave function can be determined as well as the electron density. Calculation of excited states has to be established as well. This can be done with the *configuration interaction* CI calculations. This calculations rely on occupied and unoccipied or *virtual* orbitals. Therefore in the *multiconfiguration self-consistent field method* (MCSCF) optimizes the unknown coefficients c_{om} of the Roothaan equations 27, with the set of N_o basis functions, the overlap matrix S_o, the Fock matrix F_o and the diagonal matrix of the orbital energies ε_m as well as the expansion coefficients C_j of eq. 28.

$$\begin{aligned} \sum_{o=1}^{N_0} F_{o'o} c_{om} &= \varepsilon_m \sum_{o=1}^{N_0} S_{o'o} c_{om} \\ S_{o'o} &= \int \chi^*_{o'}(1)\chi_o(1) d\tau_1 \\ F_{o'o} &= \int \chi*_{o'}(1)\chi_o(1) d\tau_1 \end{aligned} \tag{27}$$

$$\Psi = \sum_{J=1}^{L} C_J \Psi_J \tag{28}$$

This arises the problem of computational effort but the development of more efficient methods like the *complete active-space self-consistent field method* (CASSCF) which divides the spatial wavefunctions, optimizing themselves during calculation *via* trail calculations on c_{om}, into three categories: The inactive or doubly *occupied* orbitals, the virtual or *unoccupied* orbitals and the active orbitals which are demanded for excited state calculations due to the fact that they are a energetic intermediat between occupied and unoccupied orbitals. The choice of which orbitals are included in the active orbitals is challenging. The choice has impact on the computational effort as this arises with the number of active orbitals. A guess can be taken by the qualitative MO theory, form the valence atomic orbitals of the atoms, which gives the three categories of bonding, non-bonding and anti-bonding orbitals.[39]

4.4 Møller-Plesset pertubation theory

The configuration interactions calculations provide a good start to excited state calculations due to the possibility of calculating single, double or even more excited configurations from the ground state configuration. On the one hand CI is variational but on the other hand it has a lack of size-consistency. A theory with a good size-consistency but lack of variaton is the pertubation theory. This can be applicated on a many particle problem as *many-body pertubation theory* (MBPT). For the *Møller Plesset pertubation theory* (MPPT) the zero-order Hamiltonian $H^{(0)}$ from the Fock-operator of the HF-SCF method is used to find the correlation energy of the ground state.

$$H^{(0)} = \sum_{i=1}^{N_e} f_i \tag{29}$$

The *pertubation* $H^{(1)}$ can be calculated with the electronic Hamiltonian H_{el}.

$$\begin{aligned} H^{(1)} &= H_{el} - H^{(0)} \\ H^{(1)}(i) &= j_0 \sum_i \frac{1}{r_{ij}} - \sum_m [2j_m(i) - K_m(i)] \end{aligned} \tag{30}$$

The first sum is the sum over j omited electrons i and the second sum is the sum over the occupied molecular orbitals.
In the *second order Møller Plesset pertubation theory* (MP2) the energy correction can be calculated with the eigenfunction of the zero order Hamiltonian Ψ_j and the eigenvalue of this Hamiltonian $E_j^{(0)}$.

$$E^{(2)} = \sum_{J \neq 0} \frac{\langle \Psi_j | H^{(1)} | \Psi_0 \rangle \langle \Psi_j | H^{(1)} | \Psi_j \rangle}{E_0^{(0)} - E_j^{(0)}} \tag{31}$$

The energy can be described by a four-center-two-electron Integral between occupied $(m'n')$ and unoccupied (m, n) orbitals. The orbital energy ϵ is given in the amplitudes of the orbitals $t_{m'n'}^{m,n}$.

$$\begin{aligned} E_{MP2} &= \frac{1}{4} \sum_{m,n,m'n'} [t_{m'n'}^{m,n} \langle m'n' | m, n \rangle] \\ t_{m'n'}^{m,n} &= \frac{\langle m'n' | m, n \rangle}{\epsilon_{m'} + \epsilon_{n'} - \epsilon_m - \epsilon_n} \end{aligned} \tag{32}$$

The *resolution of identity* is a possible way to solve the limitation problems with the four-index, two electron integrals in *ab initio* calculations regarding the electronic structure. The number of these integrals arises with the fourth power of the number of the basis set. To solve this bottleneck, Vahtras *et al.* introduce an auxillary basis set P for two electron integrals.[40] With this method the requirements are reduced on a factor around the number of integrals. Therfore the systems which can be described by correlation methods can be larger. In the used program $TURBOMOLE$ the RI-MP2 approximation was implemented by Weigend $et\ al.$.[41]

Another improvement of the MP2-approach is the *spin component scaling* SCS, developed by Grimme $et\ al.$ which *is based on a seperate scaling of the correlation energy contributions of antiparallel and parallel pairs of electrons.*[42] The energy can be described therefore as a function of the energy E_p of electrons with parallel spin ($\alpha\alpha, \beta\beta$) and the energy E_{ap} of electrons with anti-parallel spin ($\alpha\beta$).

$$\begin{aligned} E_{SCS} &= E_p + E_{ap} \\ E_p &= \frac{1}{2}\sum_{ij} e_{ij} + \frac{1}{2}\sum_{\overline{ij}} e_{\overline{ij}} \\ E_{ap} &= \frac{1}{2}\sum_{i\overline{j}} e_{i\overline{j}} \end{aligned} \tag{33}$$

the pair energies e can be calculated *via* the following expression.

$$\begin{aligned} e_i j &= \sum_{ab} (t_{ij}^{ab} - t_{ij}^{ba})(ia|jb); \\ e_{\overline{ij}} &= \sum_{\overline{ab}} (t_{ij}^{\overline{ab}} - t_{ij}^{\overline{ba}})(\overline{ia}|\overline{jb}); \\ e_{i\overline{j}} &= \sum_{a\overline{b}} t_{ij}^{a\overline{b}}(ia|\overline{jb}) \end{aligned} \tag{34}$$

The amplitudes t can be determined analogous to eq. 34 in a Møller Plesset environment.

4.5 The coupled cluster method

The electron correlation energy can also be estimated by another size-consistent but not variational method, which is called *coupled-cluster* (CC) method. Therefore Cizek invented the *cluster operator* C which links the exact electronic wavefunction Ψ to the Hartee-Fock wavefunction Ψ_{HF}.

$$\Psi = e^C \Psi_{HF} \tag{35}$$

The *exponential operator* e^C is defined by the series expansion of the cluster operator C which is the sum of the effects of all electron excitation operators.

$$\begin{aligned} C &= C_1 + C_2 + \cdots C_N \\ e^C &= 1 + C + \frac{1}{2!}C^2 + \frac{1}{3!}C^3 + \cdots \end{aligned} \tag{36}$$

Therefore every electron excitation operator can be described by the sum, for the one-electron excitation operator C_1, of the single-excitation amplitudes t_a^p and for the two-electron excitation operator C_2, of the double excitation amplitudes t_{ab}^{pq}. This scheme is only limited to the operator

C_N due to the number of electrons in N occupied spinorbitals of the Hartee Fock wavefunction.

$$C_1\Psi_0 = \sum_{a,p} t_a^p \Psi_a^p \qquad C_2\Psi_0 = \sum_{a,b,p,q} t_{ab}^{pq} \Psi_{ab}^{pq} \tag{37}$$

The effect of the operator C is achieved by the values of the amplitudes t and the values for each amplitude. Through the calculations the exponential operator e^C has an important effect on the HF wavefunction Ψ_0. The results point out that there are certain products like $C_1\Psi_0, C_2\Psi_0 \ldots$ but also combinations like $C_1C_1\Psi_0, C_1C_2\Psi_0$ or others. The $C_1\Psi_0$ describes a single excitation while $C_2\Psi_0$ describes a double excitation. Regarding to the product $C_1C_1\Psi_0$ this can be calculated with the product of $t_a^p t_b^q$ as a sort of disconnected double excitation while $C_2\Psi_0$ is calculated with the double excitation amplitude and therefore can be described as connected excitation (compare figure 10).

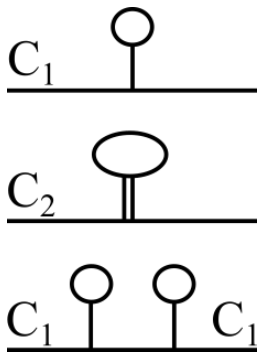

Figure 10: Scheme of possible connection of clusters[39]

The coupled cluster approach is commonly used to reduce the computational effort especially the computation time and therefore the concept of *coupled cluster singles and doubles* (CCSD) is given where C is approximated by $C_1 + C_2$. Combined with the resolution of identity[43] and the spin-component scaling[44] meantioned above the coupled cluster (CC2) approach was used for the calculations of the electronic ground and the electronic exctited state in this work.[45,46]

4.6 Vibrational Frequencies Calculations

To calculate the vibrational frequencies of the electronic ground and excited state the $NumForce$ script of the $Turbomole$ program was used. In this script a mass-weight and diagonalized hessian is calculated numerically. The yield of this hessian are the eigenvalues λ_i which corresponds to the force constants of molecular vibrations and the eigenvectors of the system. These correspond to the normal coordinates of the molecule.[47] The mass-weight coordinates q_i for the nucleus i can be calculated with the mass of the nucleus m_i and the cartesian displacement coordinate x_i *via* the following equation.

$$q_i = \sqrt{m_i} x_i \tag{38}$$

The Hamiltonian for the vibrational wavefunction is a sum of terms defined as given equation.

$$\hat{H}_{vib} = \sum_i \hat{H}_i \qquad \hat{H}_i = -\frac{1}{2}\hbar^2 \frac{\delta^2}{\delta Q_i^2} + \frac{1}{2}\lambda_i Q_i^2 \tag{39}$$

With the normal coordinates Q_i and the eigenvalues of the nucleus. If the Hamiltonian is a sum of terms the same approach counts for the wavefunctions. This means the vibrational wavefunction Ψ_{vib} is a product of normal mode wavefunctions Ψ_{ν_i}.

$$\Psi_{vib} = \Psi_{\nu_1}(Q_1)\Psi_{\nu_2}(Q_2)\cdots = \prod_i \Psi_{\nu_i}(Q_i) \tag{40}$$

The energy levels of the ith normal mode can be described with the quantum number of the harmonic oscillator and the eigenvalues.

$$E_{\nu_i} = (\nu_i + \frac{1}{2})\hbar\sqrt{\lambda_i} \qquad \nu_i = 0, 1, 2, 3, \ldots \tag{41}$$

The frequency of a mode can be calculated in wavenumbers with the speed of light c and the eigenvalues in case of the internal coordinate system (left side) or with the reduced mass of the system μ and the cartesian coordinates (right side). This should point out the relevance of the chosen coordinate system for quantum mechanical calculations.

$$\tilde{\upsilon}_i = \sqrt{\frac{\lambda_i}{4\pi^2 c^2}} \qquad \tilde{\upsilon}_i = \frac{1}{2\pi}\sqrt{\frac{\lambda_i}{\mu}} \tag{42}$$

4.7 One-dimensional Franck-Condon-Factors

As shown in section (Franck-Condon Principle) the Franck-Condon equations are based on the harmonic oscillator approximation. Therefore the solutions of the wavefunctions for each vibrational state ν can be calculated with the *Hermite polynomials* $H_\nu(\alpha x)$, the displacement factor αx and the scale factor N_ν.

$$\Psi_\nu(x) = N_\nu H_\nu(\alpha x) e^{-\alpha^2 x^2/2} \qquad \alpha = \left(\frac{m k_f}{\hbar}\right)^{1/4} \qquad N_\nu = \sqrt{\frac{\alpha}{2^\nu \nu! \sqrt{\pi}}} \tag{43}$$

The Hermite polynomials can be calculated recursevly from a starting point $H_0(\alpha x)$, when the state ν is zero. The Hermite polynomal for $\nu = 1$ is $H_1(\alpha x) = 2\alpha x$ and gives the same wavefunction like the Gaussian one for the ground state multiplied by $2\alpha x$ but with a different normalization factor.

$$\Psi_0(x) = \sqrt{\left(\frac{\alpha}{\sqrt{\pi}}\right)} e^{-\alpha^2 x^2/2} \qquad \Psi_1(x) = \sqrt{\left(\frac{2\alpha^3}{\sqrt{\pi}}\right)} x e^{-\alpha^2 x^2/2} \tag{44}$$

To calculate Franck-Condon factors these wavefunctions are of certain interest. For a two electronic state example just differing by the shift of the potential curves ΔR following equations for the wavefunctions are given.

$$\Psi_0(x) = \sqrt{\left(\frac{\alpha}{\sqrt{\pi}}\right)} e^{-\alpha^2 x^2/2} \qquad \Psi_0'(x) = \sqrt{\left(\frac{\alpha}{\sqrt{\pi}}\right)} e^{-\alpha^2 (x-\Delta R)^2/2} \tag{45}$$

with normalizing the wavefunctions like in equation 46 and the displacement factor $\alpha = (mk_f/\hbar^2)^{1/4}$, as a function of mass m and force constant k_f,

$$\int_{-\infty}^{+\infty} |\Psi_0|^2 dx = 1 \tag{46}$$

the Franck-Condon factor of the transition is given by equation 47. Additionally the sum of all Franck-Condon factors for transitions in a given state ν is equal to 1.

$$|S(0', 0)|^2 = e^{-\alpha^2 (\Delta R)^2/2} \tag{47}$$

$$\sum_{\nu'} |S(\nu', \nu)|^2 = 1 \tag{48}$$

4.8 Multi Dimensional Franck-Condon Factors

To develop the two state system the Duschinky transformation is needed. Therefore the two states have to be defined. The structures of both states shall be different and due to this the eigenvectors of these states have to differ too. The second state is developed out of the first state and this results in the rotation and moving of the eigenvectors and system of the first state to generate these values for the second state. The *Duschinsky matrix* S or rotation matrix and the displacement vector $\vec{d}$ can be described with the *force constant matrices* of both states and the nuclear masses, with the row matrix L containing the eigenvectors and the diagonal matrix M containing the atomic masses and the equilibrium geometry $\vec{R_{eq}}$ for given states.[48]

$$\begin{aligned} Q'' &= SQ' + \vec{d} \\ S &= (L'')^T L' \\ \vec{d} &= (L'')^T M^{-1} \left(\vec{R''_{eq}} - \vec{R'_{eq}}\right) \end{aligned} \tag{49}$$

With the *Eckart conditions* a seperation of the rotational and translational motion from the vibrational motion and minimising the coupling between those, is possible. Therefore the orientation of the molecular axis in given electronic state in a multi-dimensional system can be described with

the mass m_i and the equilibrium position of the ith nucleus $\vec{R_{eq,i}}$ in given state as:

$$\sum_{i=1}^{N_{nuc}} m_i \vec{R_{eq,i}} = \vec{0} \tag{50}$$

The origin of the internal coordinate system is always positioned at the center of mass.

$$\sum_{i=1}^{N_{nuc}} m_i \vec{R_{eq,i}} \vec{R_i} = \vec{0} \tag{51}$$

The Eckart conditions solve the seperation of vibrational, translational and rotational motion but due to the applicance of these conditions to both involved electronic states, *axis switching* can occur between those states.[49] Hougen and Watson adressed this effect by reorientation of the internal coordinate system upon electronic excitation with a matrix (eq. 53). This leads to corrections to the Duschinsky matrix S and the displacement vector $\vec{d}$.

$$\begin{aligned} S &= (L'')^T B^{-1} L' \\ \vec{d} &= (L'')^T M^{-1} \left(B^{-1} \vec{R''_{eq}} - \vec{R'_{eq}} \right) \end{aligned} \tag{52}$$

The $N_{nuc} \times N_{nuc}$ diagonal block matrix B contains a 3x3 Hougen-Watson axis switching matrix T along its diagonal.

$$\sum_{i=1}^{N} m_i \begin{pmatrix} \vec{R''_{3i-2}} \\ \vec{R''_{3i-1}} \\ \vec{R''_{3i}} \end{pmatrix} \times \left(T^{-1} \begin{pmatrix} \vec{R''_{eq,3i-2}} \\ \vec{R''_{eq,3i-1}} \\ \vec{R''_{eq,3i}} \end{pmatrix} \right) = 0 \tag{53}$$

With the *zero-order axis-switching* approximation by Sando and Spears, the movement of the nuclei during vibration period is neglected.[50] Therefore the equation 53 is replaced by equation.54

$$\sum_{i=1}^{N} m_i \begin{pmatrix} \vec{R''_{3i-2}} \\ \vec{R''_{3i-1}} \\ \vec{R''_{3i}} \end{pmatrix} \times \left(T_0^{-1} \begin{pmatrix} \vec{R''_{eq,3i-2}} \\ \vec{R''_{eq,3i-1}} \\ \vec{R''_{eq,3i}} \end{pmatrix} \right) = 0 \tag{54}$$

The envolved Hougen-Watson matrix T_0 needs to be solved. This is done stepwise. Therefore a 3×3 matrix is developed. The placeholder α and β stand for the cartesian coordinates x,y and z.

$$C_{\alpha\beta} = \sum_{i=1}^{N} m_i \left[\left(\vec{R_i^{''eq}} \right)_\alpha \left(\vec{R_i^{'eq}} \right)_\beta \right] \tag{55}$$

In a planar molecule C_{zz} is equal to zero. If the product of $C^T C$ is diagonalized, this results in an additional matrix Ω where the eigenvectors are columns and the corresponding diagonal matrix depends on the eigenvalues ρ. The envolved Hougen-Watson matrix T_0, with an additional 3×3

matrix Λ which is $+1/-1$ along the diagonal, can be calculated *via* following expression.

$$T^0 = \Omega\Lambda\rho^{\frac{1}{2}}\Omega^T C^{-1} \tag{56}$$

Through the addition of the matrix Λ eight solutions for T are possible. The matrix T is a rotation matrix and therefore the determinant must be +1. The finding of the right solution of the Hougen-Watson matrix leads to the smallest displacement between the given states.
Finding the overlap integral $\langle\nu'|\nu''\rangle$ of wavefunctions describing the vibration in the initial and the final electronic state is necessary. On that account Doktorov $et\ al.$ invented the one-multi-dimensional wavefunction for each state in contrast to the one-dimensional harmonic oscillator functions Duschinsky used to adress the multi-dimensional problem.[51,52] The overlap integral can be calculated by the generation function $\langle\gamma|\alpha\rangle$ with the intial state $|\alpha\rangle$ and the final state $\langle\gamma|$. The used elements α and γ are complex numbers and therefore not interchargeable in this integral. They define the classical coordinates of the beginning of the curve in a N_{vib} dimensional space. Additionally the coherent states are defined as the eigenstates of all the annihilation operators $\alpha_i|\alpha\rangle = \alpha_i|\alpha\rangle$. The coherent state $|\alpha\rangle$ can be described with the following equation.

$$|\alpha\rangle = (\pi\hbar)^{N_{vib}/4}\left(\prod_{j=1}^{N}\omega_j^{\frac{1}{4}}\right) exp\left[\sum_{j=1}^{N_{vib}}\left(-\frac{1}{2}\frac{\omega_i}{\hbar}q_i^2 + \sqrt{\frac{2\omega_i}{\hbar}}\alpha_i q_i - \frac{1}{2}\alpha_i^2 - \frac{1}{2}|\alpha_i|^2\right)\right] \tag{57}$$

The generation function for the overlap integral $\langle\nu'|\nu''\rangle$ and the overlap integral $\langle\gamma'|\alpha''\rangle$, is expressed by equation 58.

$$\begin{aligned}\langle\gamma|\alpha\rangle = \langle 0'|0''\rangle exp\left[-\frac{1}{2}\left(|\alpha|^2 + |\gamma|^2\right)\right] exp\left[-\frac{1}{2}(\alpha\gamma*)\right]\begin{pmatrix}1-2Q & -2R\\ -2R^T & 1-2P\end{pmatrix}\begin{pmatrix}\alpha\\ \gamma*\end{pmatrix}\\ +\sqrt{2}(\alpha\gamma*)\begin{pmatrix}-R & 0\\ 0 & 1-P\end{pmatrix}\begin{pmatrix}\delta\\ \delta\end{pmatrix}\end{aligned} \tag{58}$$

The electronic origin can be calculated by the overlap integral of $\langle 0'|0''\rangle$.

$$\langle 0'|0''\rangle = 2^{N/2}\left[\prod_{j=1}^{N}\sqrt{\frac{\omega_j'}{\omega_j''}}\right]\sqrt{detQ}exp\left[-\frac{1}{2}\delta(1-P)\delta\right] \tag{59}$$

With the matrices J, Q, P and R, the vector δ describes the Duschinsky transformation in multi-dimensional space and therefore properties in equation 60 are defined as:

$$\begin{aligned} P &= JQJ^T \\ R &= QJ^T \\ Q &= (1 + J^T J)^{-1} \\ J &= \lambda_{\omega''} S \lambda_{\omega'}^{-1} \\ \delta &= \frac{\lambda_{\omega'} d}{\sqrt{\hbar}} \\ \lambda_\omega &= diag(\sqrt{\omega_1}\sqrt{\omega_2}\cdots\sqrt{\omega_N}) \\ \omega &= 2\pi\nu \end{aligned} \tag{60}$$

The most general expression for the overlap integral is given with the Hermite polynomials of 2N variables.

$$\langle \nu' | \nu'' \rangle = \langle 0' | 0'' \rangle \left[\prod_{j=1}^{N} \sqrt{\nu_j'! \nu_j''!} \right] H_{\nu'\nu''}(\sigma, \tau) \tag{61}$$

With the N-dimensonal arguments σ and τ given by the following equation.

$$\begin{pmatrix} \omega \\ \tau \end{pmatrix} = \sqrt{2} \begin{pmatrix} 1 - 2Q & -2R \\ -2R^T & 1 - 2P \end{pmatrix}^{-1} \begin{pmatrix} -R & 0 \\ 0 & 1 - P \end{pmatrix} \begin{pmatrix} \delta \\ \delta \end{pmatrix} \tag{62}$$

The recurrence relations for the overlap integrals follow directly from the generation function 58. The N reccurence relations can be obtained *via* differentiating this function with respect to α_i and collecting the terms with equal powers of α_i and $\gamma *_i, i = 1, 2, 3..., N$.

$$\begin{aligned} &\langle \nu' | \nu_1'', \cdots, \nu_i'' + 1, \cdots, \nu_{N_{vib}}'' \rangle = \\ &2 \sum_{k=1}^{N_{vib}} R_{ik} \sqrt{\frac{\nu_k'}{\nu_i'' + 1}} \langle \nu_1', \cdots, \nu_k' - 1, \cdots, \nu_{N_{vib}}' | \nu_1'', \cdots, \nu_i'', \cdots, \nu_{N_{vib}}'' \rangle \\ &+ \sum_{j=1}^{N_{vib}} (2Q - 1)_{ij} \sqrt{\frac{\nu_j''}{\nu_i'' + 1}} \langle \nu' | \nu_1'', \cdots, \nu_j'' - 1, \cdots, \nu_{N_{vib}}'' \rangle \\ &- (R\delta)_i \sqrt{\frac{2}{\nu_i'' + 1}} \langle \nu' | \nu_1'', \cdots, \nu_i'', \cdots, \nu_{N_{vib}}'' \rangle \end{aligned} \tag{63}$$

With the same procedure regarding to $\gamma*_k$ the following formula for absorption can be determined.

$$\begin{aligned}
&\langle \nu'_1 \cdots, \nu''_k + 1, \cdots, \nu'_{N_{vib}} | \nu'' \rangle = \\
&2 \sum_{i=1}^{N_{vib}} R_{ki} \sqrt{\frac{\nu''_i}{\nu'_k + 1}} \langle \nu'_1, \cdots, \nu'_k + 1, \cdots, \nu'_{N_{vib}} | \nu''_1, \cdots, \nu''_i - 1, \cdots, \nu''_{N_{vib}} \rangle \\
&+ \sum_{l=1}^{N_{vib}} (2P-1)_{kl} \sqrt{\frac{\nu'_l}{\nu'_k + 1}} \langle \nu'_1, \cdots, \nu'_l - 1, \cdots, \nu'_{N_{vib}} | \nu'' \rangle \\
&+ [(1-P)\delta]_k \sqrt{\frac{2}{\nu'_k + 1}} \langle \nu'_1, \cdots, \nu'_k, \cdots, \nu'_{N_{vib}} | \nu'' \rangle
\end{aligned} \tag{64}$$

4.9 The Program FC_{FIT}

The program FC_{FIT} was written by Stephan Schumm and developed further by Petra Imhof and Daniel Krügler.[32,53] This program is based on the recurrence relations described by Doktorov $et\ al.$[51,52] and simulates absorption and emission spectra from calculated Franck-Condon factors. By application of the reccurence formulae we can consider that the reference relation can be simplified by $\nu''_i = \nu''_j = \nu''_k = \nu''_l = 0$ and $\nu'_i = \nu'_j = \nu'_k = \nu'_l = 0$ because of $1''_i = \nu''_i + 1$ and $1''_k = \nu''_k + 1$, if transitions from a vibrationaless electronic state only reach fundamental vibrations of another electronic state. For calculating the overlap integral, the Duschinsky matrix S and the vector δ need to be determined by the input files provided by *ab initio* calculations. Then the matrices J, Q, R and P can be calculated. With these results the determination of the overlap integral $\langle 0'|0'' \rangle$ is possible. After this the factors $2R$, $(2Q-1)$, $(2P-1)$, $\sqrt{2}R\delta$ and $\sqrt{2}(1-P)\delta$ can be determined and saved for further calculations.

$$\begin{aligned}
\langle 0'|0''_1, \cdots, 1''_i, \cdots, 0''_{3N-6} \rangle &= -\sqrt{2}(R\delta)_i \langle 0'|0'' \rangle \\
\langle 0'_1, \cdots, 1'_k, \cdots, 0'_{3N-6} | 0'' \rangle &= -\sqrt{2}[(1-P)\delta]_k \langle 0'|0'' \rangle
\end{aligned} \tag{65}$$

with the example of the overlap integral $\langle 001|210 \rangle$ in figure 11 the recurrence tree for the calculation of this overlap integral is shown. For excited states the vibronic state will be denoted ν' and for the non-excited state ν''. This leads to the notation $\langle \nu'|\nu'' \rangle$ for an absorbtion and $\langle \nu''|\nu' \rangle$ for an emission.

Refering to figure 11 all branches finalize in the origin $\langle 000|000 \rangle$ after different amounts of recursion steps. The computational effort of this method is maximized by the amount of calculated overlap integrals. But due to optimization in the process described below, the calculations can be cut drastically. Thus the integrals which are calculated multiple times can be stored and accessed later in the process. The second method to reduce the calculated integrals is to limit the harmonic energy due to experimental spectra length for LIF and DF spectra. In this work this means up to 3000 relative wavenumbers for LIF spectra and for DF spectra 3000-4000 wavenumbers. These

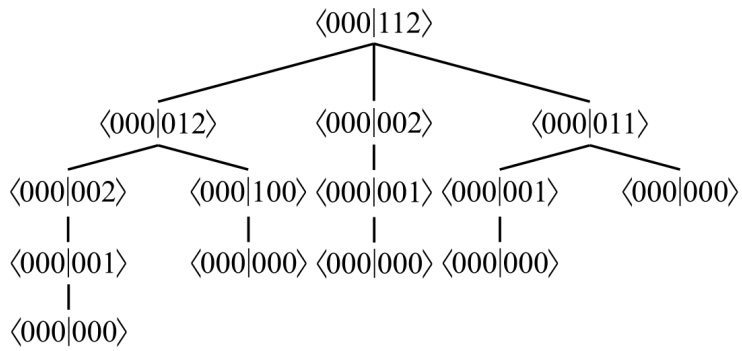

Figure 11: Recurence tree for the overlap integral $\langle 001|210\rangle$.

experimental spectra length depend on the laser performance and the fluorescence quantum yield of the investigated system. Another method is to limit the number of quanta, that a mode is excited by the final state. This can be accomplished because combinations and overtones of three quanta and more are very rare to observe. In general a limit above four quanta and 4000 cm^{-1} is not recommended due to a significant longer computation time with no reasonable improvement of the calculated result.

The program FC_{FIT} uses hash tables implemented and discusses previously by Schumm[54] and therefore just implemented on a superficial level in this work.

The quantum strings, describing the bra and the ket, are converted into polyadic numbers and used in the hash tabels. The hash table links the bra polyadic numbers to the assigned subspectra and these are linked with the ket-keys to the values of the Franck-Condon factors of the bra-ket. The relative intensities of the spectra can be calculated with these Franck-Condon factors with the correction factor χ_{corr} and the Franck-Condon factor of the reference transition FC_{ref} in the following equation 66.

$$I_{rel}(\nu'' \leftarrow \nu') = \frac{\langle \nu'|\nu''\rangle^2}{FC_{ref}} \chi_{corr} \tag{66}$$

In emission spectra the strongest transition is used as a reference. The overlap integral of $\langle 0'|0''\rangle$ cannot be used since the intensity of this integral in experimental spectra is mixed with the stray light of the excitation laser. The factor χ_{corr} implements the different proportionality of intensity and the energy needed for transition $\tilde{\upsilon}_{\kappa\mu}$. For absorption equation 67 and for emission equation 68 is defined.

$$I_{\kappa\mu} \sim \tilde{\upsilon}_{\kappa\mu} W(\upsilon) |M_{\kappa\mu}|^2 \tag{67}$$

$$I_{\kappa\mu} \sim \tilde{\upsilon}^4_{\kappa\mu} W(\mu) |M_{\kappa\mu}|^2 \tag{68}$$

With a photon counting detector (like the used ICCD chip) and not measuring the energy the energy

factor $\tilde{\upsilon}^4_{\kappa\mu}$ changes into $\tilde{\upsilon}^3_{\kappa\mu}$ and therefore χ_{corr} can be defined as:

$$\begin{aligned} \chi_{corr} &= \left(\frac{\tilde{\upsilon}_{base} + \tilde{\upsilon}'_i}{\tilde{\upsilon}_{base} + \tilde{\upsilon}'_{ref}} \right)^{n_a} && for \quad absorption \\ & && with \quad n_a = 0, 1 \\ \chi_{corr} &= \left(\frac{\tilde{\upsilon}_{base} + \tilde{\upsilon}''_i}{\tilde{\upsilon}_{base} + \tilde{\upsilon}''_{ref}} \right)^{n_e} && for \quad emission \\ & && with \quad n_e = 0, 3, 4 \end{aligned} \tag{69}$$

The energy of the basic vibronic transition of the subspectrum $\tilde{\upsilon}_{base}$ is the energy of the electronic origin in absorption spectra. In emission spectra it is the excitation energy leading to the initial state. The harmonic energy $\tilde{\upsilon}_i$ of the vibration i is excited in the final state. The total energy of the transition is the sum or differnence of these two energys. In figure 12 an example for the overlap integral $\langle 001|010 \rangle$ is shown.

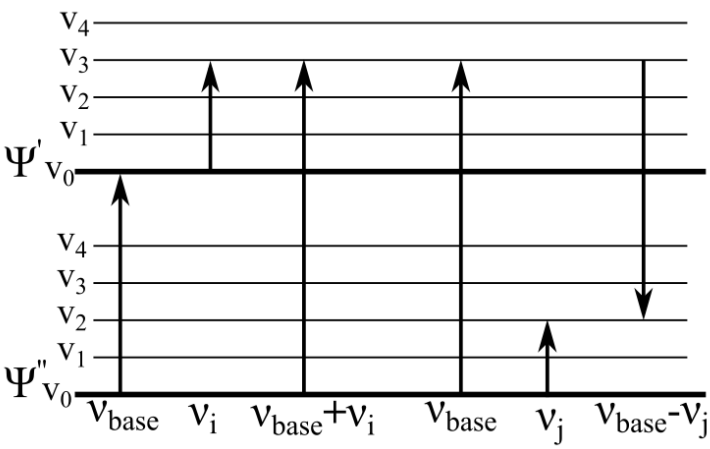

Figure 12: Schematic diagram to visualise the transitions for the line $\langle 001|010 \rangle$ for an absorption (left) and an emission spectrum (right).

The intensities which are simulated by FC_{FIT} are compared to the experimental values. To minimize the deviance χ^2 between simulated and experimental intensities, the geometry of the final state is distorted along selected normal modes. The intensities are weightend in the fit. To compensate intensities, which are poorly described by the harmonic model or are badly described by the assignment of the observed line intensities, the weightend can be maipulated. The assignment of line intensities of the experiment to the simulated line intensities is re-examined after each fit. This step is done repetitively until a good overall agreement of simulated and experimental data is reached.

Due to the harmonic approximation there are some restrictions for the geometry fit. The contraction and elongation along one normal coordinate gives the same result as the calculation of the derivation between simulation and experiment only with relative intensities. With the change of

the rotational constants, investigated *via* rotationally resolved spectroscopy, it is possible to compensate this issue. The total deviation χ^2_{total} is determined by the following equation.

$$\chi^2_{total} = \sum_{n=1}^{N_{Int}} W_n (I_{exp,n} - I_{sim,n})^2 + \sum_{m=1}^{N_{\Delta Rot}} W_m (\Delta Rot_{exp,m} - \Delta Rot_{sim,m})^2 \tag{70}$$

The shape of the harmonic potential, the parable, approximates the potential engery gradient along the normal coordinate during vibration. Therfore inversion vibrations are not well described in the model. Another disadvantage is the local maximum of the potential energy instead of a local minimum in equilibrium position. This leads to no possible investigation of vibrations excited in a double minimum potential. The generel procedure for using the program FC_{FIT} is described in figure 13.

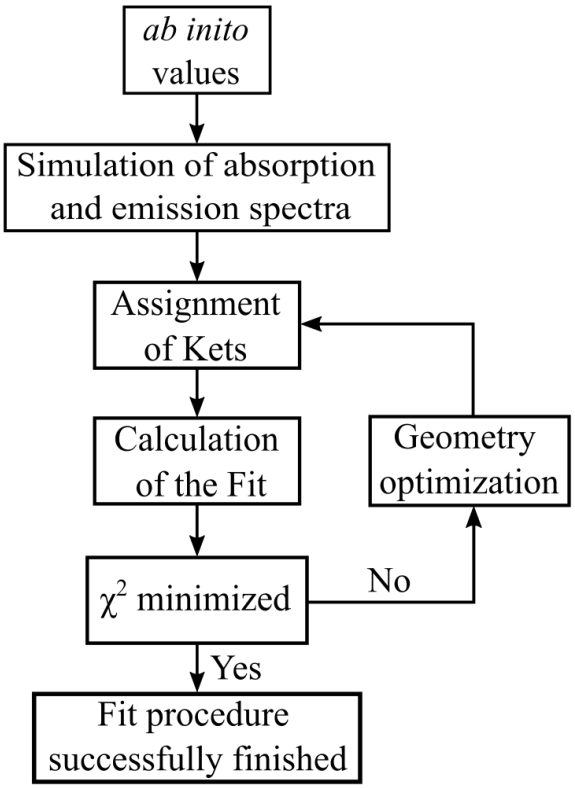

Figure 13: Schematic diagram of Fit process within the program FC_{FIT}.

5 Experimental Setup

The experimental setup has been finalized in previous work.[55,56] The setup shown in figure 14 was used in this work all along. The laser setup allows to measure laser induced fluorescence and dispersed fluorescence without further changes in the setup.
The laser setup is build by a *Nd:YAG* laser and a $dye\ laser$. The light of the *Nd:YAG* laser is frequency doubled (green light) and beam shaped by a telescope from a round beam profile of 5 mm diameter to a beam shape with rectangular profile with 5 mm height and 8 mm width. This beam is coupled into the $dye\ laser$, a modified Lambda Physics FL-3002. Here the dye solution, depending on the fluorescence wavelength needed, is pumped and frequency doubled. The then called probe beam is used for the laser spectroscopy. It is coupled into the vacuum chamber with two deflecting prisms and crosses the supersonic free jet with the vapourated sample perpendicularly. The pre-pressure is provided by a $rotary\ pump$ and the measuring pressure of $10^{-4} - 10^{-5}$ mbar is provided by an *oil diffusion pump*. While the pulsed nozzle is opened the pressure is typically around $7 - 9 \cdot 10^{-4}$ mbar.

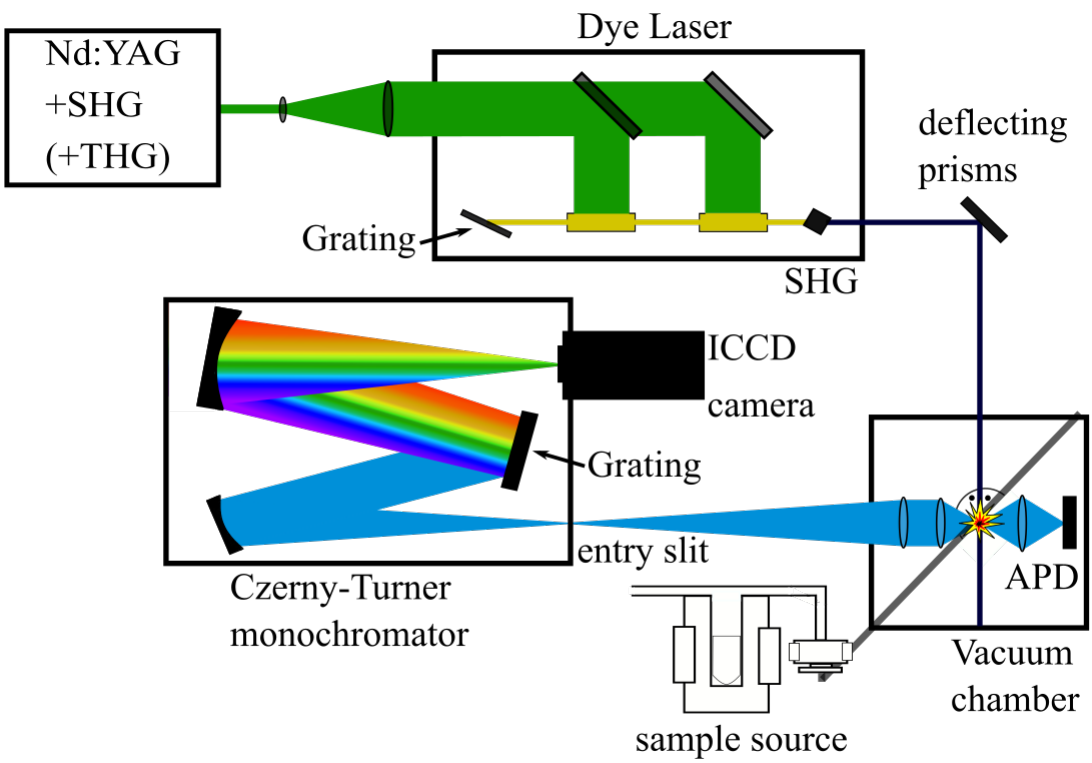

Figure 14: Schematic presentation of the experimental setup. The coloured lines indicate laser light. Green: pump laser (532 nm), yellow: fundamental of the dye laser ($\sim$ 520-640 nm), dark blue: second harmonic of the dye laser ($\sim$ 260-320 nm), light blue: fluorescence light of the sample, rainbow: dispersed fluorescence. The grey light indicates the supersonic free jet.

The *fluorescence* light, which is emitted from the sample is collected with a biconvex lens perpendicularly to the laser light with 35 mm focal length on an *avalanche photodiode* (APD) for the laser induced fluorescence spectra. For the dispersed fluorescence the light is collected with a biconvex lens with 50 mm focal length and a large angle of aperture that is situated 50 mm from the crossing point. The collected fluorescence light is focused by a plan-convex lens, with 500 mm focal length, on the entry slit opend to 30 μm of a 1 m *Czerny-Turner monochromator* (Jobin-Yvon THR 1000).
In the monochromator the fluorescence light is dispersed on the grating in first order and imaged in the *intensified charge-coupled device* (ICCD) chip for the dispersed fluorescence spectra. The ICCD chip is cooled by a Peltier element to reduce the noise-to-signal ratio due to noise from dark current. The heat, resulted of the oil diffusion pump, is lead away with tap water. The heat of the Peltier element cooling the camera is lead away by closed cooling cycle of distilled water with a small concentration of sodium azide. The sodium azide prevents the water of limescale or algae and therefore the small channels at the Peletier element to clogg.
Further information about the laser system, the time management, the sample source and the detectors is given in the sections below.

5.1 The Laser System

The laser light used in this experiment is generated by the dye laser, which is pumped by a *Nd:YAG* laser. The laser medium of this four state laser (explained in chapter 3.1.1) is a neodymium doped yttrium aluminium garnet ($Nd : Y_3Al_5O_{12}$). The emitted emission light has a wavelength of 1064 nm for the chosen emission transition. The light is then frequency doubled with a BBO crystal to a wavelength of 532 nm. This light has an energy of 100-140 mJ which is an optimal perfomance power for the dye laser.
The laser light is used to pump a dye laser. Due to this laser is called pump laser. The laser medium of a dye laser is a fluorescent dye with a high quantum yield. The dyes are used to their brought emission spectrum. This allows to carry the laser emission over a great amount of wavelengths. The dye laser is based on the principle of a four state laser. A side effect of using a dye is the usage of a solvent which widened the fluorescence emission. The solvent can be used to shift the maximum peak and the spectral area of a dye. This can be useful due to vary and optimise the scan range of the laser.
The dye laser used in this work was a modified Lambda Physics FL-3002. The laser light of the dye laser is amplified after the resonator two times due to mirror positions and two cuvettes. The output UV power in the experiments is tuned between 20 and 60 mJ.

The resonator uses a *holographic grating* to select the wavelength which will be amplified by the laser process. The grating can be tilted by a sine drive with a stepper motor and a lead screw

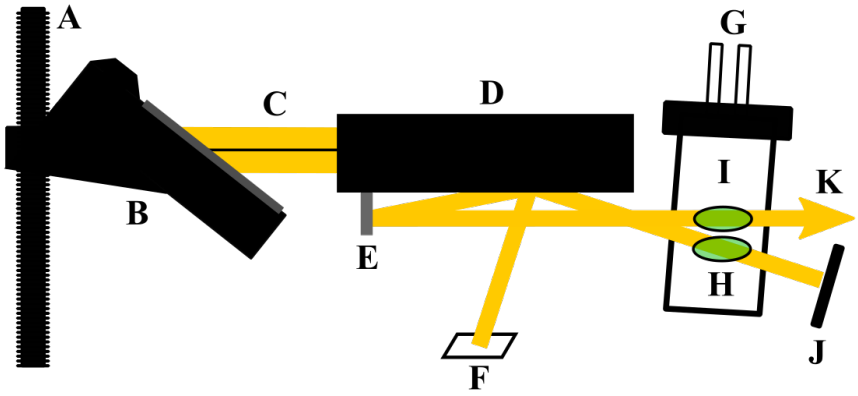

Figure 15: Schematic setup of the dye laser resonator.A: sine drive, B: grating and holder, C: expanded laser beam, D: 66x prism expander, E: feedback mirror, F: monitor reflex, G: dye cuvette, H,I: pumped volume (oscillator,pre-amp), J: cavity end mirror, K: output fundamental[57]

differing the height. The emission is amplified by deflecting the *oscillator output* between two mirros and then induce emission with the tuned light in the *pre-amplifier* region. The grating is illuminated by a *prism beam expander*. To distinguish between laser light and *amplified spontaneous emission* (ASE), while adjusting the laser, a small part of the light is deflected on a small target and is called *monitor reflex*. The modification of the Laser was done by Sirah Laser- und Plasmatechnik and provides a changing of stepper motors for the grating and the *second harmonic generation* (SHG) unit. These are controlled *via* company owend software. The mentioned parts are the only ones, which were exchanged during the modification. The characteristics of the laser are sumed up in table 2. The mechanical properties were specified by technicians of Sirah and the beam characteristics are taken of the original manual.[57] After the SHG unit the existing UV-light is seperated from the fundamental emission by two devices during this work. On the one hand a *prism seperator* and on the other a brought band filter.

Table 2: Mechanical and beam properties of the modified FL-3002 dye laser

Mechanical properties	
Property	Value
Resonator type	Littrow
Littrow grooves	600 Lines/mm
Littrow order	3-8
Maximum steps(grating)	534000
Sine drive screw pitch	0.55mm/turn
Maximum steps (SHG)	305000
Beam properties	
Property	Value
Bandwidth	$\sim$0.2 cm^{-1}
Frequency stability	$<$0.05 cm^{-1}/K
Wavelength reproducibility	$\pm 6.3 \cdot 10^{-4}$ nm
Wavelength accuracy	0.1 nm
Divergence	0.5 $mrad$
Beam diameter	2.5 mm

5.2 Sample Source and Supersonic Jet

To generate a supersonic jet a thermal sample source is used. The sample source is heated up with *heating resistors*. To prevent condensation of the evaporated sample in the pulse valve the temperature management requires a 20 K higher temperature at the valve than in the sample source. The sample source can therefore be heated to a temperature of 473 K due to the combination of polymer and metal parts. The polymer parts, gaskets and poppet, are optimised for the temperature range of 293 to 473 K due to different poppet materials as Vespel and PTFE and the brought range of temperature acceptance of the gaskets. The temperature of the sample is optimised for the best signal to noise ratio and the absence of hot bands. In all measurements helium was used as carrier gas. For water-cluster measurements a second thermal sample source was added upstream of the main sample source to the system. In this case the source was cooled down to just slowly enrich the carrier gas with water. The pulsed valve, which expands the carrier gas and the sample into the *supersonic free jet*, is a general valve type 9 with a conical nozzle of 0.5 mm diameter.

To achieve a *supersonic free jet* the gas mixture is expanded adiabatic into the vacuum with the pressure p_i. The stagnation pressure of the system is the pressure of the mixture before expansion. The following relationship between the presses must apply.

$$p_0 >> p_i \tag{71}$$

The *Knudsen number* can be used to characterize the expansion through a nozzle with the diameter *d* and the *mean free path*. This can be calculated *via* equation 72 with the stagnation pressure p_0,

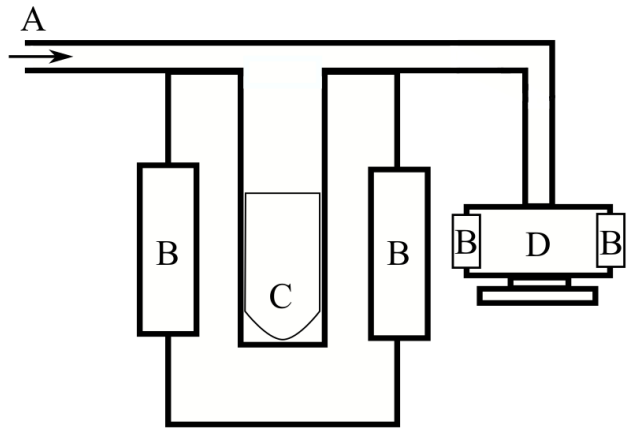

Figure 16: Schematic setup of the sample source with A: carrier gas, B: heating resistor, C: glass vessel for sample, D: pulsed valve

the Temperature *T*, the Boltzmann-constant k_B and the diameter of the molecules d_{mol}.

$$\lambda_0 = \frac{k_b T}{\sqrt{2}\pi d_{mol}^2 p_0} \tag{72}$$

As the *Knudsen number* is a dimensionless value the *mean free path* is just divided by the diameter of the nozzle 73.

$$Kn_0 = \frac{\lambda_0}{d} \tag{73}$$

Hermann $et\ al.$ explains that the Knudsen number *can be interpreted as a rarefaction parameter* which increases when the number of collisions a moleclue experiences decreases.[58] This means, if the Knudsen number is higher than one, the collisions are mainly not existing and theres no *adiabatic cooling*. These jet can be used for sub-Doppler spectroscopy. For a *Knudsen number* smaller than one the mean free path has to be small in comparison to the nozzle diameter. The number of collisions of molecules increase and therefore leading to *adiabatic cooling*.

5.3 Component time control

The time management is essential in this work. Therefore the Stanford clocks DG645 and DG535 are used. The timings of the different building parts in the setup are given in table 3 for the best setup during the measurements. The experiment is pulsed with 10 Hz. The timing of the pulsed nozzle was optimised for each measurement due to poppet material and temperature of the nozzle. This optimisation was on the scale of ± 0.8 ms. The rest of the parameters where optimised for the *optimal path length* of the setup. The Q-switch time is looped through the dye laser control to trigger the movement of the stepper motors for the grating and the SHG during the scans. The trigger for the ICCD camera control and the trigger for the Avalanche Photodiode differ due to the

Table 3: Timings for the trigger pulses

Trigger	Delay [ms]	Duration [μs]
Flash lamp INDI	2.7880	2
Q-switch INDI	3.0200	20
Pulsed valve	1.2372	350
ICCD-camera	2.992	10
Avalanche Photodiode	3.028	20

different path length. The trigger pulses can be formed and varied easily with the clock devices. The setup allows due to TTl compatible components a trigger on the rising edge with a trigger duration not very critical above a minimum of some μs.

5.4 Detectors and Processing

As previously mentioned, two detectors are used in the measuring setup. The LIF spectra are detected with the *Avalanche Photodiode* (APD) and the DF spectra are detected with the gated *intensified charge-coupled device* (ICCD) camera.

5.4.1 Avalanche Photodiode

Photodiodes are active elements, which generate photovoltage when photons are detected. This principle was improved by *avalanche* photodiodes due to higher voltages. This is accomplished by an intern reinforcement mechanism.

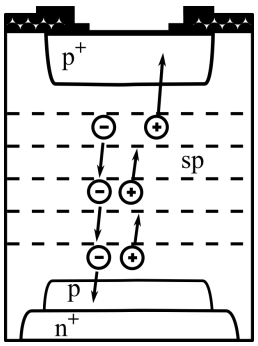

Figure 17: Schematic setup of an Avalanche Photodiode.[59]

An Avalanche Photodiode depends on a semiconductor diode, which is subdivided into different doped layers. At the edges n- and p-doped layers are added. Between these layers are a light p-doped layer (π-layer) and a normal p-doped layer. The system is held under a high blocking voltage. If a photon impinges the π-layer, electron-hole-pairs are created. The electrons are accelerated towards the outer n-layer (compare figure 17) by the diffusion voltage and the holes to the

outer p-region. The resulted voltage is a decreased *diffusion voltage* ΔV_D which is equal to the *photovoltage* V_{Ph}. The photoinduced current for photodiodes I_{ph} can be measured and calculated with the quantum efficiency ϕ_e, the frequency ν, the elementary charge e, the Planck constant h and the quantum yield $\eta(\lambda)$.

$$I_{ph} = \frac{e\psi_e}{h\nu}\eta(\lambda) \tag{74}$$

If the electron acceleration is high enough, more electron-hole pairs can be generated through impact ionization. These can be accelerated again and thus generate further electron hole pairs. This mechanism can be accomplished repetitively within the p-layer. This means one photon leads to an electron cascade or the avalanche effect within the p-layer which leads to an amplification of the signal. This means for avalanche photodiodes equation 74 has to be combined with the multiplicationfactor M, which is calculated with the reverse voltage U_R, with the voltage drop across the series resistance the diode $I \cdot R_S$ and the diod factor m $(m < 1)$ which includes specific parameters of the photodiod like material and illumination of the diode.

$$I_{APD} = I_{ph} \cdot M, \qquad M = \frac{1}{1 - \left(\frac{U_R - IR_S}{U_{BR}}\right)^m} \tag{75}$$

Because of the high reverse voltage a dark noise occurs in the signal-to-noise ratio due to the voltage fluctuation. In this work the avalanche photodiode APD130A2/M of the Thorlabs company was used. The active layer has a diameter of 1mm and the wavelength range of the diode is between 200 and 1000 nm.

5.4.2 Intensified Charge-coupled Device

The dispersed fluorescence spectra are detected with the use of a *gated ICCD camera* detector. The monochromator, to disperse the fluorescence light of the sample, is a Jobin-Yvon THR 1000, controled by a selfmade DOS-program. The grating is blazed with 2400 grooves/mm and has a lattice parameter of 400 mm. The entry slit was set to 30 μm and no exit slit is used. This allows to measure the fluorescence light, which is dispersed on the grating, with spatially resolution. With the first order grating a spectrum of 400-600 nm can be measured. With the second order grating a spectrum of 200-300 nm can be measured. The measurement principle is based on a *shot to shot* basis.

A photon which impacts the photocathode (PC) produces an electron, the *primary electron*. This electron is multiplied in a *micro-channel plate* (MCP). In a strong electric field the electrons are accelerated in direction of the *luminescent screen* (LS). Due to the channel geometry the electrons hit the walls of the channel. This induces the emitting of secondary electrons. This process continues until the cascade of electrons hit the luminescent screen. The luminescence of the screen is

guided by a lens array or an optical fibre strand on the charge-coupled device.

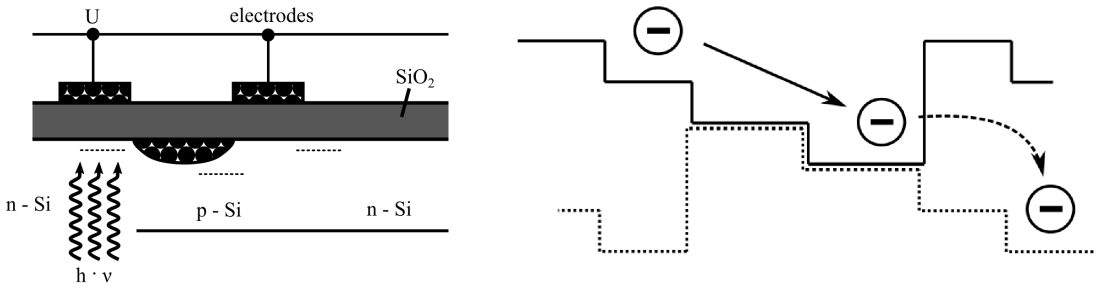

Figure 18: Schematic setup of a diode within a CCD-chip (left). Presentation of the functional principle of a CCD-array. By alternately applying positive (1) and negative (2) Voltages on the electrodes, the charges generated by the photons are forwarded one diode to the right. The speed depends on the frequency of the switching electrodes.

The pixel of the CCD are photo active transistors, which produce charges proportional to the luminescent photons. Each capacitor transfers its charge to its neighbour until the control circuit amplifier charge is reached and converged into a voltage. This voltage is amplified and processed by an analog/digital converter and software. The illumination time can be optimised for samples with a low fluorescence intensity but in this work a constant illumination time of 20 s was used for each image.

In this work a $LaVision$ Flamestar camera is used. The CCD chip has 576×384 pixels with the pixelsize 23×23 μm and has the specification number TH7863. The image region of the camera has 288×384 pixels and the other half forms the *memory zone* which is needed for the operation of the camera.

In figure 19 a typical camera image is shown. The color gradient from black over different shades of blue into red to white indicates the intensity detected by the camera. Black for zero intensity, red for maximum and white for overexposion of the camera. A different intensity sensitivity of the chip regions, from left to right a decrease of sensitivity, is only visible in the baseline if the spectrum has a very low light intensity. A vertical line on the image corresponds to a band in the dispersed fluorescence spectrum. The scattered illuminated pixels can be assigned to stray light from other sources.

To neglect these artefacts in the spectrum 50 images are processed for each spectrum by summing the intensities up, by calculating the root mean square. Due to the vertically bending and the spatial adjustment of the excitation laser, only a vertical region of 40 to 240 pixels is used to image the spectrum.

To translate the horizontal pixel position in the raw image into a spectral position in a spectrum, the CCD chip is calibrated for each monochromator position. In this case a needle on the valve cap is used to stray light from the dye laser of a certain wavelength. The horizontal position of the stray light at the given monochromator position is then used as calibration point. For calibration all

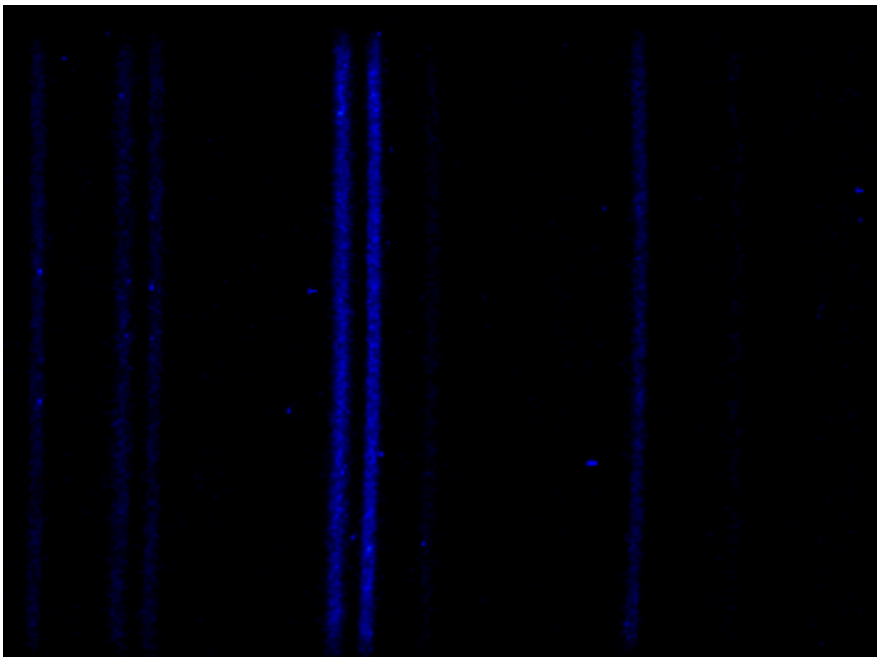

Figure 19: Example Image of the ICCD camera of the 2-cyanoindole dispersed fluorescence at monochromator position 283 nm.

calibration points for the monochromator position are plotted and fitted with a polynomial. This polynomial is then used to calculate each wavenumber for every horizontal pixel position of this monochromator position.

Now each spectrum of a monochromator position can be used to form the dispersed fluorescence spectrum of a transition. Therefore the absolute wavenumbers for each subspectrum are converted into relative wavenumbers on the excitation light. The intensities of all subspectra are normalized with respect to the strongest transition. So the strongest transition apart from the stray light of the laser has the intensity 1.

6 Publications

Contributions with first-authorship:

- **Title:** Structural changes upon electronic excitation in 1,2-dimethoxybenzene from Franck-Condon fits of the fluorescence emission spectra.
  Authors: Christian Henrichs, Marie-Luise Hebestreit, Daniel Krügler and Michael Schmitt
  submitted to: J. Mol. Struct. 1211, (2020), 127855, *published*
  The laserinduced and dispersed fluorescence spectra in this publication were measured by Malte Reineke and by myself. The quantum chemical calculations were performed by me on SCS-CC2/cc-pVTZ level of theory. The analysis of the measured spectra was carried out by myself. Rotational constanst for the FC_{FIT} procedure were investigated by Marie-Luise Hebestreit. My total share of this publication is about 65%.

- **Title:** Structural changes upon electronic excitation in 1,3-dimethoxybenzene from Franck-Condon/rotational constants fits of the fluorescence emission spectra.
  Authors: Christian Henrichs, Marie-Luise Hebestreit, Daniel Krügler and Michael Schmitt
  submitted to: J. Mol. Struct. (2021) *under review*
  The dispersed fluorescence and laser induced fluorescence spectra in this paper were measured by Benita Gutting and myself during her bachelor thesis under my supervision. I carried out the Franck-Condon fit and created the figures for this publication. Rotational constanst for the FC_{FIT} procedure were investigated by Marie-Luise Hebestreit. The *ab initio* calculations were made by myself. My total share of this publication is about 65%.

- **Title:** Excited State Structure of Isolated 4-Cyanoindole from a Combined Franck-Condon and Rotational Constants Analysis.
  Authors: Christian Henrichs, Malte Reineke, Marie-Luise Hebestreit and Michael Schmitt
  submitted to: J. Mol. Struct. 1223, (2021), 129241, *published*
  The dispersed fluorescence and laser induced fluorescence spectra in this paper were measured by myself. I carried out the Franck-Condon fit and created the figures for this publication. The quantum chemical calculations were perfomed by myself. Rotational constanst for the FC_{FIT} procedure were investigated by Marie-Luise Hebestreit. The *ab initio* calculations and further quantum mechanical analysis, like the NBO analysis, were carried out by myself. Parts of this work are also covered in the bachelor thesis of Malte Reineke, which was carried out under my supervision. My total share of this publication is about 70%.

- **Title:** Excited State Structure of Isolated 2-Cyanoindole and the Binary 2-Cyanoindole-$(H_2O)_1$ Cluster from a Combined Franck-Condon and Rotational Constants Fit.
  Authors: Christian Henrichs, Stephan Zimmermann, Marie-Luise Hebestreit, Daniel Krügler and Michael Schmitt
  submitted to: J. Mol. Struct. (2020) *accepted*

The dispersed fluorescence and laser induced fluorescence spectra in this paper were measured by Stephan Zimmermann and myself during his master thesis under my supervision. I carried out the Franck-Condon fit and created the figures for this publication. The quantum chemical calculations were perfomed, on the HPC-Cluster of the "Center for Informatin and Media Technology" (ZIM) at the Heinrich-Heine-University Düsseldorf, by myself. Rotational constanst for the FC_{FIT} procedure were investigated by Marie-Luise Hebestreit. My total share of this publication is about 65%.

Contributions with co-authorship:

- **Title:** Structural changes upon electronic excitation in 1,2-dimethoxybenzene from rotationally resolved electronic spectroscopy of various isotopologues.
  Authors: Marie-Luise Hebestreit, Christian Henrichs, Michael Schneider, Martin Wilke, W. Leo Meerts, Daniel Krügler, Michael Schmitt
  submitted to: J. Mol. Struct. 1184 (2019) 139-145, *published*

- **Title:** Excited-State Dipole Moments and Transition Dipole Orientations of Rotamers of 1,2-, 1,3, and 1,4-Dimethoxybenzene.
  Authors: Michael Schneider, Martin Wilke, Marie-Luise Hebestreit, Christian Henrichs, W. Leo Meerts, Michael Schmitt
  submitted to: ChemPhysChem 19 (2018) 307-318, *published*

7 Structural changes upon electronic excitation in 1,2-dimethoxybenzene from Franck-Condon fits of the fluorescence emission spectra.

Authors: Christian Henrichs[1], Marie-Luise Hebestreit,[1] Daniel Krügler[2], and Michael Schmitt*[1]

Journal of Molecular Structure, Volume 1211, 5 July 2020, 127855,
doi: 10.1016/j.molstruc.2020.127855

7.1 Abstract

The altered electron distribution after electronic excitation gives rise to structural changes of the heavy atom frame of aromatic molecules. These changes can be influenced by the nature of substituents as well as by their relative position in the aromatic ring. We determined the changes of the structure of 1,2-dimethoxybenzene upon electronic excitation to the first excited singlet state, from a fit of line intensities from the fluorescence emission spectra obtained through various vibronic bands and the rotational constant changes upon excitation from rotationally resolved electronic spectroscopy. The structure fit showed that the benzene ring expands unsymmetrically upon excitation. Clearly, the ring expansion can to some extent be described as *ortho*-quinoidal. Additionally, a vibrational analysis of the fluorescence emission spectrum based on comparison to an *ab initio* normal mode analysis at the coupled cluster second order perturbation SCS-CC2/cc-pVTZ level of theory is presented.

7.2 Keywords:

1,2-dimethoxybenzene, excited state, structure, Franck-Condon analysis

7.3 Highlights:

- An analysis of the excited state structure of 1,2-dimethoxybenzene has been given on the basis of a Franck-Condon-analysis.
- Additional the information from the inertial parameters of two isotopologues have been used.
- The structural changes can best be described as *ortho*-quinoidal distortion

[1]Heinrich-Heine-Universität, Institut für Physikalische Chemie I, D-40225 Düsseldorf, Germany, E-mail:mschmitt@hhu.de
[2b] Bruker-Daltonik GmbH, 28359 Bremen, Germany

7.4 Introduction

Ground state structures of stable molecules are routinely determined by microwave spectroscopy[60] or various diffraction methods. These methods cover gas phase electron diffraction,[61] neutron powder diffraction[62] and X-ray diffraction of powders or crystals.[63] Apart from the time-resolved variant of gas phase electron diffraction,[64] none of these methods gives access to excited state structures. However, these structures can be accessed by two complementary experimental spectroscopic methods: in the time domain, by rotational coherence spectroscopy, pioneered by Felker,[65] and subsequently improved by Riehn[66] and in the frequency domain, by rotationally resolved electronic spectroscopy, pioneered by Meerts[67] and Pratt[67] and subsequently continued in our group.[68,69] Both methods yield in the end the same structural informations, which are the three zero-point vibrationally averaged rotational constants about the main inertial axes of the molecules. For molecules with more than two atoms, $3N - 6$ rotational constants are needed. Kraitchman[70] and later Costain[71] showed, how structural information about polyatomic molecules can be obtained from rotational constants of various isotopologues.

Another approach to geometries of electronically excited molecules is the application of the Franck-Condon (FC) principle,[72,73] which is based on the approximation of Born and Oppenheimer.[74] Application of the Franck-Condon principle yields the displacement along the normal coordinate of a two-atomic molecule. A generalization has been given by Duschinsky who pointed out, that for the general case of an N-atomic system, the normal coordinates of the ground and the excited state are connected via a rotation and a linear displacement along the $3N - 6$ normal coordinates.[75]

Doktorov presented recursion relations, which allowed for the calculation of the multidimensional FC integrals in a time-economic fashion.[51,52] In principle, geometry changes between ground and excited states can be obtained from both absorption and emission spectra.[32] However, the presence of potentially perturbing electronic states, which are close to the electronically excited state under consideration, demands for the consideration of Herzberg-Teller effects, what makes the method extremely time consuming for absorption spectra.[76,77] Therefore, we restrict ourselves to the fit of fluorescence emission (FE) spectra.[78–81] Since the ground state is far away from the perturbing state, the FC approximation, which states that the transition takes place at a fixed nuclear geometry and the transition moment does not depend on the vibrational coordinate is better in emission, than in absorption. The accuracy of structure determinations can greatly be enhanced by simultaneously fitting of emission spectra intensities from various vibronically excited levels and use of rotational constant changes from high resolution electronic spectra.

The results concerning the question on the planarity of 1,2-DMB in condensed phase have been disputed,[82–84] but for the gas phase a planar ground state structure is beyond doubt since works from the Pratt group using high resolution electronic spectroscopy.[85] They could show, that all bands in the vibronic spectrum have the same rotational constants in the ground state and belong therefore to the same rotamer, which was identified from a comparison to quantum chemical calcu-

lations as the *trans*-1,2-dimethoxybenzene rotamer. Furthermore, the inertial defect, as measure of planarity of a molecule, shows unambiguously the planarity also in the electronically excited state. The planarity of isolated anisole (methoxybenzene) was also proven by microwave spectroscopy.[86] Suvitha *et al.* presented a vibrational analysis of 1,2-DMB in the electronic ground state S_0 on the basis of FTIR and Raman spectroscopy.[87] The vibrational spectrum of 1,2-dimethoxybenzene (1,2-DMB) in the excited S_1 state and in the ionic D_0 ground state has been investigated by Huang *et al.*[88] using resonant two-color ionization. Yang *et al.*[89] performed two-color resonant two-photon mass-analyzed threshold ionization spectroscopy to investigate 1,2-dimethoxybenzene in its ground ionic state. The excited state dipole moment of 1,2-DMB has recently been determined by Schneider *et al.* using rotationally resolved electronic Stark spectroscopy.[90] The changes of the structure of 1,2-DMB upon electronic excitation based on a *pseudo*-Kraitchman fit, using the rotational constants of two isotopologues, have been presented by Hebestreit *et al.*[91]

7.5 Computational Methods

7.5.1 Quantum chemical calculations

Structure optimizations were performed employing Dunning's correlation consistent polarized valence triple zeta basis set (cc-pVTZ) from the TURBOMOLE library.[92,93] The equilibrium geometries of the electronic ground and the lowest excited singlet states were optimized using the approximate coupled cluster singles and doubles model (CC2) employing the resolution-of-the-identity approximation (RI).[94–96] The Hessians and harmonic vibrational frequencies for both electronic states, which are utilized in the FC fit, have been obtained from numerical second derivatives using the NumForce script[97] implemented in the TURBOMOLE program suite.[98] A natural population analysis (NBO)[99] has been performed at the CC2 optimized geometries using the wavefunctions from the CC2 calculations as implemented in the TURBOMOLE package.[98]

7.5.2 Franck-Condon fits

The change of a molecular geometry upon electronic excitation can be determined from the intensities of the fluorescence emission (FE) bands according to the FC principle. Here, the relative intensity of a vibronic band depends on the overlap integral of the vibrational wave functions of both electronic states. The transition dipole moment for a transition between an initial electronic state $|m, v\rangle$ and a final electronic state $|n, w\rangle$ is defined as:

$$M_{vw} = \langle v|\mu_{mn}(Q)|w\rangle \tag{76}$$

with the electronic transition dipole moment $\mu_{mn}(Q)$.

$$\mu_{mn}(Q) = \langle \Psi_m|\mu|\Psi_n\rangle\,; \quad \mu = \sum_g er_g \tag{77}$$

where r_g is the position vector of the gth electron. The dependence of the electronic transition dipole moment μ_{mn} on the nuclear coordinates can be approximated by expanding μ_{mn} in a Taylor series about the equilibrium position at Q_0. The series is truncated after the first term in the FC approximation.

The fit has been performed using the program FCFIT, which has been developed in our group and described in detail before.[32,100] The program computes the FC integrals of multidimensional, harmonic oscillators mainly based on the recursion formula given in the papers of Doktorov, Malkin, and Man'ko.[51,52] and fits the geometry (in linear combinations of selected normal modes) to the experimentally determined intensities. This is simultaneously done for all emission spectra, which are obtained *via* pumping through different S_1 vibronic modes.

The vibrational modes of the electronically excited state can be expressed in terms of the ground state modes using the following linear orthogonal transformation, first given by Duschinsky.[75]

$$Q' = SQ'' + d \tag{78}$$

Here, Q' and Q'' are the N-dimensional vectors of the normal modes of excited and ground state, respectively, S is a N x N rotation matrix (the Duschinsky matrix) and d is an N-dimensional vector which describes the linear displacements of the normal coordinates.

The fit of the geometry to the intensities in the vibronic spectra can be greatly improved if independent information about the geometry changes upon electronic excitation is available. This additional information is provided by the change of the rotational constants upon electronic excitation, which can be obtained from rotationally resolved electronic spectroscopy. While geometry fits to the rotational constants are routinely performed using non-linear fits in internal coordinates, the combination of rotational constant changes and vibronic intensities allows for determination of many more geometric parameters and furthermore reducing the correlations between the parameters.

7.6 Experimental Methods

1,2-DMB ($\geq$ 99%) was purchased from Sigma-Aldrich and used without further purification. 1,2-DMB-d6 was purchased from CDN Isotopes and used without further purification. The experimental setup for the dispersed fluorescence (DF) spectroscopy has been described in detail elsewhere.[101,102] In brief, 1,2-DMB and 1,2-DMB-d6 were evaporated at 318 K and co-expanded through a pulsed nozzle (kept at 328 K to avoid condensation) with a 500 μm orifice (General Valve) into the vacuum chamber using helium as carrier gas. The output of a Nd:YAG (Spectra-Physics INDI) pumped dye laser (Lambda-Physik, FL3002) was frequency doubled and crossed at right angles with the molecular beam. The resulting fluorescence was imaged on the entrance slit of a f = 1 m monochromator (Jobin Yvon, grating 2400 lines/mm blazed at 400 nm in first

order). The dispersed fluorescence spectrum was recorded using a gated image intensified UV sensitive CCD camera (Flamestar II, LaVision). One image on the CCD chip spectrally covers approximately 600 cm^{-1}. Since the whole spectrum is taken on a shot-to-shot basis, the relative intensities in the DF spectra do not vary with the laser power. The relative intensities were afterwards normalized to the strongest band in the spectrum, not including the resonance fluorescence band, which also contains the stray light and is therefore excluded from the FC analysis.

7.7 Results

7.7.1 Computational Results

The calculation of multi-dimensional Franck–Condon factors for large molecules requires theoretical methods, for which numerical or analytical Hessians are known with sufficient accuracy for both electronic states. Additionally, the calculation of ground and excited states should preferentially be based on the same theoretical foundation. These calculations might be performed using (time-dependent) density functional theory (TD-DFT) with appropriate basis sets,[103,104] complete active space self-consistent field (CASSCF) theory,[105] coupled cluster singles and doubles with perturbative triples [CCSD(T)],[106] or the approximate coupled cluster singles and doubles model (CC2) employing the resolution-of-the-identity approximation (RI).[94–96] We have shown that the use of CC2 calculations in the spin-component-scaled variant shows very good agreement to experimentally determined properties in both electronic states.[79–81,107] Therefore, the electronic ground and excited state structures of the lowest singlet states have been optimized at the SCS-CC2/cc-pVTZ level of theory. The Cartesian coordinates of the SCS-CC2/cc-pVTZ optimized structures of the ground and lowest excited singlet states of 1,2-DMB are given in the online supporting material. Figure 20 shows the SCS-CC2/cc-pVTZ optimized structures of the two possible planar rotamers of 12-DMB in their electronic ground state.

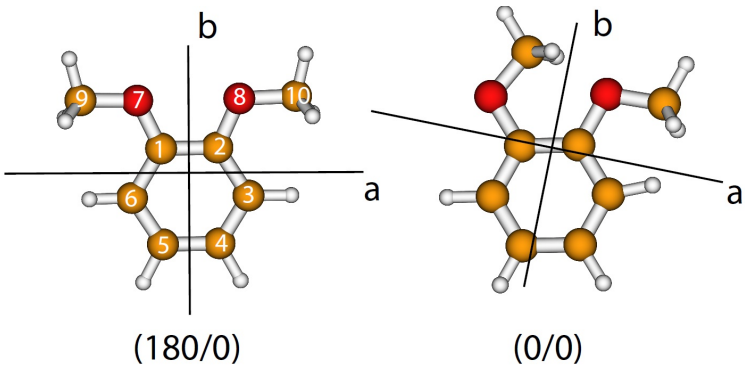

Figure 20: Calculated structures of the two possible conformers of 1,2-DMB.

From rotationally resolved electronic spectroscopy, we know that the experimentally observed isomer with an electronic origin at 35.751 cm^{-1} is the (180/0) rotamer with C_{2v} symmetry.[85,90] We therefore constrained the optimization of the ground state to C_{2v} symmetry.

Table 4: SCS-CC2/cc-pVTZ calculated and experimental wavenumbers of the 54 normal modes of the ground and first electronically excited states of 1,2-DMB dimer along with the respective symmetry labels and the coefficients of the Duschinsky matrix, which are larger than 0.4.

Mode	S_0			S_1			Duschinsky
	Sym.	Calc.	Obs.	Sym.	Calc.	Obs.	
$Q_1(S_0)$	b1	89		a'	57		$Q_1(S_1)$= +0,94 $Q_1(S_0)$
$Q_2(S_0)$	a2	112		a"	76	84	$Q_2(S_1)$= +0,91 $Q_2(S_0)$
$Q_3(S_0)$	a2	172	152	a"	118	117	$Q_4(S_1)$= $-0,90$ $Q_3(S_0)$
$Q_4(S_0)$	a1	197	190	a'	193		$Q_5(S_1)$= $-0,94$ $Q_4(S_0)$
$Q_5(S_0)$	b1	253		a'	90		$Q_3(S_1)$= +0,72 $Q_5(S_0)-0,6$ $Q_8(S_0)$
$Q_6(S_0)$	a2	285		a"	200		$Q_6(S_1)$= $-0,94$ $Q_6(S_0)$
$Q_7(S_0)$	b2	286		a"	280		$Q_8(S_1)$= $-0,99$ $Q_7(S_0)$
$Q_8(S_0)$	b1	330		a'	205		$Q_7(S_1)$= $+0,57$ $Q_3(S_0)$+0,72 $Q_8(S_0)$
$Q_9(S_0)$	a1	379	372	a'	381		$Q_{11}(S_1)$= $+0,81$ $Q_9(S_0)+0,54$ $Q_{10}(S_0)$
$Q_{10}(S_0)$	b1	478	462	a'	336		$Q_{10}(S_1)$= $+0,42$ $Q_9(S_0)-0,60$ $Q_{10}(S_0)-0,46$ $Q_{20}(S_0)$
$Q_{11}(S_0)$	b2	481		a"	436		$Q_{14}(S_1)$ = $-0,94$ $Q_{11}(S_0)$
$Q_{12}(S_0)$	a2	565	544	a"	314		$Q_9(S_1)$= $+0,73$ $Q_{12}(S_0)-0,57$ $Q_{19}(S_0)$
$Q_{13}(S_0)$	b2	581		a"	555		$Q_{17}(S_1)$ = $-0,96$ $Q_{13}(S_0)$
$Q_{14}(S_0)$	a1	582	579	a'	512	508	$Q_{15}(S_1)$ = $-0,97$ $Q_{14}(S_0)$
$Q_{15}(S_0)$	a2	696	629	a"	515		$Q_{16}(S_1)$ = $-0,94$ $Q_{15}(S_0)$
$Q_{16}(S_0)$	b1	756		a"	704		$Q_{18}(S_1)$ = $+0,70$ $Q_{16}(S_0)+0,65$ $Q_{20}(S_0)$
$Q_{17}(S_0)$	a1	760	755	a'	723		$Q_{19}(S_1)$ = $+0,96$ $Q_{17}(S_0)$
$Q_{18}(S_0)$	b2	819		a"	787		$Q_{20}(S_1)$ = $-0,72$ $Q_{18}(S_0)$ $-0,64$ $Q_{21}(S_0)$
$Q_{19}(S_0)$	a2	831		a"	432		Q_{13} (S_1)= $+0,62$ $Q_{12}(S_0)$ $+0,69$ $Q_{19}(S_0)$
$Q_{20}(S_0)$	b1	898		a'	394		Q_{12} (S_1)= $+0,54Q_{10}(S_0)+0,48Q_{16}(S_0)-0,52Q_{20}(S_0)$
$Q_{21}(S_0)$	a2	934	954	a"	795		$Q_{21}(S_1)$ = $+0,67$ $Q_{18}(S_0)$ $-0,70$ $Q_{21}(S_0)$
$Q_{22}(S_0)$	b2	1054		a"	1013		$Q_{23}(S_1)$ = $-0,97$ $Q_{22}(S_0)$
$Q_{23}(S_0)$	a1	1056	1040	a'	980		$Q_{22}(S_1)$ = $+0,71$ $Q_{23}(S_0)$ $+0,67$ $Q_{24}(S_0)$
$Q_{24}(S_0)$	a1	1078		a'	1027		$Q_{24}(S_1)$ = $+0,68$ $Q_{23}(S_0)$ $-0,71$ $Q_{24}(S_0)$
$Q_{25}(S_0)$	b2	1144	1128	a"	1089		$Q_{25}(S_1)$ = $-0,96$ $Q_{25}(S_0)$
$Q_{26}(S_0)$	a1	1183	1160	a'	1173		$Q_{28}(S_1)$ = $+0,97$ $Q_{26}(S_0)$
$Q_{27}(S_0)$	a2	1185		a"	1171		$Q_{27}(S_1)$ = $-0,88$ $Q_{27}(S_0)$ $+0,45$ $Q_{28}(S_0)$
$Q_{28}(S_0)$	b1	1186		a'	1171		$Q_{26}(S_1)$ = $-0,45$ $Q_{27}(S_0)$ $-0,88$ $Q_{28}(S_0)$
$Q_{29}(S_0)$	b2	1209		a"	1200		$Q_{29}(S_1)$ = $-0,95$ $Q_{29}(S_0)$
$Q_{30}(S_0)$	a1	1217		a'	1203		$Q_{30}(S_1)$ = $-0,97$ $Q_{30}(S_0)$
$Q_{31}(S_0)$	b2	1259		a"	1204		$Q_{31}(S_1)$ = $-0,86$ $Q_{31}(S_0)$
$Q_{32}(S_0)$	a1	1294	1297	a'	1308		$Q_{33}(S_1)$ = $+0,80$ $Q_{32}(S_0)+0,55$ $Q_{34}(S_0)$
$Q_{33}(S_0)$	b2	1313		a"	1277		$Q_{32}(S_1)$ = $+0,40$ $Q_{31}(S_0)-0,89$ $Q_{33}(S_0)$
$Q_{34}(S_0)$	a1	1395	1340	a'	1726		$Q_{44}(S_1)$ = $+0,51$ $Q_{32}(S_0)-0,80$ $Q_{34}(S_0)$
$Q_{35}(S_0)$	b2	1469		a"	1415		$Q_{34}(S_1)$ = $+0,89$ $Q_{35}(S_0)$
$Q_{36}(S_0)$	a1	1483		a'	1485		$Q_{37}(S_1)$ = $-0,79$ $Q_{36}(S_0)+0,52$ $Q_{42}(S_0)$
$Q_{37}(S_0)$	b2	1493		a"	1476		$Q_{36}(S_1)$ = $-0,91$ $Q_{37}(S_0)$
$Q_{38}(S_0)$	a2	1517	1506	a"	1514		$Q_{38}(S_1)$ = $-0,96$ $Q_{38}(S_0)$
$Q_{39}(S_0)$	b1	1518		a'	1514		$Q_{39}(S_1)$ = $-0,96$ $Q_{39}(S_0)$
$Q_{40}(S_0)$	a1	1530		a'	1527		$Q_{42}(S_1)$ = $+0,94$ $Q_{40}(S_0)$
$Q_{41}(S_0)$	b2	1531	1535	a"	1527		$Q_{41}(S_1)$ = $-0,90$ $Q_{41}(S_0)$
$Q_{42}(S_0)$	a1	1547		a'	1431		$Q_{35}(S_1)$ = $+0,58$ $Q_{36}(S_0)+0,64$ $Q_{42}(S_0)$
$Q_{43}(S_0)$	b2	1630	1626	a"	1525		$Q_{40}(S_1)$ = $-0,88$ $Q_{43}(S_0)$
$Q_{44}(S_0)$	a1	1634		a'	1566		$Q_{43}(S_1)$ = $-0,43$ $Q_{42}(S_0)-0,88$ $Q_{44}(S_0)$
$Q_{45}(S_0)$	b2	3039		a"	3055		$Q_{45}(S_1)$ = $-0,99$ $Q_{45}(S_0)$
$Q_{46}(S_0)$	a1	3040		a'	3057		$Q_{46}(S_1)$ = $-0,99$ $Q_{46}(S_0)$
$Q_{47}(S_0)$	a2	3112		a"	3138		$Q_{47}(S_1)$ = $-0,97$ $Q_{47}(S_0)$
$Q_{48}(S_0)$	b1	3112		a'	3138		$Q_{48}(S_1)$ = $+0,97$ $Q_{48}(S_0)$
$Q_{49}(S_0)$	b2	3177		a"	3183		$Q_{49}(S_1)$ = $-0,99$ $Q_{49}(S_0)$
$Q_{50}(S_0)$	a1	3177		a'	3183		$Q_{50}(S_1)$ = $+0,99$ $Q_{50}(S_0)$
$Q_{51}(S_0)$	b2	3200		a"	3193		$Q_{51}(S_1)$ = $+0,98$ $Q_{51}(S_0)$
$Q_{52}(S_0)$	a1	3218		a'	3209		$Q_{52}(S_1)$ = $+0,98$ $Q_{52}(S_0)$
$Q_{53}(S_0)$	b2	3238		a"	3255		$Q_{53}(S_1)$ = $+0,98$ $Q_{53}(S_0)$
$Q_{54}(S_0)$	a1	3241		a'	3256		$Q_{54}(S_1)$ = $+0,96$ $Q_{54}(S_0)$

The 54 ground state vibrations of 1,2-DMB transform like $\Gamma_{ired} = 18a_1 + 10a_2 + 9b_1 + 17b_2$. Upon electronic excitation the $\sigma v'$ plane of the aromatic ring is lost and the 54 vibrations transform like $\Gamma_{ired} = 27a' + 27''$ in C_s symmetry with the correlation of a_1 and b_1 transforming like a' and a_2 and b_2 as a''. The vibrational frequencies and symmetries from the calculations for both the ground and lowest electronically excited state are summarized in Tables 4 and S4. The coefficients from the Duschinsky matrix are used in order to assign correctly ground and excited state modes.

Additionally, we calculated the vibrational frequencies for the d_6 isotopologue, in which both OCH_3 groups are replaced by OCD_3 using the Hessian at the optimized geometry of the ground and excited states for the undeuterated isotopologue. These results will be used for assignment of the experimental vibrational frequencies and are shown in Table S4 of the online supporting material.

The transition dipole moment of the lowest electronically excited state is oriented along the molecular b-axis (for axis convention refer to Figure 20) and hence transforms like a_1 under C_{2v} and like a' under C_s symmetry.

7.7.2 Experimental Results

7.7.3 Fluorescence excitation spectra of 1,2-DMB (h_{10}) and 1,2-DMB (d_6)

The interpretation of the Franck-Condon spectra im emission crucially depend on the correct assignments of the vibronic levels in the excited state, through which the emission spectra are recorded. Assignment of these vibronic bands is made on basis of the isotopic shifts of the d_6 isotopologue. Figure 21 shows the fluorescence excitation spectra of 1,2-DMB (h_{10}) and of a mixture of 1,2-DMB (h_{10}) and 1,2-DMB (d_6) .

The electronic origin of the d_6 isotopologue is blue shifted by 14 cm^{-1} relative to the undeuterated isotopologue. Due to remaining undeuterated 1,2-DMB and lack of mass resolution in the fluorescence excitation, the LIF spectrum of 1,2-DMB (d_6) is a superposition of both deuterated und undeuterated 1,2-DMB. The peaks, belonging to 1,2-DMB (d_6) are obtained from the difference of both spectra and are marked by an asterisk. Assignment of the vibrational bands is made on basis of the isotopic shifts of the bands of the d_6 isotopologue in comparison to the computed isotopic shifts from the SCS-CC2 calculations, cf. Table S4. In the following we will concentrate only on bands, which are excited to obtain the FE spectra through various vibronic bands in order to increase the information for the Franck-Condon fits.

The first strong vibronic band is observed at 84 cm^{-1} for (h_{10}) and at 77 cm^{-1} for the (d_6) isotopologue. Both the absolute wavenumber as well as the isotopic shift point to the asymmetric COC out-of-plane vibration of the two methoxy groups. The next vibration at 117 cm^{-1} (106 cm^{-1} for the deuterated isotopologue) is clearly the antisymmetric torsion, calculated at 121 cm^{-1}. The third band, which we utilized for obtaining the FE spectra at 508 cm^{-1}, calculated at 512 cm^{-1} is the analogue of the Q_{14} mode of the ground state and hence an antisymmetric COC in-plane

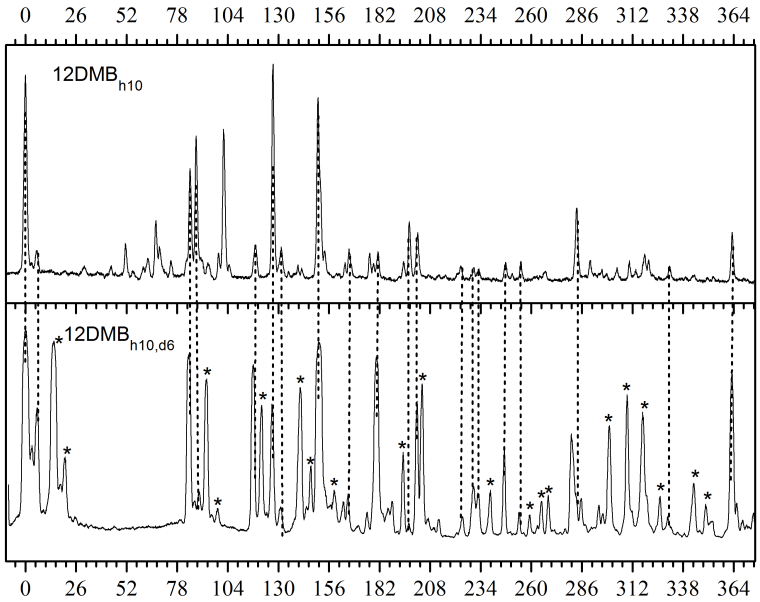

Figure 21: Fluorescence excitation spectra of 1,2-DMB (h_{10}) and of a mixture of 1,2-DMB (h_{10}) and 1,2-DMB (d_6)

bending mode. Other assignments of S_1 vibronic bands, which are not used for excitation are not discussed here, but can be inferred from Table S4 of the online supporting material.

One has to keep in mind that the S_1-state modes are strongly mixed and a straightforward description like for the ground state can only be given for selected modes. This mode mixing can best be seen in the graphical representation of the Duschinsky matrix, given in Figure 22. Black squares refer to a Duschinsky matrix element of 1, white squares of 0, intermediate values are shown grey coded. Modes, which show no mixing are represented by a black square (not necessarily on the diagonal, because the order of the vibrations might interchange upon electronic excitation. Figure 22 shows that with the exception of the CH stretching modes, all modes below 3000 cm^{-1} are heavily mixed.

7.7.4 Fluorescence emission spectra of the origins of 1,2-DMB (h_{10}) and 1,2-DMB (d_6)

Figure 23 shows a comparison of the FE spectra of 1,2-DMB (h_{10}) and 1,2-DMB (d_6), obtained after excitation of the respective origin band of each isotopologue. Corresponding transitions are connected by straight lines, the wavenumber shifts upon deuteration are given for the major peaks in the Figure and for all observed bands in Table S4 of the online supplementary material. An unambiguous assignment of the observed ground state vibrations could be given on the basis of the deuteration shifts of the individual bands, cf. Table 5.

Tuttle *et al.*[108] noted that for *ortho*-disubstituted benzenes the nomenclature of Wilson[109] and

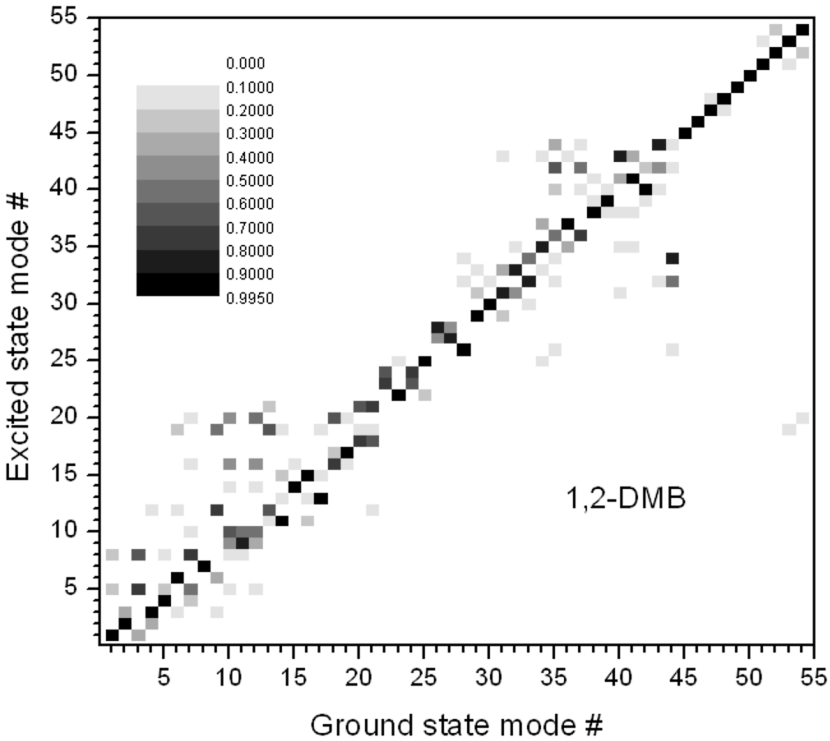

Figure 22: Duschinsky matrix of the 54 vibrational modes of 1,2-DMB.

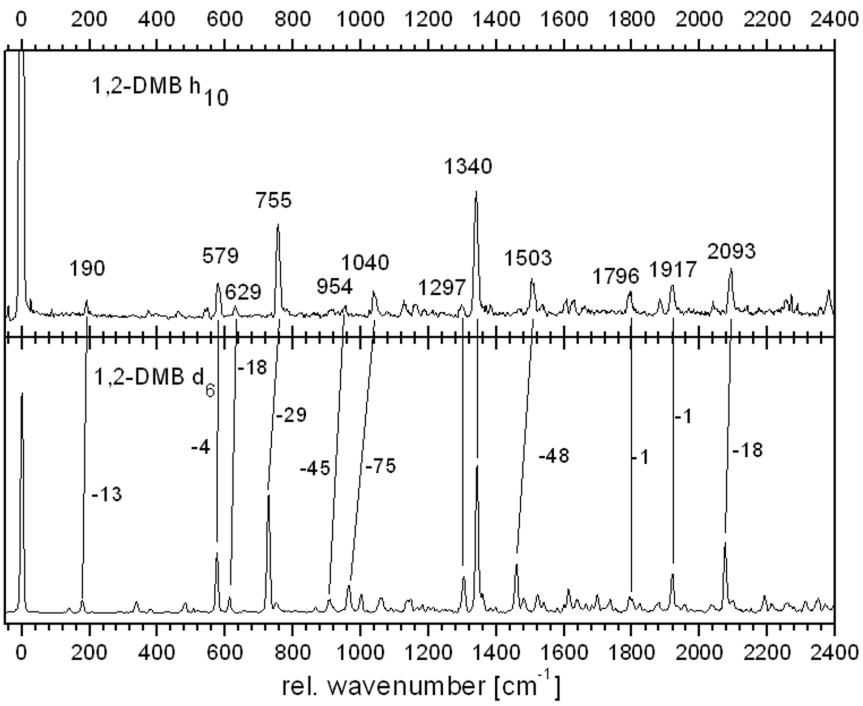

Figure 23: Fluorescence emission spectra of the electronic origins of 1,2-DMB (h_{10}) and 1,2-DMB (d_6) at 35.751 and 35.765 cm^{-1}. respectively.

Varsanyi[110] is misleading, because the same vibrational mode is designated by different labels, depending if the two substituents are "light" or "heavy". This can easily be seen when the modes of the *ortho*-disubstituted benzene derivative are expressed as linear combination of respective benzene vibrations, which are heavily mixed, depending on the mass of the substituents. We therefore adopt here the numbering scheme of Tuttle *et al.*, which is based on the more convenient Mulliken[111] or Herzberg[112] numbering schemes.

Table 5: Observed vibrational ground state vibrational wavenumbers and intensities along with the assignments of the modes, based on the SCS-CC2/cc-pVTZ calculated frequencies. Overtones and combination bands are assigned, assuming harmonic behavior. Mode numbering refers to Table 4, assignments given according to Tuttle *et al.*,[108] Mulliken[111] and Wilson.[109]

$\tilde{\nu}$	Int.	Mode	Tuttle	Mulliken	Wilson	Calc.	Description
190	0,21	Q_4	$^oD_{21}$	11	15	197	symmetric CCO in-plane bending
372	0,14	Q_9	-	-	-	379	symmetric COC in-plane bending (OCH_3)
462	0,14	Q_{10}	$^oD_{28}$	19	16b	468	symmetric CCC out-of-plane bending
544	0,15	Q_{12}	$^oD_{27}$	15	16a	564	antisymmetric CCC out-of-plane bending
579	0,34	Q_{14}	-	-	-	582	antisymmetric COC in-plane bending (OCH_3)
629	0,17	Q_{15}	$^oD_{26}$	14	4	694	antisymmetric CCC out-of-plane bending
755	0,76	Q_{16}	$^oD_{25}$	18	11	748	symmetric CH out-of-plane bending
954	0,17	Q_{21}	$^oD_{22}$	12	5	932	symmetric CH out-of-plane bending
1040	0,28	Q_{24}	$^oD_{15}$	8	18b	1077	symmetric CCH in-plane bending
1128	0,21	Q_{25}	$^oD_{14}$	27	18a	1144	antisymmetric CCH in-plane bending
1160	0,19	Q_{14}^2	-	-	-	1158	overtone
1297	0,18	Q_{32}	$^oD_{10}$	6	7a	1294	symmetric CO in-plane stretching
1340	1,00	Q_{34}	$^oD_7$	4	19b	1393	symmetric CC in-plane stretching
1506	0,37	Q_{16}^2	$^oD_{25}^2$	18^2	11	1510	overtone
1535	0,19	Q_{41}	-	-	-	1531	symmetric HCH bending (OCH_3)
1606	0,21	Q_{14}+Q_{24}	-	-	-	1619	combination
1626	0,21	Q_{43}	$^oD_6$	23	8b	1630	symmetric CC in-plane stretching
1796	0,26	Q_{10}+Q_{34}	$^oD_{28}$+$^oD_7$	19+4	16b+19b	1802	combination
1885	0,21	Q_{12}+Q_{34}	$^oD_{27}$+$^oD_7$	15+4	16a+19b	1884	combination
1917	0,32	Q_{14}+Q_{34}	-	-	-	1919	combination
2093	0,44	Q_{16}+Q_{34}	$^oD_{25}$+$^oD_7$	18+4	11+19b	2095	combination
2380	0,29	Q_{24}+Q_{34}	$^oD_{15}$+$^oD_7$	8+4	18b+19b	2380	combination

The first observed vibration at 190 cm^{-1} is assigned to the symmetric CCO bending mode, $^oD_{21}$ in the Tuttle numbering or mode 11 in Mullikan notation for C_{2v} symmetric benzene derivatives. The following band at 372 cm^{-1} can be assigned to the symmetric COC in-plane bending, mainly a methoxy group centered vibration, which therefore has no counterpart in the Tuttle or Mulliken nomenclature. The symmetric and antisymmetric CCC out-of-plane bending vibrations ($^oD_{28}$ and $^oD_{27}$) are found at 462 and 544 cm^{-1}, respectively. The following band at 579 cm^{-1} is assigned to the methoxy group centered antisymmetric COC in-plane bending vibration. The antisymmetric CCC out-of-plane bending, $^oD_{26}$ is observed at 629 cm^{-1}, a pair of symmetric CH out-of-plane bending modes, $^oD_{25}$ and $^oD_{22}$ at 755 and 954 cm^{-1}, respectively. They are followed by a pair of symmetric and antisymmetric CCH in-plane bending modes ($^oD_{15}$ and $^oD_{14}$) at 1040 and 1128 $^{-1}$. The band at 1297 cm^{-1} can be assigned to a symmetric CO in-plane stretching vibration ($^oD_{10}$), which has considerable amount of CH bending character in the methoxy group. The most prominent band in the emission spectrum of the origin is observed at 1340 cm^{-1}, the symmetric CC in-plane stretching ($^oD_7$), serves as false origin for nearly all other low frequency vibrations. The complete list of assignments including all combination bands and overtones are summarized

in Table 5, the vibrational modes are shown in Figure S1 of the online supplementary material.

7.7.5 Franck-Condon fits of the fluorescence emission spectra of vibronic bands of 1,2-DMB

Figure 24 shows the FE spectra of 1,2-DMB after excitation of the electronic origin and the vibronic bands at 84, 117, and 508 cm^{-1}, respectively along with the FC fits of the vibronic intensities. The FE spectrum of the electronic origin has been analyzed in the last section.

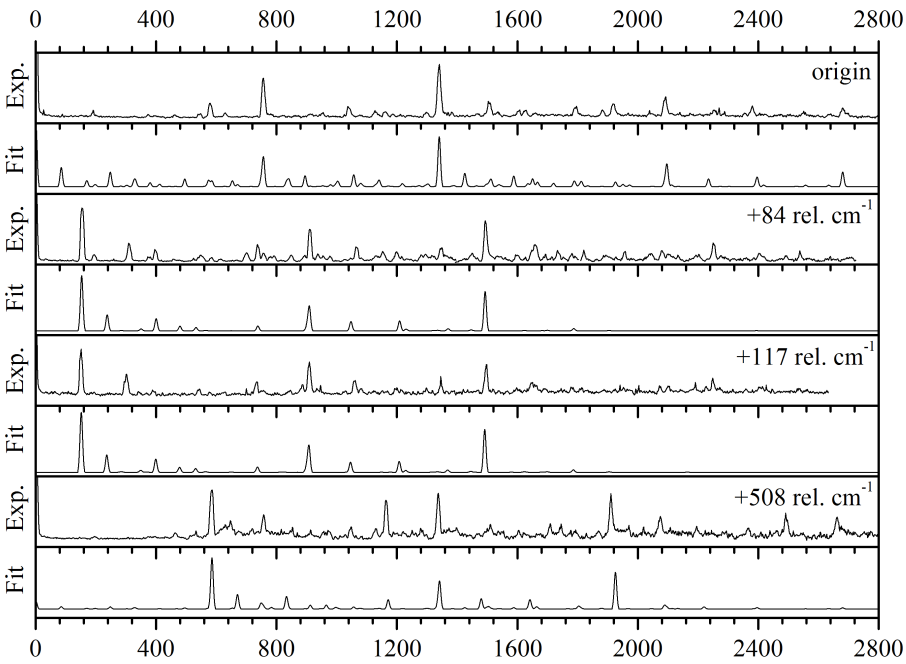

Figure 24: Fluorescence emission spectra, obtained via excitation of the electronic origin (0,0), of 0,0 + 84, 0,0 + 117, and 0,0 + 508 cm^{-1} of h_{10}-1,2-DMB, along with the respective FC fits.

FE after excitation of the asymmetric COC out-of-plane vibration of the two methoxy groups at 84 cm^{-1} has the band at 154 cm^{-1} as most intense band, which serves as false origin for all other vibrations. The following band at 909 cm^{-1}can therefore be assigned to the combination with the symmetric CH out-of plane bending mode $^oD_{25} + 154$ cm^{-1} like the band at 755 cm^{-1} in the origin spectrum. The band at 1492 cm^{-1} arises from a combination of the band at 1340 cm^{-1} which is the symmetric CC in-plane stretching mode ($^oD_7$) with the excited COC out-of-plane vibration.

For the excitation of the antisymmetric torsion at 117 cm^{-1}, the false origin can be observed at 150 cm^{-1}. As in the assignment of the observed emission bands after COC out-of-plane excitation at 84 cm^{-1}, the the symmetric CH out-of plane bending mode $^oD_{25}$ is observed in combination with the band at 908 cm^{-1}, while the $^oD_7$ mode can be assigned to the band at 1496 cm^{-1}.

The assignment in the excitation spectrum of 508 cm^{-1} can be done for the same modes.

Therefore the most intense band at 585 cm^{-1} serves as false origin for all other bands. The band at 1337 can be assigned to the mode $^{o}D_{25}$ and the band at 1910 to the $^{o}D_{25}$ mode.

7.8 Discussion

7.8.1 *Ab initio* determination of geometry changes upon electronic excitation

The left part of Figure 25 and Table 6 show the changes of the relevant bond lengths in pm upon electronic excitation as obtained from the SCS-CC2/cc-pVTZ calculations. The CC bonds in the aromatic ring, which are adjacent to the OCH_3 groups, expand by 5.8 pm, while those in the neighboring positions only expand by 1.0 pm. The aromatic CC bond between the OCH_3 substituents contracts only very slightly by -0.1 pm. Both $C_{ar}O$ bond distances decrease by -0.4 pm, while the OC_{methyl} bond lengths increase by 0.9 pm. Altogether, these geometry changes point to a partial localization of the CC double bonds in the aromatic ring after electronic excitation, which can be described as an *ortho*-quinoidal distortion of the benzene ring. Electronic excitation is accompanied by a shift of electron density from the O-Atoms into the aromatic ring, as can be seen from the electron density difference in Ref.[91]

7.8.2 Franck-Condon fit of geometry changes upon electronic excitation

Additionally to a fit of the line intensities from emission spectra using a multidimensional Franck-Condon model, we simultaneously use the rotational constants changes upon electronic excitation, when available as additional information about structural changes. The rotational constants changes of both 1,2-DMB isotopologues studied here, obtained by rotationally resolved electronic spectroscopy, have been taken from Ref.[91]

In order to fit of the structural changes, we systematically distort the excited state equilibrium Cartesian geometry relative to the ground state geometry using the intensities of all emission spectra and the changes of the rotational constants of all isotopologues, simultaneously. The goodness of the fit (χ^2) is determined from the minimum of the weighted sum of squared residuals, both of the rotational constants, as well as the intensities in the emission spectra. Since line intensities from emission spectra and rotational constants from fluorescence emission spectra have no obvious correlations, we can factorize the correlation matrix in two submatrices, which depend only on rotational constant changes Δ_{RC} and on the intensities I. The total χ^2 is therefore partitioned into two independent parts: $\chi^2_{tot} = \chi^2_{\Delta R} + \chi^2_I$. Although the rotational constants are known with a very high precision, the share of the intensities on the resulting structure is considerable, since in general the number of intensity parameters exceeds the number of rotational constants of the isotopologues largely. On the other hand, the rotational constants changes guide the fit into the correct direction. Since we adopt the harmonic approximation, any distortion ΔQ_i along the ith normal mode Q_i results in the same FC factors, wether distorted in $+Q$ or $-Q$ direction. The rotational constants changes however, define the "correct" direction automatically.

Table 6: Comparison of the bond length changes of 1,2-DMB upon electronic excitation from SCS-CC2 calculations and Franck-Condon fits.

State	S_0		S_1		S_1-S_0	
Method	SCS-CC2	FCFit	SCS-CC2	FCFit	SCS-CC2	FCFit
C1-C2	138.6	138.6	142.6	143,5	+4.1	+5.0
C2-C3	140.5	140.5	141.4	141.0	+0.9	+0.5
C3-C4	139.2	139.2	145.1	145.8	+5.9	+6.6
C4-C5	141.9	141.9	142.3	140.6	+0.4	-1.3
C5-C6	139.2	139.2	145.1	145.8	+5.9	+6.6
C6-C1	140.5	140.5	141.4	141.0	+0.9	+0.5
C5-O7	136.4	136.4	135.8	135.0	-0.6	-1.4
C4-O8	136.4	136.4	135.8	135.0	-0.6	-1.4
O7-C9	142.3	142.3	143.1	143.1	+0.8	+0.8
O8-C10	142.3	142.3	143.1	143.1	+0.8	+0.8

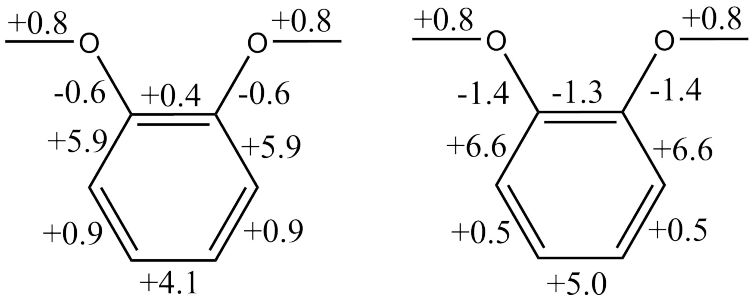

Figure 25: Geometry changes in pm upon electronic excitation obtained from the SCS-CC2/cc-pVTZ optimized structures (left) and from the Franck-Condon fits (right).

The right part of Figure 25 and Table 6 present the changes of the relevant bond lengths upon electronic excitation in pm, as obtained from the combined Franck-Condon and rotational constant fits. For phenol (monohydroxybenzene) a *para*-quinoidal distortion of the chromophore was found on the basis of the rotational constants[113,114] and Franck-Condon fits.[32] The same behavior upon electronic excitation was found for p-hydroquinone[115] and p-cyanophenol.[116] While it is immediately obvious that a substituent with a −I-effect like the cyano group can stabilize a partial charge in *para* and *ortho* position arising from shift of electron density of the hydroxy group upon electronic excitation, this is not so straightforward in the case of two identical groups like in p-hydroquinone or in 1,2-DMB.

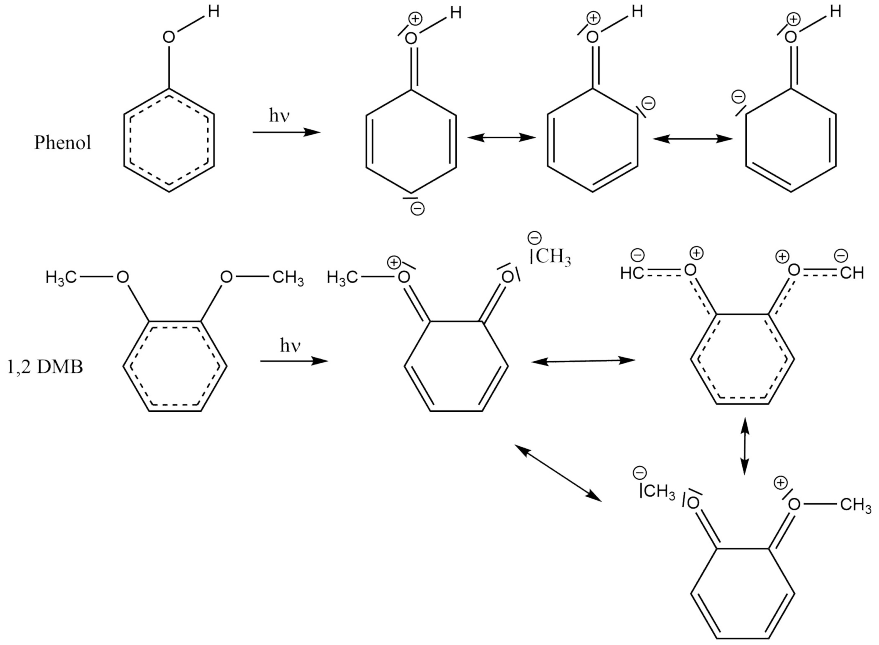

Figure 26: Schematic view of the relevant mesomeric structures that contribute to the quinoidal distortion in phenol and in 1,2-DMB.

We propose a mechanism for the *ortho*-quinoidal distortion of 1,2-DMB, which is shown in the scheme of Figure 26. The negative partial charge at the $|CH_3^-$ carbanion can be stabilized via negative hyperconjugation to σ orbital of the adjacent O-C bond. This hyperconjugation is stronger in the excited state, since electron density shifts from the oxygen atom to the aromatic ring and therefore contributes more to the mesomeric structure shown in Figure 26.

7.9 Conclusions

Based on the rotational constants and emission band intensities, the geometry changes of 1,2-DMB upon electronic excitation could be determined with a higher accuracy than on the basis of the rotational constants alone as in the preceeding paper.[91] An *ortho*-quinoidal distortion of the molecule upon electronic excitation via a hyperconjugation mechanism is validated by a comparison of the

bond length changes to the results of *ab initio* calculations. The electron density shift leads to a decrease of the $C_{ar}O$ bond length and a general increase of bond lengths within the aromatic ring. The good overall agreement between the *ab initio* calculated and the FC fit atomic displacements, gives further evidence for the mechanism of an *ortho*-quinoidal distortion of 1,2-DMB.

7.10 Acknowledgements

Financial support of the Deutsche Forschungsgemeinschaft via grant SCHM1043 12-3 is gratefully acknowledged. Computational support and infrastructure was provided by the "Center for Information and Media Technology" (ZIM) at the Heinrich-Heine-University Düsseldorf. We furthermore thank the Regional Computing Center of the University of Cologne (RRZK) for providing computing time on the DFG-funded High Performance Computing (HPC) system CHEOPS as well as support.

8 Structural changes upon electronic excitation in 1,3-dimethoxybenzene from Franck-Condon/rotational constants fits of the fluorescence emission spectra.†

Authors: Christian Henrichs [1], Marie-Luise Hebestreit,[1] Daniel Krügler,[2] and Michael Schmitt*[1]

submitted to J. Mol. Struct. (2021), *under review*

8.1 Abstract

The geometry changes of two rotamers of 1,3-dimethoxybenzene were determined from a combined fit of line intensities in fluorescence emission spectra, obtained via pumping different vibronic transition and the changes of rotational constants upon electronic excitation. The so determined changes are compared to the results of *ab initio* approximate coupled cluster singles and doubles (CC2) calculations. The bond length variations in the aromatic ring follow the calculated electron density differences from the coupled cluster wavefunctions and are in agreement with excitation to an ^1L_b-state for the C_{2v} symmetric B-conformer.

Keywords:

1,3-dimethoxybenzene, excited state, structure, Franck-Condon analysis

Highlights:

- An analysis of the excited state structure of two conformers of 1,3-dimethoxybenzene has been given on the basis of a combined Franck-Condon/rotational constant changes analysis.
- The geometry changes are compared to the results of *ab initio* calculations at the approximate coupled cluster singles and doubles (CC2) level of theory.
- The influence of the lone pair orientation of the methoxy oxygen atoms on the electron density differences between both states is surprisingly large.

8.2 Introduction

The analysis of structures of isolated molecules from their inertial parameters has a longstanding history in microwave (MW) spectroscopy. Investigation of molecular structures using different isotopologues, either in their natural abundance or of synthetic isotopologues can be used for a complete structural determination of molecules in their electronic (and vibrational) ground state.

The theories behind the different structural definitions like Costain's r_0 structures,[71] Kraitchman's r_s structures,[70] Rudolph's *pseudo-Kraitchman* (*pseudo-*r_s) structure[117] and Watson's r_m structures[118–121] are known for a long time and have intensively been compared to each other and to results from quantum chemical calculations (equilibrium r_e structures).[122–125] For electronically excited states this procedure is in general the same, but due to the experimental limitations of the (absolute) resolution in the ultraviolet (UV) range are more tedious. The most severe limitations arise from the natural life time of the excited state (10 ns excited state life time are equivalent to a Lorentz width of 16 MHz) and from the Doppler width in the molecular beam, which is proportional to the excitation frequency, i.e. in the UV at 30.000 cm^{-1} is about 30.000 times larger than in the MW at 30 GHz. Thus, individual rovibrational transitions of different isotopologues are in general overlapping and complete structure determinations require the chemical synthesis of many different isotopologues. For a complete Kraitchman determination in molecular systems without symmetry N different isotopologues are needed if N is the number of atoms. Symmetry can reduce this number largely. Therefore, complete structure determinations in excited states of large polyatomic molecules are rare.[114] In cases where the number of inertial parameters is too small for a complete structure determination, several possibilities exist. Either the coordinates are defined as internal coordinates, of which some are "frozen" at experimental values from similar systems or at *ab initio* values, or the inertial parameters are complemented by independent parameters, which also depend on the structure. Intensities of vibronic bands through the Franck-Condon (FC) principle can provide this additional information. A combination of fits to rotational constants changes from rotationally resolved spectroscopy to as many isotopologues as possible and to intensities of emission bands, after excitation to several vibronic bands in the state of interest, has been shown to yield reliable excited state geometries.[32,126,127]

Breen *et al.*[128] assigned three vibronic bands in the resonant two-photon ionization (R2PI) molecular beam spectrum of 1,3-dimethoxybenzene at 36.101,55 cm^{-1}, 36.163,9 cm^{-1}, and 36.256,9 cm^{-1} to the electronic origins of three different rotamers. Yang *et al.*[89] performed two-color resonant two-photon mass-analyzed threshold ionization spectroscopy to investigate selected rotamers of 1,3-dimethoxybenzene in their cationic states. They found three different ionization potentials for the three lowest-energy bands in the R2PI spectrum of 1,3-dimethoxybenzene from ref.[128] and also concluded the existence of three different rotamers. In contrast to the results of Breen[128] and Yang,[89] only two of the three possible conformers could be found and identified by Schneider *et al.*[129] From the rotational analysis of the three vibronic bands they concluded that what had been assigned to the C-conformer of 1,3-dimethoxybenzene is a vibronic band of the A conformer. This assignment has been confirmed by Schneider *et al.*[90] using rotationally resolved Stark spectroscopy.

In the present study we analyze the structural changes of both rotamers of 1,3-dimethoxybenzene using a Franck-Condon fit of fluorescence emission bands and rotational constants changes from Ref.[90]

8.3 Computational Methods

8.3.1 Quantum chemical calculations

We performed structure optimizations using Dunning's correlation consistent polarized valence triple zeta (cc-pVTZ) basis set from the TURBOMOLE library.[92,93] To optimize the equilibrium geometries of the ground and the lowest excited singlet state, the approximate coupled cluster singles and doubles model (CC2) employing the resolution-of-identity approximation (RI) was employed.[94–96] The program FCFit utilizes the Hessians and harmonic vibrational frequencies for both electronic states, which have been obtained from numerical second derivates of the potential energy using the NumForce script.[97]

8.3.2 Franck-Condon fits

The structural changes upon electronic excitation from the electronic ground to the electronically excited state can be accessed with the information contained in the intensities of fluorescence emission bands due to the Franck-Condon principle. The intensity of an emission band depends on the overlap of the electronic wavefunctions of the different single vibronic levels in ground and excited state. With the program FCFit, developed in our group and described before,[32,100] the fit has been performed. The user selects a set of normal modes, along which the reference geometry is distorted, minimizing the difference between the experimentally observed and the calculated intensities. To improve the results of the geometry change fit, the changes of the rotational constants of different isotopologues, obtained from rotationally resolved electronic spectroscopy, can be used additionally. To minimize the deviation of the relative intensities in all vibronic emission spectra and the rotational constant changes, a local minimizer based on a Levenberg-Marquardt variant[130,131] or a global minimizer using evolutionary strategies[132,133] can been used.

8.4 Experimental Methods

1,3-Dimethoxybenzene ($\geq$ 98%) was purchased from Sigma-Aldrich and used without further purification. The experimental setup for the dispersed fluorescence (DF) spectroscopy has been described in detail elsewhere.[101,102] In brief, 1,3-dimethoxybenzene and 1,3-dimethoxybenzene-(d6) were evaporated at 313 K and co-expanded through a pulsed nozzle (kept at 333 K to avoid condensation) with a 500 μm orifice (General Valve) into the vacuum chamber using helium as carrier gas. The output of a Nd:YAG (SpectraPhysics INDI) pumped dye laser (Lambda-Physik, FL3002) was frequency doubled and crossed at right angles with the molecular beam. The resulting fluorescence was imaged on the entrance slit of a f = 1 m monochromator (Jobin Yvon, grating 2400 lines/mm blazed at 400 nm in first order). The dispersed fluorescence spectrum was recorded using a gated image intensified UV sensitive CCD camera (Flamestar II, LaVision). One image on the CCD chip spectrally covers approximately 600 cm^{-1}. Since the whole spectrum is taken on a

shot-to-shot basis, the relative intensities in the DF spectra do not vary with the laser power. The relative intensities were afterwards normalized to the strongest band in the spectrum, not including the resonance fluorescence band, which also contains the stray light and is therefore excluded from the FC analysis.

8.5 Results and Discussion

8.5.1 Computational Results

The Hessians of both isomers of the 1,3-dimethoxybenzene in both electronic states are required for the calculation of multidimensional Franck-Condon factors for this molecule. Both electronic states should be calculated with the same level of theory. This leads to the calculation of the electronic ground and electronic excited state for both isomers on SCS-CC2/cc-pVTZ level of theory. We established this level of theory before and showed in previous work a very good agreement to experimentally determined properties.[79–81,107] The Cartesian coordinates of the SCS-CC2/cc-pVTZ optimized structures of the ground and lowest excited singlet states of both isomers A and B of 1,3-dimethoxybenzene are given in the online supporting material. In Figure 27 the SCS-CC2/cc-PVTZ optimized structures of the two experimentally observed isomers in their electronic ground state are shown. The notation for the conformers is defined by the dihedral angles formed by C(2)C(1)O(7)C(8) and by C(4)C(3)O(9)C(10).

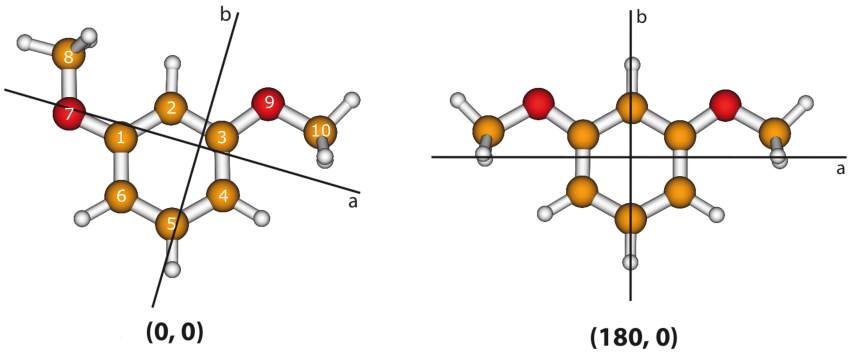

Figure 27: Calculated structures of the two experimentally observed conformers of 1,3-dimethoxybenzene.

From the rotational constants obtained by rotationally resolved electronic spectroscopy, we know that the experimentally observed band A with an electronic origin at 36.129 cm^{-1} belongs to the (0,0) rotamer with C_s symmetry in both electronic states.[129] The 54 ground state vibrations transform like $\Gamma_{ired} = 35a' + 19a''$. The vibrational frequencies for both the ground and the lowest electronically excited state, are summarized in Table 7.

Band B with an electronic origin at 36.196 cm^{-1} is assigned to the (180/0) rotamer from its rotational constants. Optimizations of the geometries of ground and excited state for the B isomer

were performed under C_{2v} constraints. The 54 ground state vibrations of 1,3-dimethoxybenzene transform like $\Gamma_{ired} = 18a_1 + 10a_2 + 9b_1 + 17b_2$ under C_{2v} symmetry. The vibrational frequencies for both the ground and the lowest electronically excited state, are summarized in Table 8. The third column of each table contains the Duschinsky matrix coefficients, which describe the composition of excited state modes Q' from the respective ground state modes Q'' according to the relation, given by Duschinsky:[75]

$$Q' = SQ'' + d \tag{79}$$

Here, Q' and Q'' are the N-dimensional vectors of the normal modes of excited and ground state, respectively, S is a N x N rotation matrix (the Duschinsky matrix) and d is an N-dimensional vector which describes the linear displacements of the normal coordinates.

To make the vibrational and vibronic assignments for both isomers more reliable, we measured and calculated also the vibrational frequencies of the d_6 isotopologue of both isomers. Here, d_6 means that both OCH_3 groups are replaced by OCD_3. We used the calculated ground and the lowest excited state Hessians, along with the respective changed isotopomeric masses for the six methoxy deuterium atoms. The results of these calculations are presented in the tables S10 and S11 of the online supporting material.

Figure 28 shows the electron density difference plots between the ground states and the lowest excited singlet states of both rotamers, calculated using the CC2 wavefunctions. For both rotamers, electron density is shifted from the methoxy O-atoms into the aromatic ring.

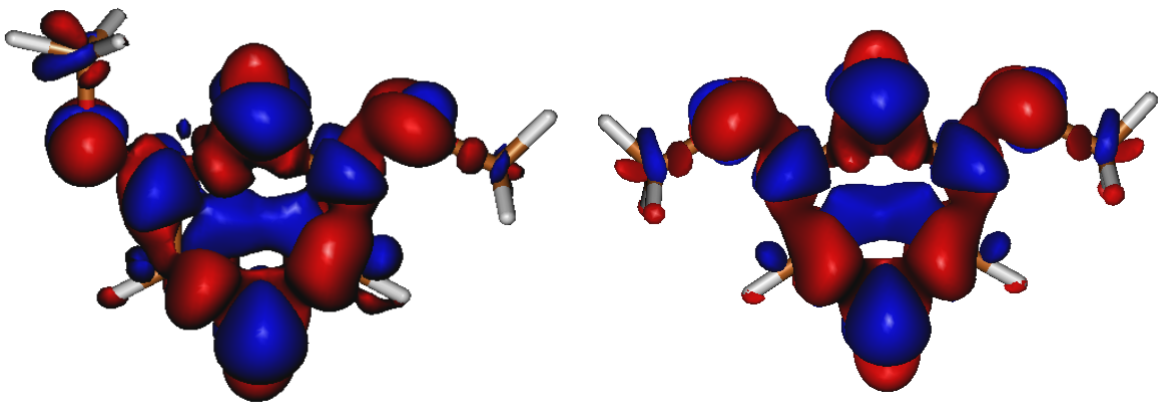

Figure 28: Electron density difference plot between the ground state and the lowest excited singlet state of the A-rotamer (left) and of the B-rotamer (right) of 1,3-dimethoxybenzene. Regions of decreasing electron density are shown in red, those of increasing electron density in blue.

Table 7: SCS-CC2/cc-pVTZ calculated and experimental wavenumber of the 54 normal modes of the ground and first electronically excited states of the A-rotamer of 1,3-dimethoxybenzene, along with the respective symmetry labels and the leading coefficients of the Duschinsky matrix.

Mode	S_0			S_1			Duschinsky
	Sym.	Calc.	Obs.	Sym.	Calc.	Obs.	
$Q_1(S_0)$	a”	89.76		a”	74.12		$Q_1(S_1)$=-0.92 $Q_1(S_0)$+0.27 $Q_2(S_0)$
$Q_2(S_0)$	a”	107.67		a”	89.00		$Q_2(S_1)$=-0.94 $Q_2(S_0)$-0.30 $Q_1(S_0)$
$Q_3(S_0)$	a’	192.88	193	a”	134.33		$Q_3(S_1)$=-0.83 $Q_4(S_0)$-0.28 $Q_{10}(S_0)$
$Q_4(S_0)$	a”	217.93		a”	179.76		$Q_4(S_1)$=-0.91 $Q_5(S_0)$
$Q_5(S_0)$	a”	226.06		a’	189.83	186	$Q_5(S_1)$=-0.99 $Q_3(S_0)$
$Q_6(S_0)$	a”	288.92		a”	220.23		$Q_6(S_1)$=+0.75 $Q_7(S_0)$+0.41 $Q_6(S_0)$-0.37 $Q_4(S_0)$
$Q_7(S_0)$	a”	291.64		a”	227.92		$Q_7(S_1)$=+0.57 $Q_{10}(S_0)$-0.46 $Q_7(S_0)$+0.40 $Q_6(S_0)$+0.29 $Q_{17}(S_0)$
$Q_8(S_0)$	a’	292.73	291	a”	269.14		$Q_8(S_1)$=+0.76 $Q_6(S_0)$-0.45 $Q_{10}(S_0)$-0.29 $Q_7(S_0)$
$Q_9(S_0)$	a’	423.27	408	a’	289.64	233	$Q_9(S_1)$=+0.99 $Q_8(S_0)$
$Q_{10}(S_0)$	a”	466.55		a”	367.51		$Q_{10}(S_1)$=+0.85 $Q_{18}(S_0)$+0.28 $Q_{21}(S_0)$
$Q_{11}(S_0)$	a’	466.74		a’	409.41		$Q_{11}(S_1)$=-0.97 $Q_9(S_0)$
$Q_{12}(S_0)$	a’	537.08		a’	425.79		$Q_{12}(S_1)$=+0.95 $Q_{11}(S_0)$-0.25 $Q_{13}(S_0)$
$Q_{13}(S_0)$	a’	588.46	587	a”	435.34		$Q_{13}(S_1)$=+0.50 $Q_{21}(S_0)$-0.49 $Q_{10}(S_0)$+0.47 $Q_{15}(S_0)$+0.44 $Q_{17}(S_0)$
$Q_{14}(S_0)$	a”	631.07		a”	454.30		$Q_{14}(S_1)$=+0.95 $Q_{14}(S_0)$
$Q_{15}(S_0)$	a”	685.84		a’	485.78		$Q_{15}(S_1)$=-0.97 $Q_{12}(S_0)$
$Q_{16}(S_0)$	a’	727.74	721	a”	503.46		$Q_{16}(S_1)$=+0.78 $Q_{15}(S_0)$-0.52 $Q_{21}(S_0)$-0.33 $Q_{17}(S_0)$
$Q_{17}(S_0)$	a”	773.33		a’	540.84		$Q_{17}(S_1)$=+0.95 $Q_{13}(S_0)$+0.27 $Q_{11}(S_0)$
$Q_{18}(S_0)$	a”	836.60		a”	638.64		$Q_{18}(S_1)$=-0.73 $Q_{17}(S_0)$+0.56 $Q_{21}(S_0)$-0.31 $Q_{18}(S_0)$
$Q_{19}(S_0)$	a”	854.27		a’	695.63		$Q_{19}(S_1)$=-0.99 $Q_{16}(S_0)$
$Q_{20}(S_0)$	a’	923.33		a”	701.99		$Q_{20}(S_1)$=-0.99 $Q_{19}(S_0)$
$Q_{21}(S_0)$	a”	949.23		a’	873.54		$Q_{21}(S_1)$=-0.97 $Q_{20}(S_0)$
$Q_{22}(S_0)$	a’	1001.33	997	a’	961.77		$Q_{22}(S_1)$=-0.98 $Q_{22}(S_0)$
$Q_{23}(S_0)$	a’	1064.65	1053	a’	1001.97		$Q_{23}(S_1)$=-0.71 $Q_{25}(S_0)$-0.56 $Q_{23}(S_0)$+0.33 $Q_{24}(S_0)$
$Q_{24}(S_0)$	a’	1079.09		a’	1034.25		$Q_{24}(S_1)$=-0.69 $Q_{24}(S_0)$-0.59 $Q_{25}(S_0)$+0.34 $Q_{23}(S_0)$
$Q_{25}(S_0)$	a’	1104.05	1105	a’	1049.00		$Q_{25}(S_1)$=-0.73 $Q_{23}(S_0)$-0.60 $Q_{24}(S_0)$+0.29 $Q_{25}(S_0)$
$Q_{26}(S_0)$	a’	1179.41		a’	1147.70		$Q_{26}(S_1)$=-0.85 $Q_{26}(S_0)$+0.42 $Q_{29}(S_0)$
$Q_{27}(S_0)$	a”	1186.98		a”	1175.87		$Q_{27}(S_1)$=+0.96 $Q_{27}(S_0)$-0.29 $Q_{28}(S_0)$
$Q_{28}(S_0)$	a”	1187.37		a”	1178.25		$Q_{28}(S_1)$=+0.96 $Q_{28}(S_0)$-0.29 $Q_{27}(S_0)$
$Q_{29}(S_0)$	a’	1196.35	1190	a’	1178.45		$Q_{29}(S_1)$=-0.86 $Q_{29}(S_0)$-0.46 $Q_{26}(S_0)$
$Q_{30}(S_0)$	a’	1217.53		a’	1211.84		$Q_{30}(S_1)$=-0.97 $Q_{30}(S_0)$
$Q_{31}(S_0)$	a’	1243.36		a’	1230.83		$Q_{31}(S_1)$=-0.97 $Q_{31}(S_0)$
$Q_{32}(S_0)$	a’	1303.07	1309	a’	1283.66		$Q_{32}(S_1)$=-0.85 $Q_{33}(S_0)$+0.40 $Q_{32}(S_0)$+0.33 $Q_{34}(S_0)$
$Q_{33}(S_0)$	a’	1319.72		a’	1311.61		$Q_{33}(S_1)$=-0.71 $Q_{32}(S_0)$+0.52 $Q_{33}(S_0)$-0.37 $Q_{34}(S_0)$
$Q_{34}(S_0)$	a’	1394.17	1374	a’	1408.78		$Q_{34}(S_1)$=+0.79 $Q_{35}(S_0)$+0.42 $Q_{40}(S_0)$
$Q_{35}(S_0)$	a’	1468.42		a’	1421.03		$Q_{35}(S_1)$=-0.58 $Q_{40}(S_0)$+0.46 $Q_{36}(S_0)$-0.40 $Q_{35}(S_0)$-0.30 $Q_{42}(S_0)$
$Q_{36}(S_0)$	a’	1479.77		a’	1476.40		$Q_{36}(S_1)$=-0.85 $Q_{36}(S_0)$-0.40 $Q_{40}(S_0)$
$Q_{37}(S_0)$	a’	1500.89		a’	1487.72		$Q_{37}(S_1)$=-0.92 $Q_{37}(S_0)$-0.35 $Q_{35}(S_0)$
$Q_{38}(S_0)$	a”	1517.66		a”	1514.29		$Q_{38}(S_1)$=-0.99 $Q_{39}(S_0)$
$Q_{39}(S_0)$	a”	1518.31		a”	1516.30		$Q_{39}(S_1)$=-0.99 $Q_{38}(S_0)$
$Q_{40}(S_0)$	a’	1523.78		a’	1528.56		$Q_{40}(S_1)$=+0.78 $Q_{42}(S_0)$+0.43 $Q_{41}(S_0)$-0.42 $Q_{40}(S_0)$
$Q_{41}(S_0)$	a’	1533.52		a’	1530.08		$Q_{41}(S_1)$=+0.89 $Q_{41}(S_0)$-0.41 $Q_{42}(S_0)$
$Q_{42}(S_0)$	a’	1534.74		a’	1546.96		$Q_{42}(S_1)$=+0.86 $Q_{44}(S_0)$+0.34 $Q_{43}(S_0)$
$Q_{43}(S_0)$	a’	1630.20		a’	1558.80		$Q_{43}(S_1)$=+0.92 $Q_{43}(S_0)$-0.33 $Q_{44}(S_0)$
$Q_{44}(S_0)$	a’	1647.80	1658	a’	1765.56		$Q_{44}(S_1)$=+0.85 $Q_{34}(S_0)$-0.45 $Q_{32}(S_0)$
$Q_{45}(S_0)$	a’	3043.28		a’	3051.06		$Q_{45}(S_1)$=-0.82 $Q_{45}(S_0)$+0.57 $Q_{46}(S_0)$
$Q_{46}(S_0)$	a’	3043.50		a’	3054.31		$Q_{46}(S_1)$=+0.82 $Q_{46}(S_0)$+0.57 $Q_{45}(S_0)$
$Q_{47}(S_0)$	a”	3117.31		a”	3130.98		$Q_{47}(S_1)$=-0.73 $Q_{48}(S_0)$+0.68 $Q_{47}(S_0)$
$Q_{48}(S_0)$	a”	3117.47		a”	3134.45		$Q_{48}(S_1)$=-0.73 $Q_{47}(S_0)$-0.68 $Q_{48}(S_0)$
$Q_{49}(S_0)$	a’	3177.05		a’	3182.23		$Q_{49}(S_1)$=+0.94 $Q_{50}(S_0)$-0.33 $Q_{49}(S_0)$
$Q_{50}(S_0)$	a’	3178.02		a’	3182.43		$Q_{50}(S_1)$=+0.94 $Q_{49}(S_0)$+0.33 $Q_{50}(S_0)$
$Q_{51}(S_0)$	a’	3201.23		a’	3224.81		$Q_{51}(S_1)$=-0.74 $Q_{52}(S_0)$+0.64 $Q_{51}(S_0)$
$Q_{52}(S_0)$	a’	3232.33		a’	3239.63		$Q_{52}(S_1)$=+0.59 $Q_{53}(S_0)$+0.58 $Q_{52}(S_0)$+0.54 $Q_{51}(S_0)$
$Q_{53}(S_0)$	a’	3249.98		a’	3254.80		$Q_{53}(S_1)$=-0.78 $Q_{53}(S_0)$+0.51 $Q_{51}(S_0)$+0.32 $Q_{52}(S_0)$
$Q_{54}(S_0)$	a’	3250.92		a’	3279.74		$Q_{54}(S_1)$=-0.99 $Q_{54}(S_0)$

Table 8: SCS-CC2/cc-pVTZ calculated and experimental wavenumber of the 54 normal modes of the ground and first electronically excited states of the B-rotamer of 1,3-dimethoxybenzene, along with the respective symmetry labels and the leading coefficients of the Duschinsky matrix.

Mode	S_0			S_1			Duschinsky
	Sym.	Calc.	Obs.	Sym.	Calc.	Obs.	
$Q_1(S_0)$	b1	72.46		b1	27.68		$Q_1(S_1)$=+0.96 $Q_1(S_0)$
$Q_2(S_0)$	a2	108.67		a2	108.80		$Q_2(S_1)$=-0.99 $Q_2(S_0)$
$Q_3(S_0)$	a1	205.63		b1	140.23		$Q_3(S_1)$=-0.63 $Q_5(S_0)$-0.46 $Q_6(S_0)$-0.46 $Q_{10}(S_0)$
$Q_4(S_0)$	a2	213.82		a2	169.02		$Q_4(S_1)$=+0.99 $Q_4(S_0)$
$Q_5(S_0)$	b1	232.90	264	a1	194.88	193	$Q_5(S_1)$=+0.71 $Q_5(S_0)$-0.43 $Q_{10}(S_0)$
$Q_6(S_0)$	b1	278.63	320	b1	231.49		$Q_6(S_1)$=-0.99 $Q_3(S_0)$
$Q_7(S_0)$	a2	300.10		a2	257.50		$Q_7(S_1)$=-0.67 $Q_7(S_0)$-0.62 $Q_6(S_0)$+0.29 $Q_{10}(S_0)$
$Q_8(S_0)$	b2	302.43		b1	285.07		$Q_8(S_1)$=+0.73 $Q_7(S_0)$-0.54 $Q_6(S_0)$+0.30 $Q_{10}(S_0)$
$Q_9(S_0)$	a1	367.10	365	b2	295.65		$Q_9(S_1)$=+0.99 $Q_8(S_0)$
$Q_{10}(S_0)$	b1	470.35		a1	353.95		$Q_{10}(S_1)$=+0.88 $Q_{19}(S_0)$+0.37 $Q_{21}(S_0)$
$Q_{11}(S_0)$	b2	477.51	476	a2	394.83		$Q_{11}(S_1)$=+0.99 $Q_9(S_0)$
$Q_{12}(S_0)$	a1	566.69	568	b2	402.60		$Q_{12}(S_1)$=-0.97 $Q_{11}(S_0)$
$Q_{13}(S_0)$	b2	584.07		b1	446.76		$Q_{13}(S_1)$=+0.56 $Q_{10}(S_0)$+0.52 $Q_{21}(S_0)$-0.44 $Q_{15}(S_0)$+0.42 $Q_{17}(S_0)$
$Q_{14}(S_0)$	a2	632.46		b1	472.71		$Q_{14}(S_1)$=+0.99 $Q_{14}(S_0)$
$Q_{15}(S_0)$	b1	682.59		a1	508.94		$Q_{15}(S_1)$=+0.98 $Q_{12}(S_0)$
$Q_{16}(S_0)$	a1	729.63	727	b1	529.54		$Q_{16}(S_1)$=+0.77 $Q_{15}(S_0)$+0.52 $Q_{21}(S_0)$+0.29 $Q_{17}(S_0)$
$Q_{17}(S_0)$	b1	766.00		b2	568.22		$Q_{17}(S_1)$=+0.98 $Q_{13}(S_0)$
$Q_{18}(S_0)$	a2	844.59		b1	616.22		$Q_{18}(S_1)$=-0.72 $Q_{17}(S_0)$+0.54 $Q_{21}(S_0)$-0.34 $Q_{19}(S_0)$
$Q_{19}(S_0)$	b1	849.76		a2	647.70		$Q_{19}(S_1)$=-0.99 $Q_{18}(S_0)$
$Q_{20}(S_0)$	b2	905.90	913	a1	723.88		$Q_{20}(S_1)$=-0.99 $Q_{16}(S_0)$
$Q_{21}(S_0)$	b1	944.45		b2	871.35		$Q_{21}(S_1)$=-0.98 $Q_{20}(S_0)$
$Q_{22}(S_0)$	a1	1001.61	994	a1	947.41		$Q_{22}(S_1)$=+0.99 $Q_{22}(S_0)$
$Q_{23}(S_0)$	a1	1069.66		a1	975.55		$Q_{23}(S_1)$=+0.94 $Q_{25}(S_0)$-0.26 $Q_{24}(S_0)$
$Q_{24}(S_0)$	b2	1073.21		b2	1036.31		$Q_{24}(S_1)$=+0.98 $Q_{23}(S_0)$
$Q_{25}(S_0)$	a1	1117.58		a1	1040.09		$Q_{25}(S_1)$=-0.95 $Q_{24}(S_0)$-0.26 $Q_{25}(S_0)$
$Q_{26}(S_0)$	b2	1184.55		b2	1150.72		$Q_{26}(S_1)$=-0.75 $Q_{26}(S_0)$-0.60 $Q_{29}(S_0)$
$Q_{27}(S_0)$	b1	1186.77		b1	1179.51		$Q_{27}(S_1)$=-0.99 $Q_{27}(S_0)$
$Q_{28}(S_0)$	a2	1186.92		a2	1180.18		$Q_{28}(S_1)$=-0.99 $Q_{28}(S_0)$
$Q_{29}(S_0)$	b2	1203.77		b2	1191.41		$Q_{29}(S_1)$=-0.74 $Q_{29}(S_0)$+0.64 $Q_{26}(S_0)$
$Q_{30}(S_0)$	a1	1219.06	1209	a1	1215.87		$Q_{30}(S_1)$=+0.99 $Q_{30}(S_0)$
$Q_{31}(S_0)$	b2	1226.65	1237	b2	1235.83		$Q_{31}(S_1)$=+0.96 $Q_{31}(S_0)$
$Q_{32}(S_0)$	b2	1313.42		b2	1281.85		$Q_{32}(S_1)$=+0.94 $Q_{32}(S_0)$
$Q_{33}(S_0)$	a1	1317.96	1290	a1	1322.79		$Q_{33}(S_1)$=+0.97 $Q_{33}(S_0)$
$Q_{34}(S_0)$	b2	1384.34		a1	1381.47		$Q_{34}(S_1)$=+0.75 $Q_{40}(S_0)$+0.54 $Q_{35}(S_0)$-0.27 $Q_{44}(S_0)$
$Q_{35}(S_0)$	b2	1478.33		b2	1424.35		$Q_{35}(S_1)$=+0.80 $Q_{36}(S_0)$-0.54 $Q_{37}(S_0)$
$Q_{36}(S_0)$	a1	1479.18		b2	1462.69		$Q_{36}(S_1)$=-0.81 $Q_{35}(S_0)$+0.48 $Q_{40}(S_0)$-0.24 $Q_{44}(S_0)$
$Q_{37}(S_0)$	a1	1500.51		a1	1478.75		$Q_{37}(S_1)$=-0.81 $Q_{37}(S_0)$-0.57 $Q_{36}(S_0)$
$Q_{38}(S_0)$	a2	1518.48		b1	1512.07		$Q_{38}(S_1)$=-0.80 $Q_{38}(S_0)$+0.60 $Q_{39}(S_0)$
$Q_{39}(S_0)$	b1	1518.64		a2	1512.08		$Q_{39}(S_1)$=+0.80 $Q_{39}(S_0)$+0.60 $Q_{38}(S_0$
$Q_{40}(S_0)$	b2	1524.53		b2	1515.59		$Q_{40}(S_1)$=-0.99 $Q_{41}(S_0)$
$Q_{41}(S_0)$	b2	1532.13		b2	1529.23		$Q_{41}(S_1)$=+0.96 $Q_{42}(S_0)$
$Q_{42}(S_0)$	a1	1534.33		a1	1530.60		$Q_{42}(S_1)$=-0.88 $Q_{44}(S_0)$-0.39 $Q_{40}(S_0)$
$Q_{43}(S_0)$	a1	1619.56	1607	a1	1677.60		$Q_{43}(S_1)$=+0.97 $Q_{43}(S_0)$
$Q_{44}(S_0)$	b2	1654.35		b2	1800.90		$Q_{44}(S_1)$=-0.99 $Q_{34}(S_0)$
$Q_{45}(S_0)$	b2	3042.70		b2	3051.68		$Q_{45}(S_1)$=+0.99 $Q_{45}(S_0)$
$Q_{46}(S_0)$	a1	3043.21		a1	3054.54		$Q_{46}(S_1)$=+0.99 $Q_{46}(S_0)$
$Q_{47}(S_0)$	a2	3116.87		a2	3134.10		$Q_{47}(S_1)$=-0.99 $Q_{48}(S_0)$
$Q_{48}(S_0)$	b1	3116.90		b1	3134.15		$Q_{48}(S_1)$=+0.99 $Q_{47}(S_0)$
$Q_{49}(S_0)$	b2	3176.82		b2	3193.87		$Q_{49}(S_1)$=+0.99 $Q_{49}(S_0)$
$Q_{50}(S_0)$	a1	3176.95		a1	3193.96		$Q_{50}(S_1)$=+0.99 $Q_{50}(S_0)$
$Q_{51}(S_0)$	a1	3199.82		a1	3214.44		$Q_{51}(S_1)$=-0.84 $Q_{51}(S_0)$+0.53 $Q_{54}(S_0)$
$Q_{52}(S_0)$	a1	3234.03		b2	3251.47		$Q_{52}(S_1)$=+0.99 $Q_{53}(S_0)$
$Q_{53}(S_0)$	b2	3248.21		a1	3254.30		$Q_{53}(S_1)$=-0.84 $Q_{51}(S_0)$-0.53 $Q_{54}(S_0)$
$Q_{54}(S_0)$	a1	3251.18		a1	3256.92		$Q_{54}(S_1)$=-0.99 $Q_{52}(S_0)$

8.5.2 Experimental Results

8.5.3 Fluorescence excitation spectra of 1,3-dimethoxybenzene-(h_{10}) and 1,3-dimethoxybenzene-(d_6)

A correct assignment of vibronic levels in the excited state is crucial for the fit of the FC intensities. The assignment of vibronic bands can made more reliable by comparison of the fluorescence excitation spectra of 1,3-dimethoxybenzene-(h_{10}) and 1,3-dimethoxybenzene-(d_6). With the isotopic shift of the d_6 isotopologue the determination of the vibronic level of can be simplified.

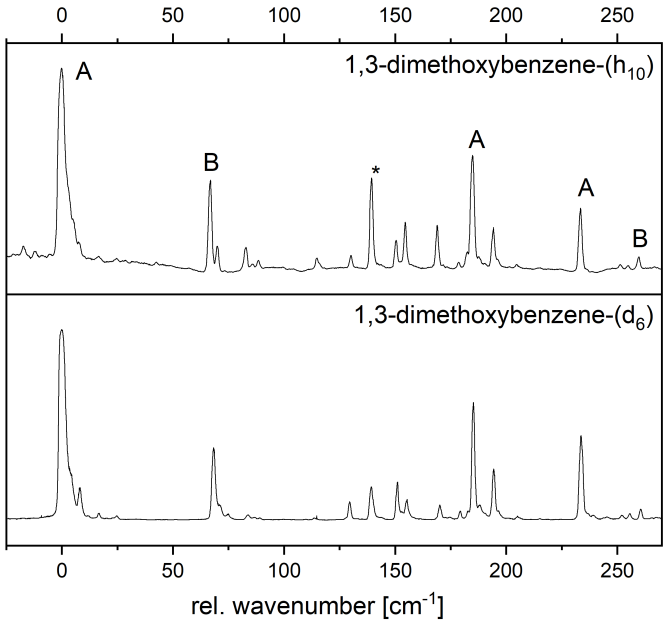

Figure 29: Fluorescence excitation spectra of 1,3-dimethoxybenzene-(h_{10}) and of 1,3-dimethoxybenzene-(d_6). The d_6 spectrum is shifted by 12 cm^{-1} to higher wavenumber, and has been offset by this value to have both origin bands at 0. The band, marked with an asterisk is due to an impurity. All labelled bands have been dispersed.

The electronic origin of the A-rotamer of 1,3-dimethoxybenzene-(d_6) is blue shifted by 12 cm^{-1} relative to the undeuterated isotopologue at 36.129 cm^{-1}. With the comparison of both spectra in Figure 29, all peaks can be assigned vice versa. Due to the isotopologic shifts from the SCS-CC2 calculations, cf. Tables S10 and S11 and the comparison of these with the experimental isotopic shifts, the assignment of the vibrational bands is performed. For the Franck-Condon fits, the correct assignment of vibronic bands is indispensable, since they represent the bra vector part $< bra|$ of the FC integrals given by $< bra|ket >$. The transitions are classified by the initial vibronic level described by a bra vector and the final vibronic level described by the respective ket vector. Each bra-ket combination is assigned an experimental intensity and an individual weight w_{int} to be used in the fit. For the rotational constant fit individual weights $w_{rotconst}$ can be chosen. From extensive tests, a relative weight of 5:1 for $w_{rotconst}/w_{int}$ was shown to perform best in terms

of accuracy and speed.

Additionally to the origin bands, the bands at 0,0 + 186 cm^{-1} and 0,0 + 233 cm^{-1} for the A-rotamer, and the band at 193 cm^{-1} for the B-rotamer are used as bras for the fit additional to the emission intensities from the electronic origin of both isomers.

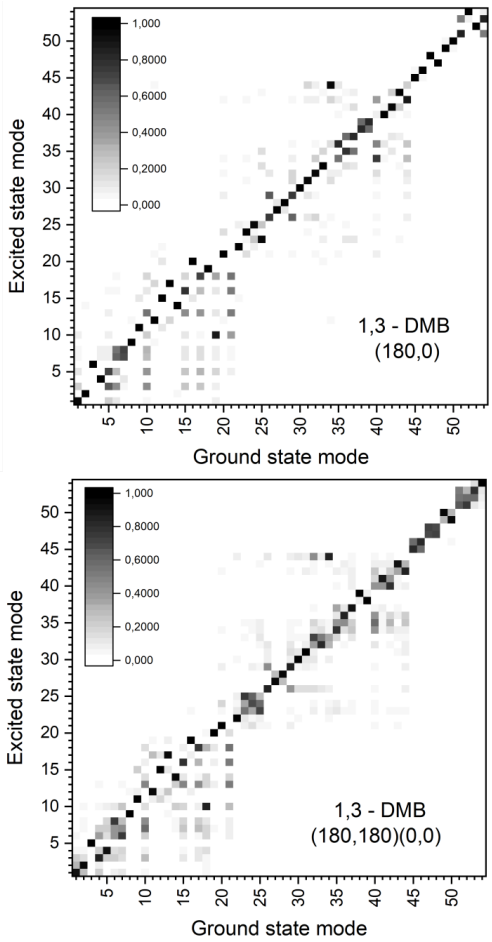

Figure 30: Graphical representations of the Duschinsky matrix of the 54 vibrational modes of the (180,0) and of the 54 vibrational modes of the (0,0) rotamer of 1,3-dimethoxybenzene.

8.5.4 Fluorescence emission spectra of the A and B rotamer origins of 1,3-dimethoxybenzene (h_{10}) and 1,3-dimethoxybenzene (d_6)

The selected modes can be assigned correctly due to the comparison of experimental and computational results. The mixing of S_1-state modes is obvious and the exact description for the S_0-state modes cannot be adopted to these modes. Figure 30 describes the mode mixing graphically with representing the Duschinsky matrix for both isomers. The black squares are matrix elements of 1, the white squares are 0 and the different shades of grey refer to the intermediate values. If no mixing occurs, the matrix element is 1 (so a black square is presented in the figure). This element does not necessarily occur on the diagonal presented in the figure due to order change of vibration

upon electronic excitation. As presented in Figure 30 only a few matrix elements show no mixing character. This impedes a straightforward assignment of S_1-state modes during the fit procedure.

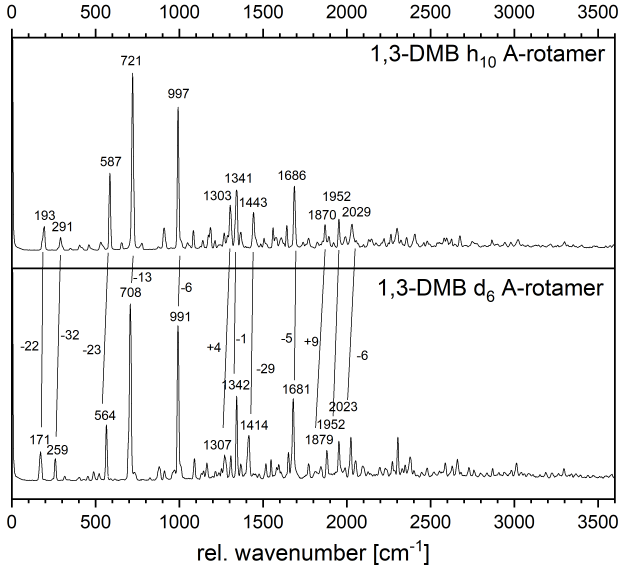

Figure 31: Fluorescence emission spectra of the electronic origins of the A-rotamer of 1,3-dimethoxybenzene-(h_{10}) and 1,3-dimethoxybenzene-(d_6) at 36.129 cm^{-1} and 36.139 cm^{-1}, respectively.

Figures 31 and 32 show the comparison of the fluorescence emission spectra after excitation of the electronic origins of the A- and B-rotamer and their deuterated isotopologues. The corresponding transitions are connected by straight lines and the wavenumber shifts are given for the major peaks with their respective wavenumber. The information for all observed bands are given in Tables S10 and S11 of the online supporting material. The assignment of ground state vibrations is given in Table 9 and is based on the absolute wavenumber and on the deuteration shifts of the individual bands. Additional to the mode number we gave the mode designations using the schemes of Tuttle,[108] Mulliken(C_{2v}),[111] and Wilson.[134] The assigned modes are shown in Figure S2 of the online supporting material.

8.5.5 Franck-Condon fit of geometry changes upon electronic excitation

In order to describe the geometry changes upon electronic excitation, the SCS-CC2/cc-pVTZ optimized ground state structures of the A- and B-conformers of 1,3-dimethoxybenzene were distorted along linear combinations of the vibrational modes Q_{22}, Q_{16}, Q_{13}, and Q_3. The expansion coefficients of the linear combinations were varied, until the least squares of all measured and calculated intensities of the emission bands, excited through the vibronic bands, and the rotational constant changes of both isotopologues were minimized. These coefficients are given in Tables S6 and S7 of the online supporting material. Figures 33 and 34 present the emission spectra through various vibronic bands of the A- and the B-conformer, along with the results of the fits.

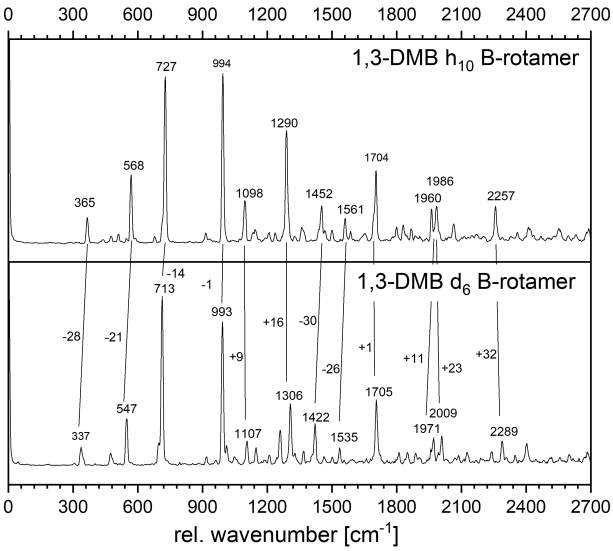

Figure 32: Fluorescence emission spectra of the electronic origins of the B-rotamer of 1,3-dimethoxybenzene-(h_{10}) and 1,3-dimethoxybenzene-(d_6) at 36.196 cm^{-1} and 36.206 cm^{-1}, respectively.

Table 9: Observed vibrational ground state wavenumbers and intensities along with the assignments of the modes, based on the SCS-CC2/cc-pVTZ calculated frequencies for the B-rotamer of 1,3-dimethoxybenzene. Overtones and combination bands are assigned, assuming harmonic behavior. Mode numbering refers to Table 8, assignments given according to Tuttle et al.,[108] Mulliken[111] and Wilson.[134]

$\tilde{\nu}$/cm^{-1}	Mode #	Tuttle	Mulliken(C_{2v})	Wilson	Calc.
264	Q_5	$m_{29}^D(a'')$	20 (b_1)	10a	232
320	Q_6	$m_{28}^D(a'')$	19 (b_1)	16b	279
365	Q_9	-	-	-	367
568	Q_{12}	$m_{18}^D(a')$	10(a_1)	6a	566
727	Q_{16}	$m_{17}^D(a')$	9(a_1)	1	729
913	Q_{20}	$m_{16}^D(a')$	28(b_2)	12	905
994	Q_{22}	$m_{15}^D(a')$	8(a_1)	18b	1001
1209	Q_{30}	$m_{21}^D(a')$	11(a_1)	15	1219
1237	Q_{31}	$m_{13}^D(a')$	7(a_1)	9a	1226
1290	Q_{33}	$m_{10}^D(a')$	6(a_1)	7a	1317
1607	Q_{43}	$m_5^D(a')$	3(a_1)	8a	1619

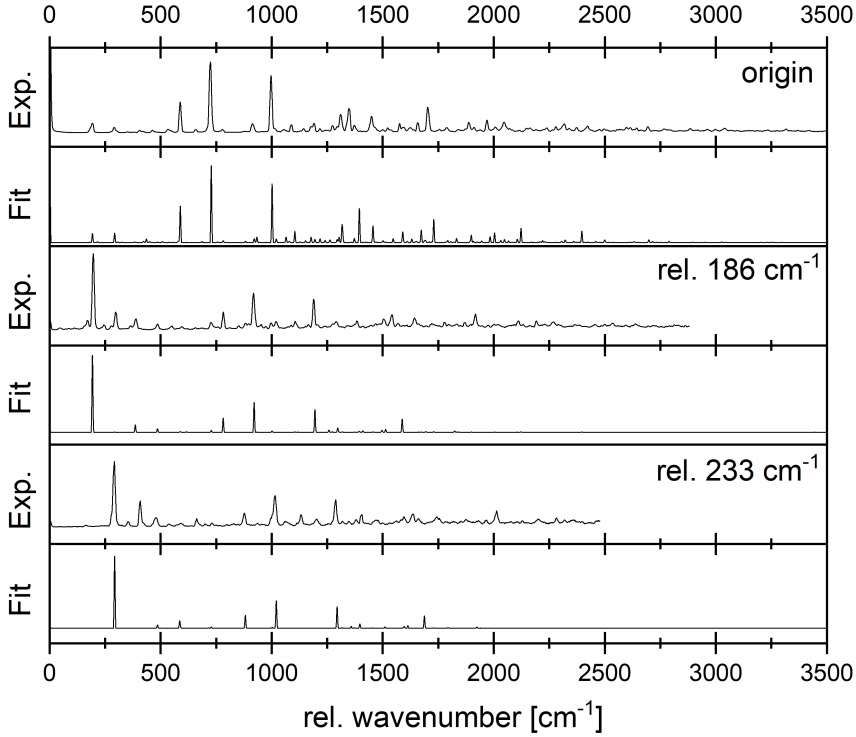

Figure 33: Fluorescence emission spectra, obtained via excitation of the electronic origin (0,0), 0,0 + 186 cm^{-1}, and 0,0 + 233 cm^{-1} of the A-rotamer of 1,3-dimethoxybenzene, along with the respective FC fits.

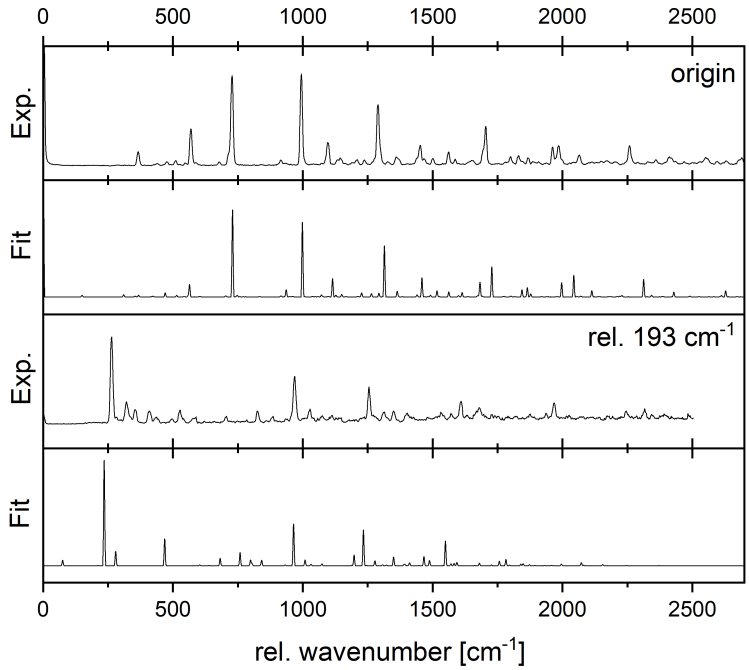

Figure 34: Fluorescence emission spectra, obtained via excitation of the electronic origin (0,0) and 0,0 + 193 cm^{-1} of the B-rotamer of 1,3-dimethoxybenzene, along with the respective FC fits.

There is a good overall agreement between the experimental and the calculated spectra, which mainly reflects the validity of the propensity rule. The distortions, which resulted from the fits, are translated into internal coordinate changes, and are compared in Figure 35 and in Tables S12 and S13 of the online supporting material to the results of the SCS-CC2/cc-pVTZ calculated geometry changes. There is a good agreement between the experimental and the calculated geometry changes.

The CC bond lengths of the aromatic ring expand upon electronic excitation between 1 and 4 pm. For the C_{2v}-symmetric B-rotamer they are, of course, symmetric with respect to the C_2-symmetry axis. CC bonds in adjacent positions to the OCH_3 groups expand by 3.0 pm, if they are in *trans* position to the methoxy group and by 2.5 pm if they are in *cis* position. The O-C_{ring} bonds contract by approximately 1 pm upon electronic excitation and the O-CH_3 bond expands by the same amount, which is due to a shift of electron density from the oxygen lone pairs to the aromatic ring. Bond expansions follow the electron density differences (EDD), shown in Figure 28. The largest reduction in the electron density (ED) is found for the C(4)-C(5) and the C(5)-C(6) bonds and consequently, these show the largest expansion followed by C(1)-C(2) and the C(2)-C(3) bonds.

The asymmetry of ring bond expansions in the C_s-symmetric A-rotamer is surprisingly large, given the similarity of both EDDs. However, the ED decrease in the C(1)-C(2) bond is larger than the respective bond in the B-rotamer, in line with the larger bond expansion. The largest increase is found in the C(5)-C(6) bond, which also has the largest decrease of ED. Since the connectivities of the atoms stay the same in both rotamers, the effect of the different EDs and the resulting differences in the bond length changes must be effects due to the lone pairs at the methoxy oxygen atoms.

8.6 Conclusions

The geometry changes of two rotamers of 1,3-dimethoxybenzene could be determined from a fit of the FC intensities and the rotational constant changes. The C_{2v}-symmetric B-rotamer shows a symmetric ring opening, which is in agreement with expected geometry changes for the excitation to an ^1L_b-state. The C_s-symmetric A-rotamer in contrast has asymmetric ring expansions, which are reflected in a strongly mixed excited state configuration. From the analysis of the rotationally resolved spectra of both rotamers Schneider *et al.*[90] concluded that the rotation of the inertial axis systems for the asymmetric rotamer, leads to a mixing of the electronically excited states. This behavior is reflected here in the asymmetric ring expansions in the A-rotamer of 1,3-dimethoxybenzene.

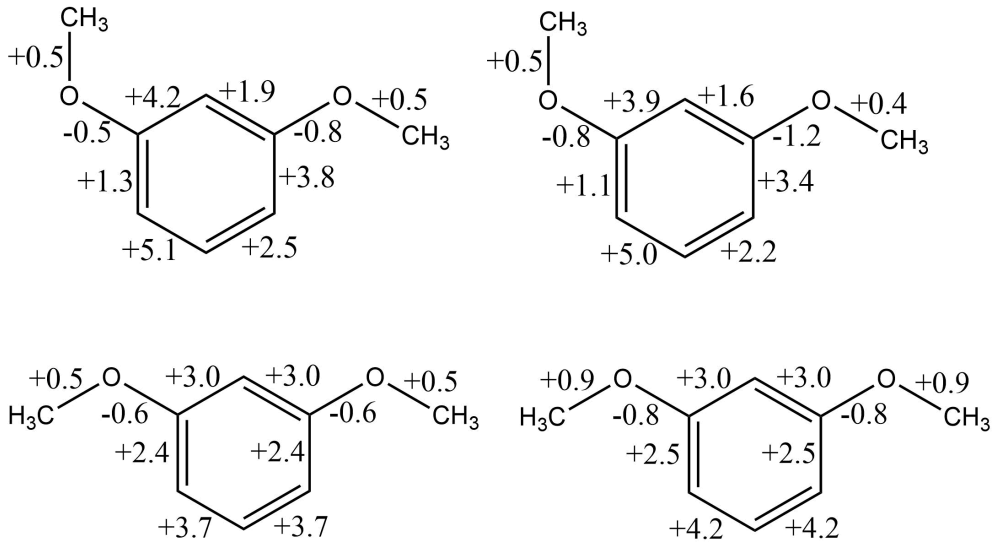

Figure 35: Geometry changes upon electronic excitation of the A-(top row) and B-rotamers (bottom row) of 1,3-dimethoxybenzene. The left scheme shows the SCS-CC2/cc-pVTZ calculated values, the right scheme the results of the Franck-Condon fits.

8.7 Acknowledgements

Financial support of the Deutsche Forschungsgemeinschaft via grant SCHM1043 12-3 is gratefully acknowledged. Computational support and infrastructure was provided by the "Center for Information and Media Technology" (ZIM) at the Heinrich-Heine-University Düsseldorf. We furthermore thank the Regional Computing Center of the University of Cologne (RRZK) for providing computing time on the DFG-funded High Performance Computing (HPC) system CHEOPS as well as support.

9 Excited State Structure of Isolated 4-Cyanoindole from a Combined Franck-Condon and Rotational Constants Analysis

Authors: Christian Henrichs,[1] Malte Reineke,[1] Marie-Luise Hebestreit,[1] and Michael Schmitt*[1]

Journal of Molecular Structure Volume 1223, 5 January 2021, 129241
10.1016/j.molstruc.2020.129241

9.1 Abstract

The changes of the structure of 4-cyanoindole upon electronic excitation have been determined from a combined Franck-Condon and rotational constants fit. The geometry changes were fit to simultaneously reproduce the intensities of 72 lines in the fluorescence emission spectra, obtained via excitation of six different vibronic bands in the first excited singlet state, along with the three rotational constants from rotationally resolved electronic spectra.

Keywords:

4-Cyanoindole;Excited state Structure; Franck-Condon analysis;Ab initio calculations

Highlights:

- An analysis of the excited state structure of 4-Cyanoindole has been given on the basis of a Franck-Condon-analysis.
- The results are compared to ab initio calculations.
- The structural changes are typical for an excitation to a La-state.
- Additional the information of Mayer and Wiberg bond order analysis and of NBO analysis is given an compared to the experimental geometry changes.

9.2 Introduction

The natural amino acid tryptophan, is a widely used intrinsic fluorescence probe for determination of protein structure. Due to its complicated decay kinetics and the relatively low fluorescence quantum yield, the search for chemically modified, i.e. unnatural amino acids has been intensified in the last years. Cyanotryptophans are used as dual infrared and fluorescence spectroscopic labels to assess structural dynamics in proteins[135] and DNA-protein interactions.[136] Markiewicz *et al.*

have shown that 5-cyanotryptophan fluorescence can be utilized as a sensitive probe of protein hydration.[137]

3-Cyanoindole has been studied by Schneider *et al.*, using rotationally resolved electronic Stark spectroscopy.[138] They identified the lowest electronically excited singlet state as Lb-state. The water clusters of 3-cyanoindole$(H_2O)_n$ with $n = 1, 2$ have been studied in the group of Choi by UV-UV hole burning and IR-dip spectroscopy.[139,140] Based on the comparison of the IR-dip spectra with the results of normal mode analyses and a Franck-Condon analysis of the mass-selected R2P spectra of 3-cyanoindole$(H_2O)_n$ with $n = 1, 2$ they deduced a linearly bound water moiety with an N-H $\cdots$ OH_2 binding motif. This structure was confirmed by the rotational constants from rotationally resolved electronic spectroscopy.[138] The excited state lifetime of 3-cyanoindole has been determined to be 9.8 ns in the gas phase, while that of the 3-cyanoindole$(H_2O)_1$ cluster shows a considerably shorter lifetime of 3.6 ns. Interestingly, the fluorescence lifetime of 3-cyanoindole in water solution is the shortest of all cyanoindoles.[141]

From the comparison of the experimental findings to quantum chemical calculations at the coupled cluster level of theory (CC2), the lowest excited singlet state of 4-cyanoindole has been shown to be of mainly La-character, unlike most other indole derivatives, which have the Lb-state as lowest excited state.[9] Furthermore, the large dipole moment in the excited state, which was determined from rotationally resolved electronic Stark spectroscopy, points to the La-state as lowest excited singlet state.

Rotationally resolved electronic spectra of 5-cyanoindole have been presented in the group of Schmitt[79,107,142] From the comparison of the transition dipole moment direction to the results of SCS-CC2 calculations, the lowest excited singlet state could also be shown to be the La- state, as in 4-cyanoindole.

The fluorescence lifetime of the different structural isomer of cyanoindole in solution has been found to depend considerably on the solvent.[141,143] A thorough theoretical study of the excited state dynamics of all structural isomers of cyanoindole has been presented by Abou-Hatab and Matsika.[144]

In the present study, we investigate the structural changes of 4-cyanoindole from a combined rotational constants and Franck-Condon fit of several fluorescence emission spectra of 4-cyanoindole.

9.3 Experimental section

9.3.1 Experimental procedures

4-Cyanoindole ($\geq 98\%$) was purchased from Tokyo Chemical Industry and used without further purification. The experimental setup for the dispersed fluorescence (DF) spectroscopy has been described elsewhere.[101,102] In brief, 4-cyanoindole was evaporated at 333 K and co-expanded through a pulsed nozzle (kept at 353 K to avoid condensation) with a 500 μm orifice (General Valve) into

the vacuum chamber using helium as carrier gas. The output of a Nd:YAG (SpectraPhysics INDI) pumped dye laser (Lambda-Physik, FL3002) was frequency doubled and crossed at right angles with the molecular beam. The resulting fluorescence was imaged on the entrance slit of a f = 1 m monochromator (Jobin Yvon, grating 2400 lines/mm blazed at 400 nm in first order). The dispersed fluorescence spectrum was recorded using a gated image intensified UV sensitive CCD camera (Flamestar II, LaVision). One image on the CCD chip spectrally covers approximately 600 cm^{-1}. Since the whole spectrum is taken on a shot-to-shot basis, the relative intensities in the DF spectra do not vary with the laser power. The relative intensities were afterwards normalized to the strongest band in the spectrum, not including the resonance fluorescence band, which also contains the stray light and is therefore excluded from the FC analysis.

9.4 Quantum chemical calculations

Structure optimizations were performed employing a Dunning's correlation-consistent polarized valence triple zeta (cc-pVTZ) basis set from the TURBOMOLE library.[92,93] The equilibrium geometries of the electronic ground and the lowest excited singlet states were optimized using the approximate coupled cluster singles and doubles model (CC2) employing the resolution-of-the-identity (RI) approximation.[94–96] For the structure optimizations spin-component scaling (SCS) modifications to CC2 were taken into account.[145] Vibrational frequencies and zero-point corrections to the adiabatic excitation energies were obtained from numerical second derivatives using the NumForce script.[97]

9.4.1 Franck-Condon Fits of the emission spectra

The *ab initio* optimized structure of the electronic ground state is distorted along a linear combination of normal modes that are manually selected by the user. The coefficients are varied until the deviation of the relative intensities in all vibronic emission spectra and the rotational constant changes from rotationally resolved electronic spectra from the calculated values are minimized. Both a local minimizer based on a Levenberg-Marquardt variant[130,131] and a global optimizer, which uses evolutionary strategies,[132] have been used for the minimization.[133]

The transitions are classified by the initial vibronic level described by a bra vector and the final vibronic level described by the respective ket vector. Each braket combination is assigned an experimental intensity and an individual weight w_{int} to be used in the fit. Additionally, a weight for the rotational constant fit $w_{rotconst}$ can be chosen. From extensive tests, a relative weight of 5:1 for $w_{rotconst}/w_{int}$ was shown to perform best in terms of accuracy and speed.

The entries for the fit of the Franck-Condon intensities are given as $\langle bra|ket\rangle$ combination, along with the intensities of the observed bands and the rotational constant changes. One entry line of the input looks like $\langle 0\ldots0000|0\ldots1021\rangle$ [int. value] [weight], where $\langle bra|$ and $|ket\rangle$ are vectors with $3N-6$ entries, each representing the occupation of the respective mode, [int. value]

is the relative intensity of the band, with the strongest band given the arbitrary intensity 1 and [weight] is a numerical value for the weight of this transition used in the fit. The example here gives the transition from the vibrationless origin to the ground state level, which is a combination of $Q_1 + Q_2^2 + Q_4$. The lowest wavenumber mode is the right most in the $|ket\rangle$ state.

9.5 Results and Discussion

9.5.1 Computational Results

The SCS-CC2/cc-pVTZ optimized structure of 4-cyanoindole in the ground and lowest excited singlet state has been found to be planar in both states. Geometry optimizations have been performed without any symmetry constraints. The Cartesian coordinates of the ground and excited states are given in the online supporting material. The lowest excited singlet state is the La-state at SCS-CC2 level of theory, what can be inferred from the calculated transition dipole moment orientation (Figure 36) and the orbital contributions to the excitation, given in Figure S3 of the online supporting material.

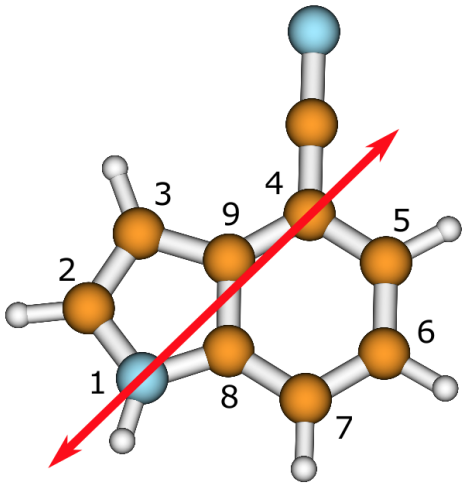

Figure 36: Optimized ground state structure, atom numbers, and transition dipole moment for excitation to the lowest excited singlet state of 4-cyanoindole.

The lowest singlet state with an adiabatic excitation energy of 34776 cm^{-1}, including zero-point energy correction, is reached by an almost pure LUMO ← HOMO transition, a strong indication for an La-state, while the vertically second excited state, which is 925 cm^{-1} higher in energy, is composed of LUMO ← HOMO-1 and LUMO+1 ← HOMO contributions typical for an Lb-state. Despite numerous attempts to optimize the geometry of the Lb-state, no stable minimum could be found. Depending on the starting geometry all attempts ran into the La minimum or into a conical intersection of the lowest two states. Also in the computational study of Abou-Hatab and Matsika[144] no minimum structure for the Lb-state of 4-cyanoindole was found, at the EOM-CCSD/6-311+G(d), EOMCCSD/PCM/6-311+G(d), and CASPT2/aug-cc-pVDZ levels of theory.

Thus, we conclude that the geometry of the Lb-state of 4-cyanoindole is probably close to a conical intersection between the upper La- and the lower Lb-state.

An additional argument for the energetic ordering $E(L_a) < E(L_b)$ are the permanent dipole moments of 4-cyanoindole the these excited singlet states. The lowest state, has a dipole moment of 9.60 D, while the second excited singlet state has a lower dipole moment of 6.77 D, while the ground state dipole moment amount to 6.39 D. Permanent dipole moments, which are similar to those of the electronic ground state belong in general to Lb-states, while larger dipole moments are attributed to La-states.

The 45 modes of 4-cyanoindole transform like Γ_{ired}=31a′ + 14a″ in C_s-symmetry. The result of a Franck-Condon simulation of ground and excited state modes, using the optimized geometries and Hessians in the ground and electronically excited state from the SCS-CC2/cc-pVTZ calculations is given in Table 10 of the online supporting material. One has to keep in mind, that the energetic ordering of modes between the two states might change, so that the same mode might have different numbers in the two states. Technically spoken, the elements in the Duschinsky matrix are predominantly off-diagonal for these modes. The last column of Table 10 gives the composition of the excited state modes in terms of ground state vibrations. $Q_1(S_1)$=+0.95 $Q_2(S_0)$ - 0.23 $Q_3(S_0)$ means, that the energetically lowest mode Q_1 in the electronically excited state (S_1) is composed of the ground state modes Q_2 and Q_3, with coefficients of +0.95 and -0.23, i.e. mode Q_1 in the excited state is mainly Q_2 in the ground state.

Figure 37 shows a graphical representation of the Duschinsky matrix for ground state and lowest excited singlet state vibrational modes. A black square indicates a matrix element of 1, a white square of 0, intermediate values of the matrix elements are coded by gray shading. Thus, unmixed modes are represented by a black square on the diagonal, if the mode ordering in the excited state is the same as in the ground state, and off-diagonal, if the mode ordering changes. The more squares in one row or one column are gray shaded, the stronger this mode is mixed in the excited state.

The electron density difference for excitation from the ground state to the lowest excited singlet state is calculated, using the CC2 wave functions and shown in Figure 38. Regions of decreasing electron density are shown in red, those of increasing electron density in blue.

9.5.2 Experimental results

9.5.3 Laser induced fluorescence spectrum and single vibronic level fluorescence spectra

Figure 39 shows the laser induced fluorescence spectrum of 4-cyanoindole recorded in a molecular beam in the region between the electronic origin at 33038.55 cm^{-1} and 0,0 + 850 cm^{-1}. For the fit of the structural changes upon excitation it is inevitable to have a save assignment of the vibronic bands that are used for excitation to ground state modes. These assignments are made on the basis of the *ab initio* calculated Duschinsky matrix and fluorescence emission spectra, recorded through

Table 10: SCS-CC2/cc-pVTZ calculated and experimental wavenumber of the 45 normal modes of the ground and first electronically excited states of 4-CI, along with the respective symmetry labels and the leading coefficients of the Duschinsky matrix. [a]The fundamental wavenumber of this mode has been determined from its overtone and/or combination bands of a" modes under harmonic assumption.

Mode	S_0			S_1			Duschinsky
	Sym.	Calc.	Obs.	Sym.	Calc.	Obs.	
$Q_1(S_0)$	a'	124.58	125	a"	104.50	95[a]	$Q_1(S_1)$=+0.95 $Q_2(S_0)$ - 0.23 $Q_3(S_0)$
$Q_2(S_0)$	a"	128.77	121[a]	a'	118.00	119	$Q_2(S_1)$=-0.99 $Q_1(S_0)$
$Q_3(S_0)$	a"	217.76	207[a]	a"	159.51	151[a]	$Q_3(S_1)$=+0.94 $Q_3(S_0)$ + 0.26 $Q_2(S_0)$
$Q_4(S_0)$	a"	249.77	254[a]	a"	231.44	239[a]	$Q_4(S_1)$=+0.93 $Q_4(S_0)$+0.26 $Q_7(S_0)$
$Q_5(S_0)$	a'	376.97	380	a"	339.10	337	$Q_5(S_1)$=+0.79 $Q_6(S_0)$-0.33 $Q_7(S_0)$
$Q_6(S_0)$	a"	391.46		a'	371.29	372	$Q_6(S_1)$=-0.98 $Q_5(S_0)$
$Q_7(S_0)$	a"	399.27		a'	403.51	400	$Q_7(S_1)$=+0.98 $Q_8(S_0)$
$Q_8(S_0)$	a'	441.61	442	a"	429.91		$Q_8(S_1)$=-0.87 $Q_{10}(S_0)$-0.31 $Q_6(S_0)$
$Q_9(S_0)$	a'	529.32	531	a"	489.88		$Q_9(S_1)$=-0.60 $Q_7(S_0)$-0.41 $Q_{13}(S_0)$
$Q_{10}(S_0)$	a"	546.77		a"	506.28		$Q_{10}(S_1)$=+0.81 $Q_{11}(S_0)$-0.48 $Q_{13}(S_0)$
$Q_{11}(S_0)$	a"	598.91		a'	519.09	509	$Q_{11}(S_1)$=-0.99 $Q_9(S_0)$
$Q_{12}(S_0)$	a'	615.37	619	a"	532.52		$Q_{12}(S_1)$=+0.50 $Q_{17}(S_0)$-0.58 $Q_{20}(S_0)$
$Q_{13}(S_0)$	a"	627.89		a'	594.60		$Q_{13}(S_1)$=+0.96 $Q_{12}(S_0)$-0.21 $Q_{14}(S_0)$
$Q_{14}(S_0)$	a'	650.22		a"	609.10		$Q_{14}(S_1)$=-0.48 $Q_7(S_0)$ +0.54 $Q_{13}(S_0)$
$Q_{15}(S_0)$	a"	720.45		a'	628.79		$Q_{15}(S_1)$=+0.96 $Q_{14}(S_0)$+0.22 $Q_{12}(S_0)$
$Q_{16}(S_0)$	a"	763.42		a"	638.79		$Q_{16}(S_1)$=-0.79 $Q_{15}(S_0)$+0.42 $Q_{16}(S_0)$
$Q_{17}(S_0)$	a"	783.04		a"	722.26		$Q_{17}(S_1)$=-0.63 $Q_{17}(S_0)$-0.70 $Q_{20}(S_0)$
$Q_{18}(S_0)$	a'	839.77	850	a"	760.43		$Q_{18}(S_1)$=-0.77 $Q_{16}(S_0)$-0.34 $Q_{15}(S_0)$
$Q_{19}(S_0)$	a"	858.03		a'	778.51		$Q_{19}(S_1)$=-0.43 $Q_{18}(S_0)$-0.80 $Q_{21}(S_0)$
$Q_{20}(S_0)$	a"	894.18		a"	842.19		$Q_{20}(S_1)$=+0.90 $Q_{19}(S_0)$+0.37 $Q_{16}(S_0)$
$Q_{21}(S_0)$	a'	901.41	902	a'	845.26		$Q_{21}(S_1)$=-0.88 $Q_{18}(S_0)$+0.44 $Q_{21}(S_0)$
$Q_{22}(S_0)$	a"	943.52		a"	867.08		$Q_{22}(S_1)$=-0.93 $Q_{22}(S_0)$-0.25 $Q_{17}(S_0)$
$Q_{23}(S_0)$	a'	1000.81	1008	a'	957.86		$Q_{23}(S_1)$=+0.95 $Q_{23}(S_0)$
$Q_{24}(S_0)$	a'	1070.63		a'	1006.99		$Q_{24}(S_1)$=-0.93 $Q_{24}(S_0)$
$Q_{25}(S_0)$	a'	1092.76	1092	a'	1051.21		$Q_{25}(S_1)$=-0.73 $Q_{25}(S_0)$+0.50 $Q_{17}(S_0)$
$Q_{26}(S_0)$	a'	1131.38	1113	a'	1100.85		$Q_{26}(S_1)$=-0.74 $Q_{27}(S_0)$+0.36 $Q_{25}(S_0)$
$Q_{27}(S_0)$	a'	1181.69	1180	a'	1163.49		$Q_{27}(S_1)$=-0.58 $Q_{26}(S_0)$-0.38 $Q_{30}(S_0)$
$Q_{28}(S_0)$	a'	1230.06		a'	1167.65		$Q_{28}(S_1)$=-0.39 $Q_{25}(S_0)$+0.58 $Q_{28}(S_0)$
$Q_{29}(S_0)$	a'	1249.45		a'	1215.28		$Q_{29}(S_1)$=+0.54 $Q_{29}(S_0)$-0.39 $Q_{34}(S_0)$
$Q_{30}(S_0)$	a'	1295.74		a'	1262.85		$Q_{30}(S_1)$=+0.60 $Q_{28}(S_0)$-0.62 $Q_{29}(S_0)$
$Q_{31}(S_0)$	a'	1378.44		a'	1283.22		$Q_{31}(S_1)$=-0.70 $Q_{30}(S_0)$+0.42 $Q_{31}(S_0)$
$Q_{32}(S_0)$	a'	1395.22		a'	1366.23		$Q_{32}(S_1)$=-0.53 $Q_{31}(S_0)$+0.64 $Q_{34}(S_0)$
$Q_{33}(S_0)$	a'	1454.01		a'	1425.47		$Q_{33}(S_1)$=+0.76 $Q_{35}(S_0)$-0.36 $Q_{33}(S_0)$
$Q_{34}(S_0)$	a'	1464.10		a'	1436.18		$Q_{34}(S_1)$=+0.48 $Q_{33}(S_0)$+0.62 $Q_{36}(S_0)$
$Q_{35}(S_0)$	a'	1527.37		a'	1477.02		$Q_{35}(S_1)$=+0.58 $Q_{33}(S_0)$+0.44 $Q_{38}(S_0)$
$Q_{36}(S_0)$	a'	1538.09	1556	a'	1515.80		$Q_{36}(S_1)$=+0.68 $Q_{32}(S_0)$-0.41 $Q_{35}(S_0$
$Q_{37}(S_0)$	a'	1613.43		a'	1565.27		$Q_{37}(S_1)$=+0.81 $Q_{37}(S_0)$-0.28 $Q_{35}(S_0)$
$Q_{38}(S_0)$	a'	1648.61		a'	1619.12		$Q_{38}(S_1)$=+0.68 $Q_{38}(S_0$+0.40 $Q_{36}(S_0)$
$Q_{39}(S_0)$	a'	2147.27	2160	a'	2053.29		$Q_{39}(S_1)$=-0.99 $Q_{39}(S_0)$
$Q_{40}(S_0)$	a'	3199.77		a'	3196.34		$Q_{40}(S_1)$=-0.71 $Q_{40}(S_0)$-0.61 $Q_{41}(S_0)$
$Q_{41}(S_0)$	a'	3214.00		a'	3220.74		$Q_{41}(S_1)$=-0.58 $Q_{41}(S_0)$-0.79 $Q_{42}(S_0)$
$Q_{42}(S_0)$	a'	3227.86		a'	3236.86		$Q_{42}(S_1)$=-0.68 $Q_{40}(S_0)$+0.52 $Q_{41}(S_0)$
$Q_{43}(S_0)$	a'	3268.50		a'	3260.49		$Q_{43}(S_1)$=+0.83 $Q_{43}(S_0)$-0.54 $Q_{44}(S_0)$
$Q_{44}(S_0)$	a'	3287.59		a'	3280.29		$Q_{44}(S_1)$=-0.53 $Q_{43}(S_0)$-0.83 $Q_{44}(S_0)$
$Q_{45}(S_0)$	a'	3681.51		a'	3631.72		$Q_{45}(S_1)$=-0.99 $Q_{45}(S_0)$

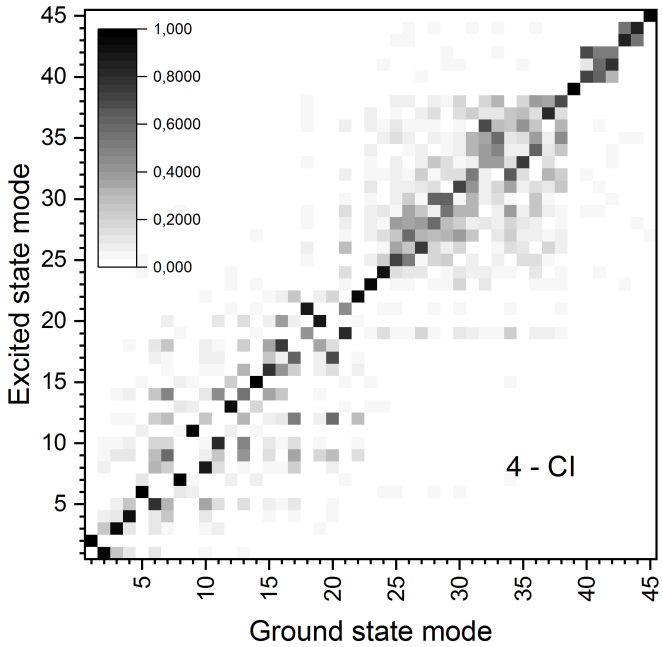

Figure 37: Graphical representation of the Duschinsky matrix for the vibrational ground and excited state modes of 4-cyanoindole. A black square indicates a matrix element of 1, a white square of 0, intermediate values of the matrix elements are coded by gray shading.

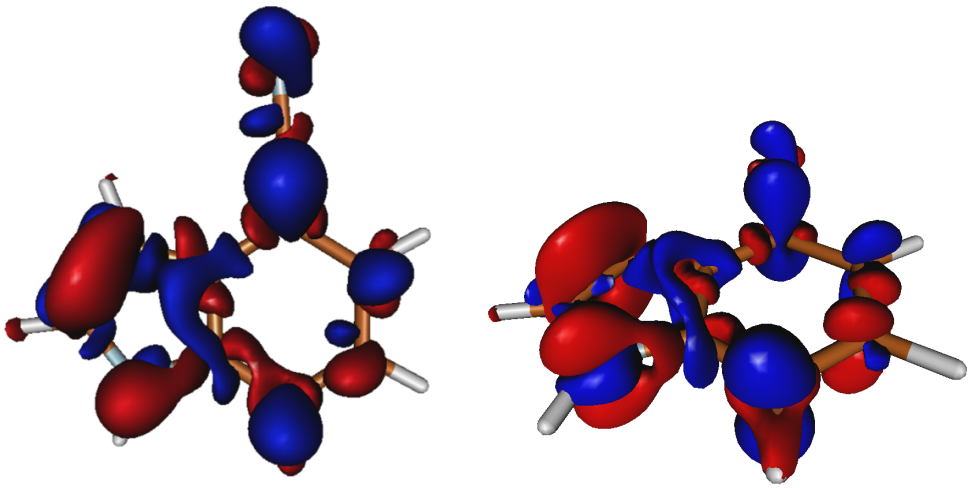

Figure 38: Two different views of the electron density difference between the ground state and the lowest excited singlet state of 4-cyanoindole. Regions of decreasing electron density are shown in red, those of increasing electron density in blue.

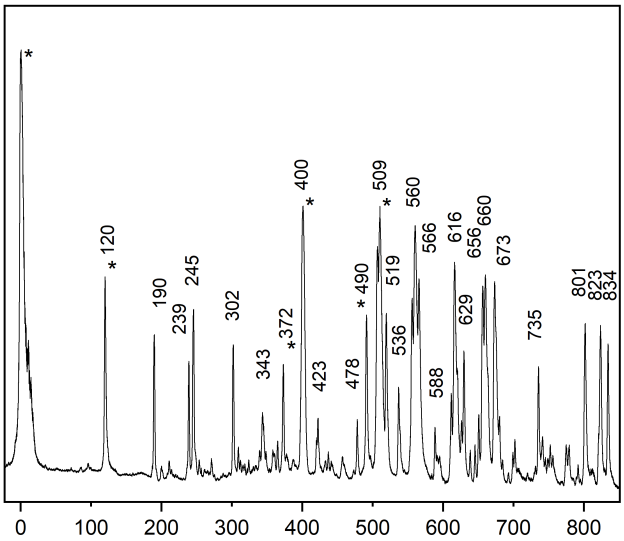

Figure 39: LIF spectrum of jet-cooled 4-cyanoindole. Vibronic bands which have been excited in order to record fluorescence emission spectra have been marked by an asterisk.

these vibronic bands (Table 10). All emission spectra, discussed in this section are given in the online supporting material.

The first observed vibronic band at 119 cm^{-1} is assigned to the in-plane CCN bending mode of the cyano group Q_2', calculated at 118 cm^{-1} as shown in Table 10. Excitation at 119 cm^{-1} leads to the fluorescence emission spectrum shown in Figure S5 of the online supplementary information. The strongest band is observed at 125 cm^{-1}, which is assigned to the fundamental of Q_1, since modes Q_1 and Q_2 change their energetic ordering upon electronic excitation.

The second band at 190 cm^{-1} can be attributed to the overtone of the out-of-plane mode Q_1' (twisting motion of the annealed rings), calculated at 104 cm^{-1}, cf. Table 10. In the harmonic approximation the fundamental of Q_1' is expected at 190 cm^{-1}/2 = 95 cm^{-1}. Excitation of this band leads to the fluorescence emission spectrum shown in Figure S6 of the online supplementary information. The strongest band in emission at 249 cm^{-1} can indeed be assigned to the Q_2'' overtone in the ground state.

A Darling-Dennison[146] resonance[3] between the overtone of Q_2' and the combination band $Q_1' + Q_3'$ is responsible for the pair of observed bands at 239/245 cm^{-1}. This assignment is completely backed by the results of the fluorescence emission spectra, presented in Figure S7 and S8 of the online supporting material. Upon excitation of 239 cm^{-1}, the diagonal transition to the respective overtone in the ground state at 249 cm^{-1} is the strongest band, but the fundamental at 124 cm^{-1} is clearly visible like the emission to the second overtone at 347 cm^{-1}. Excitation at 245 cm^{-1}, which is the combination band of Q_1' and Q_3' in the excited state (95 cm^{-1} + 151 cm^{-1} = 246 cm^{-1} from Table 10) leads to the strongest band in emission at 327 cm^{-1}, the combination of Q_1'' and

[3]In contrast to a Fermi resonance, in which an asymmetric overtone interacts with a symmetric fundamental, Darling-Dennison resonances are interactions between the overtone of a symmetric mode with a combination of asymmetric modes.

Q_2'' (121 cm^{-1} + 208 cm^{-1} = 329 cm^{-1}), keeping in mind that Q_1 and Q_2 change their order upon electronic excitation.

The overtone of out-of-plane mode Q_3' (butterfly motion of the annealed rings) is observed at 302 cm^{-1}, which leads to a fundamental of 151 cm^{-1} in harmonic approximation, in good agreement with the calculated value of 159 cm^{-1}. Figure S9 of the online supporting material shows a band at 414 cm^{-1} to be the strongest band im emission after excitation at 302 cm^{-1}. From comparison to Table 10 it can easily be inferred that this band is the overtone of Q_3'' in the ground state, in good agreement with the theoretical prediction of 217 cm^{-1}.

At 343 cm^{-1} a combination band of the two out-of-plane modes Q_1' and Q_4' is observed, which is calculated in harmonic approximation at 334 cm^{-1} (95 cm^{-1} + 239 cm^{-1}). Q_4 can best be described as twisting mode of the annealed rings.

The in-plane gearing mode Q_6', which is calculated in harmonic approximation at 371 cm^{-1} is observed at 372 cm^{-1}. This is in agreement with the results from the fluorescence emission spectrum, recorded through 371 cm^{-1}. The strongest band in emission (cf. Figure S10) is found at 380 cm^{-1}, which is assigned to Q_5'' in the ground state, the mode with the strongest propensity to mode Q_6', following Table 10.

An in-plane ring deformation Q_7', mainly localized in the benzene moiety and similar to mode 6a in benzene, is observed at 400 cm^{-1} and calculated at 403 cm^{-1}. A long progression in mode Q_8'' with a fundamental at 442 $^{-1}$ in the ground state reflects the propensity of modes Q_7' in the excited state and Q_8'' in the ground state, as can be inferred from Figure S11 and Table 10.

The band, observed at 478 cm^{-1} is the harmonic second overtone of mode Q_3' in the excited state (3 x 151 cm^{-1} = 453 cm^{-1}). The strongest propensity in the fluorescence emission is found to the band at 595 cm^{-1}. This band can hence be assigned to the harmonic second overtone of Q_3' in the ground state (3 x 207 cm^{-1} = 621 cm^{-1}).

The band at 490 cm^{-1} to is assigned to the overtone of the out-of-plane mode Q_4' (twisting mode of the annealed rings) (2 x 239 cm^{-1} = 478 cm^{-1}). The fluorescence emission spectrum recorded upon excitation at 490 cm^{-1} shows a ground state mode at 509 cm^{-1} to have the highest intensity (cf. Figure S13). The fundamental of Q_4'' in harmonic approximation at 254 cm^{-1} is in good agreement with the calculated value of 250 cm^{-1}, shown in Table 10.

The vibronic band observed at 509 cm^{-1} is assigned to the in-plane ring deformation Q_{11}', which is calculated at 519 cm^{-1}. This assignment is supported by a strong propensity to mode Q_9'' in the ground state at 531 cm^{-1}, as observed in the fluorescence emission spectrum, recorded via the band at 509 cm^{-1}, cf. Figure S14. However, the strongest band in emission is observed at 665 cm^{-1}, which can tentatively be assigned to mode Q_{14}'' in the ground state. Inspection of Table 10 shows, that this mode is connected to Q_{15}' in the excited state, calculated at 628 cm^{-1}. Therefore, this alternative assignment can safely be excluded.

9.5.4 Franck-Condon fits of the fluorescence emission spectra

Using the information from section 9.5.3 on the LIF spectrum of 4-cyanoindole, we assigned several bra states, which are the initial levels for the transitions in the Franck-Condon fits. Subsequently, the ground state levels are assigned as ket states, using the information from the fluorescence emission spectra. In total, the intensities of 72 different ket states from the excitation of 6 bra states (0,0 (electronic origin), 0,0+119, 0,0+372, 0,0+400, 0,0+490, and 0,0+509) were simultaneously used in the fit. A comparison of all experimental emission spectra and their Franck-Condon fits is presented in Figure 40. Note, that the intensity of the exciting band is not used in the intensity fit, since it is regularly contaminated by stray light from the excitation laser. A good agreement between the experimental spectra and the fits is obtained.

In addition to the 72 intensities of emission bands, three changes of the rotational constant upon electronic excitation from a rotationally resolved LIF spectrum[9] simultaneously have been used in the fit of the geometry changes. The use of these independent inertial data for the determination of structural changes is indispensable, due to the harmonic nature of the approximation for the FC integrals. For strict harmonic potentials in both electronic states connected by the spectroscopic transition, distortion along a normal mode in positive direction $+Q$ (elongation) leads to the same overlap integrals as along $-Q$. However, both possibilities lead to strongly different rotational constant changes. The resulting bond length changes are shown in Figure 41 and Table 11 and are compared to the *ab initio* calculated geometry changes.

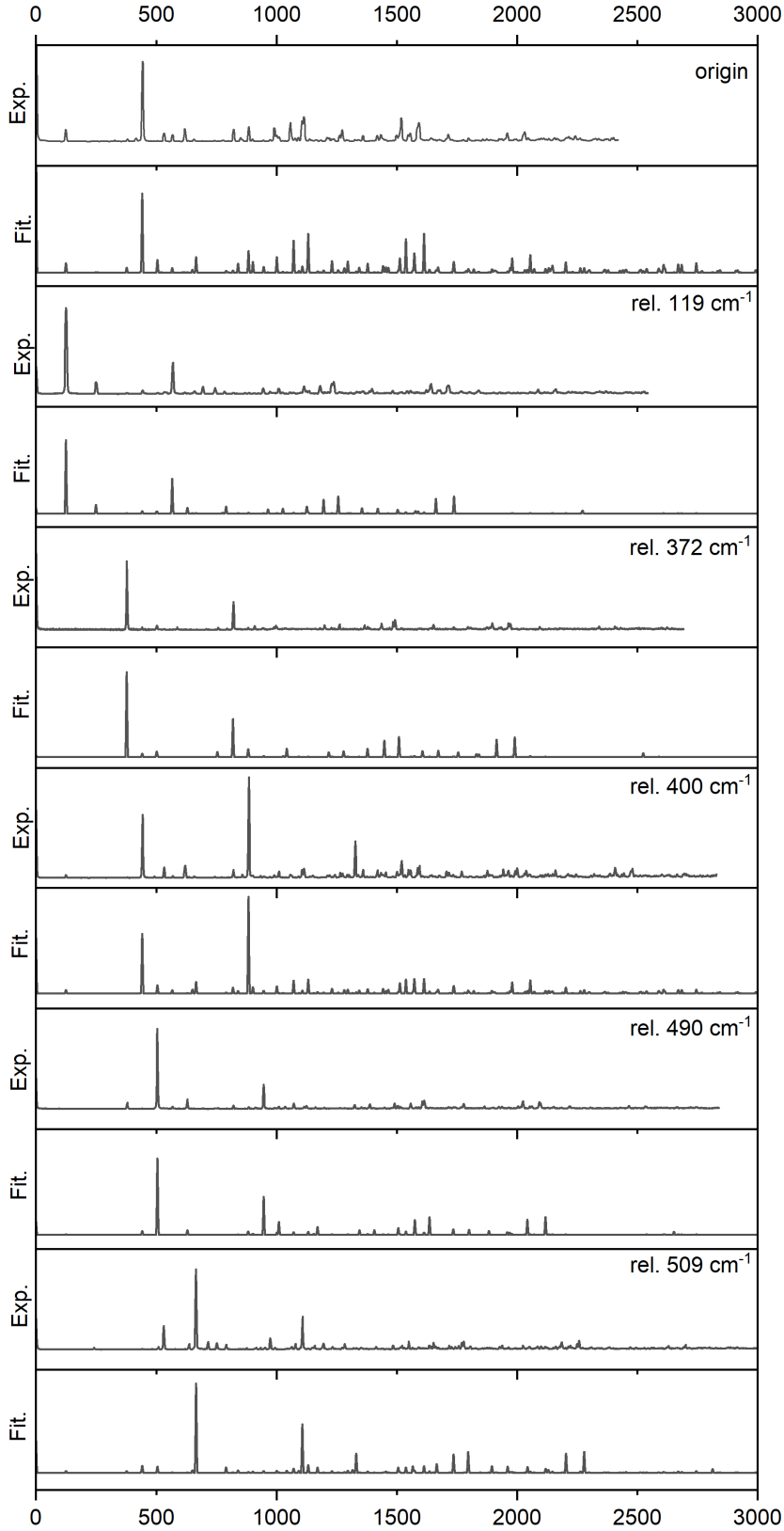

Figure 40: Experimental and fitted fluorescence emission spectra of the electronic origin and of five vibronic bands of 4-cyanoindole at 0,0 + 119, 0,0 + 372, 0,0 + 400, 0,0 + 490, and 0,0 + 509 cm^{-1}, which have been used in the fit of the geometry changes.

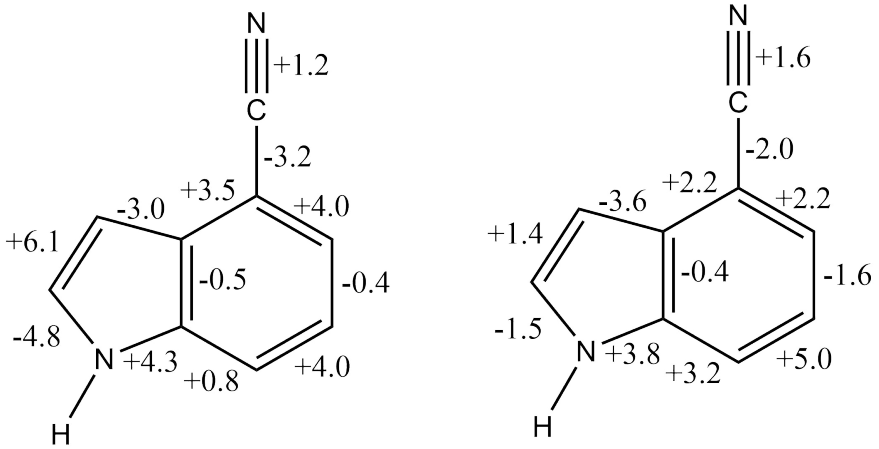

Figure 41: Geometry changes upon electronic excitation of 4-cyanoindole. The left scheme shows the SCS-CC2/cc-pVTZ calculated values, the right scheme the results of the Franck-Condon fits.

Table 11: Comparison of the bond length changes from SCS-CC2 calculations and Franck-Condon fits and of Wiberg[147] and Mayer[148] bond orders of 4-cyanoindole upon electronic excitation from SCS-CC2 calculations.

State	bond length S_0		bond length S_1		S_1-S_0		bond order(S_0)		bond order(S_1)		S_1-S_0	
Method	SCS-CC2	FCFit	SCS-CC2	FCFit	SCS-CC2	FCFit	Mayer	Wiberg	Mayer	Wiberg	Mayer	Wiberg
N1-C2	138.2	138.2	133.4	136.7	-4.8	-1.5	1.073	1.255	1.144	1.361	0.0710	0.106
C2-C3	137.5	137.5	143.6	138.9	+6.1	+1.4	1.575	1.595	1.504	1.485	-0.0710	-0.110
C3-C9	143.1	143.1	140.0	139.5	-3.0	-3.6	1.159	1.205	1.202	1.278	0.0430	0.073
C9-C4	141.2	141.2	144.7	143.4	+3.5	+2.2	1.229	1.249	1.220	1.202	-0.0090	-0.047
C4-C5	139.5	139.5	143.4	141.6	+4.0	+2.2	1.327	1.384	1.317	1.344	-0.0100	-0.040
C5-C6	140.8	140.8	140.4	139.1	-0.4	-1.6	1.266	1.373	1.297	1.415	0.0310	0.042
C6-C7	139.1	139.1	143.0	144.1	+4.0	+5.0	1.389	1.449	1.356	1.397	-0.0330	-0.052
C7-C8	134.0	134.0	140.7	143.1	+0.8	+3.2	1.264	1.341	1.289	1.370	0.0250	0.029
C8-N1	137.6	137.6	141.9	141.2	+4.3	+3.8	1.118	1.242	1.074	1.165	-0.0440	-0.077
C8-C9	142.0	142.0	141.5	141.5	-0.5	-0.4	1.180	1.212	1.165	1.219	-0.0150	0.007
C4-C10	143.5	143.5	140.3	141.5	-3.2	-2.0	0.939	1.152	0.942	1.211	0.0030	0.059
C10-N1	117.6	117.7	118.8	119.2	+1.2	+1.6	2.936	3.044	2.913	3.013	-0.0230	-0.031

9.6 Conclusions

The structural changes of 4-cyanoindole upon electronic excitation to the lowest excited singlet state could be determined from a combined Franck-Condon/rotational constants fit. Table 11 compares the interatomic distances from the SCS-CC2 calculations and the Franck-Condon/rotational constants fits. Additionally the Wiberg[147] and Mayer[148] bond orders are included in the Table, which have been obtained from the CC2 wavefunctions using the Multiwfn tool.[149] Figure 42 compares the correlation of bond length changes with Wiberg and Mayer bond order changes. Obviously, there is a closer correlation of the bond lengths to the Wiberg bond order changes than to the Mayer bond order changes.

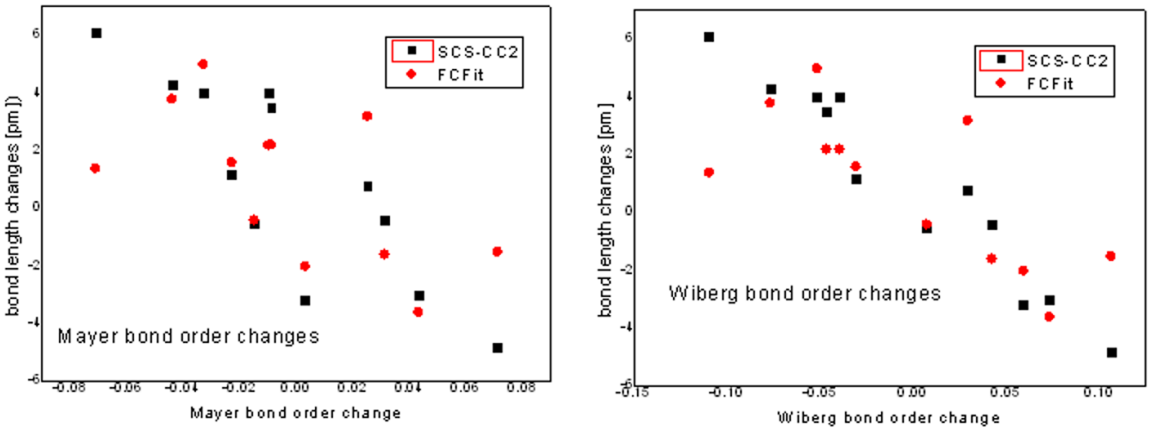

Figure 42: Correlation between bond lengths changes from SCS-CC2/FCFit and Mayer and Wiberg bond order changes.

A deeper insight into the reasons for the observed bond length changes can be obtained from a natural bond orbital analysis, which has been performed using the NBO 7.0 program from Frank Weinhold's group.[25] Table 12 displays the difference of occupation between ground and excited state in bonding and anti-bonding orbitals of selected bonds.

With the help of the EDD plot, given in Figure 38 and the changes of occupancy upon electronic excitation from Table 12, the change in bond length can be examined more precisely. The following bonds are taken out as examples for the interpretation. The bond length of the C2-C3 bond increases according to Table 11. This can be described both by the decrease in the electron density between the ground and the excited state (Figure 38) as well as by the higher occupation of the anti-binding orbitals in the excited state in this bond. The occupancy of the binding orbitals also decreases. BD 28 represents the binding sp2-hybrid overlap orbital of the C2-C3 bond, while BD 29 shows the binding π-contribution to the bond. BD*52 is the anti-bonding counterpart to BD 28, while BD*53 is the anti-bonding counterpart of BD 29.

For the bond C4-C5, an increase in the bond length can be shown based on the orbital occupation. Due to an increase in the two anti-bonding orbitals and a decrease in one of the bind-

Table 12: Comparison of the results of the occupancy upon electronic excitation from the NBO-analysis. All orbital contributions, given in the Table are summarized graphically in the online supporting material (Figure S18).

		Occupancy		
	NBO	S_0	S_1	S_1- S_0
C2-C3	BD 28	1.98321	1.98135	-0.00186
	BD 29	1.86685	1.82144	-0.04541
	BD* 52	0.00583	0.00642	0.00059
	BD* 53	0.24027	0.28870	0.04843
C4-C5	BD 15	1.97533	1.97590	0.00057
	BD 16	1.72085	1.68780	-0.03305
	BD* 39	0.01613	0.01725	0.00112
	BD* 40	0.35794	0.37567	0.01773
C4-CN	BD 34	1.98344	1.98434	0.00090
	BD* 58	0.02570	0.02378	-0.00192
C6-C7	BD 18	1.98199	1.98130	-0.00069
	BD 19	1.71880	1.68780	-0.03100
	BD* 42	0.00898	0.00914	0.00016
	BD* 43	0.31629	0.34265	0.02636
C8-C9	BD 24	1.97076	1.97315	0.00239
	BD 25	1.57930	1.57394	-0.00536
	BD* 48	0.02041	0.01966	-0.00075
	BD* 49	0.44991	0.46730	0.01739
N1	LP 12	1.68395	1.66034	-0.02361

ing orbitals, it can be described despite an increase in the electron density on both atoms. This is because the occupancy of the binding π-orbital (compare online supplementary Figure S15) decreases, while that of the two anti-bonding orbitals, shown in Figure S16 and Figure S17, increases. Accordingly, an increase in the bond length is possible despite the increasing electron density within the π-orbitals.

The bond length between the cyano group and the ring system also decreases. Here, the occupation decreases within the involved anti-bonding orbital while it increases in the binding orbital. Therefore, a correlation between increasing or decreasing bond length and a change in the occupation of binding and anti-bonding orbitals between the ground and the excited state can be shown. The natural bond orbital BD34 has a binding sp2-hybrid character while BD*58, is its anti-bonding counterpart.

The EDD plot for binding C6-C7 cannot be interpreted so readily, but also in this case, the increase in the population of anti-bonding orbitals and the decrease of binding orbitals corresponds to an increasing bond length. The electron density in the p-orbitals of the cyano group and the carbon atom C4 increases. Both NBO BD18 and NBO BD*42 are sp2-hybrid orbitals of the C6-

C7 bond, the former contributing to a bonding interaction, that latter to the anti-bonding. BD19 and BD*43 represent bonding and anti-bonding π-contributions of C6-C7.

For a small change in bond length, such as bond C8-C9, it can be seen that the population in one of the binding and one anti-bonding orbital pair behaves in the opposite direction to the other pair involved (cf. Table 12). However, the decrease in bond length can still be explained by the increase in electron density for this bond obtained from the EDD plot.

The alternating bond length changes upon electronic excitation in 4-cyanoindole are in agreement with a La excitation, while excitation to the Lb-state in general leads to a uniform bond length increase in both the benzene and the pyrrole moiety.

Conflicts of interest

There are no conflicts to declare.

9.7 Acknowledgements

Financial support of the Deutsche Forschungsgemeinschaft via grant SCHM1043/12-3 is gratefully acknowledged. Computational support and infrastructure was provided by the "Center for Information and Media Technology" (ZIM) at the Heinrich-Heine-University Düsseldorf (Germany).

10 Excited State Structure of Isolated 2-Cyanoindole and the Binary 2-Cyanoindole-$(H_2O)_1$ Cluster from a Combined Franck-Condon and Rotational Constants Fit

Authors: Christian Henrichs,[1] Stephan Zimmermann,[1] Marie-Luise Hebestreit,[1] and Michael Schmitt*[1]

submitted to J. Mol. Struct. (2020) *accepted*

10.1 Abstract

Laser induced fluorescence and fluorescence emission spectra of 2-cyanoindole and the binary 2-cyanoindole-$(H_2O)_1$ cluster in a molecular beam were analyzed using a combination of Franck-Condon (FC) fits of the emission spectra and *ab initio* calculations. The structural changes upon electronic excitation to the lowest excited singlet state have been elucidated by a combined rotational constants/vibronic intensities fit. The experimentally determined geometry changes and the *ab initio* calculations point to an L_b-like excited state for the monomer. FC fits of emission spectra of the binary water cluster and quantum chemical calculations show that the emission of the water cluster also takes place from an L_b-like excited state structure. However, for 2-cyanoindole-$(H_2O)_1$ the second highest occupied molecular orbital mixes strongly with the highest one. Therefore, the difference between L_a and L_b characteristics are smaller than for other substituted indoles, including the other positional conformers of the n-cyanoindoles.

Keywords:

Franck-Condon analysis; 2-cyanoindole; emission spectra; rotational constants; excited states; Duschinsky

10.2 Introduction

Cyanoindoles as chromophores of the fluorescence probes cyanotryptophan[136,150] have recently found considerable interest, both from the side of the experiment[9,79,107,138–143,151,152] as well as from theory.[144,153]

Recently, Brisker-Klaiman and Dreuw investigated the level inversion of L_a- and L_b-states of substituted indoles upon solvation in polar solvents.[154] They found an increasing stabilization of the L_a-state with increasing solvent polarity. Therefore, the stabilization of the L_a-state is larger in polar media than that of the L_b-state, which may lead to the level inversion with regard to the gas-phase position of the lowest excited singlet states. They accounted for the solvation effects by

using a continuum solvation model, which represents the solvent as continuous dielectric medium, characterized by its dielectric constant and its refractive index. No specific interactions between molecules in the first solvation shell with the chromophore have been taken into account. The excited state dynamics of all structural isomers of cyanoindole in gas phase and in solution has been investigated by Abou-Hatab and Matsika.[144] Their calculations predict that in absorption the L_b-excited state is always lower in energy than the L_a-state for all isomers of cyanoindole in the gas phase and in solution.

Although the use of the L_a and L_b nomenclature for close-lying excited singlet $\pi\pi^*$-states for indole and substituted indoles is not justified from a theoretical viewpoint, since they lack the necessary C2 symmetry for the unambiguous assignment[4], the nomenclature is still used extensively. The original proposal by Platt for cata-condensed aromatics [155,156] was later extended to the case of indole by Weber.[157] We will show that the use of this nomenclature has to be performed with utter care, since the molecular orbitals start heavily to mix already upon cluster formation with the first water molecule.

Recently, in our group, the rotationally resolved electronic Stark spectra of 2-cyanoindole have been measured and the dipole moments in the ground and first electronically excited singlet state were determined.[8] Interestingly, the common presumption that the dipole moment of L_a-states in indoles is always larger than that of the L_b-state has been refuted in this publication. The state with the larger dipole moment is the L_b-state, what opens the question, how the two electronically excited states shift upon solvation with polar solvents.

Gas phase spectroscopy offers the unique possibility, to study these specific interactions, like hydrogen bonds or van der Waals interaction by species selective spectroscopic techniques. There are several examples in the literature, where already the first solvating molecule has a crucial influence on the conformational space of a flexible chromophore,[68] or on the electronic nature of the excited state. For 7-azaindole it could be shown, that the lowest excited singlet state has L_b-character, while the first complexing water molecule stabilizes the L_a-state to an extent that it becomes the energetically lowest excited state.[78,158,159]

While for 3-cyanoindole[138,140] and 5-cyanoindole[152] species-selected vibronic spectra of the binary water clusters have already been published, there is, up to now, no work on size- or species-selected 2-cyanoindole-water clusters to our knowledge. All cyanoindoles have two different in-plane binding motifs: a *trans*-linear hydrogen bonded N(1)-H$^{\cdots}$OH$_2$ structure and a cyclic motif with a C≡N$^{\cdots}$HOH and a C-H$^{\cdots}$OH$_2$ hydrogen bond in adjacent position to the −C≡N group. For atomic numbering of the monomer and the structures of the water clusters cf. Figure 43. π-bound structures of the water clusters are discussed but have not been observed experimentally.

In the present contribution we will investigate the structural changes of 2-cyanoindole and the hydrogen bonded 2-cyanoindole-$(H_2O)_1$ cluster upon electronic excitation to the lowest excited singlet state from a combination of Franck-Condon analysis including the changes of inertial pa-

[4]In these cases, the nodes of the wavefunction will neither go purely through the atoms nor through the bonds.

rameters of two isotopologues, and *ab initio* calculations. For the binary water cluster, the N(1)-H bond and the −C≡N group are at adjacent positions, opening the possibility of a considerably stronger hydrogen bond compared to 3-, 4-, and 5-cyanoindole water complexes.

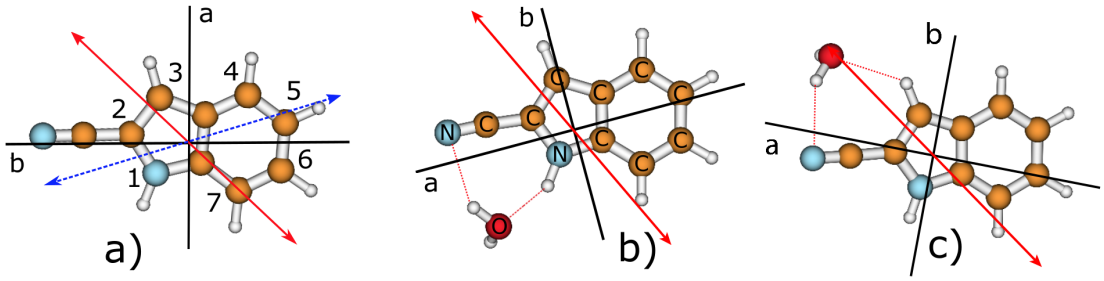

Figure 43: a) Ground state structures and atom numbering of 2-cyanoindole along with the inertial axes and the transition dipole moments for the excitation to the lowest two excited singlet states. Transition dipole moment (TDM) for excitation to the lowest excited singlet state (red, straight line). The TDM for the excitation to the S_2 state is shown as a blue dotted line.
b) Most stable ground state structure of the 2-cyanoindole-$(H_2O)_1$ clusters along with the transition dipole moment orientation for excitation to the lowest excited singlet state.
c) Second most stable ground state structure of the 2-cyanoindole-$(H_2O)_1$ clusters along with the transition dipole moment orientation for excitation to the lowest excited singlet state.

10.3 Experimental and Theoretical Methods

10.3.1 Experimental procedures

2-Cyanoindole (≥98%) was purchased from Apollo Scientific and used without further purification. The experimental setup for the dispersed fluorescence (DF) spectroscopy has been described elsewhere.[160] In brief, 2-cyanoindole was evaporated at 383 K and co-expanded through a pulsed nozzle (kept at 393 K to avoid condensation) with a 500 mm orifice (General Valve) into the vacuum chamber using helium as carrier gas. The output of a Nd:YAG (SpectraPhysics INDI) pumped dye laser (Lambda-Physik, FL3002) was frequency doubled and crossed at right angles with the molecular beam. The resulting fluorescence was imaged on the entrance slit of a f = 1 m monochromator (Jobin Yvon, grating 2400 lines/mm blazed at 400 nm in first order). The dispersed fluorescence spectrum was recorded using a gated image intensified UV sensitive CCD camera (Flamestar II, LaVision). One image on the CCD chip spectrally covers approximately 600 cm^{-1}. Since the whole spectrum is taken on a shot-to-shot basis, the relative intensities in the DF spectra do not vary with the laser power. The relative intensities were afterwards normalized to the strongest band in the spectrum, not including the resonance fluorescence band, which also contains the stray light and is therefore excluded from the FC analysis.

10.3.2 Quantum chemical calculations

Structure optimizations were performed employing a Dunning's correlation-consistent polarized valence triple zeta (cc-pVTZ) basis set from the TURBOMOLE library.[92,93] The equilibrium geometries of the electronic ground and the lowest excited singlet states were optimized using the approximate coupled cluster singles and doubles model (CC2) employing the resolution-of-the-identity (RI) approximation.[94–96] For the structure optimizations spin-component scaling (SCS) modifications to CC2 were taken into account.[145] Vibrational frequencies and zero-point corrections to the adiabatic excitation energies were obtained from numerical second derivatives using the NumForce script.[97] The basis set superposition error (BSSE) corrected stabilization energies of the water clusters have been considered using the counterpoise correction from Boys and Bernardi,[161] implemented in the jobbsse script of TURBOMOLE. All structure optimizations were performed using Dunning's cc-pVTZ basis set of triple ζ quality. In a previous study, we have shown that both structures and vibrational frequencies can be described with sufficient accuracy with basis sets of ζ quality, without augmentation of the basis, even for weakly bound argon clusters of aromatic molecules.[162] The choice for CC2-SCS as method for structure optimization is guided by our own experience that CC2 based methods (original or in their spin scaled variants SCS or SOS) describe the geometries of medium-sized molecular systems in both electronic states to a high accuracy, when compared to time-dependent density functional theory models,[107,163] or complete active space methods.[164] A thorough benchmark study on aromatic organic molecules comparing DFT/B3LYP, ADC(2), CC2, SOS-CC2 and SCS-CC2 with the results of high-resolution gas-phase data also points to SCS-CC2 as most accurate method.[165] Hättig[166] showed that, as a consequence of the lack of Hermitian symmetry, CC2 will in general not give a physically correct description of conical intersections between states of the same symmetry. This problem does not appear in ADC(2). However, in the present contribution we are interested only in stable minima structures of the ground and the lowest excited singlet states, thus SCS-CC2 with the cc-pVTZ basis set was chosen for the geometry optimization and calculation of the Hessians of both electronic states.

10.4 Franck-Condon Fits of the emission spectra

The intensities of fluorescence emission bands obtained via excitation of different single vibronic levels in the excited state contain the information that is needed to assess the structural changes upon excitation from the ground state to the electronically excited state. Additionally, the changes of the inertial parameters (rotational constants) from rotationally resolved electronic spectra can be used to improve the results of a fit of the geometry changes. The changes of the rotational constants of different isotopologues, along with the intensities from fluorescence emission spectra, obtained through different vibronic states are fit to a distortion of the ground state geometry, using a basis of linear combination of normal modes for the distortion. Both, a local minimizer based on a Levenberg-Marquardt variant[130,131] and a global optimizer, which uses evolutionary strategies,[132]

can be used for the minimization.[133]

10.5 Results and Discussion

10.5.1 Computational Results

10.5.2 2-Cyanoindole

The structure of 2-cyanoindole in its ground and lowest excited singlet state has been optimized at the SCS-CC2/cc-pVTZ level of theory. Figure 43a shows the ground state structures of 2-cyanoindole along with the inertial axis system and the transition dipole moments for the excitations to the lowest two excited singlet states. Since the molecule has been found to be planar in both electronic states, we classify the normal modes in C_s-symmetry. The Cartesian coordinates of the optimized geometry of 2-cyanoindole in the S_0 and the lowest excited singlet state S_1 are given in the online supporting material.

The zero-point corrected adiabatic excitation of the lowest excited singlet state is calculated to be 35271 cm^{-1} at the SCS-CC2/cc-pVTZ level of theory. The $\pi\pi^*$ excitation to this state is comprised of LUMO $\leftarrow$ HOMO-1 and LUMO+1 $\leftarrow$ HOMO excitations, typical for an L_b-state. The transition dipole moment (TDM) for this transition is shown as red double-headed arrow in Figure 43a. The second electronically excited singlet state, calculated at 38261 cm^{-1} is reached by a nearly pure LUMO $\leftarrow$ HOMO $\pi\pi^*$ excitation, and thus represents the L_a-state. Its TDM is shown as blue double-headed arrow in Figure 43a. The molecular orbitals of 2-cyanoindole and the transitions, associated with the L_a- and L_b-states are shown in the middle part of Figure 44 and are compared to the MOs of the parent indole (left part). Except for the additional molecular orbitals, centered at the cyano group of 2-cyanoindole, the MOs are very similar to those of indole and their energetic order is the same. The right part of the Figure shows the MOs of the water cluster, which will be discussed later.

The 45 vibrational modes of 2-cyanoindole transform like Γ_{ired}=31a$'$ + 14a$''$ in C_s-symmetry. The results of a Franck-Condon simulation of ground and excited state modes, using the optimized geometries and the respective Hessians in the ground and electronically excited state from the SCS-CC2/cc-pVTZ calculations are given in Table S22 of the online supporting material. The last column (Duschinsky) shows how the excited state modes are comprised of ground state modes. The coefficients of the Duschinsky matrix, which gives the transformation between the normal modes of the two states involved in the vibronic transition are shown graphically in Figure 45a. The value of the coefficient is grey coded with a coefficient of 0 depicted by white, those with a coefficient of 1 by black squares and values in between by different gray-shading. For the 2-cyanoindole monomer, matrix elements close to unity on the diagonal are limited to the range of low frequency vibrations (waging motions of the two aromatic rings) and high frequency vibrations (NH and CH stretching vibrations). The assignments of modes to experimentally observed vibrational (vibronic) transitions, given in this table will be discussed later.

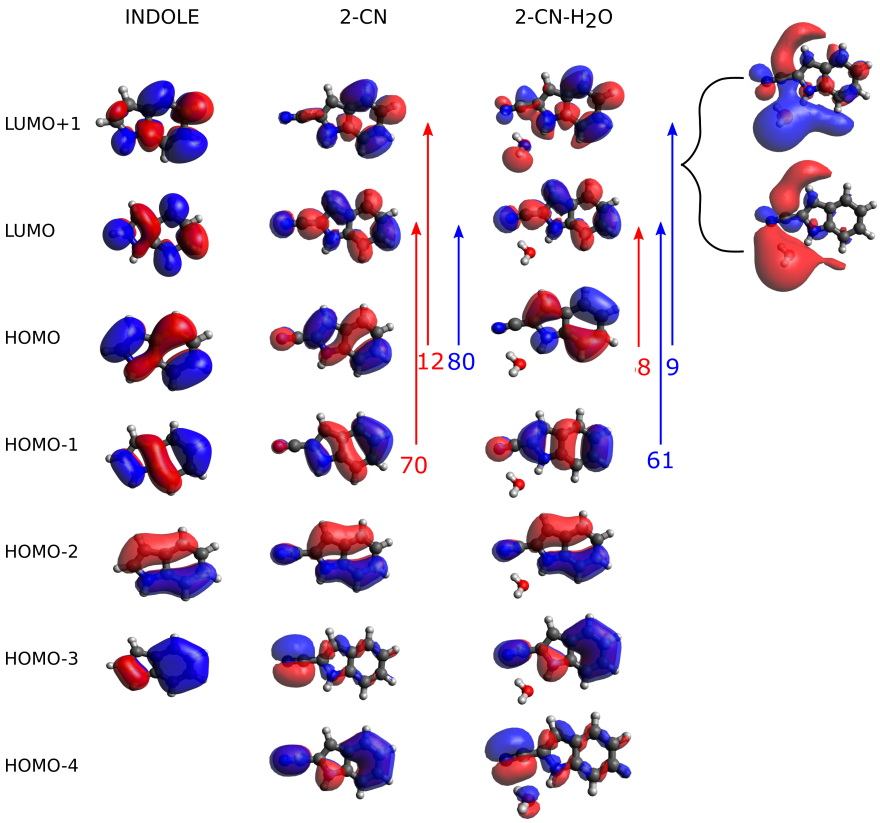

Figure 44: Molecular orbitals of indole, 2-cyanoindole, and the most stable 2-cyanoindole$(H_2O)_1$ cluster, along with the leading excitations to the L_a- and L_b-states. The red arrows show the leading contributions to the first excited singlet states, the blue arrows to the second excited singlet state. The inset shows two Rydberg orbitals, mainly localized at the water moiety in the cluster, which in the water cluster are energetically between the LUMO and LUMO+1 orbitals of the water cluster. They are omitted from counting of the respective frontier orbitals. All molecular orbitals shown here are of π symmetry, with exception of HOMO-3 for 2-cyanoindole and HOMO-4 for 2-cyanoindole$(H_2O)_1$ which are of σ symmetry, and the two Ry* orbitals.

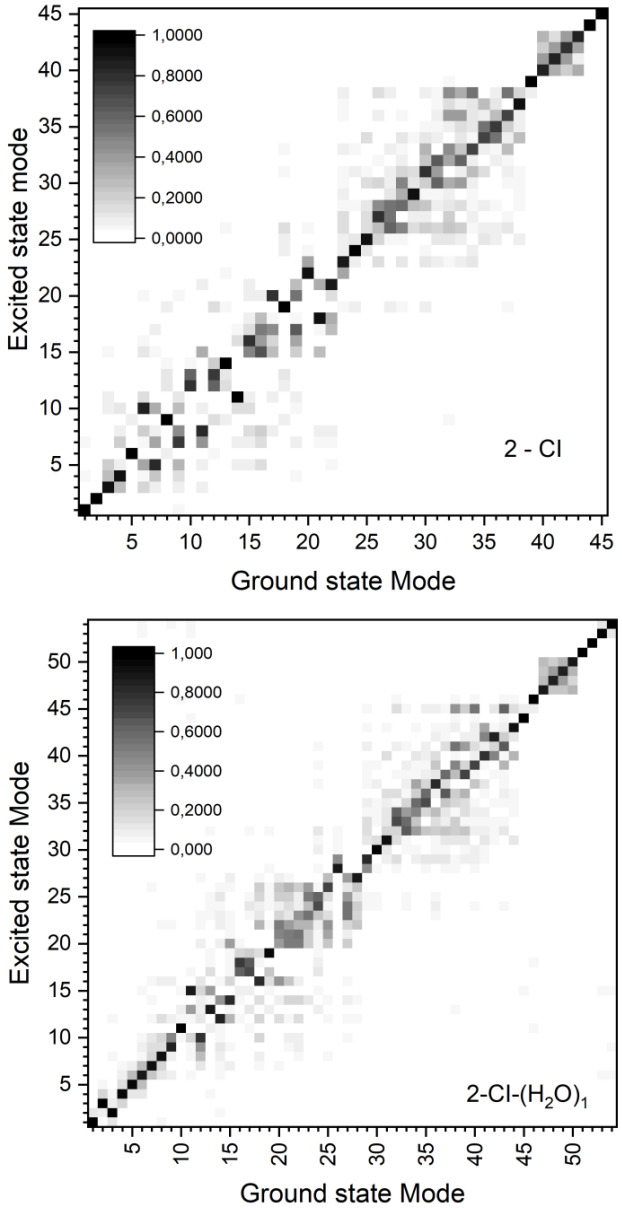

Figure 45: Graphical representation of the Duschinsky matrix for the vibrational ground and excited state modes of 2-cyanoindole and the 2-cyanoindole-$(H_2O)_1$ cluster. A black square indicates a matrix element of 1, a white square of 0, intermediate values of the matrix elements are coded by gray shading.

10.5.3 2-Cyanoindole-$(H_2O)_1$

For the 2-cyanoindole-$(H_2O)_1$ cluster, three different starting geometries for the CC2 structure optimization have been used, which are shown in the online supplementary material (Figure S19 (a), (b), and (c)). The first is a C_s-symmetric *trans*-linear structure, in which the water moiety is linearly hydrogen-bound to the NH group of the pyrrole ring, like in the indole-water cluster.[167,168] The other two are cyclic structures, with a binding motif that is similar to that of benzonitrile-water.[169,170] In one, the water is bound at the NH-side of the pyrrole ring, in the other at the CH-side. Of these three starting structures, only the two cyclic structures converged to stable minima, which are shown in Figure 43 (b) and (c). The *trans*-linear structure, (shown in Figure S19 (a)) converged to the most stable cyclic conformer. With a constraint to C_s symmetry during the optimization of the *trans*-linear structure S19 (a), a first order saddle point is reached with one imaginary frequency. The respective coordinate represents the out-of-plane rotation of the water moiety about the inertial a-axis of water. Distortion along this coordinate, using the screwer tool from the TURBOMOLE library, leads again to the most stable cyclic conformer S19 (b). Both stable cyclic water clusters have C_1-symmetry. The binding energies of the different 2-cyanoindole-$(H_2O)_1$ clusters including ZPE and BSSE corrections in the ground and the lowest two excited singlet states are compiled in Table 13. The by far most stable ground state structure is the cyclic NH bound structure (b) with a stabilization energy of 25.18 kJ/mole compared to 9.39 kJ/mole for the cyclic CH bound structure (c).

For 3-cyanoindole-$(H_2O)_1$,[138,140] and 5-cyanoindole-$(H_2O)_1$[152] the *trans*-linear binding motif of the water to the pyrrolic NH group has been found in *ab initio* calculations to be the most stable one. We therefore added the respective stabilization energies of the *trans*-linear conformer (a) to Table 13, although this conformer does not represent a minimum at the potential energy surface, but a first order transition state, instead. A value of -22.90 kJ/mole is found, which is considerably less stable than the respective 3-cyanoindole-$(H_2O)_1$ cluster (28.46 kJ/mole).

The excitation to the lowest excited singlet state of the most stable conformer (b) mainly has LUMO $\leftarrow$ HOMO character (red arrows), which seems to be typical for an L_a-state excitation. The energetically second state is mainly comprised of LUMO $\leftarrow$ HOMO-1 and LUMO+1 $\leftarrow$ HOMO excitations (blue arrows), an indication for an L_b state. Thus, the L_a- and L_b-states seem to change their energetic positions upon water cluster formation, already for the first water molecule, attached to 2-cyanoindole. Closer inspection of the MOs however, reveals that water cluster formation changes the energetic order of the frontier orbitals and mixes some of them. HOMO-3 and HOMO-4 change their relative position, because the water dipole pulls the MOs localized mainly at the cyano group down. More importantly for the assignment of the nature of the excited state, also HOMO and HOMO-1 change their order between the monomer and its water cluster. Additionally to the exchange of the MOs they start to mix, i.e. the HOMO and HOMO-1 in the water cluster are comprised of the respective orbitals in the monomer (cf. middle and right columns of Figure 44). What can be seen here is the gradual transition from the L_b state to the L_a-state in solvation. The

Table 13: CC2/cc-pVTZ calculated binding energies in kJ/mole of the most stable 2-cyanoindole-$(H_2O)_1$ clusters. Stabilization energies contain zero-point energy and correction due to the counterpoise computed BSSE. Additionally, the adiabatic excitation energies in cm^{-1} (eV) for excitation from the ground state to the respective state, including ZPE correction are given in the table.

	2-cyanoindole-$(H_2O)_1$					
	Conformer (a)*		Conformer (b)		Conformer (c)	
	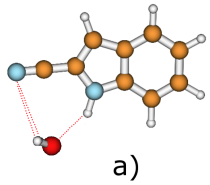		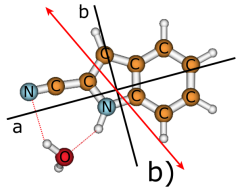		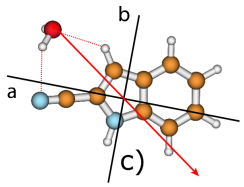	
	E_{bind}/kJ mol^{-1}	ΔE_{ad}/cm^{-1} (eV)	E_{bind}/kJ mol^{-1}	ΔE_{ad}/cm^{-1} (eV)	E_{bind}/kJ mol^{-1}	ΔE_{ad}/cm^{-1} (eV)
S_0	-22.90	-	-25.18	-	-9.39	-
S_1	-10.75	34915 (4.33)	-17.83	34839 (4.32)	-0.39	35043 (4.34)
S_2	-57.11	37789 (4.69)	-29.11	37747 (4.68)	-9.73	38073 (4.72)

*Conformer (a) is no minimum structure, but a first order saddle point instead.

first water molecule is still not sufficient to draw the L_a-state below the L_b. However, the molecular orbitals already reflect the changed electron density due to the proximity of the water dipole.

In the first electronically excited S_1 (L_b) state, both cyclic clusters (b) and (c) are considerably less stable than in the ground state. The second excited singlet state S_2 (L_a) is more stable than the ground state for conformer (b) and has nearly the same stabilization energy than conformer (c), cf. Table 13.

The adiabatic excitation energy of the most stable water cluster (b) amounts to 34839, thus -432 cm^{-1} red-shifted with respect to the monomer at 35271 cm^{-1}. The second stable water cluster (c) has an adiabatic excitation energy of 35043 cm^{-1}, -228 cm^{-1} to the red of the monomer origin.

The 54 vibrational modes of most stable water cluster are compiled in Table S23 of the online supporting material in the same manner as the monomer vibrations in Table S22. The coefficients of the Duschinsky matrix, are compared to those of the monomer in Figure 45. As for the monomer, low and high frequency vibrations are on the diagonal with large coefficients, meaning that the vibrations in the excited state are not mixed. In the medium frequency range, mixing in the water cluster is stronger than in the monomer, i.e. the excited state modes are composed of more ground state modes.

The additional nine vibration modes compared to the monomer can be divided into six intermolecular vibrations at 53.1 cm^{-1} (hydrogen bond out-of-plane waging), 78.4 cm^{-1} (hydrogen bond in-plane bending), 156.2 cm^{-1} (hydrogen bond in-plane NH$\cdots$O stretch), 161.5 cm^{-1} (water torsion), 291.6 cm^{-1} (hydrogen bond water out-of-plane rocking), and 420.8 cm^{-1} (hydrogen bond in-plane OH$\cdots$N stretch) and the three intramolecular vibrational modes of the water moiety, calculated at 3898.8 cm^{-1} (water antisymmetric stretch), 3782.2 cm^{-1} (water symmetric stretch), and 1671.3 cm^{-1} (water bending mode).

10.6 Experimental results and Discussion

10.6.1 Laser induced fluorescence spectrum and single vibronic level fluorescence spectra

The laser induced fluorescence spectrum of 2-cyanoindole, seeded in a helium molecular beam, is shown in Figure 46. The electronic origin of the monomer is found at 33422.6 cm^{-1}. Upon water addition to the seed gas, additional bands form, which are assigned to the water cluster of 2-cyanoindole. Their origin is located at 32984.5 cm^{-1}, i.e. red-shifted by 438.1 cm^{-1} relative to the monomer band. The monomer bands, which have been chosen for excitation in order to obtain the fluorescence emission spectra are marked by asterisks, the cluster band which have been dispersed are marked by crosses.

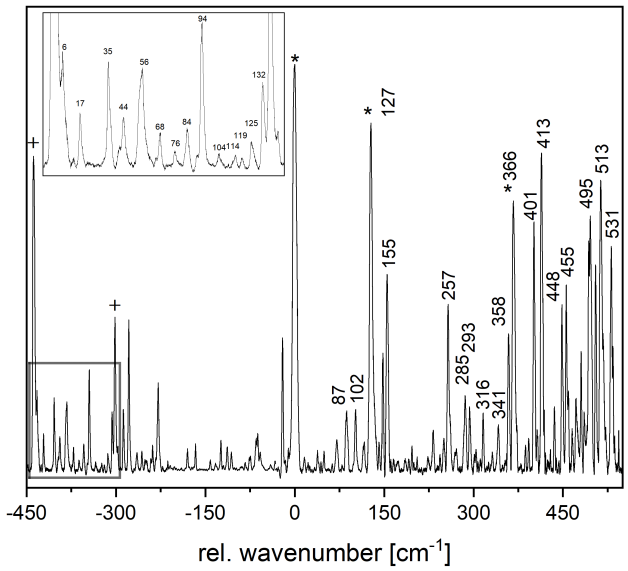

Figure 46: LIF spectrum of jet-cooled 2-cyanoindole. Vibronic bands of the monomer, which have been excited in order to record fluorescence emission spectra, have been marked by an asterisk, those of the 1:1 water cluster by a cross.

2-Cyanoindole monomer

The first band in the monomer LIF spectrum of 2-cyanoindole is found at 33422.6 cm^{-1} and is assigned to the electronic origin (0,0). The following vibronic band at 0,0 + 127 cm^{-1} is assigned to the totally symmetric vibration Q_2. From the Duschinsky coefficient in Table S22 this band corresponds to the Q_2 vibration in the electronic ground state. This vibration can best be described as in-plane N≡C−C< bending vibration of the cyano group. Inspection of the fluorescence spectrum after excitation of 0,0 + 127 cm^{-1}, shown in Figure 47b confirms this assignment. A reasonable assignment for the vibronic band at 155 cm^{-1} is to the overtone of the out-of-plane vibration Q_1, which is calculated at 83 cm^{-1}. In-plane vibration Q_6,

best described as gearing motion of the two rings, strongly coupled to a N≡C−C< bending vibration of the cyano group, which is calculated at 369 cm^{-1}, is observed at 366 in the LIF spectrum of Figure 46. According to Table S22, the strongest propensity is to mode Q_5 in the ground state, calculated at 373 cm^{-1} and observed at 390 cm^{-1} as the strongest band in the fluorescence emission spectrum shown in Figure 47c. Mode Q_9, similar to Wilson's mode 16b of *ortho*-disubstituted benzene derivatives,[134] calculated at 420 cm^{-1} is observed at 413 cm^{-1}. Other assignments of vibrational S_0 and vibronic S_1 bands, are compiled in Table S22.

2-Cyanoindole(H_2O)$_1$

To the red of the monomer spectrum additional bands appear upon water addition to the seed gas, forming the molecular beam. We assign the band at 32984.5 cm^{-1} to the electronic origin of the 1:1 water cluster of 2-cyanoindole. The number of vibronic bands, which are assigned to the water cluster spectrum is by far higher than expected from the normal mode analysis, shown in Table S23. This multitude of bands cannot be explained by combination bands or overtones, since at least two of the vibronic bands at 17 and 35 cm^{-1} shown in the inset of Figure 46 are well below the lowest computed vibronic transition at 48.5 cm^{-1} an cannot easily be assigned to a harmonic intermolecular vibration of the cluster. Thus, the possibility of a large amplitude motion of the water moiety in the cluster has to be considered. Two very similar systems can serve as guideline. The benzonitrile-water cluster, which has been extensively studied in the group of Pratt,[171] and the 3-cyanoindole-water cluster, which was investigated in our group.[138] The information on the tunneling motion in the current system is quite limited. The most important piece of information on the nature of the tunneling motion, namely the tunneling splitting of the $0^+/0^+$ and $0^-/^-$-subtorsional components is not available, since the excited state lifetime of the binary water cluster of 2-cyanoindole is so short that the rovibronic structure cannot be resolved. The reason for this short lifetime has been studied in detail in a recent contribution from our group.[8] Schäfer *et al.* attributed the splitting in the microwave and UV spectra of benzonitrile to a tunneling motion of the water moiety, best to be described as rotation of the water molecule about its inertial b-axis, which is nearly parallel to the a-axis of the cluster. They determined a ground state barrier of 440 cm^{-1}, which stayed virtually the same after electronic excitation. The binding motif of benzonitrile-water is closely related to that of 2-cyanoindole-water: the water moiety is attached to the nitrogen atom of the CN group and to a hydrogen atom of the aromatic ring forming a ring structure with two non-linear hydrogen bonds. Apart from the CN binding site, 2-cyanoindole offers two second binding sites: one adjacent CH bond and on the other side of the CN group an NH group. Our quantum chemical calculations (section 10.5.3) showed, that the hydrogen bond structure, which involves the NH group is considerably more stable. Since the effect of electronic excitation on the NH bond in the pyrrole moiety is larger than on the CH group in benzene, it can be expected that the barrier in 2-cyanoindole-water will show a larger change upon electronic excitation than in benzonitrile-water. A large amplitude motion in agreement with the findings in

benzonitrile-water and 2-cyanoindole-water is a torsion of the water moiety along an axis which does not coincide with one of the inertial axes of the cluster. Instead a more complicated path has to be considered which might involve a much smaller torsional constant than for a plain b-axis torsion. With a ground state barrier in the order of 400 to 500 cm^{-1} the difference between the 0^+ and the 0^- torsional component will not be resolvable with our resolution. Assuming a torsional constant F of 8 cm^{-1} and an excited state barrier of 40 cm^{-1}, two the torsional transitions $0^+/1^+$ and $0^-/1^-$ are calculated to be 17 and 35 cm^{-1} in agreement with the observation. The spectral information about the torsional motion is by no way sufficient to have much confidence in the quoted absolute values for torsional constant and barrier. They merely serve as proof, that a large amplitude vibration might indeed be responsible for the low frequency bands at 17 and 35 cm^{-1}. Further investigations, including isotopologues of the cluster, which might increase the life time, so that rotationally resolved spectra can be recorded, are necessary.

Comparing the following vibrations to the results of the normal mode analysis, given in Table S23 a straightforward assignment, based on the frequencies can be given for the bands, which are used for excitation in order to record the emission spectra. The band at 44 cm^{-1} is assigned to mode Q_1, which is the hydrogen bond out-of-plane waging mode. At 84 cm^{-1} mode Q_2, the hydrogen bond in-plane bending mode is observed. Mode Q_4, which is the equivalent to Q_2 in the monomer, which has been assigned to the in-plane N≡C−C< bending vibration of the cyano group, is observed at 137 cm^{-1}. Other bands in the laser induced fluorescence spectrum were too weak to obtain fluorescence emission spectra and are not discussed here.

10.6.2 Franck-Condon fits of the fluorescence emission spectra

2-Cyanoindole monomer

Figure 47 shows the fluorescence emission spectra after excitation of the vibrationless origin band 0,0 of the monomer at 33422.6 cm^{-1} and of the two vibronic bands at 0,0 + 127 cm^{-1}, 0,0 + 366 cm^{-1} along with the simulated spectra, using the best FC fits. These fits have been performed though a simultaneous fit of the 48 intensities of emission bands, given in Table S26 of the online supporting material and the six rotational constant changes of the normal and the N-D substituted isotopologue of 2-cyanoindole from Ref.[8]

Good agreement between the calculated and experimental intensities in all three emission spectra has been obtained, upon distortion of the excited state structure along the coordinates defined in Table S24 of the online supporting material. The resulting geometry changes in terms of internal coordinates from the SCS-CC2/cc-pVTZ calculated structures, and from the Franck-Condon fits are compared in Table 14 and in Figure 49. Figure 47 compares the experimental and the fitted spectra. While they are generally in good agreement, the intensities of some bands are higher in the fit than in the experiment. Mode Q_5, which represents the in-plane bending gearing motion of the two rings is found at 375 cm^{-1} and its overtone at 745 cm^{-1}. The intensities of both bands are overestimated in the fit. The same holds for the ring breathing mode Q_{18} at 842 cm^{-1}. The

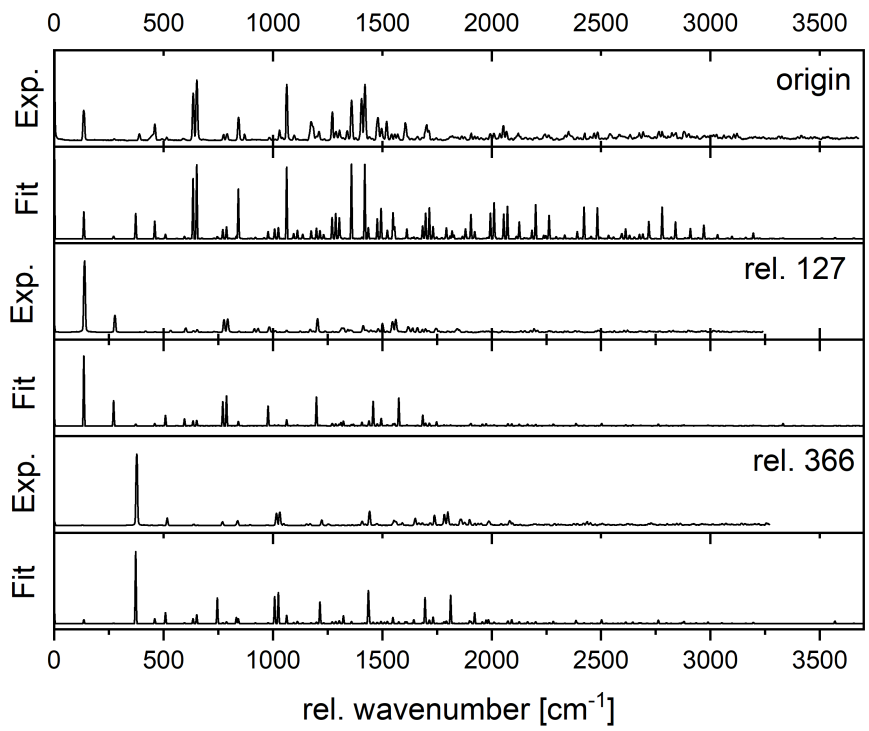

Figure 47: Experimental and fitted fluorescence emission spectra of the electronic origin 0,0 and of two vibronic bands of 2-cyanoindole at 0,0 + 127, 0,0 + 366 cm^{-1}, which have been used in the fit of the geometry changes.

intensity of mode Q_{26}, an in-plane H-C waging mode at 1173 cm^{-1} shows a rather large deviation between fit and experiment, like mode Q_{31} at 1359 cm^{-1}, which represents an in-plane C-H bending vibration. Above 1700 cm^{-1} the intensities of all modes in the experimental spectrum sharply drop, why these modes were not included in the fit.

The general agreement between the computed and the experimentally determined structures is quite good. Although numerical differences exist, there is an overall agreement in the size and the signs of the bond length changes. A general ring opening in both rings is observed with the exception of the bonds, adjacent to the bridge between the pyrrole and the benzene ring. This (symmetric) ring opening upon electronic excitation is typical for excitations to L_b-states in indole derivatives.[9,107,138,158,159,164,172]

2-Cyanoindole(H_2O)$_1$

Figure 48 shows the fluorescence emission spectra of the 2-cyanoindole(H_2O)$_1$ cluster after excitation of the vibrationless origin 0,0 and the vibronic band at 0,0 + 137 cm^{-1}. Unfortunately, no rotationally resolved spectrum could be recorded, due to the short excited state life time, thus no experimental rotational constant changes are available and the fit of the geometry changes has to rely solely on the intensities of the 40 emission bands included in the FC fit. In the water cluster origin spectrum no large differences between experiment and fit occur. The deviations of the emission intensities after excitation of the vibronic band at 0,0+137 cm^{-1} are mainly in mode Q_5

Table 14: Comparison of the bond length changes from SCS-CC2cc-pVTZ calculations and Franck-Condon fits of 2-cyanoindole upon electronic excitation.

State	bond length S_0		bond length S_1		S_1-S_0	
Method	SCS-CC2	FCFit	SCS-CC2	FCFit	SCS-CC2	FCFit
N1-C2	138.5	138.5	144.2	143.7	+5.7	+5.2
C2-C3	138.1	138.1	139.8	140.6	+1.7	+2.5
C3-C9	142.9	142.9	142.2	142.5	-0.7	-0.4
C9-C4	140.9	140.9	140.0	140.7	-0.9	-0.3
C4-C5	138.5	138.5	143.8	143.7	+5.3	+5.2
C5-C6	141.5	141.5	141.5	143.2	± 0	+1.7
C6-C7	138.7	138.7	142.2	144.5	+3.5	+5.8
C7-C8	140.2	140.2	140.6	140.4	+0.4	+0.2
C8-N1	137.6	137.6	135.3	135.4	-2.3	-2.2
N1-H	100.6	100.6	101.0	101.0	+0.3	+0.4
C8-C9	142.0	142.0	147.2	147.9	+5.2	+5.9
C2-C10	142.2	142.2	139.8	137.1	-2.4	-5.1
C10-N2	117.7	117.7	118.6	118.1	+0.9	+0.4

at 154 cm^{-1}, which represents the O-H-C in-plane stretching vibration. The ground state geometry has been distorted along the coordinates defined in Table S25 of the online supporting material. The comparison of the calculated and the FC-fitted geometry changes is given in Figure 49 and in Table 15. As for the monomer, the excitation of the water cluster leads to an L_b-like structure for the excited state.

10.7 Conclusions

The geometry changes of 2-cyanoindole and the binary 2-cyanoindole$(H_2O)_1$ water cluster upon electronic excitation determined from FC fits of fluorescence emission spectra though various vibronic bands show an L_b-like structure for the lowest excited singlet state of monomer and water cluster. Quantum chemical calculations at the SCS-CC2/cc-pVTZ level of theory showed, that the water moiety in the binary water cluster leads to a considerable mixing of frontier orbitals, especially of the HOMO and HOMO-1. Thus, the statement that L_a-states in indoles are due to LUMO $\leftarrow$ HOMO excitation and L_b-states due to a mixture of LUMO-1 $\leftarrow$ HOMO and LUMO $\leftarrow$ HOMO-1 excitations[154,173–175] has no generality. Instead, the frontier MOs have carefully to be compared to those of the parent indole in order to obtain a reliable assignment of excited states. It is well-known that the emitting state in nearly all indole derivatives in polar solvents is the L_a-state. In general the L_a has a larger permanent dipole moment than the L_b-state and is thus stronger stabilized in polar media. The question arises, if this effect is caused by the electric field of the solvent cavity, or if it is due to a direct interaction of the first water molecule(s) at specific binding positions and geometries. Brisker-Klaiman *et al.* discussed non-specific solute-solvent interactions to be responsible for the large fluorescence Stokes shift of indole and its derivatives.[154] Consequently, they used the COnductor-like Screening MOdel (COSMO) to account for the main solute-solvent inter-

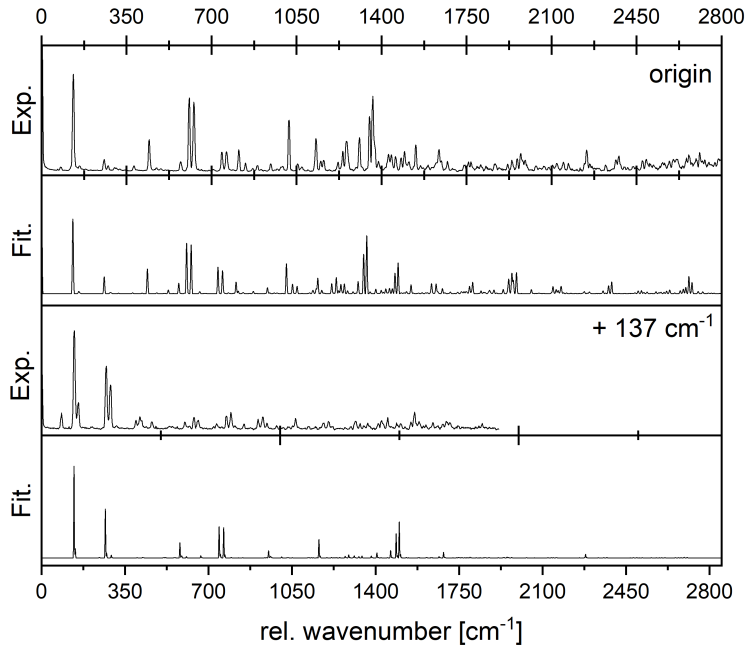

Figure 48: Experimental and fitted fluorescence emission spectra of the electronic origin and of the vibronic band of 2-cyanoindole$(H_2O)_1$ at 0,0 + 137 cm^{-1}, which have been used in the fit of the geometry changes.

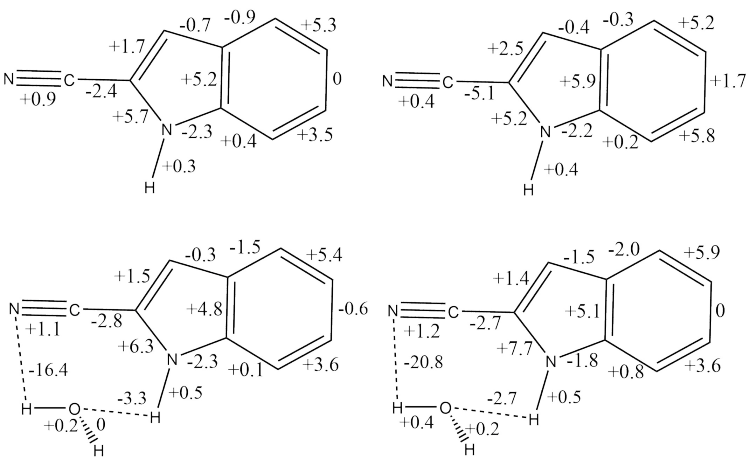

Figure 49: Geometry changes (in pm) upon electronic excitation of 2-cyanoindole (upper row) and 2-cyanoindole$(H_2O)_1$ (lower row). The left column shows the SCS-CC2/cc-pVTZ calculated values, the right column the results of the Franck-Condon fits.

Table 15: Comparison of the bond length changes from SCS-CC2/cc-pVTZ calculations and Franck-Condon fits of 2-cyanoindole(H_2O)$_1$ upon electronic excitation.

State	bond length S_0		bond length S_1		S_1-S_0	
Method	SCS-CC2	FCFit	SCS-CC2	FCFit	SCS-CC2	FCFit
N1-C2	138.3	138.3	144.6	146.0	+6.3	+7.7
C2-C3	138.3	138.3	139.8	139.7	+1.5	+1.4
C3-C9	142.8	142.8	142.5	141.3	-0.3	-1.5
C9-C4	141.0	141.0	139.5	139.0	-1.5	-2.0
C4-C5	138.5	138.5	143.9	144.4	+5.4	+5.9
C5-C6	141.6	141.6	141.0	141.6	-0.6	± 0
C6-C7	138.6	138.6	142.2	142.2	+3.6	+3.6
C7-C8	140.4	140.4	140.5	141.2	+0.1	+0.8
C8-N1	137.2	137.2	134.9	135.4	-2.3	-1.8
N1-H1	101.5	101.5	102.0	102.0	+0.5	+0.5
C8-C9	142.3	142.3	147.1	147.4	+4.8	+5.1
C2-C10	142.2	142.2	139.4	139.5	-2.8	-2.7
C10-N2	117.8	117.8	118.9	119.0	+1.1	+1.2
N2-H2	253.2	253.2	236.8	232.4	-16.4	-20.8
H2-O1	96.5	96.5	96.7	96.9	+0.2	+0.4
O1-H3	96.2	96.2	96.2	96.4	± 0	+0.2
H1-O1	198.5	198.5	195.2	195.8	-3.3	-2.7

actions. In 2-cyanoindole, both geometry changes and orientation of the transition dipole moment, point to the L_b-state as lowest excited singlet state also in the 1:1 water cluster. In this respect, 2-cyanoindole(H_2O)$_1$ is similar to indole(H_2O)$_1$ [168] and to 3-cyanoindole(H_2O)$_1$, [138] in which the lowest excited singlet state has L_b-character for both monomer and binary water cluster. In contrast, tryptamine, [163] 7-azaindole, [158,159] and 3-methylindole [176] switch from L_b- to L_a-character upon 1:1 water cluster formation. Recent electronic Stark measurements and *ab initio* calculations have shown that the permanent dipole moment of 2-cyanoindole in the L_a-state is smaller than in the L_b-state in contrast to nearly all other substituted indoles. Thus, it seems reasonable that water cluster formation does not stabilize the L_a-state more upon electronic excitation. In the light of these studies we suggest to incorporate specific solute-solvent interactions in quantum chemical investigations of solvated indoles.

10.8 Acknowledgements

Financial support of the Deutsche Forschungsgemeinschaft via grant SCHM1043/12-3 is gratefully acknowledged. Computational support and infrastructure was provided by the "Center for Information and Media Technology" (ZIM) at the Heinrich-Heine-University Düsseldorf (Germany).

11 Summary

This work can be categorized into two subject areas due to the two different substance classes that were examined. The first topic is the issue of double methoxy substituted benzenes. Both the ortho- and the meta-substituted dimethoxybenzene were investigated. The measurement method has already been used in previous work[55] and is based on the combination of laser-induced and dispersed fluorescence spectra of the molecules to be investigated with the FC_{FIT} program, established in our working group.[32,100]

This methodology can be improved by using rotational constants of the molecule in the program FC_{FIT} to be investigated by Hebestreit *et al.* and Schneider *et al.*.[8,9,90,91,129] In addition, studying the isotopologues of the molecule can improve the fit results. Therefore the d_6 isotopologues, i.e. the OCD_3-deuterated species, of 1,2-dimethoxybenzene and 1,3-dimethoxybenzene were investigated. Using four dispersed spectra, an ortho-quinoidal distortion of the geometry of 1,2-dimethoxybenzene could be determined. The results of this fit, like the other results achieved in this work, can be supported by *ab initio* calculations.

For 1,3-dimethoxybenzene, or for the two distinguishable rotamers, the asymmetrical A rotamer and the symmetrical B rotamer, a ring opening can be represented by electronic excitation. This runs asymmetrically in the case of the A rotamer and symmetrically in the case of the B rotamer.

The second topic of this work are the singly cyano-substituted indoles. The indoles substituted in the 2- and 4-position were examined. For the indoles the nomenclature of Platt can be used to characterize them. An ^1L_a structure for the lowest electronically excited state could be determined for 4-cyanoindole due to the alternating bond length changes. The bond length changes could also be confirmed by a *natural bond orbital* analysis (NBO analysis).

When investigating 2-cyanoindole, the simple water cluster of this compound, 2-cyanoindole-$(H_2O)_1$, could also be investigated. For both geometry changes after electronic excitation, an L_b-like structure can be established for the lowest electronically excited state.

Both subject areas show that changes in the geometry of molecules can be explained by electronic excitation with a combination of dispersed fluorescence spectroscopy and Franck-Condon analysis. The fit results can be improved by using rotational constants and isotopologe measurements. Furthermore, *ab initio* calculations at a high level are necessary in order to compare the experimentally obtained results with theoretical results and to mutually confirm them.

12 Zusammenfassung

Diese Arbeit lässt sich aufgrund der zwei unterschiedlichen Substanzklassen, welche untersucht wurden, in zwei Themengebiete kategorisieren. Die erste Thematik der zweifach methoxysubstituierten Benzole. Hierbei wurden sowohl das ortho- als auch das meta-substituierte Dimethoxybenzol untersucht. Die Messmethodik wurde schon in vergangenen Arbeiten[55] genutzt und basiert auf der Kombination von Laserinduzierten und dispergierten Fluoreszenzspektren der zu untersuchenden Moleküle, mit dem in unserer Arbeitsgruppe etablierten Programm FC_{FIT}.[32,100]
Eine Verbesserung dieser Methodik lässt sich durch das heranziehen von Rotationskonstanten, des zu untersuchenden Moleküls, für das Programm FC_{FIT}, aus den Arbeiten von Hebestreit *et. al.* und Schneider *et. al.*, erzielen.[8,9,90,91,129] Des weiteren kann die Untersuchung der Isotopologe des Moleküls zu einer Verbesserung der Fitergebnisse führen. Daher wurden für das 1,2-Dimethoxybenzol und für das 1,3-Dimethoxybenzol die d_6-Isotopologe, dass heißt die OCD_3-deuterierten Spezies untersucht. Hierbei konnte unter Verwendung von vier dispergierten Spektren eine ortho-chinoidale Verzerrung der Geometrie festgestellt werden. Die Ergebnisse dieses Fits können, wie auch die restlichen in dieser Arbeit erreichten Ergebnisse, durch *ab initio* Rechnungen gestützt werden. Für das 1,3-Dimethoxybenzol, beziehungsweise für die beiden unterscheidbaren Rotamere, das asymmetrische A-Rotamer und das symmetrische B-Rotamer, lässt sich eine Ringöffnung durch elektronische Anregung darstellen. Diese läuft asymmetrisch im Fall des A-Rotamers und symmetrisch im Fall des B-Rotamers ab.
Das zweite Themengebiet dieser Arbeit sind die einfach Cyano-substituierten Indole. Es wurden das an zweiten und an der vierten Position substituierte Indol untersucht. Für die Indole lässt sich die Nomenklatur von Platt für angeregte Zustände heranziehen, um diese zu charakterisieren. Dabei konnte für das 4-Cyanoindol, aufgrund der alternierenden Bindungslängenänderungen, eine ^1L_a-Struktur für den niedrigsten elektronisch angeregten Zustand ermittelt werden. Die Bindungslängenänderungen konnten des weiteren durch eine *natural bond orbital* Analyse (NBO-Analyse) bestätigt werden.
Bei der Untersuchung des 2-Cyanoindols, konnte auch der einfache Wassercluster dieser Verbindung, 2-Cyanoindol-(H_2O), untersucht werden. Für beide Geometrieänderungen nach elektronischer Anregung, lässt sich eine L_b-artige Struktur für den niedrigsten elektronisch angeregten Zustand etablieren.
Beide Themengebiete zeigen, dass Geometrieänderungen von Molekülen durch elektronische Anregung mit einer Kombination von dispergierter Fluoreszenzspektroskopie und Franck-Condon-Analyse aufgeklärt werden können. Dabei kann man durch die Verwendung von Rotationskonstanten und Isotopologenmessungen die Fitergebnisse verbessern. Des weiteren sind *ab initio* Rechnungen auf hohem Niveau notwendig, um die experimentell erlangten Ergebnisse mit theoretischen Ergebnissen zu vergleichen und wechselseitig zu bestätigen.

13 References

References

[1] N. I. of Standards and Technology, Retrieved 2020-08-20.

[2] B. Ferguson and X.-C. Zhang, *Nat Mater*, 2002, **1(1)**, 26–33.

[3] P. Siegel, *MTT*, 2002, 910–928.

[4] B. Williams, *Nature Photonics*, 2007, **1**, 517–525.

[5] P. van Amersfoort, J. B. R.J. Bakker, R. v. B. R.W.B. Best, P. Delmee, B. Faatz, C. van der Geer, D. Jaroszynski, P. Manintveld, W. Mastop, B. Meddens, A. van der Meer, J. Nijman, D. Oepts, J. Pluygers, M. van der Wiel, W. Gillespie, P. Martin, M. Kimmitt, C. Pidgeon, M. Poole and G. Saxon, *Nucl Instrum Meth A*, 1992, **318**, 42–46.

[6] M.-L. Hebestreit, M. S. Christian Henrichs, M. Wilke, W. L. Meerts, D. Krügler and M. Schmitt, *J. Mol. Struct.*, 2019, **1184**, 139–145.

[7] J. R. Platt, *J. Chem. Phys.*, 1949, **17(5)**, 484–495.

[8] M.-L. Hebestreit, H. Lartian, R. Kühnemuth, W. L. Meerts and M. Schmitt, *Phys. Chem. Chem. Phys.*, 2020, submitted.

[9] M.-L. Hebestreit, M. Schneider, H. Lartian, V. Betz, M. Heinrich, M. Lindic, M. Y. Choi and M. Schmitt, *Phys. Chem. Chem. Phys.*, 2019, **21**, 14766–14774.

[10] W. Demtröder, *Laserspektroskopie 1*, Springer Spektrum, 2014, vol. 6. Auflage.

[11] A. Jablonski, *Nature*, 1933, **131**, 839–840.

[12] G. G. Stokes, *Phil. Trans. R. Soc.*, 1852, **142**, 463–562.

[13] P. Klan and J. Wirz, *Photochemistry of Organic Compounds.*, Wiley-VCH, 2009, vol. Postgraduate Chemistry Series.

[14] E. Condon, *Phys. Rev.*, 1926, **28**, 1182–1201.

[15] E. U. Condon, *Phys. Rev.*, 1928, **32**, 858–872.

[16] J. Franck and E. G. Dymond, *Trans. Faraday Soc.*, 1926, **21**, 536–542.

[17] M. Born and R. Oppenheimer, *Annalen der Physik*, 1927, **389(20)**, 457–484.

[18] P. Atkins, *Physikalische Chemie*, Wiley-VCH Verlag GmbH, 2001, vol. 3rd edition.

[19] G. Weber, *Biochem. J.*, 1960, 335–345.

[20] F. Hund, *Z. Phys.*, 1925, **33**, 345–371.

[21] R. S. Mulliken, *Phys. Rev.*, 1932, **41**, 49–71.

[22] J. Lennard-Jones, *Trans. Faraday Soc.*, 1929, **25**, 668–686.

[23] P.-O. Löwdin, *Phys. Rev.*, 1956, **101**, 1730–1739.

[24] F. Weinhold and C. R. Landis, *Chem. Educ. Res. Pract. Eur.*, 2001, **2**, 91–104.

[25] E. D. Glendening, J. K. Badenhoop, A. E. Reed, J. E. Carpenter, J. A. Bohmann, C. M. Morales, P. Karafiloglou, C. R. Landis and F. Weinhold, *NBO version 7.0*, Theoretical Chemistry Institute, University of Wisconsin, Madison, WI, 2018.

[26] E. D. Glendening, C. R. Landis and F. Weinhold, *WIREs Comput Mol Sci.*, 2012, **2**, 1–42.

[27] L. Pauling, *J. Am. Chem. Soc.*, 1947, **69**, 542–553.

[28] S. J. Chalk, *IUPAC. Compendium of Chemical Terminology, 2nd ed. (the "Gold Book")*, Blackwell Scientific Publications, 2019.

[29] A. J. Bridgeman, G. Cavigliasso, L. R. Ireland and J. Rothery, *J. Chem. Soc., Dalton Trans.*, 2001, 2095–2108.

[30] *TURBOMOLE V6.6 2014, a development of University of Karlsruhe and Forschungszentrum Karlsruhe GmbH, 1989-2007, TURBOMOLE GmbH, since 2007; available from* `http://www.turbomole.com`.

[31] *TmoleX V4.5.3, 2020, a development of COSMOlogic GmbH Co. KG, 2010-2020 COSMOlogic GmbH Co. KG; available from* `http://www.cosmologic.com`.

[32] D. Spangenberg, P. Imhof and K. Kleinermanns, *Phys. Chem. Chem. Phys.*, 2003, **5**, 2505–2514.

[33] C. J. Cramer, *Essentials of Computational Chemistry: Theories and Models*, Wiley, 2004.

[34] J. C. Slater, *Phys. Rev.*, 1929, **34**, 1293–1322.

[35] F. Jensen, *Introduction to Computational Chemistry*, Wiley, 2017.

[36] E. G. Lewars, *Computational Chemistry, Introduction to the Theory and Applications of Molecular and Quantum Mechanics*, Springer, 2016.

[37] E. R. Davidson and D. Feller, *Chemical Reviews*, 1986, **86(4)**, 681–696.

[38] J. M. L. Pecourt, J. Peon and B. Kohler, *J. Am. Chem. Soc.*, 2001, **123**, 10370–10378.

[39] P. Atkins and R. Friedman, *Molecular Quantum Mechanics*, Oxford University Press, 2011.

[40] O. Vahtras, J. Almlöf and M. W. Feyereisen, *Chem. Phys. Lett.*, 1993, **213**, 514–518.

[41] F. Weigend and M. Häser, *Theor. Chem. Acc.*, 1997, **97**, 331.

[42] S. Grimme, *J. Chem. Phys.*, 2003, **118(20)**, 9095–9102.

[43] C. Hättig and F. Weigend, *J. Chem. Phys.*, 2000, **113**, 5154–5161.

[44] A. Hellweg, S. Grün and C. Hättig, *Phys. Chem. Chem. Phys.*, 2008, **10**, 1159–1169.

[45] C. Hättig, *J. Chem. Phys.*, 2003, **118(17)**, 7751–7761.

[46] C. Hättig and A. Köhn, *J. Chem. Phys.*, 2002, **117**, 6939–69510.

[47] J. W. Ochterski, *Vibrational Analysis in Gaussian*, Gaussian inc. white paper, 1999.

[48] T. E. Sharp and H. M. Rosenstock, *J. Chem. Phys.*, 1964, **41**, 3453–3463.

[49] R. J. LeRoy, *J. Mol. Spec.*, 1998, **192**, 237–238.

[50] G. M. Sando and K. G. J. Spears, *J. Chem. Phys. A*, 2001, **105**, 5326.

[51] E. V. Doktorov, I. A. Malkin and V. I. Man'ko, *J. Mol. Spec.*, 1975, **56**, 1–20.

[52] E. V. Doktorov, I. A. Malkin and V. I. Man'ko, *J. Mol. Spec.*, 1977, **64**, 302–326.

[53] S. Schumm, M. Gerhards and K. Kleinermanns, *J. Phys. Chem. A*, 2000, **104**, 10648.

[54] S. Schumm, *Ph.D. thesis*, Heinrich Heine-Universität, Düsseldorf, 1998.

[55] F. O. B. Stuhlmann, *Ph.D. thesis*, Heinrich-Heine-Universität Düsseldorf, Düsseldorf, 2014.

[56] C. Henrichs, *Hochauflösende elektronische Spektroskopie von 1-Phenylethinylnaphthalin*, 2016.

[57] Lambda Physik GmbH, Göttingen, Deutschland, *Dye Laser FL 3001/2 Instruction Manual*.

[58] M. Herman, R. Georges, M. Hepp and D. Hurtmans, *International Reviews in Physical Chemistry*, 2000, **19(2)**, 277–325.

[59] E. Hering, K. Bressler and J. Gutekunst, *Elektronik für Ingenieure und Naturwissenschaftler*, Springer Vieweg, 2017, vol. 7. Auflage.

[60] J.-U. Grabow and W. Caminati, in *Microwave Spectroscopy*, ed. J. Laane, Elsevier, Amsterdam, 2009, pp. 383–552.

[61] I. Hargittai, in *Gas-Phase Electron Diffraction for Molecular Structure Determination*, ed. T. E. Weirich, J. L. Lábár and X. Zou, Wiley-Interscience, Dordrecht, 2006, pp. 197–206.

[62] H. Dachs, *Neutron Diffraction*, Springer Berlin Heidelberg, 2011.

[63] H. R. Powell, *Annu. Rep. Prog. Chem., Sect. C: Phys. Chem.*, 2013, **109**, 240–265.

[64] S. T. Park, A. Gahlmann, Y. He, J. S. Feenstra and A. H. Zewail, *angi*, 2008, **47**, 9496 –9499.

[65] P. M. Felker, *J. Phys. Chem.*, 1992, **96**, 7844–7857.

[66] C. Riehn, *Chem. Phys.*, 2002, **297**, 283.

[67] W. A. Majewski and W. L. Meerts, *J. Mol. Spectrosc.*, 1984, **104**, 271–281.

[68] M. Schmitt, M. Böhm, C. Ratzer, C. Vu, I. Kalkman and W. L. Meerts, *J. Am. Chem. Soc.*, 2005, **127**, 10356–10364.

[69] W. L. Meerts and M. Schmitt, *Int. Rev. Phys. Chem.*, 2006, **25**, 353–406.

[70] J. Kraitchman, *Am. J. Phys.*, 1953, **21**, 17.

[71] C. Costain, *J. Chem. Phys.*, 1958, **29**, 864.

[72] J. Franck, *Trans. Faraday Soc.*, 1926, **21**, 536–542.

[73] E. Condon, *pr*, 1926, **28**, 1182–1201.

[74] M. Born and R. Oppenheimer, *Ann. Phys.*, 1927, **4**, 457–484.

[75] F. Duschinsky, *Acta Physicochimica U.R.S.S.*, 1937, **7**, 551–577.

[76] R. Berger, C. Fischer and M. Klessinger, *J. Phys. Chem. A*, 1998, **102**, 7157–7167.

[77] M. Böhm, J. Tatchen, D. Krügler, K. Kleinermanns, M. G. D. Nix, T. A. LeGreve, T. S. Zwier and M. Schmitt, *J. Phys. Chem. A*, 2009, **113**, 2456–2466.

[78] R. Brause, D. Krügler, M. Schmitt, K. Kleinermanns, A. Nakajima and T. A. Miller, *J. Chem. Phys.*, 2005, **123**, 224311.

[79] B. Stuhlmann, A. Gräßle and M. Schmitt, *Phys. Chem. Chem. Phys.*, 2014, **16**, 899–905.

[80] F. Gmerek, B. Stuhlmann, L. Alvarez-Valtierra, D. W. Pratt and M. Schmitt, *J. Chem. Phys.*, 2016, **144**, 084304.

[81] F. Gmerek, B. Stuhlmann, E. Pehlivanovic and M. Schmitt, *J. Mol. Struct.*, 2017, **1143**, 265–273.

[82] G. M. Anderson, P. A. Kollman, L. N. Domelsmith and K. N. Houk, *jacs*, 1979, **101**, 2344–2352.

[83] A. L. Vokin and V. K. Turchaninov, *Russian Chemical Bulletin*, 1995, **44**, 2261–2264.

[84] M. Makriyannis and S. Fesik, *jacs*, 1982, **104**, 6462.

[85] J. T. Yi, J. W. Ribblett and D. W. Pratt, *J. Phys. Chem. A*, 2011, **109**, 9456–9464.

[86] M. Onda, A. Toda, S. Mori and I. Yamaguchi, *J. Mol. Struct.*, 1986, **144**, 47–51.

[87] A. Suvitha, S. Periandy and P. Gayathri, *Spectrochim. Acta A*, 2015, **138**, 357–369.

[88] J.-H. Huang, W.-B. Tzeng and K.-L. Huang, *Chinese J. Chem.*, 2008, **26**, 51–54.

[89] S. C. Yang, S. W. Huang and W. B. Tzeng, *J. Phys. Chem. A*, 2010, **114**, 11144–11152.

[90] M. Schneider, M. Wilke, M.-L. Hebestreit, C. Henrichs, W. L. Meerts and M. Schmitt, *cpc*, 2018, **19**, 307–318.

[91] M.-L. Hebestreit, C. Henrichs, M. Schneider, M. Wilke, W. L. Meerts, D. Krügler and M. Schmitt:, *jmst*, 2019, **1184**, 139–145.

[92] R. Ahlrichs, M. Bär, M. Häser, H. Horn and C. Kölmel, *Chem. Phys. Lett.*, 1989, **162**, 165–169.

[93] J. T. H. Dunning, *J. Chem. Phys.*, 1989, **90**, 1007–1023.

[94] C. Hättig and F. Weigend, *J. Chem. Phys.*, 2000, **113**, 5154–5161.

[95] C. Hättig and A. Köhn, *J. Chem. Phys.*, 2002, **117**, 6939–6951.

[96] C. Hättig, *J. Chem. Phys.*, 2002, **118**, 7751–7761.

[97] P. Deglmann, F. Furche and R. Ahlrichs, *Chem. Phys. Lett.*, 2002, **362**, 511–518.

[98] *TURBOMOLE V6.3 2012, a development of University of Karlsruhe and Forschungszentrum Karlsruhe GmbH, 1989-2007, TURBOMOLE GmbH, since 2007; available from* `http://www.turbomole.com`.

[99] A. E. Reed, R. B. Weinstock and F. Weinhold, *J. Chem. Phys.*, 1985, **83**, 735–746.

[100] R. Brause, M. Schmitt, D. Spangenberg and K. Kleinermanns, *Mol. Phys.*, 2004, **102**, 1615–1623.

[101] M. Schmitt, U. Henrichs, H. Müller and K. Kleinermanns, *J. Chem. Phys.*, 1995, **103**, 9918–9928.

[102] W. Roth, C. Jacoby, A. Westphal and M. Schmitt, *J. Phys. Chem. A*, 1998, **102**, 3048–3059.

[103] M. Dierksen and S. Grimme, *J. Chem. Phys.*, 2004, **120**, 3544–3554.

[104] R. F. Theisen, L. Huang, T. Fleetham, J. B. Adams and J. Li, *J. Chem. Phys.*, 2015, **142**, 094310.

[105] I. Pugliesi and K. Müller-Dethlefs, *J. Chem. Phys.*, 2006, **110**, 4657–4667.

[106] J.-L. Chang, *J. Chem. Phys.*, 2008, **128**, 174111.

[107] O. Oeltermann, C. Brand, B. Engels, J. Tatchen and M. Schmitt, *Phys. Chem. Chem. Phys.*, 2012, **14**, 10266–10270.

[108] W. D. Tuttle, A. M. Gardner, A. Andrejeva, D. Kemp, J. C. A. Wakefield and T. G. Wright, *Phys. Chem. Chem. Phys.*, 2018, **344**, 46–60.

[109] E. Wilson, Jr., *Phys. Rev.*, 1934, **45**, 706–714.

[110] G. Varsanyi, *Assignments for Vibrational Spectra of 700 Benzene Derivatives*, Wiley, New York, 1974.

[111] R. S. Mulliken, *J. Chem. Phys.*, 1955, **23**, 1997–2011.

[112] G. Herzberg, *Molecular Spectra and Molecular Structure, III. Electronic Spectra and Electronic Structure of Polyatomic Molecules*, van Nostrand Reinhold Company, New York, 1966.

[113] J. Christoffersen, J. M. Hollas and G. H. Kirby, *Proc. Roy. Soc. A.*, 1968, **307**, 97–110.

[114] C. Ratzer, J. Küpper, D. Spangenberg and M. Schmitt, *Chem. Phys.*, 2002, **283**, 153–169.

[115] S. J. Humphrey and D. W. Pratt, *J. Chem. Phys.*, 1993, **99**, 5078–5086.

[116] J. Küpper, M. Schmitt and K. Kleinermanns, *Phys. Chem. Chem. Phys.*, 2002, **4**, 4634–4639.

[117] H. D. Rudolph, *Struc. Chem.*, 1991, **2**, 581–588.

[118] J. K. G. Watson, *J. Mol. Spec.*, 1973, **48**, 479–502.

[119] J. G. Smith and J. K. G. Watson, *J. Mol. Spec.*, 1978, **69**, 47–52.

[120] J. K. G. Watson, A. Roytburg and W. Ulrich, *J. Mol. Spec.*, 1999, **196**, 102–119.

[121] J. K. G. Watson, *J. Mol. Spec.*, 2001, **207**, 16–24.

[122] J. Demaison, *Mol. Phys.*, 2007, **105**, 3109–3138.

[123] G. Czakó, E. Mátyus and A. G. Császár, *J. Phys. Chem. A*, 2009, **113**, 11665–11678.

[124] J. Demaison and H. Rudolph, *J. Mol. Spec.*, 2002, **215**, 78 – 84.

[125] J. Demaison and N. Vogt, in *Equilibrium Structures from Spectroscopy*, Springer International Publishing, Cham, 2020, pp. 127–166.

[126] B. Stuhlmann, F. Gmerek, D. Krügler and M. Schmitt, *J. Mol. Struct.*, 2014, **1042**, 45–52.

[127] C. Henrichs, M.-L. Hebestreit, D. Krügler and M. Schmitt, *J. Mol. Struct.*, 2020, **1211**, 127855.

[128] P. J. Breen, E. R. Bernstein, H. V. Sector and J. I. Seeman, *J. Am. Chem. Soc.*, 1989, **111**, 1958–1968.

[129] M. Schneider, M. Wilke, M.-L. Hebestreit, J. A. Ruiz-Santoyo, L. Álvarez Valtierra, J. T. Yi, W. L. Meerts, D. W. Pratt and M. Schmitt, *Phys. Chem. Chem. Phys.*, 2017, **19**, 21364–21372.

[130] K. Levenberg, *Q. Appl. Math. Meth.*, 1944, **2**, 164–168.

[131] D. D. Marquardt, *J. Soc. Ind. Appl. Math.*, 1963, **11**, 431–441.

[132] D. Levine, *PGAPack V1.0, PGAPack can be obtained via anonymous ftp from: ftp://ftp.mcs.anl.gov/pub/pgapack/pgapack.tar.Z*, 1996.

[133] M. Schmitt, D. Krügler, M. Böhm, C. Ratzer, V. Bednarska, I. Kalkman and W. L. Meerts, *Phys. Chem. Chem. Phys.*, 2006, **8**, 228–235.

[134] E. B. Wilson, *Phys. Rev.*, 1934, **45**, 706.

[135] L. J. G. W. van Wilderen, H. Brunst, H. Gustmann, J. Wachtveitl, J. Broosc and J. Bredenbeck, *Phys. Chem. Chem. Phys.*, 2018, **20**, 19906–19915.

[136] P. Talukder, S. Chen, B. Roy, P. Yakovchuk, M. M. Spiering, M. P. Alam, M. M. Madathil, C. Bhattacharya, S. J. Benkovic and S. M. Hecht, *Biochem.*, 2015, **54**, 7457–7469.

[137] B. N. Markiewicz, D. Mukherjee, T. Troxler and F. Gai, *J. Phys. Chem. B*, 2016, **210**, 936–944.

[138] M. Schneider, M.-L. Hebestreit, M. M. Lindic, H. Parsian, A. Y. Torres-Boy, L. Álvarez Valtierra, L. Meerts, R. Kühnemuth and M. Schmitt, *Phys. Chem. Chem. Phys.*, 2018, **20**, 23441–23452.

[139] A. Ahn, A. Min, C. J. Moon, J. H. Lee and M. Y. Choi, *Chem. Phys. Lett.*, 2014, **616–617**, 55–60.

[140] A. Min, A. Ahn, C. J. Moon, J. H. Lee, M. Y. Choi and S. K. Kim, *Chem. Phys. Lett.*, 2014, **614**, 263–268.

[141] M. R. Hilaire, D. Mukherjee, T. Troxler and F. Gai, *Chem. Phys. Lett.*, 2017, **685**, 133–138.

[142] C. Brand, B. Happe, O. Oeltermann, M. Wilke and M. Schmitt, *J. Mol. Struct.*, 2013, **1044**, 21–25.

[143] M. R. Hilaire, I. A. Ahmed, C.-W. Lin, H. Jo, W. F. DeGrado and F. Gai, *Proc. Natl. Acad. Sci. USA*, 2017, **114**, 6005–6009.

[144] S. Abou-Hatab and S. Matsika, *J. Phys. Chem. B*, 2019, **123**, 7424–7435.

[145] A. Hellweg, S. Grün and C. Hättig, *Phys. Chem. Chem. Phys.*, 2008, **10**, 1159–1169.

[146] B. T. Darling and D. M. Dennison, *Phys. Rev.*, 1940, **57**, 128–139.

[147] K. B. Wiberg, *Tetrahedron*, 1966, **24**, 1083–1096.

[148] A. J. Bridgeman, G. Cavigliasso, L. R. Ireland and J. Rothery, *J. Chem. Soc., Dalton Trans.*, 2001, 2095–2108.

[149] T. Lu and F. Chen, *J. Comp. Chem.*, 2012, **33**, 580–592.

[150] M. M. Waegele, M. J. Tucker and F. Gai, *Chem. Phys. Lett.*, 2009, **478**, 249–Ð253.

[151] Y. Huang and M. Sulkes, *Chem. Phys. Lett.*, 1996, **254**, 242–248.

[152] A. Min, C. J. Moon, A. Ahn, J. H. Lee, S. K. Kim and M. Y. Choi, *Chem. Phys. Lett.*, 2016, **658**, 63–70.

[153] M. M. Waegele and F. Gai, *J. Phys. Chem. Lett.*, 2010, **1**, 781Ð–786.

[154] D. Brisker-Klaiman and A. Dreuw, *Chem. Phys. Chem.*, 2015, **16**, 1695–1702.

[155] J. R. Platt, *J. Chem. Phys.*, 1949, **17**, 484–495.

[156] J. N. Murrell, *The Theory of the Electronic Spectra of Organic Molecules*, Chapman and Hall, London, 1971.

[157] G. Weber, *Biochem. J.*, 1960, **75**, 335–345.

[158] T. B. C. Vu, I. Kalkman, W. L. Meerts, Y. N. Svartsov, C. Jacoby and M. Schmitt, *J. Chem. Phys.*, 2008, **128**, 214311(1–8).

[159] Y. Svartsov and M. Schmitt, *J. Chem. Phys.*, 2008, **128**, 214310(1–9).

[160] B. Stuhlmann, F. Gmerek, D. Krügler and M. Schmitt, *J. Mol. Struct.*, 2014, **1072**, 45–52.

[161] S. F. Boys and F. Bernardi, *Mol. Phys.*, 1970, **19**, 553–566.

[162] I. Kalkman, C. Brand, T.-B. C. Vu, W. L. Meerts, Y. N. Svartsov, O. Dopfer, X. Tong, K. Müller-Dethlefs, S. Grimme and M. Schmitt, *J. Chem. Phys.*, 2009, **130**, 224303–1–224303–9.

[163] M. Schmitt, R. Brause, C. Marian, S. Salzmann and W. L. Meerts, *J. Chem. Phys.*, 2006, **125**, 124309(1–10).

[164] C. Brand, J. Küpper, D. W. Pratt, W. L. Meerts, D. Krügler, J. Tatchen and M. Schmitt, *Phys. Chem. Chem. Phys.*, 2010, **12**, 4968–4997.

[165] N. O. C. Winter, N. K. Graf, S. Leutwyler and C. Hättig, *Phys. Chem. Chem. Phys.*, 2013, **15**, 6623–6630.

[166] C. Hättig, *Adv. Quant. Chem.*, 2005, **50**, 37–60.

[167] S. Blanco, J. C. Lopez, J. L. Alonso, P. Ottaviani and W. Caminati, *J. Chem. Phys.*, 2003, **119**, 880–886.

[168] T. M. Korter, D. W. Pratt and J. Küpper, *J. Phys. Chem. A*, 1998, **102**, 7211–7216.

[169] S. Melandri, D. Consalvo, W. Caminati and P. G. Favero, *J. Chem. Phys.*, 1999, **111**, 3874–3879.

[170] R. M. Helm, H. P. Vogel, H. J. Neusser, V. Storm, D. Consalvo and H. Dreizler, *Z. Naturforsch.*, 1997, **52**, 655–664.

[171] M. Schäfer, D. Borst, D. W. Pratt and K. Brendel, *Mol. Phys.*, 2002, **100**, 3553–3562.

[172] J. Küpper, D. W. Pratt, W. L. Meerts, C. Brand, J. Tatchen and M. Schmitt, *Phys. Chem. Chem. Phys.*, 2010, **12**, 4980–4988.

[173] B. Albinsson and B. Nordén, *J. Phys. Chem.*, 1992, **96**, 6204.

[174] C. A. Nicolaides and D. Beck, *Excited States in Quantum Chemistry*, D. Reidel Publishing Company, Dordrecht, Holland, 2012.

[175] M. Klessinger and J. Michl, *Excited States and Photochemistry of Organic Molecules*, Wiley-VCH Verlag GmbH, 1995.

[176] K. W. Short and P. R. Callis, *J. Chem. Phys.*, 2000, **113**, 5235–5244.

14 Supporting Material

14.1 Online Supporting Material of Structural changes upon electronic excitation in 1,2-dimethoxybenzene from Franck-Condon fits of the fluorescence emission spectra

Table S1: Fitted factors of the displacements of 1,2-DMB upon electronic excitation along 4 normal modes from the FC fit.

Mode	displacement
Q_{34}	-0.020192 $\pm$ 0.00041826
Q_{20}	-0.21516 $\pm$ 0.05801
Q_{17}	0.026136 $\pm$ 0.00074507
Q_{14}	-0.019464 $\pm$ 0.00048389

Table S2: SCS-CC2/cc-pVTZ calculated optimized S_0 cartesian coordinates of 1,2-DMB (in bohr).

c	-4.23118488	-1.30928450	0.00000000
c	-4.23118488	1.30928450	0.00000000
c	-1.93353744	2.63861219	0.00000000
c	0.35485305	1.34061730	0.00000000
c	0.35485305	-1.34061730	0.00000000
c	-1.93353744	-2.63861219	0.00000000
h	-5.99110837	-2.34896229	0.00000000
h	-5.99110837	2.34896229	0.00000000
h	-1.95965565	4.67872467	0.00000000
o	2.68764248	-2.43677833	0.00000000
h	-1.95965565	-4.67872467	0.00000000
c	2.73032769	-5.12573123	0.00000000
h	1.81392662	-5.88813689	1.68528201
h	1.81392662	-5.88813689	-1.68528201
h	4.71478473	-5.64843456	0.00000000
o	2.68764248	2.43677833	0.00000000
c	2.73032769	5.12573123	0.00000000
h	1.81392662	5.88813689	-1.68528201
h	1.81392662	5.88813689	1.68528201
h	4.71478473	5.64843456	0.00000000

Table S3: SCS-CC2/cc-pVTZ calculated optimized S_1 cartesian coordinates of 1,2-DMB (in bohr).

c	-1.34782560	4.23134156	0.20980073
c	1.34782560	4.23134156	0.20980073
c	2.76812326	1.96742532	0.26208103
c	1.34478967	-0.37522232	0.17047800
c	-1.34478967	-0.37522232	0.17047800
c	-2.76812326	1.96742532	0.26208103
h	-2.32559841	6.02801718	0.19411418
h	2.32559841	6.02801718	0.19411418
h	4.78335010	1.99091575	0.55299571
o	-2.43871467	-2.67961248	-0.10557812
h	-4.78335010	1.99091575	0.55299571
c	-5.13664514	-2.74739871	-0.28586199
h	-6.00395819	-2.08913709	1.46395950
h	-5.79591823	-1.60648308	-1.86879529
h	-5.61062934	-4.71984613	-0.59319376
o	2.43871467	-2.67961248	-0.10557812
c	5.13664514	-2.74739871	-0.28586199
h	5.79591823	-1.60648308	-1.86879529
h	6.00395819	-2.08913709	1.46395950
h	5.61062934	-4.71984613	-0.59319376

Table S4: SCS-CC2/cc-pVTZ calculated isotopic shifts of the 54 normal modes of 1,2-DMB in the ground and first electronically excited states.

	S_0						S_1					
	Calc.			Exp.			Calc.			Exp.		
	h_{10}	d_6	Ratio	h_{10}	d_6	Ratio	h_{10}	d_6	Ratio	h_{10}	d_6	Ratio
$Q_1(S_0)$	89	80	0,90				57	52	0,91			
$Q_2(S_0)$	112	105	0,94				76	70	0,92			
$Q_3(S_0)$	172	154	0,90				90	83	0,92			
$Q_4(S_0)$	197	181	0,92	190	177	0,93	118	109	0,92	118	106	0,89
$Q_5(S_0)$	253	189	0,75				193	155	0,80	197	160	0,81
$Q_6(S_0)$	285	225	0,79				200	157	0,79	223	173	0,77
$Q_7(S_0)$	286	262	0,92				205	179	0,87	230	197	0,85
$Q_8(S_0)$	330	317	0,96				280	257	0,92	283	265	0,93
$Q_9(S_0)$	379	347	0,92	372	339	0,91	314	311	0,99	318	311	0,98
$Q_{10}(S_0)$	478	471	0,99				336	324	0,96			
$Q_{11}(S_0)$	481	474	0,99				381	358	0,94			
$Q_{12}(S_0)$	565	555	0,98				394	390	0,99			
$Q_{13}(S_0)$	581	567	0,98				432	426	0,99			
$Q_{14}(S_0)$	582	576	0,99	579	575	0,99	436	430	0,99			
$Q_{15}(S_0)$	696	696	1,00				512	506	0,99			
$Q_{16}(S_0)$	756	733	0,97	755	726	0,96	515	514	1,00			
$Q_{17}(S_0)$	760	757	1,00				555	532	0,96			
$Q_{18}(S_0)$	819	803	0,98				704	696	0,99			
$Q_{19}(S_0)$	831	831	1,00				723	708	0,98			
$Q_{20}(S_0)$	898	898	1,00				787	775	0,98			
$Q_{21}(S_0)$	934	918	0,98				795	792	1,00			
$Q_{22}(S_0)$	1054	919	0,87				980	903	0,92			
$Q_{23}(S_0)$	1056	934	0,88				1013	903	0,89			
$Q_{24}(S_0)$	1078	974	0,90	1040	965	0,93	1027	955	0,93			
$Q_{25}(S_0)$	1144	979	0,86				1089	956	0,88			
$Q_{26}(S_0)$	1183	1013	0,86				1171	986	0,84			
$Q_{27}(S_0)$	1185	1016	0,86				1171	990	0,85			
$Q_{28}(S_0)$	1186	1074	0,91				1173	991	0,84			
$Q_{29}(S_0)$	1209	1103	0,91				1200	1085	0,90			
$Q_{30}(S_0)$	1217	1103	0,91				1203	1100	0,91			
$Q_{31}(S_0)$	1259	1108	0,88				1204	1100	0,91			
$Q_{32}(S_0)$	1294	1108	0,86				1277	1105	0,87			
$Q_{33}(S_0)$	1313	1142	0,87				1309	1105	0,84			
$Q_{34}(S_0)$	1395	1149	0,82				1415	1122	0,79			
$Q_{35}(S_0)$	1469	1152	0,78				1431	1130	0,79			
$Q_{36}(S_0)$	1483	1184	0,80				1476	1175	0,80			
$Q_{37}(S_0)$	1493	1257	0,84				1485	1206	0,81			
$Q_{38}(S_0)$	1517	1306	0,86				1514	1283	0,85			
$Q_{39}(S_0)$	1518	1316	0,87				1514	1312	0,87			
$Q_{40}(S_0)$	1530	1392	0,91				1525	1419	0,93			
$Q_{41}(S_0)$	1531	1479	0,97	1506	1458	0,96	1527	1437	0,94			
$Q_{42}(S_0)$	1547	1540	1,00				1527	1520	1,00			
$Q_{43}(S_0)$	1630	1629	1,00				1566	1565	1,00			
$Q_{44}(S_0)$	1634	1634	1,00				1726	1725	1,00			
$Q_{45}(S_0)$	3039	2186	0,72				3055	2195	0,72			
$Q_{46}(S_0)$	3040	2186	0,72				3057	2196	0,72			
$Q_{47}(S_0)$	3112	2316	0,74				3138	2336	0,74			
$Q_{48}(S_0)$	3112	2317	0,74				3138	2336	0,74			
$Q_{49}(S_0)$	3177	2362	0,74				3183	2368	0,74			
$Q_{50}(S_0)$	3177	2363	0,74				3183	2368	0,74			
$Q_{51}(S_0)$	3200	3200	1,00				3193	3193	1,00			
$Q_{52}(S_0)$	3218	3218	1,00				3209	3209	1,00			
$Q_{53}(S_0)$	3238	3238	1,00				3255	3254	1,00			
$Q_{54}(S_0)$	3241	3242	1,00				3256	3256	1,00			

Table S5: Intensities of the observed emission bands of four vibronic bands of 1,2-DMB. The first line gives the wavenumber of the excited bands, the first column the wavenumber of the emission bands. The entries of the table represent the intensities, with the most intense band (apart from the excited band whose intensity is biased by stray light.) in each of the emission spectra normalized to 1.

S_0/S_1	0,0	0,0 + 84	0,0 + 117	0,0 + 508
150			1	
152	0.01			
154		1		
190	0.21			
194		0.17		
302			0.53	
308		0.37		
372	0.14	0.13		
395		0.26		
462	0.13			0.21
532				0.25
544	0.13		0.25	
548		0.16		
579	0.33			
585		0.11		1
629	0.17			
646				0.43
699		0.21		
735		0.35	0.39	
755	0.76			0.54
847		0.16		
852				0.31
886			0.34	
908			0.76	
912	0.14	0.61		0.27
936		0.18		
954	0.18	0.15		
956				0.24

Continued next page

Table S5: Intensities of the observed emission bands of four vibronic bands ... continued

S_0/S_1	0,0	0,0 + 84	0,0 + 117	0,0 + 508
970				0.25
977		0.14		
1040	0.25			
1047				0.31
1062		0.31	0.42	
1128	0.17			0.29
1152		0.22		
1160	0.18			0.81
1186	0.14			
1199		0.22	0.29	
1279				0.29
1297	0.18			
1337				0.94
1340	1			
1345			0.49	
1348		0.29		
1397				0.3
1449		0.19		
1498			0.71	
1506	0.32			
1535	0.19			0.36
1604	0.19			
1626	0.21			
1650			0.38	
1658		0.35		
1708				0.38
1733		0.24		
1745				0.37
1793	0.24			
1820		0.25		
1881	0.22			
1910				0.93
1918	0.31			
1958		0.22		

Continued next page

Table S5: Intensities of the observed emission bands of four vibronic bands ... continued

S_0/S_1	0,0	0,0 + 84	0,0 + 117	0,0 + 508
2038	0.21			
2040		0.19		
2074				0.51
2081		0.24		
2092	0.44			
2250		0.37	0.46	
2491				0.57
2662				0.5
2837		0.28		

End of Table

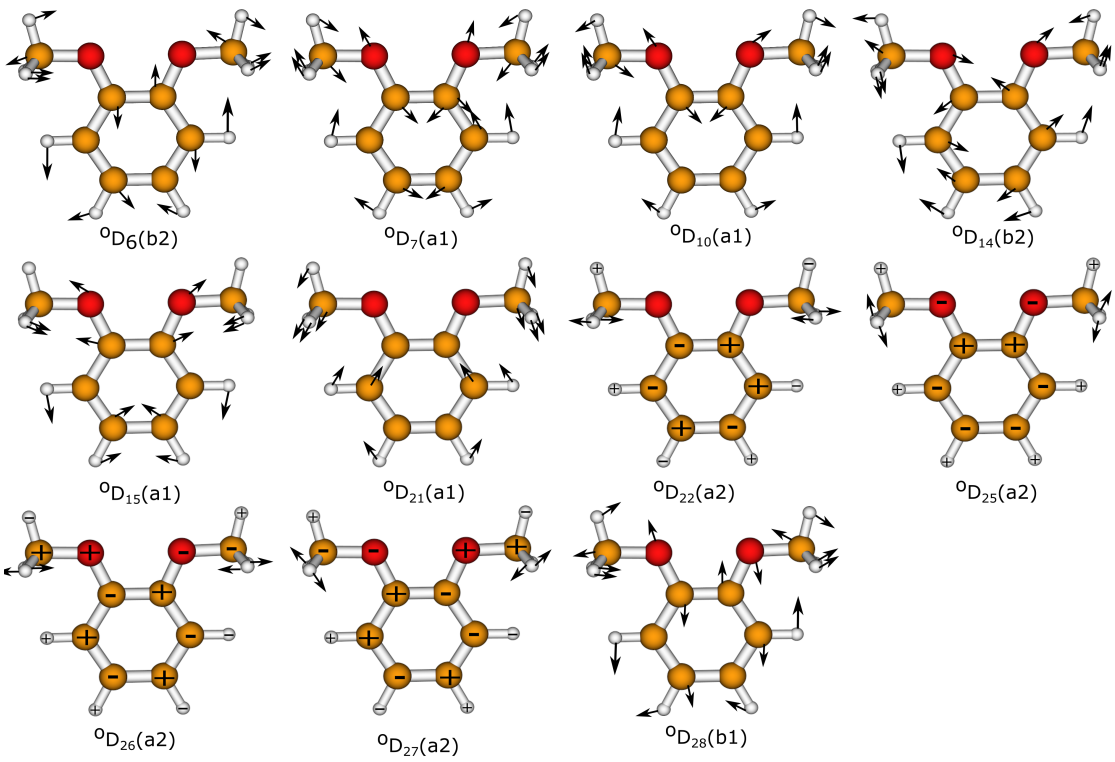

Figure S1: Vibrational modes of 1,2-DMB, labelled by the scheme given by Tuttle *et al.* [108] .

14.2 Online Supporting Material of Structural changes upon electronic excitation in 1,3-dimethoxybenzene from Franck-Condon/rotational constants fits of the fluorescence emission spectra.

Table S6: Fitted factors of the displacements of of the A-rotamer of 1,3-dimethoxybenzene upon electronic excitation along 4 normal modes from the FC fit.

Mode	displacement
Q_{22}	-0.0060658 $\pm$ 0.0043368
Q_{16}	-0.017154 $\pm$ 0.0022321
Q_{13}	-0.013498 $\pm$ 0.01085
Q_{3}	-0.02442 $\pm$ 0.0042989

Table S7: Fitted factors of the displacements of of the B-rotamer of 1,3-dimethoxybenzene upon electronic excitation along 4 normal modes from the FC fit.

Mode	displacement
Q_{33}	-0.011781 $\pm$ 0.004535
Q_{16}	0.012287 $\pm$ 0.00076135
Q_{12}	0.10727 $\pm$ 0.010011
Q_{9}	-0.038688 $\pm$ 0.0030241

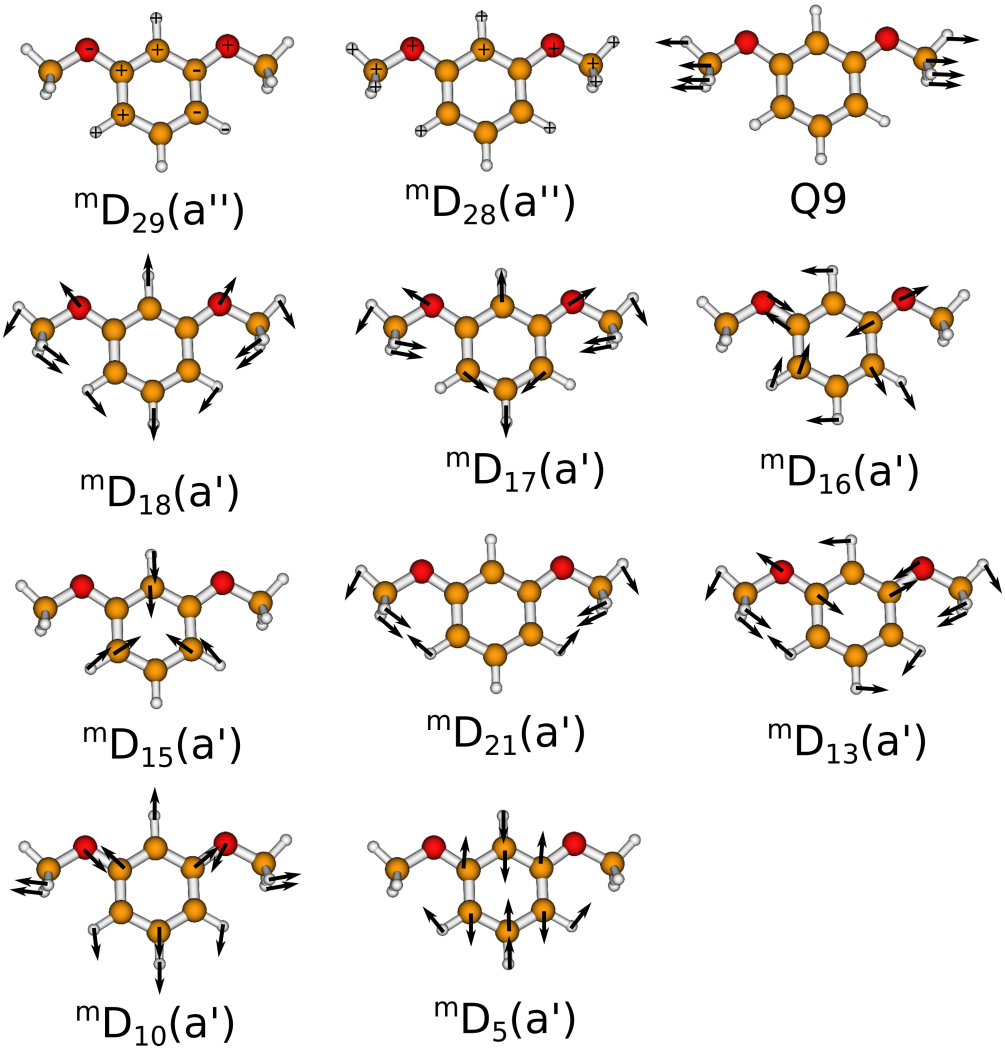

Figure S2: Vibrational modes of the B rotamer of 1,3-dimethoxybenzene, labelled by the scheme given by Tuttle et al.[108]

Table S8: Intensities of the observed emission bands of two vibronic bands of the A-rotamer of 1,3-Dimethoxybenzene. The first line gives the wavenumber of the excited bands, the first column the wavenumber of the emission bands. The entries of the table represent the intensities, with the most intense band (apart from the excited band whose intensity is biased by stray light.) in each of the emission spectra normalized to 1.

S_0/S_1	Assignment	Theory	0,0	+186	+233
193	Q_3	192	0.13	1	
291	Q_8	292	0.07	0.24	1
387	Q_3^2		0.15		
408	Q_9	423		0.4	
478	$Q_3 + Q_8$			0.15	
587	Q_{13}	588	0.4		
723	Q_{16}	727	1	0.1	
782	$Q_3 + Q_{13}$			0.24	
877	$Q_8 + Q_{13}$		0.2		
914	$Q_3 + Q_{16}$		0.12	0.48	
997	Q_{22}	1001	0.8		
1021	$Q_8 + Q_{16}$			0.11	0.48
1053	Q_{23}	1064	0.04		
1105	Q_{25}	1104	0.11	0.12	
1132	$Q_9 + Q_{16}$			0.2	
1190	Q_{29}	1196	0.13	0.4	
1275	$Q_8 + Q_{22}$		0.09		0.42
1291	$Q_3 + Q_{25}$			0.11	
1309	Q_{32}	1303	0.4		
1349	$Q_8 + Q_{23}$		0.34		
1374	Q_{34}	1394	0.1		
1383	$Q_3 + Q_{29}$			0.12	
1449	Q_{16}^2		0.23		
1502	$Q_3 + Q_{16}$			0.14	
1541	$Q_3 + Q_{34}$		0.12	0.2	
1643	$Q_3 + Q_{47}$			0.16	
1658	Q_{44}	1647	0.14		
1703	$Q_{13} + Q_{25}$		0.36		
1969	$Q_{13} + Q_{34}$		0.17		

Table S9: Intensities of the observed emission bands of two vibronic bands of the B-rotamer of 1,3-Dimethoxybenzene. The first line gives the wavenumber of the excited bands, the first column the wavenumber of the emission bands. The entries of the table represent the intensities, with the most intense band (apart from the excited band whose intensity is biased by stray light.) in each of the emission spectra normalized to 1.

S_0/S_1	Assignment	Theory	0,0	+193
264	Q_5	234		1
320	Q_6	279		0.27
365	Q_9	367	0.15	
568	Q_{12}	563	0.4	
727	Q_{16}	729	0.98	
824	$Q_5 + Q_{12}$			0.17
913	Q_{20}	907	0.78	
967	$Q_5 + Q_{16}$			0.55
994	Q_{22}	997	0.78	
1027	$Q_6 + Q_{16}$			0.19
1098	$Q_9 + Q_{16}$		0.25	
1209	Q_{30}	1211	0.07	
1237	Q_{31}	1226	0.07	
1254	$Q_5 + Q_{22}$			0.44
1290	Q_{33}	1313	0.1	
1358	$Q_9 + Q_{22}$		0.1	
1452	Q_{16}^2		0.22	
1561	$Q_{12} + Q_{22}$		0.15	
1607	Q_{43}			0.27
1704	$Q_{16} + Q_{22}$		0.43	
1799	$Q_{16} + Q_{24}$		0.1	
1830	$Q_{16} + Q_{25}$		0.1	
1960	$Q_9 + Q_{43}$		0.2	
1986	Q_{22}^2		0.2	
2064	$Q_{16} + Q_{33}$		0.12	

Table S10: SCS-CC2/cc-pVTZ calculated isotopic shifts of the 54 normal modes of the A-rotamer of 1,3-dimethoxybenzene in the ground and the first electronically excited states.

	S_0						S_1					
	Calc.			Exp.			Calc.			Exp.		
	h_{10}	d_6	Ratio	h_{10}	d_6	Ratio	h_{10}	d_6	Ratio	h_{10}	d_6	Ratio
$Q_1(S_0)$	89.76	81.23	0.90				74.12	68.24	0.92			
$Q_2(S_0)$	107.67	98.66	0.92				89.00	81.49	0.92			
$Q_3(S_0)$	192.88	174.93	0.91	193	171	0.88	134.33	121.17	0.90			
$Q_4(S_0)$	217.93	174.93	0.80				179.76	151.47	0.84			
$Q_5(S_0)$	226.06	180.52	0.80				189.83	170.40	0.90	186	185	0.99
$Q_6(S_0)$	288.92	254.17	0.88				220.23	172.47	0.78			
$Q_7(S_0)$	291.64	259.26	0.89				227.92	216.54	0.95			
$Q_8(S_0)$	292.73	264.43	0.90	291	259	0.89	269.14	240.38	0.89			
$Q_9(S_0)$	423.27	397.53	0.94				289.64	262.49	0.91	233	233	1.0
$Q_{10}(S_0)$	466.55	455.89	0.98				367.51	361.23	0.98			
$Q_{11}(S_0)$	466.74	465.02	1.00				409.41	389.25	0.95			
$Q_{12}(S_0)$	537.08	519.39	0.97				425.79	418.10	0.98			
$Q_{13}(S_0)$	588.46	566.93	0.96	587	564	0.96	435.34	434.59	1.00			
$Q_{14}(S_0)$	631.07	629.93	1.00				454.30	453.65	1.00			
$Q_{15}(S_0)$	685.84	685.32	1.00				485.78	466.04	0.96			
$Q_{16}(S_0)$	727.74	711.39	0.98	721	708	0.98	503.46	503.30	1.00			
$Q_{17}(S_0)$	773.33	772.53	1.00				540.84	521.70	0.96			
$Q_{18}(S_0)$	836.60	836.08	1.00				638.64	636.37	1.00			
$Q_{19}(S_0)$	854.27	853.84	1.00				695.63	677.91	0.97			
$Q_{20}(S_0)$	923.33	874.32	0.95				701.99	700.68	1.00			
$Q_{21}(S_0)$	949.23	918.99	0.97				873.54	842.92	0.96			
$Q_{22}(S_0)$	1001.33	919.56	0.92	997	991	0.99	961.77	908.12	0.94			
$Q_{23}(S_0)$	1064.65	949.25	0.89				1001.97	910.63	0.91			
$Q_{24}(S_0)$	1079.09	976.52	0.90				1034.25	955.19	0.92			
$Q_{25}(S_0)$	1104.05	988.20	0.90				1049.00	960.04	0.92			
$Q_{26}(S_0)$	1179.41	999.70	0.85				1147.70	970.41	0.85			
$Q_{27}(S_0)$	1186.98	1019.73	0.86				1175.87	989.14	0.84			
$Q_{28}(S_0)$	1187.37	1054.58	0.89				1178.25	1014.73	0.86			
$Q_{29}(S_0)$	1196.35	1102.42	0.92				1178.45	1029.07	0.87			
$Q_{30}(S_0)$	1217.53	1102.77	0.91				1211.84	1100.14	0.91			
$Q_{31}(S_0)$	1243.36	1104.95	0.89				1230.83	1101.34	0.89			
$Q_{32}(S_0)$	1303.07	1108.83	0.85	1309	1307	0.99	1283.66	1105.79	0.86			
$Q_{33}(S_0)$	1319.72	1110.83	0.84				1311.61	1106.67	0.84			
$Q_{34}(S_0)$	1394.17	1148.30	0.82				1408.78	1126.96	0.80			
$Q_{35}(S_0)$	1468.42	1150.59	0.78				1421.03	1136.48	0.80			
$Q_{36}(S_0)$	1479.77	1181.62	0.80				1476.40	1150.42	0.78			
$Q_{37}(S_0)$	1500.89	1223.47	0.82				1487.72	1210.83	0.81			
$Q_{38}(S_0)$	1517.66	1308.85	0.86				1514.29	1284.19	0.85			
$Q_{39}(S_0)$	1518.31	1325.46	0.87				1516.30	1318.27	0.87			
$Q_{40}(S_0)$	1523.78	1392.79	0.91				1528.56	1415.57	0.93			
$Q_{41}(S_0)$	1533.52	1480.85	0.97				1530.08	1424.64	0.93			
$Q_{42}(S_0)$	1534.74	1520.43	0.99				1546.96	1541.53	1.00			
$Q_{43}(S_0)$	1630.20	1628.85	1.00				1558.80	1557.17	1.00			
$Q_{44}(S_0)$	1647.80	1646.29	1.00				1765.56	1765.09	1.00			
$Q_{45}(S_0)$	3043.28	2188.43	0.72				3051.06	2192.77	0.72			
$Q_{46}(S_0)$	3043.50	2188.70	0.72				3054.31	2195.00	0.72			
$Q_{47}(S_0)$	3117.31	2320.37	0.74				3130.98	2330.95	0.74			
$Q_{48}(S_0)$	3117.47	2320.51	0.74				3134.45	2333.51	0.74			
$Q_{49}(S_0)$	3177.05	2362.98	0.74				3182.23	2367.62	0.74			
$Q_{50}(S_0)$	3178.02	2363.67	0.74				3182.43	2367.80	0.74			
$Q_{51}(S_0)$	3201.23	3201.22	1.00				3224.81	3224.78	1.00			
$Q_{52}(S_0)$	3232.33	3232.31	1.00				3239.63	3239.52	1.00			
$Q_{53}(S_0)$	3249.98	3249.85	1.00				3254.80	3254.75	1.00			
$Q_{54}(S_0)$	3250.92	3250.81	1.00				3279.74	3279.67	1.00			

Table S11: SCS-CC2/cc-pVTZ calculated isotopic shifts of the 54 normal modes of the B-rotamer of 1,3-dimethoxybenzene in the ground and the first electronically excited states.

	S_0						S_1					
	Calc.			Exp.			Calc.			Exp.		
	h_{10}	d_6	Ratio	h_{10}	d_6	Ratio	h_{10}	d_6	Ratio	h_{10}	d_6	Ratio
$Q_1(S_0)$	72.46	63.49	0.88				27.68	23.41	0.85			
$Q_2(S_0)$	108.67	98.01	0.90				108.80	98.29	0.90			
$Q_3(S_0)$	205.63	168.29	0.82				140.23	126.56	0.90			
$Q_4(S_0)$	213.82	187.45	0.88				169.02	151.83	0.90			
$Q_5(S_0)$	232.90	187.65	0.81				194.88	178.47	0.92	193	192	0.99
$Q_6(S_0)$	278.63	243.04	0.87				231.49	179.75	0.78			
$Q_7(S_0)$	300.10	261.10	0.87				257.50	207.44	0.81			
$Q_8(S_0)$	302.43	275.90	0.91				285.07	270.17	0.95			
$Q_9(S_0)$	367.10	340.56	0.93	365	337	0.92	295.65	273.23	0.92			
$Q_{10}(S_0)$	470.35	466.89	0.99				353.95	329.77	0.93			
$Q_{11}(S_0)$	477.51	470.47	0.99				394.83	394.37	1.00			
$Q_{12}(S_0)$	566.69	547.40	0.97	568	547	0.96	402.60	399.02	0.99			
$Q_{13}(S_0)$	584.07	557.54	0.95				446.76	446.69	1.00			
$Q_{14}(S_0)$	632.46	632.63	1.00				472.71	472.70	1.00			
$Q_{15}(S_0)$	682.59	681.97	1.00				508.94	492.83	0.97			
$Q_{16}(S_0)$	729.63	714.12	0.98	727	713	0.98	529.54	529.48	1.00			
$Q_{17}(S_0)$	766.00	760.66	0.99				568.22	541.69	0.95			
$Q_{18}(S_0)$	844.59	841.62	1.00				616.22	615.71	1.00			
$Q_{19}(S_0)$	849.76	846.97	1.00				647.70	647.08	1.00			
$Q_{20}(S_0)$	905.90	867.76	0.96				723.88	702.17	0.97			
$Q_{21}(S_0)$	944.45	918.33	0.97				871.35	836.89	0.96			
$Q_{22}(S_0)$	1001.61	918.54	0.92	994	993	0.99	947.41	912.31	0.96			
$Q_{23}(S_0)$	1069.66	942.68	0.88				975.55	912.80	0.94			
$Q_{24}(S_0)$	1073.21	974.65	0.91				1036.31	941.76	0.91			
$Q_{25}(S_0)$	1117.58	982.42	0.88				1040.09	955.75	0.92			
$Q_{26}(S_0)$	1184.55	999.12	0.84				1150.72	976.15	0.85			
$Q_{27}(S_0)$	1186.77	1020.30	0.86				1179.51	979.89	0.83			
$Q_{28}(S_0)$	1186.92	1048.19	0.88				1180.18	1018.02	0.86			
$Q_{29}(S_0)$	1203.77	1102.95	0.92				1191.41	1021.89	0.86			
$Q_{30}(S_0)$	1219.06	1103.19	0.90				1215.87	1098.03	0.90			
$Q_{31}(S_0)$	1226.65	1107.80	0.90				1235.83	1098.05	0.89			
$Q_{32}(S_0)$	1313.42	1108.47	0.84				1281.85	1106.98	0.86			
$Q_{33}(S_0)$	1317.96	1124.61	0.85	1290	1306	1.01	1322.79	1109.32	0.84			
$Q_{34}(S_0)$	1384.34	1146.68	0.83				1381.47	1114.41	0.81			
$Q_{35}(S_0)$	1478.33	1152.62	0.78				1424.35	1128.84	0.79			
$Q_{36}(S_0)$	1479.18	1188.71	0.80				1462.69	1152.41	0.79			
$Q_{37}(S_0)$	1500.51	1216.90	0.81				1478.75	1224.49	0.83			
$Q_{38}(S_0)$	1518.48	1312.11	0.86				1512.07	1285.14	0.85			
$Q_{39}(S_0)$	1518.64	1327.82	0.87				1512.08	1331.35	0.88			
$Q_{40}(S_0)$	1524.53	1382.08	0.91				1515.59	1384.79	0.91			
$Q_{41}(S_0)$	1532.13	1489.79	0.97				1529.23	1426.44	0.93			
$Q_{42}(S_0)$	1534.33	1517.27	0.99				1530.60	1505.48	0.98			
$Q_{43}(S_0)$	1619.56	1618.33	1.00				1677.60	1676.17	1.00			
$Q_{44}(S_0)$	1654.35	1652.61	1.00				1800.90	1799.57	1.00			
$Q_{45}(S_0)$	3042.70	2188.11	0.72				3051.68	2191.73	0.72			
$Q_{46}(S_0)$	3043.21	2188.58	0.72				3054.54	2194.40	0.72			
$Q_{47}(S_0)$	3116.87	2320.09	0.74				3134.10	2333.35	0.74			
$Q_{48}(S_0)$	3116.90	2320.10	0.74				3134.15	2333.35	0.74			
$Q_{49}(S_0)$	3176.82	2362.74	0.74				3193.87	2377.45	0.74			
$Q_{50}(S_0)$	3176.95	2362.81	0.74				3193.96	2377.51	0.74			
$Q_{51}(S_0)$	3199.82	3199.81	1.00				3214.44	3214.35	1.00			
$Q_{52}(S_0)$	3234.03	3233.93	1.00				3251.47	3251.41	1.00			
$Q_{53}(S_0)$	3248.21	3248.02	1.00				3254.30	3254.28	1.00			
$Q_{54}(S_0)$	3251.18	3251.05	1.00				3256.92	3256.84	1.00			

Table S12: Comparison of the bond lengths and bond length changes in pm from SCS-CC2 calculations and Franck-Condon fits of the A-rotamer of 1,3-dimethoxybenzene upon electronic excitation.

State	bond length S_0		bond length S_1		S_1-S_0	
Method	SCS-CC2	FCFit	SCS-CC2	FCFit	SCS-CC2	FCFit
C1-C2	139.2	139.2	143.5	143.2	+4.3	+4.0
C2-C3	140.6	140.6	142.6	142.2	+1.6	+1.6
C3-C4	139.4	139.4	143.3	142.8	+3.9	+3.4
C3-O1	136.8	136.8	136.0	135.8	-0.8	-1.0
O1-C7	142.4	142.4	142.9	142.8	+0.5	+0.4
C4-C5	140.4	140.4	142.9	142.7	+2.5	+2.3
C5-C6	138.5	138.5	143.7	143.5	+5.2	+5.0
C6-C1	140.6	140.6	142.0	141.7	+1.4	+1.1
C1-O2	136.6	136.6	136.1	135.8	-0.5	-0.8
O2-C8	142.4	142.4	142.9	142.9	+0.5	+0.5

Table S13: Comparison of the bond lengths and bond length changes in pm from SCS-CC2 calculations and Franck-Condon fits of the B-rotamer of 1,3-dimethoxybenzene upon electronic excitation.

State	bond length S_0		bond length S_1		S_1-S_0	
Method	SCS-CC2	FCFit	SCS-CC2	FCFit	SCS-CC2	FCFit
C1-C2	139.4	139.4	142.4	142.4	+3.0	+3.0
C2-C3	139.4	139.4	142.4	142.4	+3.0	+3.0
C3-C4	140.1	140.1	142.6	142.7	+2.5	+2.6
C3-O1	136.6	136.6	135.9	135.8	-0.7	-0.8
O1-C7	142.1	142.1	142.7	143.0	+0.6	+0.9
C4-C5	139.4	139.4	143.2	143.6	+3.8	+4.2
C5-C6	139.4	139.4	143.2	143.6	+3.8	+4.2
C6-C1	140.1	140.1	142.6	142.7	+2.5	+2.6
C1-O2	136.6	136.6	135.9	135.8	-0.7	-0.8
O2-C8	142.1	142.1	142.7	143.0	+0.6	+0.9

Table S14: SCS-CC2/cc-pVTZ calculated optimized S_0 cartesian coordinates of the A-rotamer of 1,3-dimethoxybenzene (in bohr).

c	2.26380233	-3.19877003	0.00000000
c	-0.20829330	-4.05889787	0.00000000
c	-2.26660653	-2.38438563	0.00000000
c	-1.77735744	0.20440562	0.00000000
c	0.71737876	1.11917984	0.00000000
c	2.72414324	-0.58138939	0.00000000
h	3.85115376	-4.48367014	0.00000000
h	-0.56919351	-6.07233528	0.00000000
h	-4.16823020	-3.11807166	0.00000000
o	-3.59166292	2.04632826	0.00000000
h	0.98586007	3.14033571	0.00000000
o	5.21186512	0.10899829	0.00000000
c	5.72350863	2.75119328	0.00000000
h	4.95249125	3.65895524	-1.68519147
h	4.95249125	3.65895524	1.68519147
h	7.76845411	2.92303165	0.00000000
c	-6.14731075	1.20404012	0.00000000
h	-6.56417998	0.08854821	1.68525474
h	-7.29518921	2.90531525	0.00000000
h	-6.56417998	0.08854821	-1.68525474

Table S15: SCS-CC2/cc-pVTZ calculated optimized S_1 cartesian coordinates of the A-rotamer of 1,3-dimethoxybenzene (in bohr).

c	2.29013802	-3.20147189	0.00000000
c	-0.24224185	-4.18025671	0.00000000
c	-2.28661994	-2.41472678	0.00000000
c	-1.78756509	0.24617208	0.00000000
c	0.71318362	1.24824734	0.00000000
c	2.73682208	-0.55610302	0.00000000
h	3.91175529	-4.44361216	0.00000000
h	-0.59504285	-6.18754010	0.00000000
h	-4.20730758	-3.09955800	0.00000000
o	-3.63824548	2.02999856	0.00000000
h	0.97833886	3.26456461	0.00000000
o	5.22176161	0.11128450	0.00000000
c	5.78469424	2.75332165	0.00000000
h	5.02730673	3.66394410	-1.68656389
h	5.02730673	3.66394410	1.68656389
h	7.83261289	2.88031707	0.00000000
c	-6.20210005	1.18445700	0.00000000
h	-6.61106181	0.07356899	1.68770736
h	-7.34267361	2.88987967	0.00000000
h	-6.61106181	0.07356899	-1.68770736

Table S16: SCS-CC2/cc-pVTZ calculated optimized S_0 cartesian coordinates of the B-rotamer of 1,3-dimethoxybenzene (in bohr).

c	2.64031654	0.00080712	-1.12085600
c	0.36693406	0.00188929	0.21041539
c	0.37444592	0.00253840	2.84494981
c	2.66351306	0.00222510	4.17677581
c	4.91533557	0.00116126	2.80920325
c	4.95003029	0.00041232	0.17492404
o	-1.95542714	0.00340382	3.95569584
c	-1.98141757	0.00385857	6.64166041
o	2.41426470	0.00021205	-3.69201287
h	-1.40686475	0.00219920	-0.80272988
h	2.71710204	0.00275061	6.21432527
h	6.69110426	0.00084286	3.82387278
h	6.73243248	-0.00042139	-0.81378301
h	-3.96011289	0.00440853	7.18037065
h	-1.06005738	-1.67968906	7.39790552
h	-1.05927404	1.68722314	7.39735434
c	4.71498080	-0.00072757	-5.07824681
h	4.17441814	-0.00094638	-7.05642703
h	5.83480877	1.68245869	-4.66830992
h	5.83382940	-1.68441062	-4.66767616

Table S17: SCS-CC2/cc-pVTZ calculated optimized S_1 cartesian coordinates of the B-rotamer of 1,3-dimethoxybenzene (in bohr).

c	2.62839697	0.00091981	-1.13907995
c	0.26921604	0.00192011	0.15480574
c	0.35293481	0.00245798	2.84420624
c	2.67711833	0.00206818	4.20771630
c	5.03183494	0.00111095	2.87547731
c	4.98341218	0.00057088	0.17044227
o	1.95033906	0.00333671	3.98190812
c	2.00042790	0.00389972	6.67742668
o	2.43853256	0.00032575	-3.70099307
h	1.49942724	0.00219358	-0.85546637
h	2.67956218	0.00251760	6.24704647
h	6.80128752	0.00074511	3.88628763
h	6.74134843	-0.00003908	-0.86326389
h	3.98497549	0.00452983	7.19128740
h	1.08362107	-1.68231431	7.42754270
h	1.08273256	1.68993662	7.42685230
c	4.73503325	-0.00078643	-5.11322181
h	4.16967129	-0.00113544	-7.08372406
h	5.84730641	1.68509152	-4.70437145
h	5.84623068	-1.68715317	-4.70346712

14.3 Online Supporting Material of Excited State Structure of Isolated 4-Cyanoindole from a Combined Franck-Condon and Rotational Constants Analysis

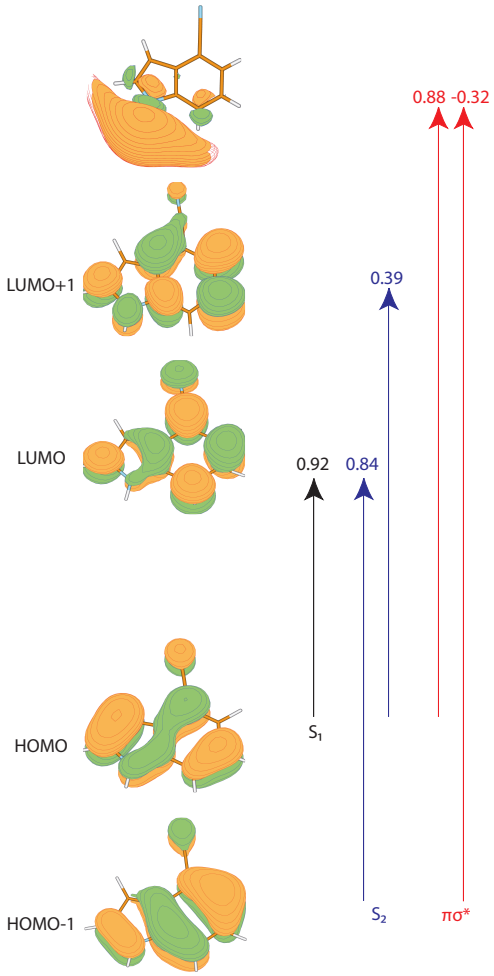

Figure S3: Frontier orbitals and leading contributions to the lowest two excited singlet states of 4-cyanoindole.[9]

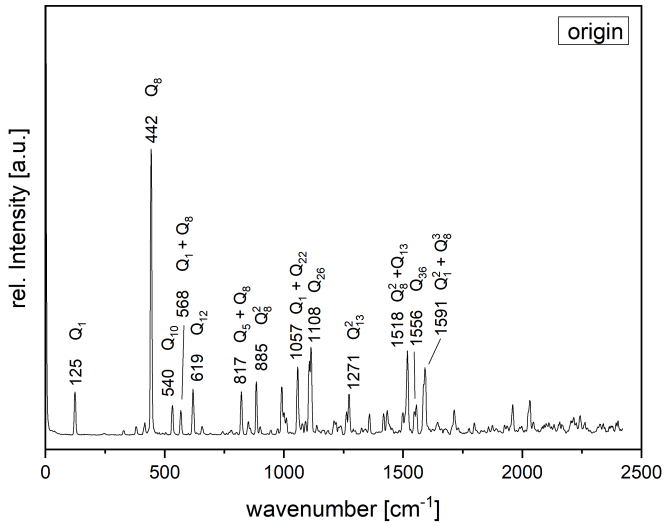

Figure S4: Fluorescence emission spectrum upon excitation of the electronic origin at 33038.55 cm^{-1}.

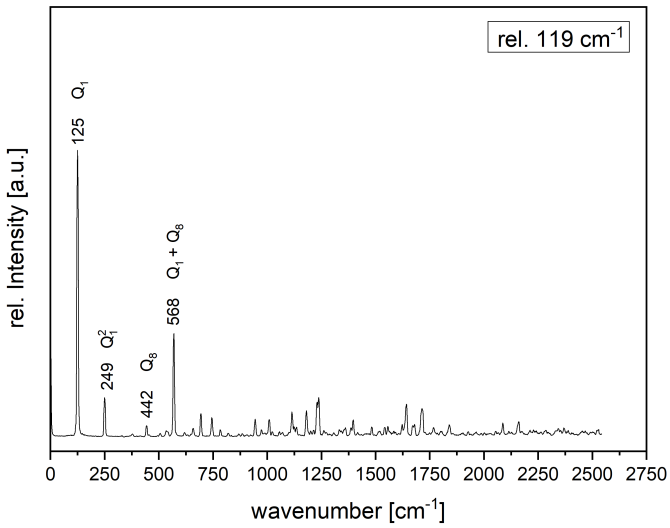

Figure S5: Fluorescence emission spectrum upon excitation of 0,0 + 119 cm^{-1}.

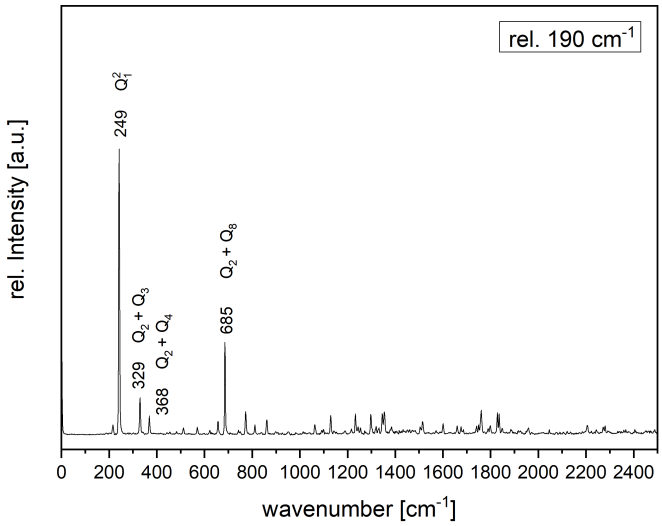

Figure S6: Fluorescence emission spectrum upon excitation of 0,0 + 190 cm^{-1}.

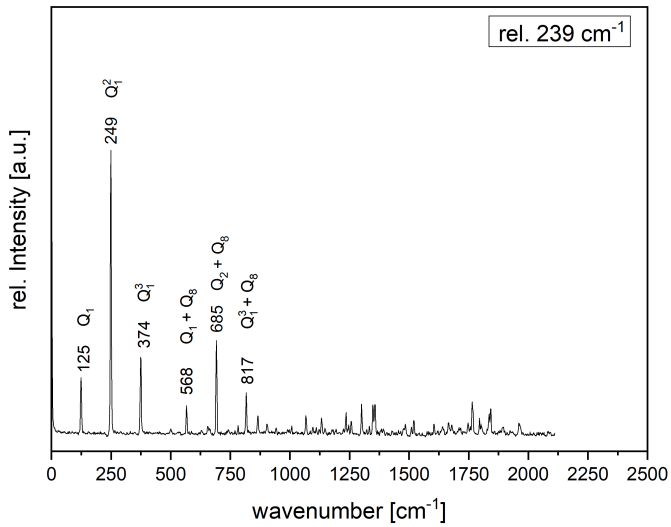

Figure S7: Fluorescence emission spectrum upon excitation of 0,0 + 239 cm^{-1}.

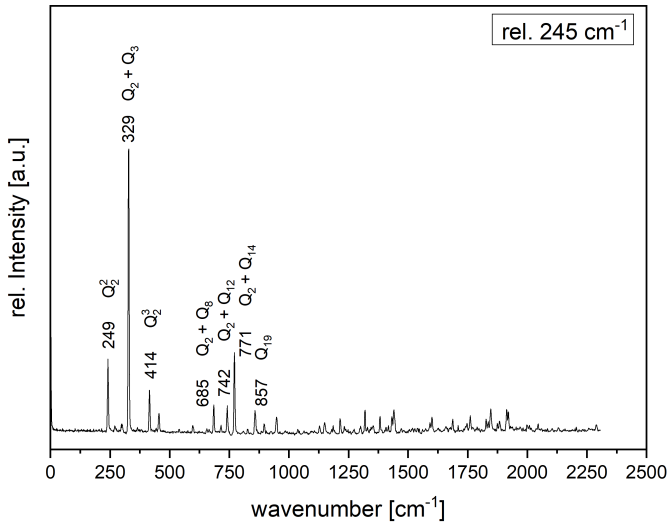

Figure S8: Fluorescence emission spectrum upon excitation of 0,0 + 245 cm^{-1}.

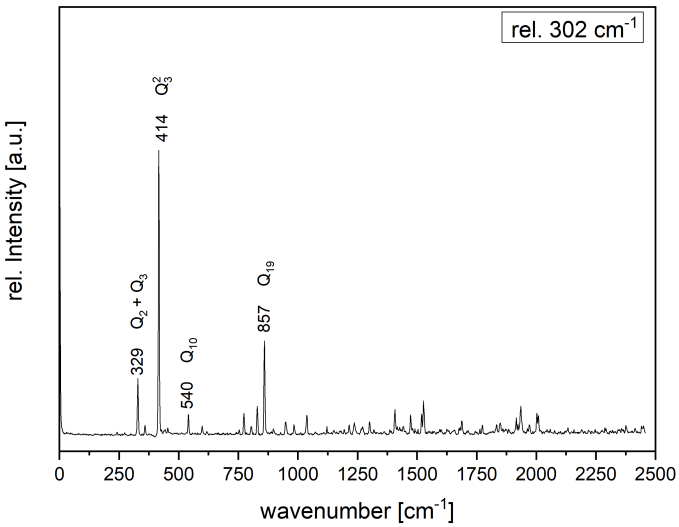

Figure S9: Fluorescence emission spectrum upon excitation of 0,0 + 302 cm^{-1}.

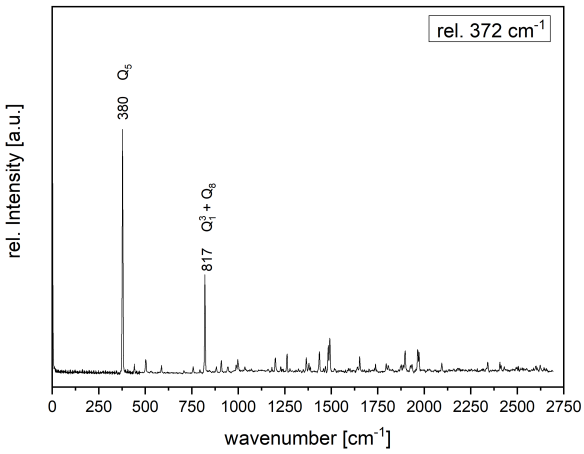

Figure S10: Fluorescence emission spectrum upon excitation of 0,0 + 372 cm^{-1}.

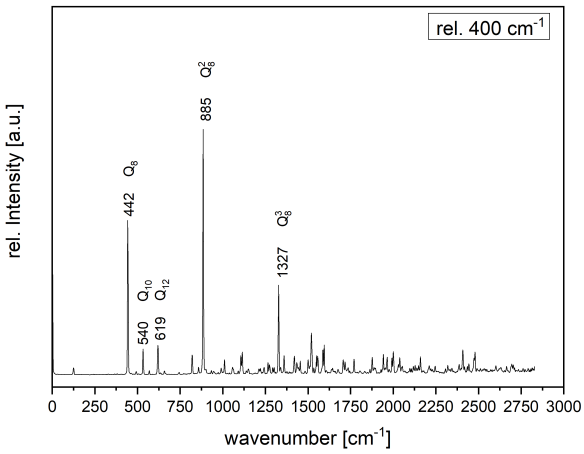

Figure S11: Fluorescence emission spectrum upon excitation of 0,0 + 400 cm^{-1}.

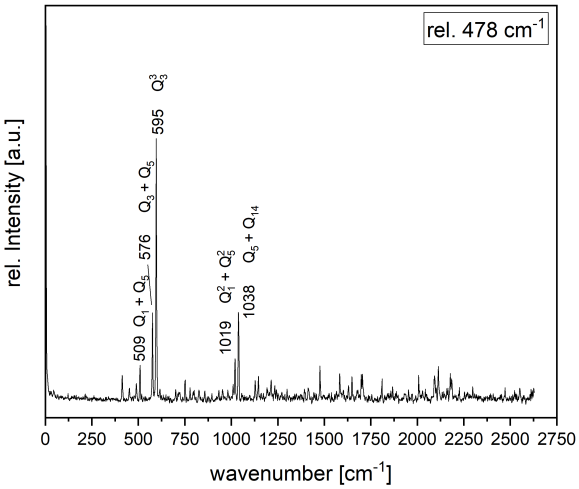

Figure S12: Fluorescence emission spectrum upon excitation of 0,0 + 478 cm^{-1}.

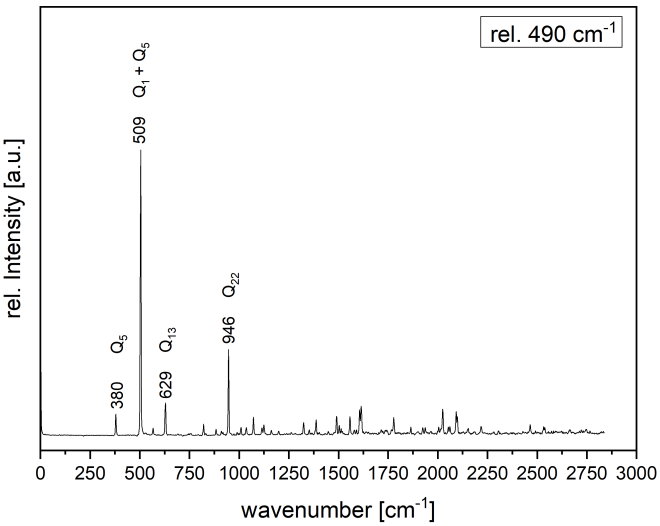

Figure S13: Fluorescence emission spectrum upon excitation of 0,0 + 490 cm^{-1}.

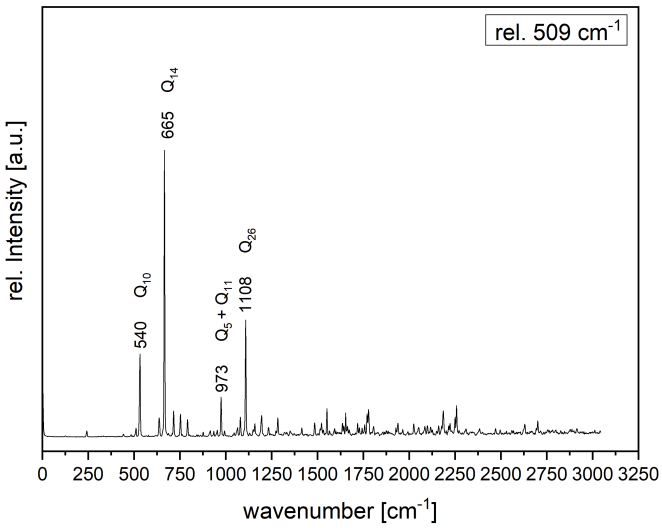

Figure S14: Fluorescence emission spectrum upon excitation of 0,0 + 509 cm^{-1}.

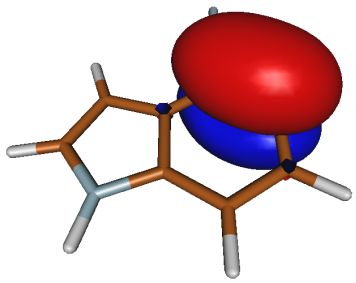

Figure S15: Natural bonding orbtial of bond C4-C5 with bonding character calculated via NBO 7.0

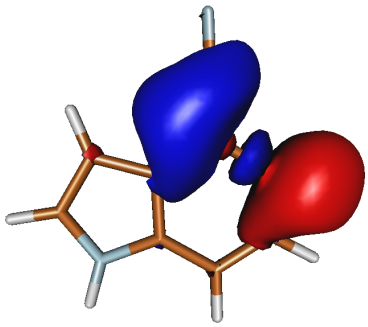

Figure S16: Natural bonding orbtial of bond C4-C5 with antibond character calculated via NBO 7.0

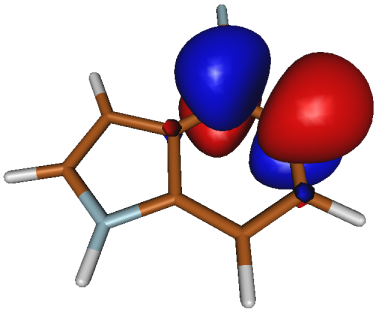

Figure S17: Natural bonding orbtial of bond C4-C5 with antibond character calculated via NBO 7.0

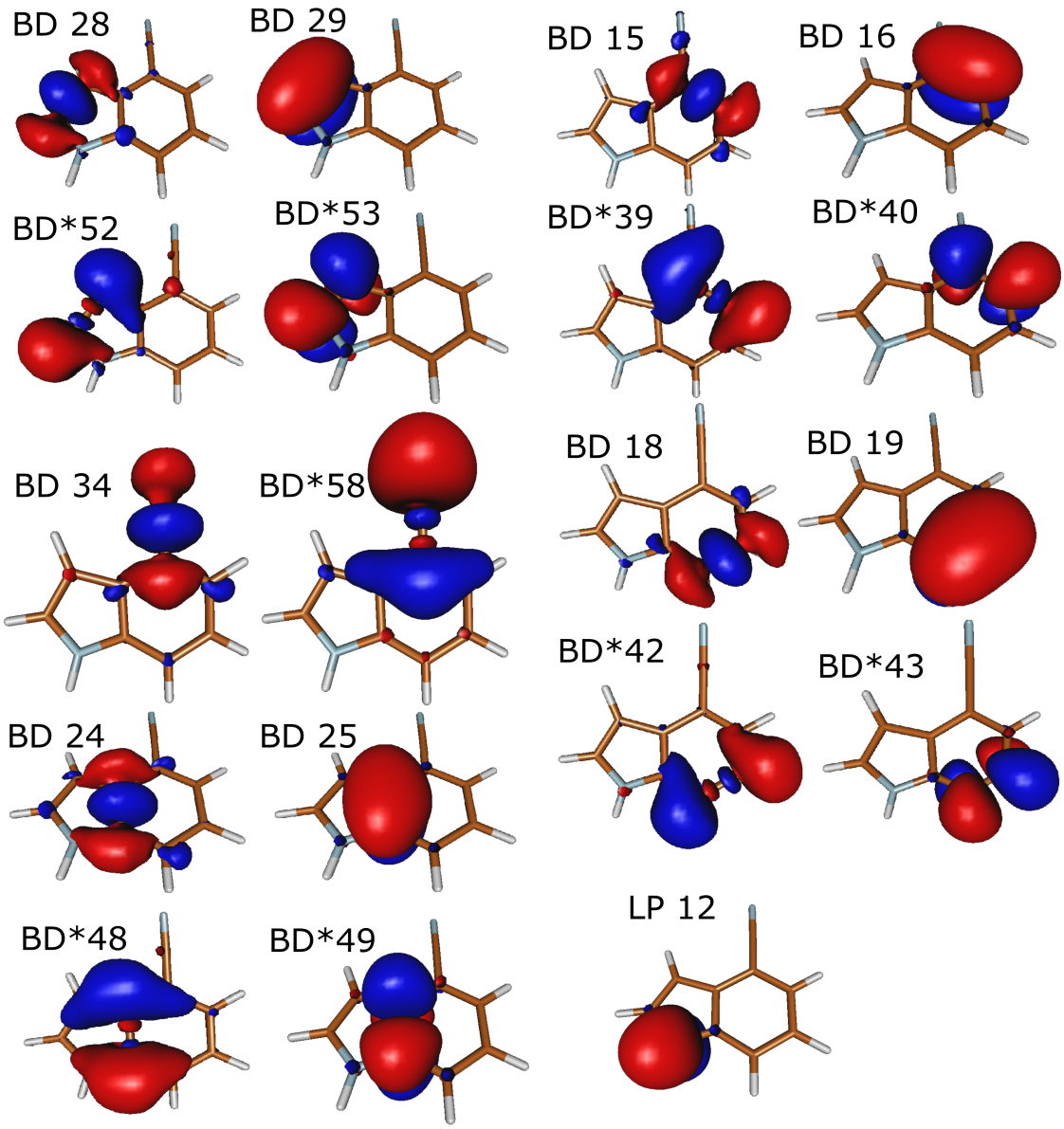

Figure S18: NBO contribution from Table 12 calculated via NBO 7.0

Table S18: Fitted factors of the displacements of 4-CI upon electronic excitation along 10 normal modes from the FC fit.

Mode	displacement
Q_{36}	-0.08101 $\pm$ 0.011921
Q_{25}	-0.027851 $\pm$ 0.02402
Q_{21}	-0.016686 $\pm$ 0.016493
Q_{18}	-0.061802 $\pm$ 0.013314
Q_{14}	0.017524 $\pm$ 0.004375
Q_{12}	0.087258 $\pm$ 0.0082843
Q_{9}	0.001113 $\pm$ 0.0016864
Q_{8}	0.0053528 $\pm$ 0.0031573
Q_{5}	-0.0054993 $\pm$ 0.024081
Q_{1}	-0.030844 $\pm$ 0.006651

Table S19: Intensities of the observed emission bands of six vibronic bands of 4-CI. The first line gives the wavenumber of the excited bands, the first column the wavenumber of the emission bands. The entries of the table represent the intensities, with the most intense band (apart from the excited band whose intensity is biased by stray light.) in each of the emission spectra normalized to 1.

S_0/S_1	Assigment	Theory	0,0	+ 119	+ 239	+ 372	+ 400	+ 490
125	Q_1	125	0.15	1	0.2	-	0.03	-
249	Q_2^2	258	-	0.13	1	-		-
329	$Q_2 + Q_3$	347	0.02	-	-	-	-	-
374	Q_1^3	375	-	-	0.27	1	-	-
380	Q_5	377	0.03	-	-	-	-	0.08
414	Q_2^3	387	0.04					
442	Q_8	442	1	0.04			0.62	
509	Q_4^2	500				0.06		1
531	Q_9	529					0.1	
540	Q_{10}	547	0.1				0.1	
568	$Q_1 + Q_8$	567	0.08	0.36	0.1			0.02
619	Q_{12}	615	0.15				0.12	
629	$Q_1 + Q_9$							0.11
665	Q_{14}	650	0.03					
685	$Q_4 + Q_8$			0.08	0.33			
817	$Q_5 + Q_8$	819	0.15		0.15	0.41	0.08	0.04
850	Q_{18}	839	0.05					
885	Q_8^2	884	0.18				1	0.02
902	Q_{21}	901	0.03		0.04			
946	Q_4^4	1000	0.02	0.06				0.3
991	$Q_5 + Q_{12}$		0.17					
1008	Q_{23}	1001		0.06			0.06	
1057	Q_{25}	1092	0.24		0.07			0.06
1108	Q_{26}	1131	0.3	0.09			0.09	
1180	Q_{27}	1182		0.09				
1211	$Q_5 + Q_{18}$		0.05					
1234	Q_{28}			0.11	0.08			
1271	$Q_5 + Q_{21}$		0.14					
1327	Q_8^3	1326					0.36	0.04
1360	$Q_1 + Q_{28}$		0.07		0.11			0.06
1492	$Q_{14} + Q_{18}$					0.15		0.07
1518	$Q_{12} + Q_{21}$		0.29					
1556	Q_{36}	1538	0.11					0.07
1591	$Q_1 + Q_{34}$		0.24				0.12	
1770	$Q_{14} + Q_{26}$				0.12		0.06	0.06
1961	$Q_8 + Q_{35}$		0.11		0.05			
2030	$Q_{21} + Q_{26}$		0.12					0.09
2160	Q_{39}	2147					0.07	

Table S20: SCS-CC2/cc-pVTZ calculated optimized S_0 cartesian coordinates of 4CI (in bohr).

c	-0.84429380	-3.86526812	0.00000000
c	1.81590270	-3.84529598	0.00000000
c	3.16859777	-1.59217728	0.00000000
c	1.78679065	0.66302505	0.00000000
n	2.59401828	3.13557854	0.00000000
c	0.51827204	4.71939211	0.00000000
c	-1.66106425	3.30485604	0.00000000
c	-0.89593636	0.71157894	0.00000000
c	-2.20956035	-1.61087826	0.00000000
h	-1.85097164	-5.64406050	0.00000000
h	2.82299141	-5.62397287	0.00000000
h	5.21459336	-1.59273883	0.00000000
h	0.76454588	6.74053161	0.00000000
h	-3.56428891	4.02557873	0.00000000
h	4.40559086	3.70364199	0.00000000
c	-4.92098715	-1.62705913	0.00000000
n	-7.14420050	-1.60273203	0.00000000

Table S21: SCS-CC2/cc-pVTZ calculated optimized S_1 cartesian coordinates of 4-CI (in bohr).

c	-0.84438532	-3.92468146	0.00000000
c	1.80701209	-3.84875359	0.00000000
c	3.25257881	-1.56465731	0.00000000
c	1.76933203	0.64313170	0.00000000
n	2.57528373	3.20065850	0.00000000
c	0.58466870	4.74719867	0.00000000
c	-1.65573648	3.21450369	0.00000000
c	-0.90357882	0.67712652	0.00000000
c	-2.32864524	-1.65647887	0.00000000
h	-1.78760220	-5.73740415	0.00000000
h	2.81885088	-5.62788358	0.00000000
h	5.29287398	-1.55845878	0.00000000
h	0.78280690	6.77413229	0.00000000
h	-3.56271811	3.93803372	0.00000000
h	4.39731932	3.76123927	0.00000000
c	-4.97872389	-1.59518531	0.00000000
n	-7.21933639	-1.44252131	0.00000000

14.4 Online Supporting Material of Excited State Structure of Isolated 2-Cyanoindole and the Binary 2-Cyanoindole-$(H_2O)_1$ Cluster from a Combined Franck-Condon and Rotational Constants Fit

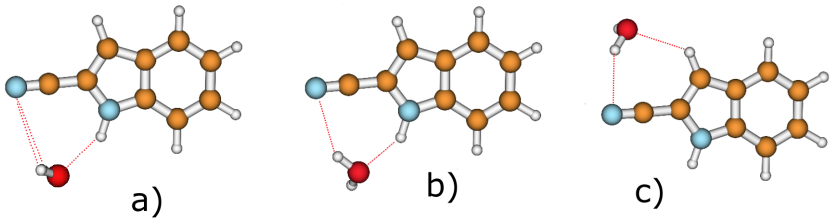

Figure S19: Starting geometries for the structure optimizations of 2-cyanoindole-$(H_2O)_1$ clusters.

Table S22: SCS-CC2/cc-pVTZ calculated and experimental wavenumber of the 45 normal modes of the ground and first electronically excited states of 2-CI, along with the respective symmetry labels and the leading coefficients of the Duschinsky matrix.
[a]The fundamental wavenumber of this mode has been determined from its overtone and/or combination bands of a" modes under harmonic assumption.

Mode	S_0			S_1			Duschinsky
	Sym.	Calc.	Obs.	Sym.	Calc.	Obs.	
$Q_1(S_0)$	a"	96.93		a"	83.44	87	$Q_1(S_1)$=+0.99 $Q_1(S_0)$
$Q_2(S_0)$	a'	134.00	136	a'	131.53	127	$Q_2(S_1)$=-0.99 $Q_2(S_0)$
$Q_3(S_0)$	a"	237.45		a"	188.12		$Q_3(S_1)$=+0.93 $Q_3(S_0)$-0.25 $Q_4(S_0)$
$Q_4(S_0)$	a"	251.61		a"	210.10		$Q_4(S_1)$=+0.92 $Q_4(S_0)$+0.25 $Q_3(S_0)$
$Q_5(S_0)$	a'	373.00	390	a"	317.04		$Q_5(S_1)$=-0.82 $Q_7(S_0)$-0.36 $Q_6(S_0)$
$Q_6(S_0)$	a"	375.91		a'	369.29	366	$Q_6(S_1)$=-0.99 $Q_5(S_0)$
$Q_7(S_0)$	a"	423.90		a"	398.72		$Q_7(S_1)$=+0.77 $Q_9(S_0)$-0.42 $Q_{11}(S_0)$
$Q_8(S_0)$	a'	443.26	460	a"	417.20		$Q_8(S_1)$=-0.82 $Q_{11}(S_0)$-0.44 $Q_9(S_0)$
$Q_9(S_0)$	a"	479.90		a'	420.53		$Q_9(S_1)$=-0.98 $Q_8(S_0)$
$Q_{10}(S_0)$	a'	560.94		a"	458.96		$Q_{10}(S_1)$=-0.86 $Q_6(S_0)$+0.32 $Q_7(S_0)$
$Q_{11}(S_0)$	a"	567.62		a"	514.41		$Q_{11}(S_1)$=-0.97 $Q_{14}(S_0)$
$Q_{12}(S_0)$	a'	607.44	635	a'	557.57		$Q_{12}(S_1)$=+0.78 $Q_{10}(S_0)$+0.58 $Q_{12}(S_0)$
$Q_{13}(S_0)$	a'	623.70	652	a'	567.07		$Q_{13}(S_1)$=+0.75 $Q_{12}(S_0)$-0.62 $Q_{10}(S_0)$
$Q_{14}(S_0)$	a"	650.46		a'	591.80		$Q_{14}(S_1)$=+0.97 $Q_{13}(S_0)$
$Q_{15}(S_0)$	a"	729.03		a"	630.96		$Q_{15}(S_1)$=+0.66 $Q_{16}(S_0)$-0.48 $Q_{15}(S_0)$-0.34 $Q_{11}(S_0)$
$Q_{16}(S_0)$	a"	760.29		a"	657.17		$Q_{16}(S_1)$=+0.81 $Q_{15}(S_0)$+0.38 $Q_{16}(S_0)$+0.36 $Q_{19}(S_0)$
$Q_{17}(S_0)$	a"	812.33		a"	719.26		$Q_{17}(S_1)$=-0.64 $Q_{19}(S_0)$+0.50 $Q_{16}(S_0)$+0.47 $Q_{17}(S_0)$
$Q_{18}(S_0)$	a'	813.42	842	a"	736.24		$Q_{18}(S_1)$=-0.89 $Q_{21}(S_0)$+0.33 $Q_{22}(S_0)$
$Q_{19}(S_0)$	a"	850.13		a'	746.95		$Q_{19}(S_1)$=+0.97 $Q_{18}(S_0)$
$Q_{20}(S_0)$	a'	899.78		a"	773.02		$Q_{20}(S_1)$=+0.80 $Q_{17}(S_0)$+0.55 $Q_{19}(S_0)$
$Q_{21}(S_0)$	a"	933.08		a"	825.89		$Q_{21}(S_1)$=+0.88 $Q_{22}(S_0)$+0.34 $Q_{21}(S_0)$
$Q_{22}(S_0)$	a"	957.84		a'	875.90		$Q_{22}(S_1)$=+0.92 $Q_{20}(S_0)$-0.36 $Q_{23}(S_0)$
$Q_{23}(S_0)$	a'	985.76		a'	891.00		$Q_{23}(S_1)$=+0.88 $Q_{23}(S_0)$+0.35 $Q_{20}(S_0)$
$Q_{24}(S_0)$	a'	1027.28	1063	a'	966.89		$Q_{24}(S_1)$=+0.97 $Q_{24}(S_0)$
$Q_{25}(S_0)$	a'	1136.84		a'	1061.12		$Q_{25}(S_1)$=+0.93 $Q_{25}(S_0)$
$Q_{26}(S_0)$	a'	1150.61	1173	a'	1115.97		$Q_{26}(S_1)$=-0.62 $Q_{27}(S_0)$+0.49 $Q_{28}(S_0)$
$Q_{27}(S_0)$	a'	1175.04		a'	1169.85		$Q_{27}(S_1)$=-0.78 $Q_{26}(S_0)$+0.53 $Q_{27}(S_0)$
$Q_{28}(S_0)$	a'	1231.95		a'	1177.22		$Q_{28}(S_1)$=-0.43 $Q_{26}(S_0)$-0.52 $Q_{27}(S_0)$-0.56 $Q_{28}(S_0)$
$Q_{29}(S_0)$	a'	1249.78	1271	a'	1226.70		$Q_{29}(S_1)$=+0.92 $Q_{29}(S_0)$-0.34 $Q_{28}(S_0)$
$Q_{30}(S_0)$	a'	1322.29	1339	a'	1279.52		$Q_{30}(S_1)$=-0.49 $Q_{28}(S_0)$+0.58 $Q_{31}(S_0)$+0.34 $Q_{32}(S_0)$+0.39 $Q_{33}(S_0)$
$Q_{31}(S_0)$	a'	1359.19	1359	a'	1313.90		$Q_{31}(S_1)$=-0.80 $Q_{30}(S_0)$-0.41 $Q_{31}(S_0)$
$Q_{32}(S_0)$	a'	1404.21	1420	a'	1373.25		$Q_{32}(S_1)$=-0.63 $Q_{31}(S_0)$+0.37 $Q_{32}(S_0)$+0.62 $Q_{33}(S_0)$
$Q_{33}(S_0)$	a'	1439.45		a'	1407.53		$Q_{33}(S_1)$=-0.44 $Q_{32}(S_0)$+0.74 $Q_{34}(S_0)$
$Q_{34}(S_0)$	a'	1477.38	1497	a'	1444.65		$Q_{34}(S_1)$=-0.73 $Q_{35}(S_0)$-0.55 $Q_{36}(S_0)$
$Q_{35}(S_0)$	a'	1524.46	1519	a'	1484.86		$Q_{35}(S_1)$=+0.56 $Q_{35}(S_0)$-0.75 $Q_{36}(S_0)$
$Q_{36}(S_0)$	a'	1549.07	1557	a'	1487.64		$Q_{36}(S_1)$=+0.40 $Q_{32}(S_0)$-0.37 $Q_{33}(S_0)$+0.74 $Q_{37}(S_0$
$Q_{37}(S_0)$	a'	1612.23	1605	a'	1592.35		$Q_{37}(S_1)$=+0.92 $Q_{38}(S_0)$
$Q_{38}(S_0)$	a'	1659.05		a'	1691.68		$Q_{38}(S_1)$=-0.46 $Q_{32}(S_0$-0.40 $Q_{34}(S_0)$+0.53 $Q_{37}(S_0)$
$Q_{39}(S_0)$	a'	2150.19		a'	2058.87		$Q_{39}(S_1)$=-0.99 $Q_{39}(S_0)$
$Q_{40}(S_0)$	a'	3195.56		a'	3202.36		$Q_{40}(S_1)$=+0.85 $Q_{40}(S_0)$+0.33 $Q_{41}(S_0)$+0.35 $Q_{43}(S_0)$
$Q_{41}(S_0)$	a'	3203.90		a'	3213.21		$Q_{41}(S_1)$=-0.37 $Q_{40}(S_0)$+0.84 $Q_{41}(S_0)$+0.38 $Q_{42}(S_0)$
$Q_{42}(S_0)$	a'	3214.88		a'	3223.44		$Q_{42}(S_1)$=-0.41 $Q_{41}(S_0)$+0.81 $Q_{42}(S_0)$+0.36 $Q_{43}(S_0)$
$Q_{43}(S_0)$	a'	3224.67		a'	3237.95		$Q_{43}(S_1)$=-0.39 $Q_{42}(S_0)$+0.85 $Q_{43}(S_0)$
$Q_{44}(S_0)$	a'	3275.51		a'	3268.65		$Q_{44}(S_1)$=-0.99 $Q_{44}(S_0)$
$Q_{45}(S_0)$	a'	3668.57		a'	3628.67		$Q_{45}(S_1)$=-0.99 $Q_{45}(S_0)$

Table S23: SCS-CC2/cc-pVTZ calculated and experimental wavenumber of the 54 normal modes of the ground and first electronically excited states of 2-cyanoindole$(H_2O)_1$, along with the respective symmetry labels and the leading coefficients of the Duschinsky matrix.
[a]The fundamental wavenumber of this mode has been determined from its overtone and/or combination bands of a" modes under harmonic assumption.

Mode	S_0			S_1			Duschinsky
	Sym.	Calc.	Obs.	Sym.	Calc.	Obs.	
$Q_1(S_0)$	a	53.14		a	48.52	44	$Q_1(S_1)$=+0.99 $Q_1(S_0)$
$Q_2(S_0)$	a	78.44	82	a	82.54	84	$Q_2(S_1)$=-0.99 $Q_3(S_0)$
$Q_3(S_0)$	a	95.46		a	95.27	94	$Q_3(S_1)$=-0.98 $Q_2(S_0)$
$Q_4(S_0)$	a	130.40	131	a	137.09	137	$Q_4(S_1)$=+0.96 $Q_4(S_0)$
$Q_5(S_0)$	a	156.20	156	a	160.44		$Q_5(S_1)$=+0.94 $Q_5(S_0)$-0.28 $Q_6(S_0)$
$Q_6(S_0)$	a	161.46		a	180.32		$Q_6(S_1)$=+0.29 $Q_5(S_0)$+0.90 $Q_6(S_0)$
$Q_7(S_0)$	a	241.57		a	189.46		$Q_7(S_1)$=-0.27 $Q_6(S_0)$+0.92 $Q_7(S_0)$
$Q_8(S_0)$	a	249.42		a	216.83		$Q_8(S_1)$=+0.93 $Q_8(S_0)$+0.26 $Q_{12}(S_0)$
$Q_9(S_0)$	a	291.64		a	312.33		$Q_9(S_1)$=+0.86 $Q_9(S_0)$+0.42 $Q_{12}(S_0)$
$Q_{10}(S_0)$	a	378.63	381	a	339.34		$Q_{10}(S_1)$=-0.48 $Q_9(S_0)$+0.80 $Q_{12}(S_0)$
$Q_{11}(S_0)$	a	420.85		a	375.00		$Q_{11}(S_1)$=-0.99 $Q_{10}(S_0)$
$Q_{12}(S_0)$	a	422.90		a	406.09		$Q_{12}(S_1)$=+0.86 $Q_{14}(S_0)$-0.33 $Q_{15}(S_0)$
$Q_{13}(S_0)$	a	448.82	443	a	424.30		$Q_{13}(S_1)$=+0.89 $Q_{13}(S_0)$+0.39 $Q_{11}(S_0)$
$Q_{14}(S_0)$	a	478.63		a	426.70		$Q_{14}(S_1)$=+0.82 $Q_{15}(S_0)$+0.42 $Q_{14}(S_0)$
$Q_{15}(S_0)$	a	561.73		a	483.91		$Q_{15}(S_1)$=+0.89 $Q_{11}(S_0)$-0.38 $Q_{13}(S_0)$
$Q_{16}(S_0)$	a	570.78	572	a	500.00		$Q_{16}(S_1)$=-0.83 $Q_{18}(S_0)$+0.40 $Q_{20}(S_0)$+0.25 $Q_{21}(S_0)$
$Q_{17}(S_0)$	a	607.48	608	a	563.07		$Q_{17}(S_1)$=-0.69 $Q_{17}(S_0)$-0.63 $Q_{16}(S_0)$-0.25 $Q_{19}(S_0)$
$Q_{18}(S_0)$	a	613.01		a	580.45		$Q_{18}(S_1)$=-0.74 $Q_{16}(S_0)$+0.65 $Q_{17}(S_0)$
$Q_{19}(S_0)$	a	626.25	627	a	598.98		$Q_{19}(S_1)$=+0.94 $Q_{19}(S_0)$
$Q_{20}(S_0)$	a	707.26		a	624.47		$Q_{20}(S_1)$=+0.52 $Q_{21}(S_0)$+0.51 $Q_{22}(S_0)$-0.38 $Q_{15}(S_0)$-0.40 $Q_{20}(S_0)$
$Q_{21}(S_0)$	a	734.43		a	665.79		$Q_{21}(S_1)$=-0.48 $Q_{20}(S_0)$+0.51 $Q_{21}(S_0)$-0.56 $Q_{22}(S_0)$-0.36 $Q_{25}(S_0)$
$Q_{22}(S_0)$	a	754.95		a	699.34		$Q_{22}(S_1)$=+0.51 $Q_{20}(S_0)$-0.41 $Q_{25}(S_0)$+0.39 $Q_{21}(S_0)$+0.32 $Q_{22}(S_0)$+0.31 $Q_{23}(S_0)$
$Q_{23}(S_0)$	a	807.70		a	744.82		$Q_{23}(S_1)$=+0.55 $Q_{27}(S_0)$+0.54 $Q_{23}(S_0)$+0.43 $Q_{22}(S_0)$
$Q_{24}(S_0)$	a	815.42	811	a	750.29		$Q_{24}(S_1)$=+0.70 $Q_{24}(S_0)$+0.55 $Q_{27}(S_0)$
$Q_{25}(S_0)$	a	845.89	839	a	756.46		$Q_{25}(S_1)$=-0.53 $Q_{23}(S_0)$-0.60 $Q_{24}(S_0)$+0.38 $Q_{27}(S_0)$
$Q_{26}(S_0)$	a	899.70	890	a	767.36		$Q_{26}(S_1)$=-0.71 $Q_{25}(S_0)$-0.37 $Q_{23}(S_0)$-0.33 $Q_{21}(S_0)$-0.25 $Q_{28}(S_0)$
$Q_{27}(S_0)$	a	930.03		a	835.62		$Q_{27}(S_1)$=-0.87 $Q_{28}(S_0)$+0.38 $Q_{27}(S_0)$+0.27 $Q_{25}(S_0)$
$Q_{28}(S_0)$	a	953.47		a	875.96		$Q_{28}(S_1)$=-0.87 $Q_{26}(S_0)$+0.45 $Q_{29}(S_0)$
$Q_{29}(S_0)$	a	984.68		a	888.17		$Q_{29}(S_1)$=-0.83 $Q_{29}(S_0)$-0.46 $Q_{26}(S_0)$
$Q_{30}(S_0)$	a	1026.42	1018	a	972.01		$Q_{30}(S_1)$=+0.97 $Q_{30}(S_0)$
$Q_{31}(S_0)$	a	1136.49	1130	a	1060.26		$Q_{31}(S_1)$=+0.92 $Q_{31}(S_0)$
$Q_{32}(S_0)$	a	1151.18		a	1116.17		$Q_{32}(S_1)$=-0.66 $Q_{33}(S_0)$-0.38 $Q_{34}(S_0)$
$Q_{33}(S_0)$	a	1174.41	1162	a	1169.49		$Q_{33}(S_1)$=-0.68 $Q_{32}(S_0)$+0.58 $Q_{33}(S_0)$
$Q_{34}(S_0)$	a	1245.78	1240	a	1175.05		$Q_{34}(S_1)$=-0.63 $Q_{32}(S_0)$+0.49 $Q_{34}(S_0)$-0.39 $Q_{33}(S_0)$+0.27 $Q_{36}(S_0)$
$Q_{35}(S_0)$	a	1269.42	1257	a	1239.10		$Q_{35}(S_1)$=+0.69 $Q_{35}(S_0)$-0.58 $Q_{34}(S_0)$
$Q_{36}(S_0)$	a	1326.86	1309	a	1286.95		$Q_{36}(S_1)$=+0.63 $Q_{37}(S_0)$+0.58 $Q_{35}(S_0)$+0.32 $Q_{39}(S_0)$
$Q_{37}(S_0)$	a	1364.42	1363	a	1313.30		$Q_{37}(S_1)$=-0.83 $Q_{36}(S_0)$+0.36 $Q_{34}(S_0)$
$Q_{38}(S_0)$	a	1407.36		a	1388.46		$Q_{38}(S_1)$=+0.72 $Q_{39}(S_0)$-0.59 $Q_{37}(S_0)$
$Q_{39}(S_0)$	a	1444.31	1441	a	1414.28		$Q_{39}(S_1)$=+0.72 $Q_{40}(S_0)$-0.48 $Q_{38}(S_0$-0.31 $Q_{43}(S_0)$
$Q_{40}(S_0)$	a	1479.12	1479	a	1448.23		$Q_{40}(S_1)$=-0.77 $Q_{41}(S_0)$-0.48 $Q_{42}(S_0)$+0.31 $Q_{44}(S_0)$
$Q_{41}(S_0)$	a	1529.80		a	1463.18		$Q_{41}(S_1)$=+0.66 $Q_{43}(S_0)$-0.54 $Q_{38}(S_0)$+0.38 $Q_{39}(S_0)$
$Q_{42}(S_0)$	a	1548.65		a	1498.34		$Q_{42}(S_1)$=+0.83 $Q_{42}(S_0)$-0.46 $Q_{41}(S_0)$
$Q_{43}(S_0)$	a	1610.49		a	1584.03		$Q_{43}(S_1)$=+0.91 $Q_{44}(S_0)$+0.34 $Q_{41}(S_0)$
$Q_{44}(S_0)$	a	1659.36		a	1673.78		$Q_{44}(S_1)$=+0.99 $Q_{45}(S_0)$
$Q_{45}(S_0)$	a	1671.32	1670	a	1683.60		$Q_{45}(S_1)$=+0.60 $Q_{43}(S_0)$+0.56 $Q_{40}(S_0)$+0.42 $Q_{38}(S_0)$
$Q_{46}(S_0)$	a	2143.82		a	2039.74		$Q_{46}(S_1)$=-0.99 $Q_{46}(S_0)$
$Q_{47}(S_0)$	a	3193.77		a	3200.05		$Q_{47}(S_1)$=+0.88 $Q_{47}(S_0)$+0.31 $Q_{50}(S_0)$+0.25 $Q_{48}(S_0)$+0.25 $Q_{49}(S_0)$
$Q_{48}(S_0)$	a	3202.88		a	3213.58		$Q_{48}(S_1)$=+0.86 $Q_{48}(S_0)$+0.37 $Q_{49}(S_0)$-0.28 $Q_{47}(S_0)$
$Q_{49}(S_0)$	a	3214.20		a	3220.36		$Q_{49}(S_1)$=+0.84 $Q_{49}(S_0)$-0.37 $Q_{48}(S_0)$+0.31 $Q_{50}(S_0)$-0.24 $Q_{47}(S_0)$
$Q_{50}(S_0)$	a	3223.39		a	3236.11		$Q_{50}(S_1)$=+0.87 $Q_{50}(S_0)$-0.30 $Q_{49}(S_0)$-0.29 $Q_{47}(S_0)$
$Q_{51}(S_0)$	a	3274.14		a	3267.00		$Q_{51}(S_1)$=-0.99 $Q_{51}(S_0)$
$Q_{52}(S_0)$	a	3513.77		a	3442.37		$Q_{52}(S_1)$=-0.99 $Q_{52}(S_0)$
$Q_{53}(S_0)$	a	3782.20		a	3755.13		$Q_{53}(S_1)$=-0.99 $Q_{53}(S_0)$
$Q_{54}(S_0)$	a	3898.78		a	3890.16		$Q_{54}(S_1)$=-0.99 $Q_{54}(S_0)$

Table S24: Fitted displacement factors of 2-CI upon electronic excitation along 9 normal modes from the FC fit.

Mode	displacement
Q_{35}	0.04262 ± 0.01235
Q_{29}	-0.054786 ± 0.025119
Q_{24}	-0.041954 ± 0.0080509
Q_{18}	0.042886 ± 0.0062327
Q_{13}	0.14043 ± 0.0044982
Q_{12}	0.12904 ± 0.009293
Q_{8}	0.00062161 ± 0.0019915
Q_{5}	-0.04222 ± 0.030025
Q_{2}	-0.071149 ± 0.0085876

Table S25: Fitted displacement factors of 2-cyanoindole(H_2O)$_1$ upon electronic excitation along 7 normal modes from the FC fit.

Mode	displacement
Q_{37}	-0.049751 ± 0.010681
Q_{30}	0.016004 ± 0.015779
Q_{19}	0.020952 ± 0.0080348
Q_{17}	-0.021059 ± 0.007891
Q_{13}	-0.0086228 ± 0.016225
Q_{4}	-0.03777 ± 0.0032701
Q_{2}	0.019872 ± 0.10625

Table S26: Intensities of the observed emission bands of three vibronic bands of 2-CI. The first line gives the wavenumber of the excited bands, the first column the wavenumber of the emission bands. The entries of the table represent the intensities, with the most intense band (apart from the excited band whose intensity is biased by stray light.) in each of the emission spectra normalized to 1.

S_0/S_1	Assigment	Theory	0,0	+ 127	+ 366
136	Q_2	134	0.49	1	
275	Q_2^2		0.02	0.23	
390	Q_5	373	0.11	0.02	1
460	Q_8	443	0.27		
514	$Q_2 + Q_5$		0.05	0.03	0.1
590	$Q_2 + Q_8$		0.1		
635	Q_{12}	607	0.78	0.06	
652	Q_{13}	623	1	0.03	
774	$Q_2 + Q_{12}$		0.1	0.17	
791	$Q_2 + Q_{13}$		0.1	0.18	
842	Q_{18}	813	0.38		
1030	$Q_5 + Q_{12}$		0.17		0.18
1063	Q_{24}	1027	0.8		
1173	Q_{26}	1150	0.31		
1210	$Q_5 + Q_{18}$		0.15	0.19	
1271	Q_{29}		0.47		
1286	$Q_2 + Q_{26}$		0.15		
1339	Q_{30}	1322	0.16		
1359	Q_{31}	1359	0.67		
1405	$Q_5 + Q_{24}$		0.69		
1420	Q_{32}	1404	0.93		
1442	$Q_{13} + Q_{18}$				0.2
1480	$Q_8 + Q_{24}$		0.38		
1497	Q_{34}	1477	0.2		
1519	Q_{35}	1524	0.31		
1542	$Q_2 + Q_{32}$		0.1		
1557	Q_{36}	1549	0.1		0.07
1605	Q_{37}	1612	0.29		
1659	$Q_{13} + Q_{24}$		0.6		0.1
1702	$Q_8 + Q_{28}$		0.26		
1738	$Q_5 + Q_{31}$				0.14
1782	$Q_5 + Q_{32}$				0.14
1800	$Q_5 + Q_{34}$				0.18
2483	Q_{29}^2		0.13		

Table S27: Intensities of the observed emission bands of two vibronic bands of 2-cyanoindole(H_2O)$_1$. The first line gives the wavenumber of the excited bands, the first column the wavenumber of the emission bands. The entries of the table represent the intensities, with the most intense band (apart from the excited band whose intensity is biased by stray light.) in each of the emission spectra normalized to 1.

S_0/S_1	Assigment	Theory	0,0	+ 137
82	Q_2	78	0.03	0.17
131	Q_4	130	1	1
156	Q_5	161		0.26
259	Q_4^2	260	0.11	
271	$Q_4 + Q_5$			0.64
289	$Q_4 + Q_6$			0.45
381	Q_{10}	378	0.04	0.13
443	Q_{13}	448	0.32	0.08
572	Q_{16}	570	0.09	
608	Q_{17}	607	0.75	0.08
627	Q_{19}	626	0.71	0.13
742	$Q_4 + Q_{17}$		0.19	
761	$Q_4 + Q_{19}$		0.19	0.13
811	Q_{24}	815	0.21	0.18
839	Q_{25}	845	0.07	
890	Q_{26}	899	0.05	
944	$Q_4 + Q_{24}$		0.07	
1018	Q_{30}	1026	0.4	
1130	Q_{31}	1136	0.33	
1162	Q_{33}	1174	0.11	
1240	Q_{34}	1245	0.19	
1257	Q_{35}	1269	0.30	
1309	Q_{36}	1326	0.34	
1350	$Q_2 + Q_{35}$		0.56	
1363	Q_{37}	1364	0.77	
1428	$Q_{17} + Q_{24}$		0.17	
1441	Q_{39}	1444	0.16	
1458	$Q_4 + Q_{36}$		0.13	
1479	Q_{40}	1479	0.12	
1494	$Q_4 + Q_{37}$		0.19	
1541	$Q_4 + Q_{38}$		0.26	
1638	$Q_{17} + Q_{30}$		0.22	
1670	Q_{45}	1671	0.09	

Table S28: SCS-CC2/cc-pVTZ calculated optimized S_0 cartesian coordinates of 2CI (in bohr).

c	-1.38997045	-4.54173926	0.00000000
c	1.28382066	-4.53334711	0.00000000
c	2.64547773	-2.29356771	0.00000000
c	1.25709447	-0.03651957	0.00000000
n	2.08118102	2.42917139	0.00000000
c	-0.00059703	4.01676973	0.00000000
c	-2.18857466	2.59321299	0.00000000
c	-1.42700003	0.00188555	0.00000000
c	-2.75506969	-2.30764559	0.00000000
h	-2.37733626	-6.33206735	0.00000000
h	2.28849634	-6.31450045	0.00000000
h	4.69087633	-2.29384018	0.00000000
h	-4.08023378	3.34582258	0.00000000
h	3.88950945	3.01463036	0.00000000
h	-4.80052635	-2.32992130	0.00000000
c	0.30203779	6.68740674	0.00000000
n	0.58081445	8.89424918	0.00000000

Table S29: SCS-CC2/cc-pVTZ calculated optimized S_1 cartesian coordinates of 2CI (in bohr).

c	-1.34815763	-4.56491406	0.00000000
c	1.32621809	-4.60541600	0.00000000
c	2.69837420	-2.29485216	0.00000000
c	1.28378913	-0.04502771	0.00000000
n	2.05685856	2.39186580	0.00000000
c	-0.06025908	4.10682125	0.00000000
c	-2.24116954	2.61568227	0.00000000
c	-1.49722526	0.03417365	0.00000000
c	-2.79904174	-2.26633047	0.00000000
h	-2.36041851	-6.34289885	0.00000000
h	2.31368733	-6.39133840	0.00000000
h	4.74218223	-2.26040262	0.00000000
h	-4.14614630	3.33689148	0.00000000
h	3.87238039	2.97373831	0.00000000
h	-4.84092334	-2.34117779	0.00000000
c	0.31408034	6.72138198	0.00000000
n	0.68577112	8.93180333	0.00000000

Table S30: SCS-CC2/cc-pVTZ calculated optimized S_0 cartesian coordinates of 2-cyanoindole-$(H_2O)_1$ (in bohr).

c	-2.28760076	-5.57188333	-0.15575320
c	0.38003472	-5.43861046	0.00430845
c	1.63219012	-3.13974112	0.10829511
c	0.14417797	-0.94476421	0.04773378
n	0.85919518	1.54681362	0.12211280
c	-1.29184302	3.02689951	0.01422481
c	-3.41964270	1.51549866	-0.12955282
c	-2.53811497	-1.03503215	-0.11164531
c	-3.75402070	-3.40488640	-0.21409553
h	-3.18740089	-7.40643383	-0.23219821
h	1.46453872	-7.17204359	0.04799987
h	3.67111563	-3.04246438	0.23456927
h	-5.34111583	2.18130497	-0.23002844
h	2.62473921	2.29031135	0.22041802
h	-5.79281096	-3.52340164	-0.33525188
c	-1.06398558	5.70369004	0.07247900
n	-0.74432291	7.90531921	0.13487293
o	4.93335187	5.24483370	0.30503692
h	3.84488877	6.66123640	0.67455971
h	5.76292214	5.73223966	-1.23769131

Table S31: SCS-CC2/cc-pVTZ calculated optimized S_1 cartesian coordinates of 2-cyanoindole-$(H_2O)_1$ (in bohr).

c	-2.23191289	-5.58350366	-0.13719523
c	0.42805897	-5.50169172	-0.00240046
c	1.68899920	-3.13001972	0.08474002
c	0.18107096	-0.94463354	0.02952163
n	0.84918747	1.51445653	0.08415697
c	-1.35077677	3.13172402	-0.00740629
c	-3.46452645	1.55010216	-0.12626903
c	-2.59522772	-0.99913495	-0.10929894
c	-3.78384489	-3.35024626	-0.19321649
h	-3.16382869	-7.40409557	-0.20115586
h	1.49762375	-7.23959781	0.03679913
h	3.72588238	-2.99974952	0.19541759
h	-5.40102297	2.17666322	-0.21136034
h	2.62296299	2.26344215	0.16925752
h	-5.81796092	-3.51935281	-0.29727083
c	-1.03454351	5.74665622	0.05147788
n	-0.56639494	7.94354554	0.11607286
o	4.85195697	5.19573874	0.35505563
h	3.66070040	6.55877741	0.60852086
h	5.79989266	5.71980556	-1.10505260

15 Danksagung

Zum Abschluss meiner Dissertation möchte ich mich bei einigen Leuten für ihre Hilfe und Unterstützung bedanken. Insbesondere bei

- Prof. Dr. Michael Schmitt für die Aufnahme in den Arbeitskreis, die Bereitstellung des interessanten Themas und für den freundlichen Umgang im Arbeitskreis
- Marie-Luise Hebestreit für ihre Ratschläge, Tipps und Freundschaft
- meiner Familie für die Motivation und Hilfe über das ganze Studium hinweg
- dem Großteil der Mitarbeiter des Lehrstuhls PC I für das angenehme Arbeitsklima
- Prof. Dr. Rainer Weinkauf für seine Bereitschaft sich als Zweitgutachter zur Verfügung zu stellen

Eigenständigkeitserklärung

Ich versichere an Eides Statt, dass die Dissertation von mir selbständig und ohne unzulässige fremde Hilfe unter Beachtung der „Grundsätze zur Sicherung guter wissenschaftlicher Praxis an der Heinrich-Heine-Universität Düsseldorf“ erstellt worden ist.

Düsseldorf, den _____

Christian Henrichs